

UNIVERSIDAD POLITÉCNICA DE MADRID

**ESCUELA TÉCNICA SUPERIOR DE
INGENIEROS INDUSTRIALES**

Instituto de Fusión Nuclear



**Simulación atomística de metales líquidos y
aleaciones para reactores de fusión nuclear**

**Atomistic simulation of liquid metals and alloys
for nuclear fusion reactors**

TESIS DOCTORAL

Alberto Fraile García

Licenciado en Ciencias Físicas por la Universidad de Zaragoza

2013

UNIVERSIDAD POLITÉCNICA DE MADRID

**ESCUELA TÉCNICA SUPERIOR DE
INGENIEROS INDUSTRIALES**

Instituto de Fusión Nuclear



**Simulación atomística de metales líquidos y aleaciones
para reactores de fusión nuclear**

**Atomistic simulation of liquid metals and alloys for
nuclear fusion reactors**

TESIS DOCTORAL

Alberto Fraile García

Licenciado en Ciencias Físicas por la Universidad de Zaragoza

Directores de Tesis:

Dr. José Manuel Perlado Marín

Catedrático de Ingeniería Nuclear

Universidad Politécnica de Madrid

Dr. Santiago Cuesta-López

Advanced Materials, Nuclear technology

Universidad de Burgos

2013

Tribunal nombrado por el Magfco. Y Excmo. Sr. Rector de la Universidad Politécnica de Madrid, el día 22 de _Enero_ de 2013.

Presidente: D. Jose María Martínez-Val Peñalosa

Vocal: D. Eduardo Marcial Bringa

Vocal: D. Angel Ibarra Sánchez

Vocal: D. Roberto Luis Iglesias Pastrana

Secretario: D. Pedro Velarde Mayol

Suplente: Dña. María José Caturla Terol

Suplente: D. Javier Sanz Gozalo

Opta a la mención de “Doctor Internacional”

Evaluadores de organizaciones internacionales:

Dr. Máximo Victoria (LLNL, USA)

Dr. Enrique Martínez (LANL, USA)

Realizado el acto de defensa y lectura de la Tesis el día 1 de Marzo de 2013 en la E.T.S. de Ingenieros Industriales de Madrid.

CALIFICACIÓN:

EL PRESIDENTE

LOS VOCALES

EL SECRETARIO

A mis padres



Aknowledment / Agradecimientos

I owe my sincere gratitude to all who have helped me, encouraged me, and believed in me through this challenging journey.

Foremost, I am deeply indebted to my thesis advisors, Professor Manuel Perlado and Dr Santiago Cuesta-López, for every advice and opportunity they provided me through the years. Their exceptional insight and broad-minded guidance led me the way to be a critical-thinking and self-stimulating physicist.

I would also like to express my sincere gratefulness to Dr Alfredo Caro for guiding me during my two summers in Los Alamos across the vast field of Molecular Dynamics.

Together with Dr Caro I would like to express my sincere gratitude to all the friends I met in Los Alamos, Magdalena Serrano-Caro, Enrique Martínez, Sonia Ballesteros, Alankar Alankar, Yelena Bagdasarova (that Rioja in The Dragonfly remains in my memory as the best wine ever!), Niraj Gupta, Jeffery Hetherly, Shivraj Karewar, Anand Kanjarla and Liang Zhang. I considered myself very fortunate to be able to spend a lot of time with these outstanding people. I hope to see all of you again and to repeat our trip to Las Vegas some day!

I owe my sincere thanks to Professor Jose María Martínez-Val, Dr. Pedro Velarde, Dr. Eduardo Bringa, Dr. Roberto Iglesias and Dr. Angel Ibarra for their precious time being in my thesis defense committee.

Special thanks for his help with paperwork in the Department of Nuclear Engineering to Dr. Eduardo Gallego and Dr. Oscar Cabellos, always examples of super-efficiency.

There are so many great people at Institute of Nuclear Fusion and in the Department of Nuclear Engineering who have helped and inspired me in various ways. I will not attempt to write all their names. Just to say that their friendship and enthusiasm for science make the Institute the most exciting and stimulating place for working. However I have to add especial thanks to Nuria Gordillo, Carlo Guerrero, Miguel Magán, Santiago Terrón and Fernando Sordo.

All good things are three and so is the number of secretaries I had the opportunity to be assisted by: Elena Carpintero and Nuria Martínez at IFN and Francisca García Campayo at Depto of Nuclear Engineering.

I am thankful to current Science friends around UK, Dr Jorge Kohanoff, Dr Emilio Artacho Dr Felix Fernández-Alonso and Dr Franz Demmel, for a number of interesting discussions, and especially to Dr. Devashibhai Adroja, for so many things during my stay in ISIS, long time ago. I am deeply indebted not only because, there, I learned so much about Physics and I really enjoyed a nice time, but also, and more important, because I learned quite a lot about scientific integrity.

Y para terminar algunas líneas en español.

Quiero dedicar unas líneas a mis mejores amigos después de aquellos turbulentos años en la Universidad de Zaragoza, especialmente a mi colega de aventuras psicodélicas Cristian Burguete, a Ibón Toribio y a Luis Castillo (esos bocatas durante los días del cuento del monocristal de Ho aún son recordados), y muy especialmente también a Roberto Martínez compañero de viajes sin destino. Gracias especiales a Ana Arizaga, Capitán (o ya Comandante!) Alberto García-García (ese quenching del VSM ha pasado ya a la historia de las urgencias criogénicas!!) Roberto Boada y David Serrate por tan buenos ratos allá en el Laboratorio de Materia Condensada.

Gracias infinitas al Instituto de “Modified Ultra-high Studies” o MUS para abreviar. Muchas gracias por distintos consejos o ayudas informáticas y distintas discusiones informales. Han sido muchos días de fructíferas deliberaciones estadísticas “no te quedes los ases!”, teoremas “con tres figuras haces juego”, conjeturas “pares y la una es más improbable que la una sin pares (to be published 2014)” enunciados perfectamente demostrables (topológicamente) pero de escasa utilidad (“quito medias de seises”) disquisiciones geoestratégicas y muchas cosas más... pero siempre con permanente actitud “can-do” “will-do” y siempre dispuestos a olvidar las redencillas. Ellos son Manuel Cotelo, Alain Flores, Sergey Galushin, José Javier Herrero, Alberto García de la Varga, David Portillo, Santiago Sánchez-Cervera y también las vertiginosas y esquivas chicas que ya nos abandonaron hace tiempo Raquel Ochoa y Nuria Moral. Y como no, a los miembros fundadores Javier Jimenez y Eduardo Oliva. Ellos saben que pertenecerán siempre al Consejo de Sabios. Me siento afortunado de haberos conocido a todos y haber compartido tan buenos ratos.

Muchas gracias también a Jesús Salvador Martínez, investigador independiente y poeta de las ciencias. Todo cambia con buenos compañeros de despacho, y más si la gráfica está en unidades esotéricas! Volveremos al James Joyce y esta vez terminaremos la noche allí.

Gracias también a mis mejores amigos fuera del trabajo, en este caso amigas, Begoña Salvador, Sabina Falcó, Valeria Raciti y Aleksandra Nogueira. नमस्ते

Finalmente gracias de corazón a mi querida familia, especialmente a mis padres, hermanos y sobrinos por todo su apoyo, inspiración y ánimo.

Index

Abstract	19
Resumen	21
List of Figures	25
List of Tables	36

Chapter 1: Nuclear Fusion Technologies

1.1 Nuclear Fusion	42
1.2 Magnetic Fusion	45
1.3 Inertial Fusion	50

Chapter 2: Liquid metals and fusion technology

2.1 Liquid metals	58
2.1.1 Lithium divertor and plasma facing materials	59
2.1.2 Blanket	60
2.1.3 Pb-Li in the context of fusion energy	61
2.1.4 Li17Pb physical properties	63
2.1.5 Hydrogen isotopes inside liquid LiPb	69
2.1.6 Helium inside liquid LiPb	71
2.1.7 Helium bubbles inside liquid metals	73

Chapter 3: Molecular Dynamics in short

3.1 Thermodynamical ensembles	78
3.2 Molecular Dynamics	79
3.2.1 Integrators	80
3.2.2 Thermostats	81
3.2.3 Nosé-Hoover Thermostat	82
3.2.4 Periodic boundary conditions	83
3.3 Computational details	84
3.3.1 Sample creation	85
3.3.2 Energy minimization	85
3.3.3 Initial heating in the microcanonical ensemble (NVE)	85
3.3.4 Berendsen thermostat and barostat	86
3.3.5 Final heating and equilibration: N-H thermostat-barostat	86
3.4 Interatomic Potentials	87
3.5 Theory of EAM potentials	92
3.6 High pressure	95
3.7 Computational effort	97
3.8 Mathematical properties of EAM potentials	97
3.8.1 Stochastic properties of EAM model	98

Chapter 4: Atomistic molecular point of view for liquid lead and lithium.

4.1 Methodology	100
4.1.2 EAM potential for Pb	101
4.1.3 EAM potential for Li	103

4.2 Computational details	106
4.3 Results. Validation of Li and Pb EAM potentials	106
4.3.1. Study of static properties	107
4.3.2 Lindemann criterion	108
4.3.3 Structural properties	109
4.4 Thermodynamic properties	113
4.4.1 Free energy calculations	113
4.4.2 Solid / Einstein	116
4.4.3 Liquid / Ideal gas	117
4.5 Entropy of Melting	120
4.6 Liquid-Liquid Phase transitions	120
4.6.1 Pb high temperature: transition around 1000 K	121
4.7 Conclusions.....	123
 Chapter 5: LiPb interatomic potential	
5.1 The road to LiPb cross potential	125
5.1.1 Pb-Li. Effective representation	127
5.1.2 Mixing energy calculation (theory)	129
5.1.3 Cut-off	132
5.1.4 Pb-Li cross potential	132
5.1.5 Enthalpy of mixing	135
5.1.6 Potentials, Polynomials and Targets	136
5.1.7 Heat capacity	136
5.1.7.2 Heat capacity in LiPb system	138
5.1.8 Density of LiPb system	139

5.1.9 Volume	140
5.1.10 Eutectic	140
5.1.11 Structural properties	141
5.1.12 $\text{Li}_{50}\text{Pb}_{50}$	144
5.1.13 Structural factors	145
5.1.14 Problems: segregation	146
5.1.15 Pot-4 and Pot-5 comparison	147
5.1.16 (Visual) Segregation	149
5.1.17 Understanding segregation	151
5.1.18 $\text{Li}_{50}\text{Pb}_{50}$ crystal structure	152
5.2 A Brand New Potential	
5.2.1 $\text{Li}_{50}\text{Pb}_{50}$ cohesive energy and lattice parameter in the target	154
5.2.2 Fitting potential procedure	157
5.2.3 Short Range Order	161
5.2.4 Structural properties	162
5.2.5 Volume contraction	164
5.2.6 Heat capacity	165
5.2.7 Structure factors and neutron diffraction theory	166
5.2.8 $\text{Li}_{50}\text{Pb}_{50}$ $S(Q)$	171
5.2.9 SRO Analysis	174
5.2.10 Eutectic point	176
5.2.11 Phase Diagram	177
5.3 Conclusions	179

Chapter 6: Hydrogen in liquid metals

6.1 Computational details	183
6.2 Results	185
6.4. Discussion	187
6.5 Conclusions	191
Appendix A: Structure of liquid metals	192
Appendix B: Liquid metal diffusivities	196
Appendix C: Short Range Order	198
Appendix D: Literature Review	200

Chapter 7: Ab initio calculations of Helium inside Lithium and Lead

7.1 Introduction	204
7.1.1 He potential (Morisita He-He potential)	206
7.2 Computational details	207
7.3 Methodology	208
7.4 Results	211
7.4.1 Formation Energies	211
7.4.2 Charge transfer	214
7.4.3 Charge character	216
7.4.4 Density of States of He (inside metals)	219
7.4.5 Bader analysis	222
7.4.6 Charge Visualization	224
7.4.7 Forces	226
7.5 Conclusion	228

Appendix 1: Exploring the limits of classical molecular dynamics. Liquid Li and Pb under high pressure

A1 Introduction	229
A2 Computational details	231
A3 Results; Validation of the Li and Pb EAM potentials	231
A3.1 Bulk modulus in liquid phase	233
A3.2. Structural properties	234
A3.4. Uniform compression model	236
A3.5. Liquids under high pressure	239
A3.6. Thermodynamics	241
A3.6.1 Melting point	241
A4 Conclusions	244
References and Bibliography	247
Time will tell	267

Abstract

Classical Molecular Dynamics (CMD) simulations via EAM potentials have showed to be a powerful tool to simulate and understand liquid metals and alloys, in our particular case, Li and Pb. Our results prove the validity of these potentials and provide useful structural and thermodynamic data in conditions of interest to Nuclear Fusion technology. Reported figures are in agreement with experimental results available in the literature. In addition, our work represents a base methodology for the extrapolation of liquid Pb and Li properties into regions of temperature and composition where direct experimental measurements either do not exist, or are not accessible. Moreover, we have tested that our particular choice constitutes a solid base for the development of a future PbLi alloy potential.

The main results presented in Chapter 4 have been recently published in Journal of Nuclear Materials (Fraile 2013).

In addition our results prove the validity of these potentials and provide useful structural and thermodynamic data under high pressures (up to 5 or 10 GPa). Reported figures are in agreement with experimental or *ab initio* calculation results available in the literature up to certain limits. In addition, our work represents a base methodology for the extrapolation of liquid Pb and Li properties into regions of temperature and pressures where direct experimental measurements either do not exist, or are not accessible. In general, both potentials are realistic up to pressures around half the bulk modulus of the solid material. Structural properties can be well modeled with EAM potentials. Thermodynamic properties are much more difficult to match. For a realistic study of liquid under pressure ZBL modification of short range part of pair potentials is strongly encouraged.

As main goal of this Thesis we have developed a new LiPb interatomic potential. Our MD simulations gave good match of many structural, thermodynamic and dynamic properties around the eutectic concentration. This is not so difficult to accomplish and different potentials can lead to very similar structural properties but different thermodynamic ones so a careful examination of different physical properties is mandatory.

Higher Li concentrations showed more difficult to describe by a simple EAM/alloy potential due to possible charge transfer between Li and Pb ions. The difference observed between calculated structural properties compared with experiments can be explained in terms of the

Batia-Thorton theory. The main results described in that chapter will be submitted probably to Physical Review B.

A realistic interatomic potential like the proposed one would be useful to simulate several problems of scientific and technological interest like solidification process and the study of cooling ratio effect in the solid structure of the alloy, determination of the optimal composition for eutectic behavior etc.

Introduction of a third kind of atom (He and/or H) in the system is being studied. This, for example, will permit to study the solubility of tritium (or helium) in LiPb eutectic alloy *in silico*.

In Chapter 7 we have shown that H diffusion in liquid metals seems to be not as simple as a classical molecular dynamics study suggest. In an oversimplified point of view the main results point to some simple kinetic behavior of H diffusion in our MD simulations, i.e. H diffusivity values are given by the host metal self diffusivity multiplied by some mass ratio factor. However, the diffusional properties of H in metals is likely to be influenced, or even controlled, by quantum and tunneling effects since H is the lightest of all elements.

The main results were presented in the recent TNT 2012 (Trends on Nanotechnology International Congress) in Madrid, in an oral presentation.

And to conclude, we have determined some elementary properties of He in Pb and Li by *ab initio* calculations. The most stable configuration for He in interstitial configuration is the substitutional one both in fcc Pb and bcc Li. For Lithium both tetrahedral and octahedral interstitial are similar energetically. For Pb the octahedral position is slightly favoured. Our spin-orbit coupling calculations suggest that the magnetism in fcc Pb affects the formation energy of He interstitials but does not alter their relative stabilities. Charge transfer and hybridization effects are being carefully examined.

The simulations presented in this chapter are the first step to develop a ternary interatomic potential for LiPb+He CMD simulations. He interaction with both Li and Pb will be mainly repulsive as expected. However taking into account spin orbit coupling in the Pb simulations will give a different set of forces leading ultimately to a different potential.

Resumen

La presente tesis comprende un estudio de metales líquidos, Li, Pb y eutéctico Li17Pb en el ámbito de la tecnología de fusión nuclear. Uno de los problemas fundamentales en futuros reactores de fusión es la producción y extracción de tritio (T) en la denominada envoltura regeneradora (blanket en inglés). Dicho blanket tendrá dos propósitos, la extracción del calor generado por las reacciones de fusión para su posterior conversión en energía eléctrica así como la producción de T para realimentar el proceso. Dicha producción se realizará mediante el “splitting” del Li con los neutrones provenientes de la fusión. Esta reacción produce T y helio (He) por lo que la interacción del T y el He con el metal líquido, con los materiales estructurales así como la interacción del T con el He en forma de burbujas es un problema fundamental aun no bien entendido y de gran importancia para futuros diseños.

Los capítulos 1, 2 y 3 presentan una introducción a dichos problemas. El capítulo 1 introduce al lector en la tecnología de fusión nuclear. El segundo capítulo explica en mayor detalle el uso de metales líquidos en reactores de fusión, no solo en blankets sino también como primera pared, divertor etc, lo que se denomina en general “plasma facing materials”. Por último se ofrece una breve introducción a las técnicas de dinámica molecular clásica (CMD) y un breve resumen de los potenciales más usados.

El estudio se ha llevado a cabo utilizando simulación atomística mediante potenciales semi-empíricos del tipo átomo embebido (EAM). La Tesis consta de 4 partes bien definidas.

En primer lugar se verificó la idoneidad de los potenciales tipo EAM para simular las propiedades de los metales Li y Pb en fase líquida. Dicho estudio se detalla en el Capítulo 4 y en su extensión, el Apéndice 1, en el que se estudia los límites de validez de esta aproximación.

Los resultados de dicho estudio han sido publicados y presentados en diversos congresos internacionales. Un resumen de la metodología seguida fue publicado como capítulo de libro en Technofusión 2011. Los resultados se presentaron en diversos congresos internacionales, entre ellos ICENES 2011, (Artículo en ICENES Proceedings), ICOPS-SOFE 2011, en una presentación oral etc.

El trabajo ha sido aceptado recientemente en Journal of Nuclear Materials (Fraile *et al* 2013).

La segunda parte y más importante comprende el desarrollo de un potencial para el estudio de la mezcla de ambos metales. Éste es el trabajo más novedoso e importante dado que no existía en la literatura un potencial semejante. Se estudiaron dos aproximaciones distintas al problema, un potencial tipo EAM/cd y un potencial EAM/alloy. Ambos potenciales dan resultados satisfactorios para la simulación del eutéctico (y concentraciones de Li menores que el 17%). Sin embargo el sistema LiPb en todas las concentraciones es un sistema que se aparta enormemente de una solución ideal y dicho potencial no daba buenos resultados para mezclas PbLi con concentraciones de Li grandes. Este problema fue solventado mediante el desarrollo de un segundo potencial, tipo EAM/alloy (segunda parte del Capítulo 5).

Dicho trabajo será enviado a Physical Review B, y una extensión junto con un estudio detallado de las propiedades del eutéctico de acuerdo con nuestras simulaciones será publicada a continuación.

En tercer lugar se estudió el problema de la difusividad del H en metales líquidos aprovechando distintos potenciales existentes en la literatura. El problema del H en metales líquidos es importante no solo en metalurgia sino también en geofísica. En dicho capítulo se estudió la difusividad del H en Pd, Ni y Al con potenciales tipo EAM, y también con un potencial más sofisticado que tiene en cuenta la dependencia angular de las interacciones (ADP por sus siglas en inglés). De este modo disponemos de un estudio detallado del problema con diferentes modelos y diferentes metales. La conclusión apunta a que si se compara con los resultados experimentales (muy escasos) los resultados obtenidos mediante CMD dan valores bajos de la difusividad del H. Las razones de dicho desacuerdo entre simulación y experimentos se detallan en el Capítulo 6.

Este estudio ha sido presentado en una presentación oral en el reciente congreso internacional “Trends on Nanotechnology” TNT 2012 celebrado en Madrid. El trabajo será publicado en un futuro próximo.

Por último, como se dijo anteriormente, el estudio del He, la formación de burbujas en metales líquidos, su difusión nucleación y cavitación es otro problema deseable de ser estudiado mediante técnicas atómicas. Para ello es necesario el desarrollo de diversos potenciales, He-Li, He-Pb y un potencial ternario Pb-Li-He. Para ello se han realizado simulación *ab initio* de los sistemas Pb+He y Li+He. Dicho estudio pretende calcular las fuerzas entre los átomos del metal (Pb o Li) con intersticiales de He. De este modo aplicaremos el “force matching method” (FMM) para el desarrollo de dichos potenciales.

En el Capítulo 7 se detallan los resultados obtenidos referidos a las posiciones más favorables de las impurezas de He dentro de redes cristalinas de Pb y Li así como el efecto de tener en cuenta el acoplo spin-orbita (SOC en inglés). El análisis de los resultados en términos de transferencia de carga y análisis de las densidades electrónicas, así como la creación de los potenciales mencionados está en progreso.

En conjunto la tesis presenta un estudio de los diversos problemas relacionados con el uso de metales líquidos en reactores de fusión y representa un primer paso en la determinación de parámetros de gran importancia para el diseño de blankets y sistemas de primera pared. Con la simulación MD de dichos problemas mediante, importante, potenciales realistas, valores de difusión, solubilidad etc de especies ligeras, H (o sus isotopos) y He en metales líquidos podrá ser calculada complementando así la base de datos que presenta enormes incertidumbres.

List of Figures

Chapter 1: Nuclear Fusion Technologies

Fig. 1.1. The temperatures and densities of different plasmas. Extreme matter exists inside gamma-ray bursts, hot neutron stars, and the plasmas produced by high-power lasers. Non-extreme matter includes sea-level air at room temperature and, the surface of the sun.

Fig. 1.2. Three parameters (plasma temperature, T_e , density, n_e , and confinement time, τ_e) need to be simultaneously achieved for sustained fusion to occur in a plasma for three different nuclear reactions, D-T, D-D and D- ^3He as labelled.

Fig. 1.3. Left) The Fusion Triple Product can be compared with leading edge performance of the devices year-on-year. Right) The Fusion Triple Product (here quality of confinement) for inertial fusion experiments along the years.

Fig. 1.4. Illustrating the main features of a tokamak.

Fig 1.5. JET chamber in Culham, U. K. Picture taken from <http://www.jet.efda.org>.

Fig. 1.6. Summary of different magnetic and inertial (upper left corner) experiments around the world. (figure taken from (Meade 2010)).

Fig. 1.7. The W7-X stellarator with its helically shaped plasma and the coils required to support it. The average major radius of a plasma is 5.5 m. Figure taken from (Boozer 2004).

Fig. 1.8. In ICF, a spherically converging shock (green arrows) compresses a millimeter-size metal capsule (blue) filled with DT gas (red).

Fig. 1.9. Historical development of ICF with different drivers, laser, heavy ions and pulsed power.

Fig. 1.10. Direct-drive (*a*) and indirect-drive (*b*) laser fusion.

Fig. 1.11. The physics of high power laser interactions with solid targets (Thomas 2012).

Fig. 1.12. Phase diagram for the deuterium and hydrogen, the difference between H_2 and D_2 is shown (Kawamura 2008).

Fig. 1.13. Left) LIFE project, picture from NIF website. Right) European Inertial Confinement Fusion HiPER project. Both pictures are artist's impressions.

Fig. 1.14. Timeline for the proposed Laser Energy Programme [HiPER website].

Chapter 2: Liquid metals and fusion technology

Fig. 2.1: Scheme of Li limiter concept and its interaction with tokamak plasmas (Mirnov 2009).

Fig. 2.2: Left) Dual Coolant Lead-Lithium (DCLL) concept. Taken from Wong *et al* (Wong 2006). Right). Cut-off view of a blanket design taken from (Wu 2007).

Fig. 2.3: Density of liquid Li (Ohse, 1985) and Pb (Brandes 1983, Gurvich 1991) compared to the Li17Pb (Mas de les Valls 2008). Blue triangles stand for the linear interpolation of Li and Pb densities. Note the break in the y-axis.

Fig. 2.4: Viscosity of liquid Li (Ohse, 1985) and Pb (Brandes 1983, Gurvich 1991) compared to the Li17Pb eutectic (Mas de les Valls 2001). Blue triangles stand for the linear interpolation.

Fig. 2.5: Thermal conductivity of liquid Li (Ohse, 1985) and Pb (Brandes 1983, Gurvich 1991) compared to the Li17Pb (Mas de les Valls 2008).

Fig. 2.6: Surface tension of liquid Li (Ohse, 1985) and Pb (Brandes 1983, Gurvich 1991) compared to the Li17Pb (Mas de les Valls 2008).

Fig. 2.7: Tritium solubility database. Scatter reflects experimental approaches and measurement techniques applied. Knowledge of dynamic transport properties (diffusion, mass transfer, interface processes) is much more limited.

Fig. 2.8. He solubility (in mole of gas/mole of metal units) vs temperature (in K) in liquid Pb, Li and Li17Pb. Data taken from (Reed 1970) and (Shpil'rain 2007), blue triangles (this work).

Fig. 2.9. Helium diffusivity vs $1/T$ in liquid Li17Pb estimated from He and H diffusivities inside liquid Li (taken from (Mas de les Valls 2008)).

Fig. 2.10. Mechanisms of the pressure wave mitigation by bubbling (Futakawa 2008).

Chapter 3: Molecular Dynamics in short

Fig. 3.1. A general flow chart for molecular dynamics simulation. Up-right corner shows an initial sample of LiPb (B2 phase). Down-right corner shows the sample in liquid phase.

Fig. 3.2. Computer CPU time (in seconds) with two different integrators in different simulation stages (from left to right; NVE, Berendsen heating and final equilibration with N-H thermostat).

Fig. 3.3. Comparison of two different algorithms (black and green lines rESPA and red and blue ones to Verlet) in a MD run simulating the heating of a Pb sample with two different EAM potentials ((Pb) Zhou 2001) and ((Pb-Cu) Hoyt 2003).

Fig. 3.4. Illustration of periodic boundary conditions in 3D.

Fig. 3.5. Pair interatomic potential, $V(r)$ vs interatomic distance. Two distinct regimes depending on the distance are shown, repulsion (due to Pauli principle) and dipole-dipole attraction.

Fig. 3.6. Schematic relation of some physical properties with the interatomic potential.

Fig. 3.7: Universal screening potential (ZBL) and other approximations. Figure taken from <http://www.iue.tuwien.ac.at/phd/wittmann/node8.html>

Chapter 4: Atomistic molecular point of view for liquid lead and lithium

Fig. 4.1. Pair potentials for Pb and Li following references (Zhou 2001, Belaschenko 20011).

Fig. 4.2. Energy (in eV/at) of pure elements Pb and Li (in fcc and bcc structures respectively) vs lattice parameter, a_0 . The minimum corresponds to the cohesive energy. The experimental values of cohesive energy y-axis and lattice parameter (x-axis) are represented by triangles.

Fig. 4.3. Left) Melting of Pb using Lindemann criterion; $T_m(\text{Pb}) = 0.114 \text{ eV/at} / 8.61710\text{e}5 \text{ eV/K} \rightarrow 1322 \text{ K}$. Experimental melting point is 600 K. Right) Same calculation for Li; $T_m(\text{Li}) = 0.04 \text{ eV/at} / 8.61710\text{e}5 \text{ eV/K} \rightarrow 464 \text{ K}$. Experimental melting point is 453 K.

Fig. 4.4. Lithium $g(r)$ calculated (red circles) compared with experimental results (black squares) at $T = 460$ and 520 K . In both cases an excellent agreement between MD simulation – experiment in the radial distribution of the liquid phase is obtained. (Experimental data from (Waseda 1980)).

Fig. 4.5. Lead $g(r)$ calculated (red circles) compared with experimental results (black squares) temperature ranging from $T = 610 \text{ K}$ to $T = 1170 \text{ K}$. (Experimental data from (Waseda 1980)).

Fig. 4.6. Lithium $S(q)$ calculated (circles) compared with experimental results (triangles) at $T = 460$ and 520 K . (Experimental data from [Waseda website]).

Fig. 4.7. Lead $S(q)$ calculated (circles) compared with experimental results (triangles) at temperatures ranging from 610 to 1120 K. (Experimental data from [Waseda web]).

Fig. 4.8. Enthalpy, H , in eV/at, for both Pb and Li calculated in a MD run. The jump in H corresponds to the melting of the sample, but not with the melting temperature.

Fig. 4.9. Volume, V , in cm^3/mole , for both Pb (black) and Li (red) calculated in a MD run. The jump in V corresponds to the melting of the sample, but not with the melting temperature.

Fig. 4.10. Schematic representation of switching Hamiltonian technique in solid phase.

Fig. 4.11. Schematic representation of switching Hamiltonian technique in liquid phase.

Fig. 4.12. Liquid runs. Left), liquid switch vs λ , right), volume expansion vs density. Three different potentials are used. Results in liquid switch are almost potential independent.

Fig. 4.13. Free energies vs temperature for pure Li (up) and Pb (down) in solid (black lines) and liquid (red lines) phase. Crossing point of both correspond to T_m . The blue dashed lines are a guide to the eye.

Fig. 4.14. Reciprocal of Pb magnetic susceptibility versus temperature during cooling process (Hou 2006).

Fig. 4.15. Left) Wendt Abraham parameter, R^{WA} , vs temperature in liquid Pb. Red line represents a linear fit and dashed line is a guide to the eye. Right) Translational order parameter vs temperature in liquid Pb.

Chapter 5: LiPb interatomic potential

Fig. 5.1. Experimental phase diagram for LiPb system (Okamoto 1993).

Fig. 5.2. Minimum in the total energy (y axis) for lead (left) and lithium (right) calculated from original EAM potentials (Zhou 2001, Belashchenko 2009), x axis is distance in Å.

Fig. 5.3. Left) Experimental partial enthalpy of Li and the integral enthalpy of mixing for the Li-Pb liquid alloys (Gasior 2001) at 800 K. Right) Measured heat of formation ΔH (Ruppertsberg 1976) and electron-gas contribution ΔH_{eg} at $T = 1000$ K (Hafner 1984).

Fig. 5.4. EAM potentials. Pair potentials vs interatomic distance in Å.

Fig. 5.5. Contribution of the embedding function to the enthalpy of mixing of LiPb alloys. Ideally it should be exactly zero.

Fig. 5.6: Left) Calculated ΔH at $T = 800$ K compared with experimental data (Gasior 2001). Right) **5.7:** Calculated ΔH at $T = 1000$ K compared with experimental data (Ruppertsberg 1976).

Fig. 5.7. Left) Targets for LiPb EAM/cd potentials. Right) Polynomials obtained with the targets shown in left picture.

Fig. 5.8 Calculated enthalpy of Li17Pb from two different MD simulations. (Black squares 2048 atoms, red circles 13500). Blue arrow signals the enthalpy jump at melting.

Fig. 5.9: Calculated heat capacity of liquid Li17Pb using different potentials compared to experimental data (Mas de les Valls 2001). MD heating runs with T ranging from 900 to 1400K.

Fig. 5.10. Heat capacity of LiPb system using two different potentials (pot4 and pot5) compared with experimental data (Saar 1987).

Fig. 5.11. Calculated density of Li-Pb system from MD simulations. ($N = 4000$ atoms) compared with experimental values (green triangles) taken from (Saar 1987).

Fig. 5.12. Calculated volume of $\text{Li}_{1-x}\text{Pb}_x$ compounds with 3 different potentials. MD heating run, $N=13500$ atoms, total simulation time 45 ps. Experimental data from (Saar 1987).

Fig. 5.13. Calculated density of Li_{17}Pb from MD simulations ($N = 13500$) compared with experimental values (black).

Fig. 5.14. Partial $g(r)$ calculated from MD cooling runs at $T = 508$ K (left) and $T = 594$ K (right).

Fig. 5.15. Calculated density of $\text{Li}_{50}\text{Pb}_{50}$ from MD simulations ($N = 13500$) compared with experimental values (cyan) taken from (Saar 1987).

Fig. 5.16. RDF $g_{\text{LiLi}}(r)$, $g_{\text{LiPb}}(r)$ and $g_{\text{PbPb}}(r)$ for the liquid $\text{Li}_{0.8}\text{Pb}_{0.2}$ (solid line - black) and $\text{Li}_{50}\text{Pb}_{50}$ (broken line - red) alloys. Left graphs taken from (Senda 2001).

Fig. 5.17. Left) Pb SRO in LiPb system calculated using potentials number 4 and 5. Right) Li SRO.

Fig. 5.18. Left) Pb SRO in LiPb system calculated using potential 5 at several simulation times, 8 ps 15 ps 30 ps and 45 ps as labelled. Right) Li SRO in LiPb system.

Fig. 5.19. Li SRO values calculated from MD runs data for nine different LiPb systems at four different times. ($T = 1000$ K and $N = 13500$ atoms, potential number 5)

Fig. 5.20. Calculated SRO for $\text{Li}_{80}\text{Pb}_{20}$ at $T = 1100$ K for two different size simulations ($N = 500$ and $N = 13500$). In black fcc Pb SRO, in red Li SRO.

Fig. 5.21. Snapshot after a MD heating run up to 1300 K of a $\text{Li}_{50}\text{Pb}_{50}$ sample starting from a bcc lattice ClCs type. System shows homocoordination.

Fig. 5.22. Snapshot after a MD heating run up to 1300 K of a $\text{Li}_{50}\text{Pb}_{50}$ sample starting from a fcc lattice ($N = 500000$). System still shows homocoordination.

Fig. 5.23. Calculated SRO for LiPb system at liquidus temperature for two different size simulations ($N = 10000$ and $N = 500000$). In black Pb SRO, in red Li SRO.

Fig. 5.24. A $\text{Li}_{40}\text{Pb}_{60}$ alloy “artificially” segregates in two “phases”, one rich in Li (around 75% Li +Pb) and another one rich in Pb (10 % Li +Pb).

Fig. 5.25. LiPb CS: Left at high temperature ($T > 200$ °C) CS is a bcc cubic like the ClCs one (cP2, Pm-3m). At room temperature CS is the hR6 (Pearson Symbol) R-3m (Space group).

Fig. 5.26. Sample for LiPb B2 phase (ClCs-like) visualized with OVITO (Stukowski 2010).

Fig. 5.27. Partial RDFs of $\text{Li}_{50}\text{Pb}_{50}$ at 800 K (left) and 1300 K (right) starting from two different initial CS; In red the results using a fcc lattice with random substitution of Pb atoms and in black the same with a bcc lattice CICs type. From up to down, Li-Li, Li-Pb and Pb-Pb partial $g(r)$, as indicated in the figures.

Fig. 5.28. $\text{Li}_{50}\text{Pb}_{50}$ CS and nine first nearest neighbours. 1, 4 and 7 are different (\neq). The others are equal to the origin atom ($=$).

Fig. 5.29. $\text{Li}_{50}\text{Pb}_{50}$ Partial radial distribution functions (with $a = 3.5 \text{ \AA}$). The $g(r)$ peak positions and number of NN are given in table 5.VI.

Fig. 5.30: Match between our fitted potential (red line) and the original (black line) for very short distances ($r < 2.5 \text{ \AA}$).

Fig. 5.31. Different potentials obtained with two different definitions of energy in B2 phase compared with the average of Pb and Li pair potentials, V_{mix} .

Fig. 5.32. Fit of V_{mix} to a sum of splines. In black the average of Pb and Li pair potentials V_{mix} , and in red the fitting function.

Fig. 5.33. Enthalpy of mixing vs Li concentration. Experimental values taken from (Ruppertsberg 1975), MD results as labelled. Cohesive energy of LiPb in B2 phase, (purple square) is also used as a target. Orange square represent the result obtained with potential M1.

Fig. 5.34. SRO values vs Li concentration calculated with new potentials. As can be observed now SRO is not positive for intermediate Li concentrations (See figures 5.19-20 and 5.25).

Fig. 5.35. $Q(S(Q)-1)$ of liquid Li17 at $T = 775 \text{ K}$. Black squares are the experimental data (Ruppertsberg 1975) red circles and green triangles represent calculated data with pot. M1 and M3 respectively.

Fig. 5.36. Density of liquid eutectic calculated with potentials M1 and M3 (red circles and green triangles respectively). Black squares are the experimental data taken from (Mas 2008). Blue dashed line represents the result with Pot.5 (See figure 5.13).

Fig. 5.37. Li self diffusion in Li17Pb calculated with potentials M1 and M3 as labelled. Black squares taken from (Mas de les Valls 2008). Blue dashed line stands for the interpolation of theoretical data. Blue arrow denotes the working temperature window in breeder blankets.

Fig. 5.38. Volume contraction in liquid LiPb system. The system departs from ideal behavior (blue line). Experimental data from (Saar 1987). MD values calculated with three different potentials M1, M2 and M3 as labelled.

Fig. 5.39. Liquid LiPb alloys at 1000 K. Experimentally, C_p present a strong departure from ideality (violet dashed line). Remarkably the MD results also present similar behaviour.

Fig. 5.40. Liquid total structure factor $S(Q)$ of $\text{Li}_{50}\text{Pb}_{50}$ at 775 K. X-Ray scattering (red squares) and neutron scattering results (black squares). MD results: EAM/cd pot.5 (red line) or EAM/alloy potentials (blue and green squares).

Fig. 5.41. Weight factors, w , in $\text{Li}_{1-x}\text{Pb}_x$ alloys vs Pb concentration, x , (right part of LiPb phase diagram).

Fig. 5.42. Total structure factor, $S(q)$, of $\text{Li}_{50}\text{Pb}_{50}$ alloys at 775 K calculated from MD simulations (green and blue lines (pot M1 and Pot M3)) compared to $S_{\text{NN}}(q)$ taken from (Ruppersberg 1982).

Fig. 5.43. $S(q)$ of $\text{Li}_{50}\text{Pb}_{50}$ alloys at 775 K calculated from MD simulations green and blue lines (Pot M1 and Pot M3) compared to theoretical hard-sphere curve (Ruppersberg 1982). **Inset** shows liquid $\text{Li}_{50}\text{Pb}_{50}$ density vs T . Red squares represent the values obtained with MD. Black squares are the experimental values (Ruppersberg 1976). Blue dashed line stands for the results shown in Fig. 5.15.

Fig 5.44. Total pair distribution functions of liquid LiPb alloys ($T = 1000$ K) as labelled. Left) results with EAM/cd Pot-5. Right) Results with Potential M1.

Fig. 5.45. The difference of the electron-density distribution for the ionic configuration of the liquid $\text{Li}_{80}\text{Pb}_{20}$ alloy from the linear combination of the atomic valence-electron-density distribution. The Li and Pb ions are drawn as blue and red balls, respectively (Senda 2000).

Fig. 5.46. Ordering potential, φ_{CC} , is symmetric by definition \rightarrow SRO will be also symmetric!?

Fig 5.47. Left) Partial, Wendt–Abraham Parameter, $r_{\text{AB}}^{\text{WA}}$, for LiPb alloys close to the eutectic point at $T=1000$ K. Right) Partial translational parameter, ζ , for LiPb alloys close to the eutectic point at 1000K.

Fig 5.48. Left) KE/PE ratio for six different LiPb eutectics vs temperature. Right) Critical temperature vs Li concentration calculated from Li and Pb SRO in the melt.

Fig 5.49. $\text{Li}_{50}\text{Pb}_{50}$ (B2) free energies calculated with potential M1: Melting point is very close to the experimental value, MD = 720, Exp 755 K.

Fig 5.50. Pb-rich part of LiPb phase diagram; Red and green lines represent a simple the estimation from MD heating cycles. Black lines represent the experimental phase diagram according to (Okamoto 1993).

Chapter 6: Hydrogen in liquid metals

Fig. 6.1. Taken from Ref. (Karpov 2007). Structures of gasars: (a) longitudinal section, (b) transverse section ($\times 5$), (c) image in the scanning electron microscope ($\times 20$).

Fig. 6.2. Diffusivity values for H in Pd compared with host metal self-diffusivity (black squares). H diffusivity (red triangles) is close to the calculated (blue) following Eq. 6.1.

Fig. 6.3. Diffusivity values for H in Ni compared with host metal self-diffusivity (black squares). H diffusivity (black triangles) is close to the calculated (blue = Eq 6.1). Green triangles represent the experimental data (Sacris 1970).

Fig. 6.4. Diffusivity values for H in Al compared with host metal self-diffusivity (black squares). H diffusivity (red circles) is very close to the calculated (blue). Green line represents the experimental data (Eichenauer 1974).

Fig. 6.5. log-log plot of hydrogen diffusivity values divided by the host metal self diffusivity vs the mass ratio m_M/m_H . The slope value is ~ 0.9 , and not ~ 0.1 as reported in (Bearman 1981).

Fig. 6.6. Diffusivity values for H in Pd at $T = 2250$ K vs “screening” constant, k . Inset shows the pair potentials Pd-H (being $k = 1$ the original (Zhou 2008)).

Fig. 6.7. Quantum effects dominate when Ξ is much larger than 1, but are important over the entire temperature range (Jardine 2010).

Fig. A1. Calculated pair distribution function of liquid Palladium ($T = 1850$ K) compared to the experimental data from (Waseda 1975).

Fig. A2. Calculated pair distribution function of liquid Nickel at 1750 K and 2025 K compared to the experimental data from (Waseda 1975).

Fig. A3. Calculated pair distribution function of liquid aluminum (1000 K and 1300 K as labelled) compared to the experimental data from (Waseda 1975).

Fig A4: $S_1(Q)$ values calculated using MD simulation with two different potentials (EAM and ADP) compared with experimental results (Waseda 1975).

Fig A5: Heat capacity, C_p , values calculated using MD simulation with two different potentials (EAM and ADP) compared with experiment and other MD results from (Forsblom 2005).

Fig. B1. Self diffusion of pure Pd compared to MD results (black squares). Blue triangle and red squares correspond to the MD results from (Ahmed 2004, Mei 1990).

Fig. B2. Self diffusion of pure Al. Experimental data (black line) from recent neutron diffraction experiments (Demmel 2011). MD simulations (red and green symbols).

Fig. C1. SRO values dependence with H concentration (in atom %) for Pd-H and Al-H systems. Pd-H and Ni-H systems are almost a random solution independently of H concentration while Al-H system rapidly shows segregation.

Fig. C2. SRO evidence in Al-H system (using EAM/alloy (Angelo 1995)). Yellow balls represent H atoms while blue ones represent Al ones. Here the H concentration is high (20%) for clarity sake.

Fig. D1. Hydrogen diffusivity in liquid metals. Experimental data taken from (Sacris 1970). Self diffusivity of pure metals taken from MD results in reference (Ahmed 2004). Experimental data for liquid Cu and Ni taken from (Meyer 2008).

Fig. D2. Ratio of H diffusivity in liquid metals divided by the host metal self-diffusivity. Black squares stand for our MD results, red circles are experimental data taken from the abovementioned references.

Chapter 7: Ab initio calculations of Helium inside Lithium and Lead

Fig. 7.1. Multi-scale model from nuclear reaction to property change due to irradiation (Kawai 2011).

Fig. 7.1b. He bubbles in liquid mercury observed through a glass window placed on the surface of the mercury. The height of this image corresponds to 1.62 mm (taken from (Ida 2007)).

Fig. 7.2. Schematic representation of the importance of He bubbles inside liquid metals in breeder blanket design. (taken from (Fradera 2011)).

Fig. 7.3. High symmetry interstitial sites in a bcc structure, (a) tetrahedral and (b) octahedral, and in an fcc structure, (c) tetrahedral and (d) octahedral.

Fig. 7.4. He defects inside pure lithium (bcc) for two different scenarios, unrelaxed (black squares) and relaxed (red circles).

Fig. 7.5. He defects inside pure lead (fcc) for the three different studied scenarios; unrelaxed (black squares), relaxed (red circles) and (unrelaxed) taking into account SOC (green triangles).

Fig. 7.6. Helium atom and Li total charge relaxed and unrelaxed as labelled. Note the break in the y axis.

Fig. 7.7. Helium atom and Pb total charge relaxed and unrelaxed as labelled. Note the break in the y axis.

Fig. 7.8. Helium atom (green triangles) and Li charge character (unrelaxed). Dashed lines are just guides to the eye. Note the break in the y axis.

Fig. 7.9. Helium atom and Pb charge character unrelaxed. Note the break in the y axis.

Fig. 7.10. Helium (open symbols) atom and Pb (closed symbols) charge character (s, p and d, black, red and green respectively) after relaxation. Note the break in the y axis.

Fig. 7.11. Charge density of the metallic electrons in the vicinity of the helium atom. The dashed curve is the unperturbed metallic density. (taken from (Zaremba 1977)).

Fig. 7.12. (Fig. 3 in Trioni 1998). The variations of the $1s$ level (line with diamonds) of a He atom, of the bare metal electrostatic potential V_{es} (dashed line), and of the bare metal effective potential V_{eff} (solid line) as functions of the atom jellium edge distance.

Fig. 7.13. Total (left) and projected DOS (right) of He inside Li after relaxation. The units are number of states/unit cell. p and d DOS are shifted upwards +0.2 and 0.5 units for clarity. Octahedral (black line), substitutional (red) and tetrahedral (green).

Fig. 7.14. Total (left) and projected DOS (right) of Li with different interstitials after relaxation; octahedral (black line), substitutional (red), tetrahedral (green) and pure Li (blue line).

Fig. 7.15. Total (left) and partial (right) DOS of He inside Pb after relaxation for three different configurations; octahedral (black line), substitutional (red) and tetrahedral (green). p and d-DOS are shifted upwards +0.2 and 0.5 units for clarity.

Fig. 7.16. Total (left) and partial (right) DOS of Pb after relaxation with three different He interstitial; octahedral (black line), substitutional (red) and tetrahedral (green). Partial p- and d-DOS are shifted upwards +0.2 and 0.5 units for clarity.

Fig. 7.17. Total DOS of Pb before relaxation without SOC (left) and with SOC (right) and with three different He interstitials; octahedral (black line), substitutional (red) and tetrahedral (green). Blue line stands for the pure fcc Pb DOS.

Fig. 7.18. Dividing surfaces separating the oxygen and hydrogen Bader regions in a water molecule. The integration over the Bader regions indicates that 0.58 e are transferred from each hydrogen atom to the oxygen atom (taken from (Henkelman 2006)).

Fig. 7.19. He charge inside Li (left) and Pb (right) after relaxation calculated using Bader analysis. Dashed lines are just guide to the eye.

Fig. 7.20. Schematic illustration of the difference in charge of pure Pb and Pb with an He interstitial in tetrahedral position.

Fig. 7.21. Schematic illustration of the difference in charge of pure Pb and Pb with an He interstitial in tetrahedral position. Yellow color represent the s “orbitals”.

Fig. 7.22. Schematic illustration of the (a) $\langle 100 \rangle$ dumbbell, (b) $\langle 110 \rangle$ dumbbell, (c) $\langle 111 \rangle$ dumbbell and (d) $\langle 111 \rangle$ crowdion, in a bcc CS.

Fig. 7.23. Example of force fitting taken from (Izvekov 2004); intramolecular component of the HH effective force field (solid line) and least-squares fit using a cubic polynomial (dashed line).

Appendix 1: Exploring the limits of classical molecular dynamics. Liquid Li and Pb under high pressure

Fig. A1. Fermi surface of bcc lithium at (a) equilibrium and (b) $P=8$ GPa and fcc at (c) $P=30$ GPa. Taken from ref (Rodriguez 2006).

Fig.A2: Bulk modulus for liquid Li and Pb at different temperatures. The experimental values of Pb are taken from (Mustafin 1983). Li experimental values have been calculated from (Yokohama 2001) using Eq (A.2).

Fig. A3. Lithium and lead (shifted 2 units upwards) $g(r)$ at different pressures (0, black squares, 1 GPa red circles, 5 GPa green triangles) at $T = 1800$ K.

Fig. A4. Lithium $g(r)$ at high pressures and high temperatures as labelled. Red line represents the same result from *ab initio* calculations taken from Yang *et al* (Yang 2010).

Fig. A5. Lead $g(r)$ at very high pressures and high temperatures as labelled. Symbols are our MD data and lines represent the same result from *ab initio* calculations (Cricchio 2006).

Fig. A6. r_2/r_1 ratio for liquid Pb and Li at different temperatures (Pb 1800 K, black circles and Li 1700 K red triangles) and pressures up to 40 GPa (Dashed blue lines are linear fits).

Fig. A7. Volume dependence of nearest-neighbour distance, r_1 , for liquid Li (full symbols) and Pb (open symbols). Volume, V , and r_1 are normalized by values at atmospheric pressure, V_0 and $r_{1(0)}$, respectively, and $(r_1/r_{1(0)})$ is plotted as a function of $(V/V_0)^{1/3}$.

Fig. A8. Maximum and minimum coordination number (CN) of lithium atoms at high pressures ($T = 1000$ K) compared to *ab initio* calculations (Yang 2010).

Fig. A9. Left) Li CNA analysis at 2000 K vs pressures. A clear jump in the number of atoms in an fcc structure takes place around 7 GPa, as expected. Right). Pb CNA analysis at 2000 K vs pressures. Some ordering to a bcc structure takes place around 100 GPa.

Fig. A10. Left) Li CNA visualization at 2000 K and $P = 20$ GPa. ($N = 120000$ Atoms). Green spheres correspond to fcc atoms, red ones to hcp, blue to bcc and white to others. Right) Pb under pressure ($P = 200$ GPa and $T = 2000$ K) visualization of CNA.

Fig. A11. Low (left) and high (right) pressure heating-cooling Pb MD simulations: Enthalpy vs temperature at different pressures as labelled.

Fig. A12. Low pressure Pb MD simulations. Pb volume versus temperature at different pressures. Clearly the jump in volume decreases when pressure is applied.

Fig. A13. Pb and Li (inset) melting point estimated from MD runs (red circles) compared with experimental values (black squares) at different pressures; from 0 to 5 GPa for Li and up to 80 GPa for Pb. Blue line stands for the Lindemann predictions for Pb (Errandonea 2010) and Li (Kraut 1996).

List of Tables

Chapter 1: Nuclear Fusion

Table 1.I. Nuclear fusion reactions which occur at the lowest plasma temperatures. The quantities E and E^* refer to the local nuclear energy release in one reaction and to the energy released in the form of charged particles, respectively (Ribe 1975). E_{eq} is the total equivalent energy (Sheffield 1994).

Table 1.II. Parameters of modern tokamaks and ITER (Sheffield 1994). JET axial magnetic field up to 4.0 T from 1997 onwards (Keilhacker 2001).

Chapter 2: Liquid metals and fusion technology

Table 2.I: Physical properties of eutectic LiPb (eutectic point to be determined) compared with other possible breeding materials.

Table 2.II: (I continued) Physical properties of Li17Pb compared with other possible breeding materials. T solubility and diffusivity is one of the main issues for blanket design.

Chapter 3: Molecular Dynamics in short

Table 3.I. Different ensembles, their names and the independent and dependent properties in each case.

Table 3.II. Potentials and parameters of the rare gas series taken from (Lombardi 2008).

Table 3.III. Computational effort (schematic). Time refers to computational time in arbitrary units.

Chapter 4: Atomistic molecular point of view for liquid lead and lithium

Table 4.I. Parameters to define the EAM potentials for Pb (Zhou 2001).

Table 4.II. Parameters to define the EAM potentials for Li. Li parameters a, b and c are expressed in eV (from Refs (Belaschenko 2011, 2012)).

Table 4.III. Parameters to define Li pair potential (in eV) as defined in Eq's (14) and (15). From Ref (Belaschenko 2012), distance, r, in Å.

Chapter 5: LiPb interatomic potential

Table 5.I. Calculated cohesive energy, E_c , and lattice parameter, a_0 , for Pb and Li in fcc and bcc phases. All values have been calculated using Pb and Li EAM potentials in the effective representation. The results are exactly the same that those obtained with the original potentials.

Table 5.II. Main results for Li17Pb total $g(r)$. Comparison between MD and experiments (Mudry 2008), all distances in Å.

Table 5.III. Main results for Li17Pb eutectic partial $g(r)$'s. Comparison between MD and experiments (Mudry 2008). $r_{1\text{ Pb-Li}}$ and $r_{1\text{ Li-Li}}$ does not match the experimental results.

Table 5.IV. Crystal data for $\text{Li}_{50}\text{Pb}_{50}$ compound (Zalkin 1957) at two different temperature ranges, room temperature (rt), and high temperature (ht).

Table 5.V. Left) Table 1 from (Hubberstey 1997). Right: Table 1 from (Molina 1998). Both papers give the same cohesive energy for LiPb in bcc B2 phase.

Table 5.VI. B2 phase. Distances (in lattice parameter, in a_0 units), number of nearest neighbours and atom type, different (\neq) or same ($=$) as "origin one".

Table 5.VII. Partial $g(r)$ peaks with Pot. M1. The results are as good as or better than the obtained with previous potentials (last column). General agreement is better than 10% of error in first peaks position.

Table 5.VIII. Coherent and incoherent scattering cross sections (in barns) for Pb and Li according to (Ruppersberg 1975).

Table 5.IX. Weight factors defined in Eq.s (5.34) for eutectic composition and some Li-Pb alloys using only the coherent cross sections given in Table 5.VIII.

Chapter 6: Hydrogen in liquid metals

Table 6.I. Some parameters used in this study. Debye temperature, vibrational frequencies of H-M system and activation energies taken from (Dhawan 1981).

Table 6.II. Some parameters used in this study. $\epsilon_{AB}/\epsilon_{AA}$ is the hydrogen to metal atomic ratio of various typical hydride-forming metals. r_{HS} values from (Protopapas 1973)

Table 6.III. Some parameters used in this study. Density at melting point units are gr/cm^3 , ϵ is the electronegativity (Pauling scale). ΔH_s is the enthalpy of solution of hydrogen in the metal in the low concentration limit (Fukai 1993).

Chapter 7: Ab initio calculations of Helium inside Lithium and Lead

Table 7.I. Summary of formation energies of high symmetry He interstitials in Pb and Li.

Table 7.II. Magnetic moment components, μ_i , for Pb and He atoms. Pb values are the average of the first nearest neighbors.

Table 7.III. Volume per atom (in \AA^3) for pure Pb, Li, and He interstitials, before and after relaxation, and taking into account SOC.

Table 7.IV. Total charge of He and host metals according to this work. (2) Some relevant data: effective charge (Shpil'rain 2007), polarizability, α_0 , (Mitroy 2010). (1) electronic density, r_s , (Zaremba 1977).

Appendix 1: Exploring the limits of classical molecular dynamics. Liquid Li and Pb under high pressure

Table A.I. Experimental bulk modulus (Ashcroft 1976), B , (in GPa) and its derivative, B' , and MD results using Pb and Li EAM potentials described above ($T = 300$ K).

“A man must shape himself to a new mark directly the old one goes to ground.”

Ernest Shackleton

Chapter 1

Nuclear Fusion Technologies

The Physics involved in nuclear fusion is a vast and complex field very close to astrophysics. The temperatures and densities reached in the core of stars is what should be reproduced in some nuclear reactor in order to achieve fusion. Therefore the physics involved and technology needed to build a reactor is by no means simple. Many problems arise when someone wants to create a small Sun in the laboratory... materials should withstand very high temperatures and radiation doses so materials science finds here another very challenging problem to face.

To write a long introduction dealing with all the aspects of nuclear fusion technology would be clearly unnecessary because several excellent books have been written on the matter. Contrary, here we will present a short introduction with a long references list with classical papers, reviews and good books about the different physical phenomena and technological problems involved in the design of a nuclear fusion reactor.

Nuclear fusion seems to have two different and well established pathways, magnetic confinement or inertial fusion. The biggest international projects are well magnetic confinement experimental reactors (tokamaks or stellarators, being ITER the flagship) or inertial confinement experiments (National Ignition Facility, NIF, in the U.S.A. is the best example). So a very short introduction of both kind of reactors and some of the well known facilities as the Joint European Torus (JET) or NIF will be presented. This two kind of reactors present similar problems related with a future commercial fusion reactor, namely tritium production and extraction, plasma facing materials just to mention some of them. These common problems will be shortly reviewed too. The idea of using liquid metals for breeding blankets, and also as plasma facing materials, will be explained in more detail in Chapter 2.

"But still try, for who knows what is possible."

M. Faraday

1. 1 Nuclear Fusion

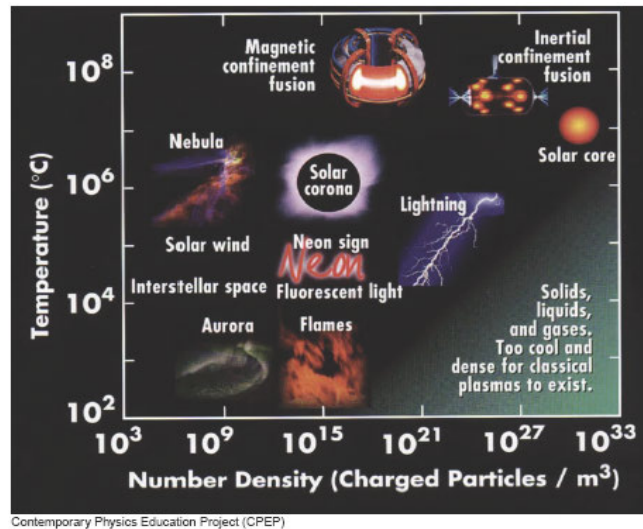
The chemical reduction of CO₂ will be one of the most important challenges in the 21st century. As a greenhouse gas, CO₂ contributes to global climate change, and therefore anthropogenic emission of CO₂ is resulting in increasing global concern. In order to limit the global mean temperature increase by 2.0-2.4 °C, (based on the emission level in 2000) the global CO₂ emission would have to be reduced by 50-80% by 2050 (Metz 2007). The most effective, and perhaps unlikely, route to decreasing anthropogenic CO₂ emissions would be the replacement of all current (13 Terawatt) and future (23 Terawatt by 2050) global energy requirements with non-emissive and renewable resources (Kamat 2007). However, the US Department of Energy (DOE) has predicted that we will have to wait another five decades, minimum, before fusion power becomes practical. Meanwhile, the United States continues to depend on fossil fuels for 85 percent of its energy. A nice review of the energetic problem in the forthcoming years can be found in (Ongena 2001).

The ultimate goal of worldwide research in nuclear fusion is to develop fusion as an inexhaustible, economic, environmentally safe source of electric power. Fusion energy can potentially provide a nearly unlimited source of clean sustainable power. Such power plants would be safe and environmentally friendly. In particular, one of the main problems of fission reactors, namely that of a possible uncontrollable nuclear reaction is banished; also the problem of radiotoxic waste is reduced by literally orders of magnitude. Fusion reactors would have almost limitless supplies of fuel and could be sited anywhere in the world. Fusion is, however, still in the development stage and it is not expected that commercial power plants will start operation before the middle of this century.

The two main attractions of fusion are that a very large amount of nuclear energy is released in each fusion and that virtually unlimited amounts of deuterium (D) exist on the surface of the Earth in water molecules. Tritium (T) can be made from lithium in the overall production process. Thus, fusion fuel is available in virtually unlimited quantities for commercial production of electrical power.

Fusion of two light nuclei, normally D and T, only occurs in plasmas at elevated temperatures (see Figure 1.1) where the particles have sufficient kinetic energy to overcome the Coulomb barrier. The nuclei in a plasma are all positively charged, so they strongly repel each other when they're close together. But in a hot, dense plasma, they approach each other at such high speeds

and so often that many pairs of them can overcome their repulsion and fuse— releasing enormous amounts of nuclear energy.



Contemporary Physics Education Project (CPEP)

Fig. 1.1. The temperatures and densities of different plasmas. Extreme matter exists inside gamma-ray bursts, hot neutron stars, and the plasmas produced by high-power lasers. Non-extreme matter includes sea-level air at room temperature and, the surface of the sun.

In order to develop a viable fusion reactor there are three basic physics requirements which must be satisfied. (1) A sufficient density of plasma must be: (2) confined for a sufficiently long time at: (3) a sufficiently high temperature to produce net thermonuclear power.

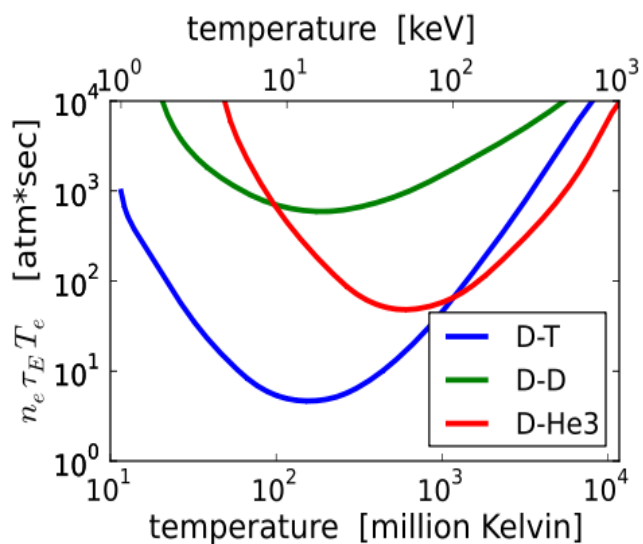


Fig. 1.2. Three parameters (plasma temperature, T_e , density, n_e , and confinement time, τ_e) need to be simultaneously achieved for sustained fusion to occur in a plasma for three different nuclear reactions, D-T, D-D and D-³He as labelled.

In its most elementary form the net power balance for a magnetic fusion system is described in terms of the Lawson parameter $n\tau_E$, with n the plasma number density and τ_E the energy confinement time (Lawson 1957). Similar criterion exist for inertial fusion as well; see (Chang 2010) and references therein.

	E(MeV)	E*(MeV)	E _{eq} (kWh/g)
D+T → ⁴ He (3.52 MeV) + n(14.06 MeV)	17.58	3.52	94000
D+D → ³ He (0.82 MeV) + n(2.45 MeV)	3.27	0.82	22000
D+D → T (1.01 MeV) + n(3.03 MeV)	4.04	4.04	27000
D+ ³ He → ⁴ He (3.67 MeV) + p (14.67 MeV)	18.34	18.34	98000
T+T → ⁴ He + n + n	11.32	-	-

Table 1.I. Nuclear fusion reactions which occur at the lowest plasma temperatures. The quantities E and E* refer to the local nuclear energy release in one reaction and to the energy released in the form of charged particles, respectively (Ribe 1975). E_{eq} is the total equivalent energy (Sheffield 1994).

DD system which requires no fuel breeding, and for which neutron activation of the reactor structure would be greatly reduced because of the smaller neutron energy. The D³He system would greatly reduce the need for thermal conversion of the nuclear energy to electrical work, since the reaction of the charged particles on magnetic and electrical fields can produce this work directly, converting fusion energy at high efficiency. The TT reaction occurs with a small reaction rate (see (Ribe 1975) for a review of fusion reactor systems).

A solid foundation for fusion power has been made by the results from many fusion facilities over the past 50 years. See (Meade 2010, Smirnov 2010) and (Mima 2011) for a historical reviews on magnetic and inertial confinement respectively. After all this research effort around the world, today, the best plasmas need an improvement of only $\times 6$ in performance. In magnetic confinement this requires a new larger device. Figure 1.3 represent the advance regarding the Fusion Triple Product ($P_i\tau_E = n_iT_i\tau_E$) required to reach ignition in both MCF and ICF along the years.

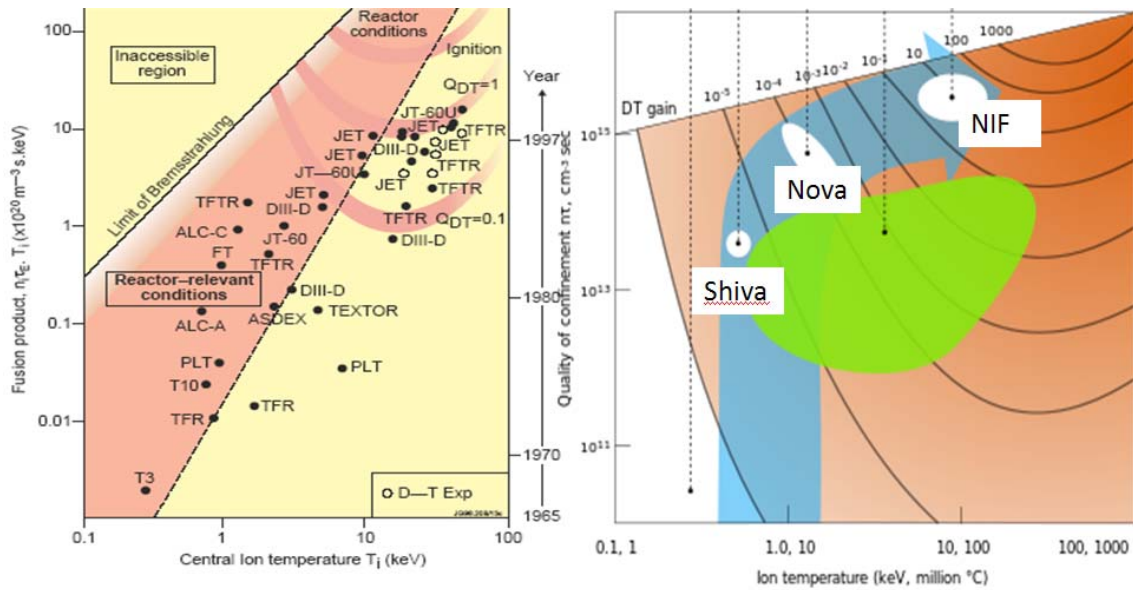


Fig. 1.3. Left) The Fusion Triple Product can be compared with leading edge performance of the devices year-on-year. Right) The Fusion Triple Product (here quality of confinement) for inertial fusion experiments along the years.

1.2 Magnetic fusion

Materials cannot survive at the elevated temperatures needed to achieve fusion, thus leading to innovative isolation and containment schemes. Two approaches to containment are magnetic fusion energy in which the fusion plasma is confined by magnetic fields (Sheffield 1994, Freidberg 1982) and inertial confinement fusion (ICF) (Nuckolls 1972) in which the fusion plasma is produced in the core of an imploded spherical capsule. Inertial fusion reactors will make use high-repetition-rate drivers such as lasers or heavy ion particle beams to produce ICF capsule implosions several times per second. ICF will be shortly reviewed in next section.

Magnetic confinement research started in the fifties in the old USSR. The papers of Tamm, Sakharov and their collaborators were first published in a four-volume book ‘Physics of Plasma and Controlled Thermonuclear Reaction Problem’ published just before the Second Geneva Conference in 1958 (Tamm, Sakharov and Bezbatchenko, 1959).

Together with Sakharov, Tamm proposed a tokamak resulting in the T-3 Soviet magnetic confinement device from 1968, when the plasma parameters unique for that time were obtained,

of showing the temperatures in their machine to be over an order of magnitude higher than what was expected by the rest of the community (Tamn 1961).

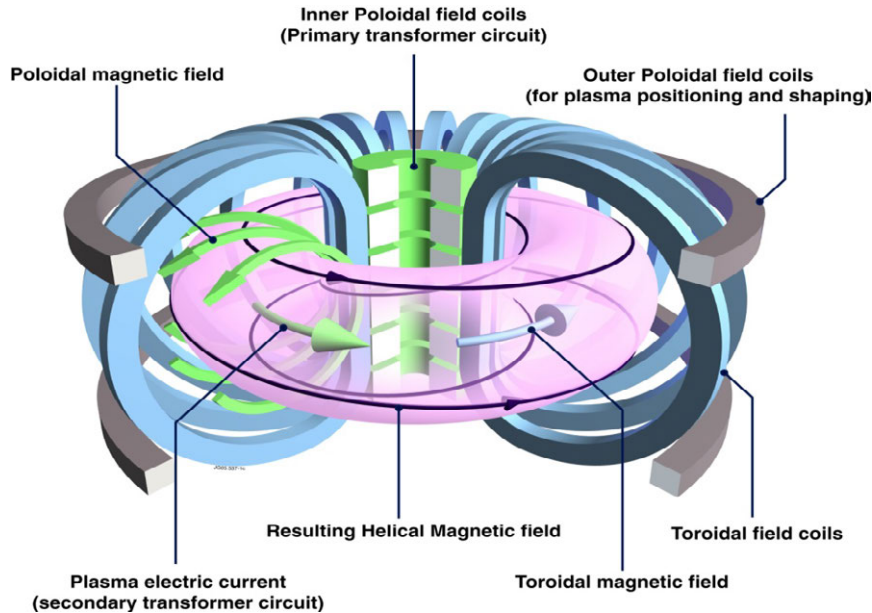


Fig. 1.4. Illustrating the main features of a tokamak.

The essential features of a tokamak are shown in Fig. 1.4. The plasma of major radius R and minor radius a forms the secondary of a set of transformer cores whose primaries are driven by a pulse of current which induces an axial (or toroidal) current I_ϕ and current density j_ϕ in the plasma. This current serves two purposes: **(a)** it heats the plasma by Ohmic processes and **(b)** the poloidal field, B_θ , which encircles the plasma ring, contains the plasma.

From an oversimplified view of the physics, the problem of maximizing $n\tau_E$ separates into two relatively independent parts. First, the maximum energy confinement time, τ_E , is determined by the microscopic behavior of the plasma. This behavior ultimately leads to macroscopic transport, which can be either classical or anomalous depending on the processes involved (Bohm diffusion is one example (Bohm 1949, Krall 1973, Hinton 1976)). These phenomena require knowledge of individual particle motion on short length and time scales and they are usually treated by kinetic models (Montgomery 1964). Such models are also used to determine the energy disposition and plasma temperature T associated with various methods of heating. Second, the maximum density, n , is almost always determined, not by microscopic kinetic processes, but rather by macroscopic equilibrium and stability limits set by the magnetic

geometry. Actually, at a given T, the critical figure of merit is $\beta = 2\mu_0 nT/B^2$, the ratio of plasma energy to magnetic energy (Friedberg 1982).

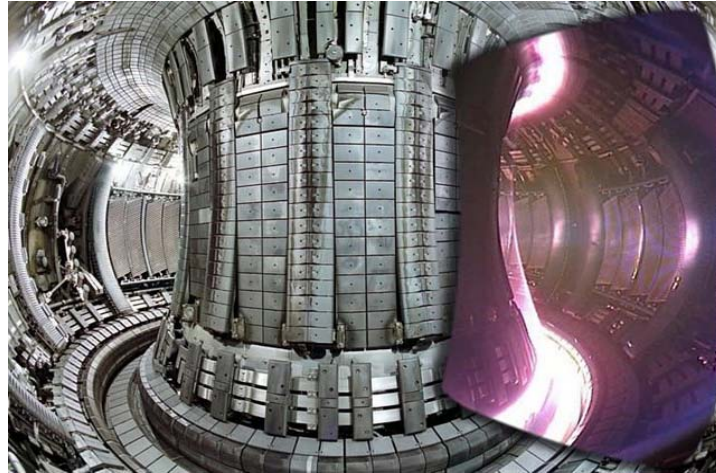


Fig 1.5. JET chamber in Culham, U. K. Picture taken from <http://www.jet.efda.org>.

The energy confinement time is a measure of how long the energy in the plasma is retained before being lost. It is defined as the ratio of the thermal energy contained in the plasma and the power input required to maintain these conditions. A significant fraction of losses in a magnetically-confined plasma is due to radiation. The confinement time increases dramatically with plasma size (large volumes retain heat much better than small volumes)

In short, energy confinement time t scales as some functions of: plasma current, I , major radius, R , minor radius, a , toroidal magnetic field, B . The scaling law is roughly

$$t \propto I_p^a R^b a^g B^l \quad (1.1)$$

with indices a, b, g, l all positive. Then to achieve sufficient value of $n\tau T$ requires: scaling of present generation of Tokamaks upwards in terms of, I , R , a and B .

However this is much more complex. Further details of advanced tokamaks can be found in (Taylor 1997, Kikuchi 2012) and references therein.

TABLE III. Parameters of modern large tokamaks and ITER.

Tokamak	TFTR	JET	JT-60	ITER
Major radius $R(m)$	2.45	3.10	3.40	7.75
Aspect ratio R/a	2.90	2.82	4.0	2.8
Ellipticity κ	1.0	1.8	1.6	1.55
Current $I(\text{MA})$	3.0	6.0	6.0	25
Field B_ϕ (T)	5.12	3.4	4.2	6.0
Divertor	No	Yes	Yes	Yes
Coil type	Cu	Cu	Cu	SC
Fuel	H,D,T	H,D,T	H,D	D-T
Pulse length (s)	2	20+	20+	1000
Estimated fusion power (MW) ^a	~ 15	~ 50		~1500

^aProjected fusion power. Obtained, JET 1992, 2 MW; TFTR 1993, 6 MW.

Table 1.II. Parameters of modern tokamaks and ITER (Sheffield 1994). JET axial magnetic field up to 4.0 T from 1997 onwards (Keilhacker 2001).

During the past two decades there have been substantial advances across the board in magnetic fusion research. In tokamaks, the main line of experimental research in the world program, reactor-level plasma conditions have been achieved.

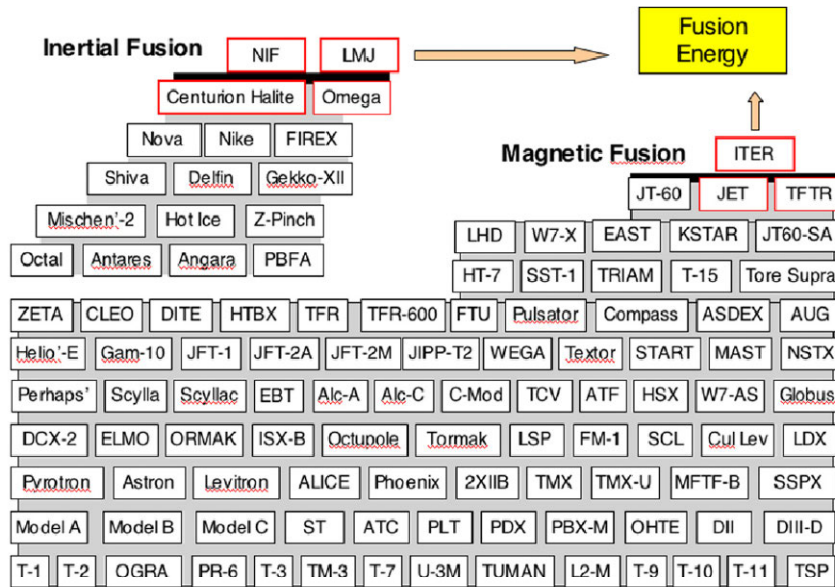


Fig. 1.6. Summary of different magnetic and inertial (upper left corner) experiments around the world. (figure taken from (Meade 2010)).

Initial tests with DT fuel in the JET tokamak in 1991 led to the generation of 1.8 MW of fusion power (Bickerton 1997, Keilhacker 2001). More recently, the TFTR tokamak obtained over 6 MW of fusion power (Stambaugh 1990, Strachan 1999). The characteristic time scale of plasma

sustainment typical of the 1970s was 1 s. The fusion program is now on the verge of demonstrating the scientific and technological feasibility of fusion power (ITER and NIF).

1.2.2 Stellerators

It would be incomplete to finish this section without mentioning the “stellerator” concept. A stellerator is like a tokamak but the toroidal camera is twisted in a helical way making the plasma more stable. To summarize, when one considers ways of confining some thermonuclear plasma, a toroidal solenoidal magnetic field is the more obvious possibility. But such a simple field would not work from the fact that its non-uniformity causes charge separation by the oppositely flowing $B \times \text{div}B$ drifts of the ions and electrons.

This separation would create electric fields and the consequent $E \times B$ drift would move the plasma across the field lines to the outside of the system. This charge-separation problem can be solved by twisting the magnetic field lines, giving them a poloidal rotation as they go around the torus toroidally. The field lines then connect regions where positive electric charge would tend to accumulate to regions where there is a deficiency and the electrons can flow freely along the magnetic lines and neutralize the charge accumulations. This is the basic idea of the stellerator concept (Spitzer 1958, Lyon 1990). This is another very promising approach and, for example, Wendelstein 7-X, a large stellerator (which goal is to achieve times of confinement of about 30 minutes) is today under construction in Greifswald, Germany (Wanner 2003).

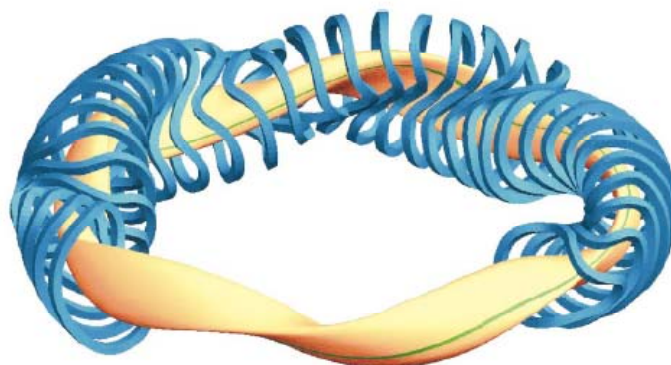


Fig. 1.7. The W7-X stellarator with its helically shaped plasma and the coils required to support it. The average major radius of a plasma is 5.5 m. Figure taken from (Boozer 2004).

Tokamak and stellarator plasma parameters improved well above those attained in the 1970s have now been sustained for tens of seconds. For different reviews of advances in tokamak configurations and magnetic confinement see for example (El-Guebaly 2010, Allen 2012, Gates 2012) and references therein. Scientific progress on TJ-II stellarator in Spain is described in the work of Alejaldre and collaborators (Alejaldre 1990, 1999 and references therein). As will be explained a little further in next chapter, some Li plasma facing solutions have been studied in the TJ-II as well (Tabarés 2008).

1.3 Inertial Fusion

In the mid-1960s, scientists realized that intense laser light could compress and heat matter enough to produce significant amounts of fusion energy. Research in laser driven inertial confinement fusion (ICF) began soon after the invention of the laser (Lindl 1998, Atzeni 2004). The U.S. research in this field is a direct result of weapons work. John Nuckolls, based his seminal paper in *Nature* (Nuckolls 1972) on work he initiated in the later 1950s in creating the smallest possible fusion explosion. In a very real sense ICF is, and has been from the beginning, an attempt to shrink thermonuclear weapons physics and design to laboratory scale. His paper was published at about the time when laser technology, diagnostic development, and numerical modeling were becoming mature enough so that an expanded ICF program could begin to evaluate the limits and requirements for the success of ICF.

After about 45 years of intense research, the first ignition experiments are being performed at the National Ignition Facility (NIF). Although important ICF research has and is being conducted in Japan, France and UK, the world's major ICF research program has been the U.S. program funded by the Department of Energy. Much of the progress made in this program has been cloaked in secrecy due to the relationship between laboratory scale ICF, especially indirect-drive ICF, and thermonuclear weapons design, since thermonuclear weapons are essentially enormous indirect-drive ICF systems.

In the Institute of Nuclear Fusion (Madrid, Spain) there is a long tradition on ICF research, starting with the work of Prof. G. Velarde on plasma physics (Velarde 1986, 1989) and continued by Dr. P. Velarde and co-workers (Velarde 2005, Ogando 2001). Different aspects of neutron damage are also explored (Perlado 2000, Gordillo 2012). The research effort continues vigorously in collaboration with Lawrence Livermore National Laboratory in the USA, CEA in France etc (Oliva 2012). Another important issue, the mechanical properties of DT ices, is today

investigated by means of *ab initio* simulations (Guerrero 2013). Needless to say, that this short list of references makes no claim to completeness.

Something important to be noted, inertial-confinement works. Experiments carried out by the US military in the 1980s showed that the X-ray output from an atomic bomb could ignite little capsules of DT. By 1975 the U.S. ICF program had largely abandoned direct-drive ICF in favor of indirect-drive radiation implosion, (the foundation of the Teller-Ulam fusion weapon architecture). Due the limitations of existing lasers, in 1978 the Halite/Centurion program was undertaken jointly by LLNL and Los Alamos (Halite was the LLNL portion, and Centurion the LANL part). This secret program used underground nuclear explosions at the Nevada Test Site to provide the high intensity radiation flux needed to test ICF targets (fuel capsule/hohlraum systems). It continued until 1988.

These bombs use an initial fission explosion to rapidly compress a DT mixture, with shock waves created inside the mixture heating it to the point of ignition. This “central ignition” process is being reproduced in a controlled way at billion-dollar facilities — the NIF at the LLNL in the US and the Mégajoule laboratory in France — where a single set of lasers both compresses and heats the fuel. HiPER, on the other hand, will use a separate laser pulse to do the heating, a process known as “fast ignition” because the second laser must heat the fuel within 10^{-11} s of the implosion.

Next figure shows schematically the idea of direct drive. With sufficient compression, the pressure and temperature ignite the DT fuel, forming a self-sustaining fusion reaction (burning). However, any small bumps or imperfections in the spherical implosion will cause the capsule material, melted by the shock, to grow fingerlike projections that mix with the fuel and rob it of its heat.

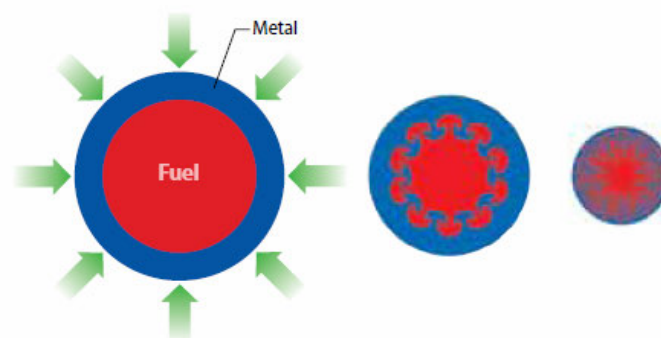


Fig. 1.8. In ICF, a spherically converging shock (green arrows) compresses a millimeter-size metal capsule (blue) filled with DT gas (red).

NIF is the most complex optical instrument ever constructed, with over 38,000 large and small optics and 60,000 points controlled by two million lines of software (Moses 2008, 2010). With 192 laser beam NIF, is now operational and conducting experiments at LLNL in Livermore, CA. NIF, the flagship facility of the U.S. Inertial ICF Program, will achieve high-energy-density conditions never previously obtained in the laboratory—temperatures over 100 million K, densities of 1000 g/cm³, and pressures exceeding 100 billion atmospheres. Such conditions exist naturally only in the interiors of the stars and during thermonuclear burn.

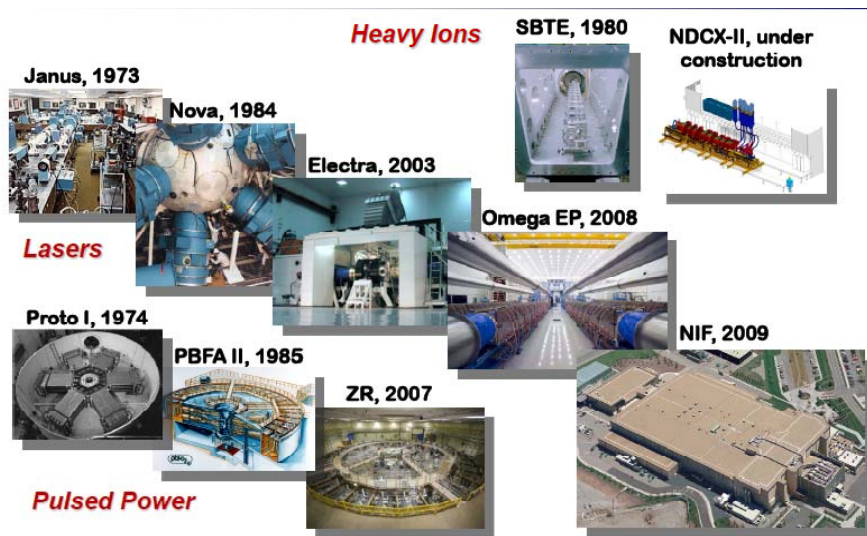


Fig. 1.9. Historical development of ICF with different drivers, laser, heavy ions and pulsed power.

In “hot-spot” ICF designs, a cryogenic DT capsule is driven to implode either directly by intense laser pulses (McCrory 2008) or indirectly by x rays in a hohlraum (Lindl 1998). At the stagnation stage, a high-density shell ($\rho > 1000\rho$ solid DT density) is assembled around the hot spot for the fusion burn to propagate, thereby generating a net energy gain. Accurate knowledge of the equation of state (EOS) of the DT fuel is essential for ICF designs (Atzeni 2004) because the compressibility is determined by the EOS (Hu 2008).

Dynamically compressed by shocks and/or adiabatic compression waves driven by laser ablation (Hu 2008), the imploding DT shell undergoes a wide range of plasma conditions at densities from $< 1 \text{ gr/cm}^3$ up to 1000 g/cm^3 and at temperatures varying from a few to several hundreds of electron volts (Lindl 1998).

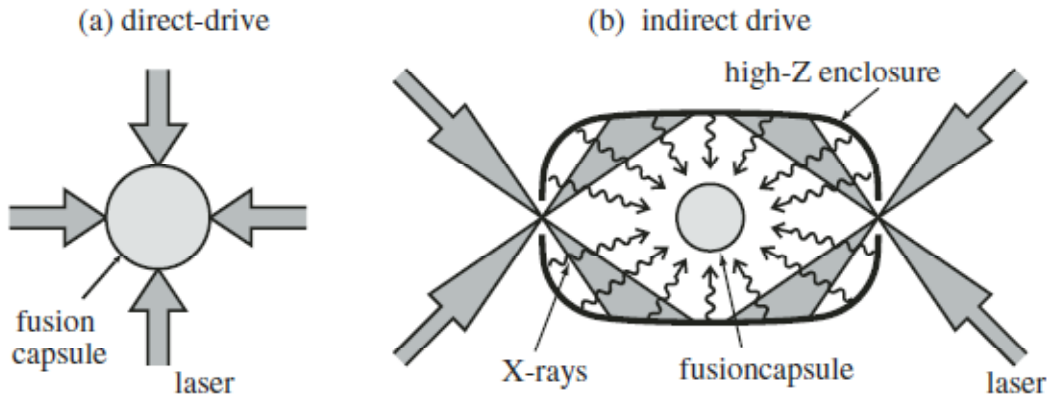


Fig. 1.10. Direct-drive (a) and indirect-drive (b) laser fusion.

In recent experiments, the DD and TT reaction yields have shown to be anomalously low and high, respectively, when compared to the DT reaction yield maybe caused by a stratification of the fuel (Casey 2012). This stratification of the fuel may be driven by plasma baro-diffusion (Amendt 2010) of the fuel ions, which pushes the lighter ions from the imploding ICF core. The implications of these anomalous yields in the ignition experiments planned on the NIF, potentially imply a more restrictive ignition threshold (Betti 2010, Haan 2011) and reduced DT yield.

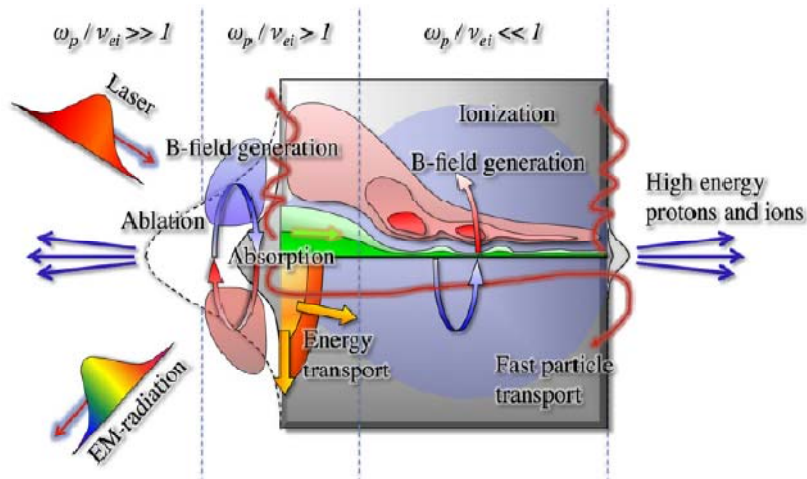


Fig. 1.11. The physics of high power laser interactions with solid targets (Thomas 2012).

A plane shock wave in a fluid (Hirschfelder 1954, Zel'dovich 1966 Atzeni 1994) is known to be inaccurately described by the Navier-Stokes equations of fluid dynamics; in the case of a gas, deviations occur already for Mach numbers $M \sim 2$. There is an excellent treatment of shockwaves in Chapter IX of Landau and Lifshitz' "Fluid Mechanics" text (Landau 1959). The Navier-Stokes equations represent a continuum theory based on linear relations between

thermodynamic forces and fluxes. These relations are known as the linear laws: Newton's law of friction and Fourier's law of heat conduction. In a strong shock wave, the forces, i.e., gradients in hydrodynamic densities are large, and the failure of the Navier-Stokes equations can be attributed to deviations from the linear laws.

Another problem is that ICF capsule implosions are typically modeled as charge-neutral, average-atom, single-component fluids despite their plasma nature (Marinak 2001). As a result, plasma-related phenomena arising from self-generated electric ($\geq 10^9$ V/m) and magnetic fields (~ 1 MG) as can be seen in Figure 1.11. A description of the experiments quantifying these effects can be found in (Li 2008, 2009). Their implications for ICF target performance in general, and upcoming ignition tuning campaigns on NIF (Peisner 1999) in particular, have not been well established (Glenzer 2010).

Central hot spot ignition with high implosion velocities (350–400 km/s), this scheme is prone to hydrodynamic instabilities. Conversely, fast ignition does not rely on hydrodynamics to trigger ignition but on an auxiliary high intensity short laser pulse (Dunne 2006, 2007 and references therein). Another important issue will be the crystal structure of DT ices and its mechanical properties. Different shock wave propagation due to different crystal structures, grain boundaries and concentration gradients (DT ice will not be completely uniform in average concentration) will be important in the first stages of shock compression triggering hydrodynamic instabilities.

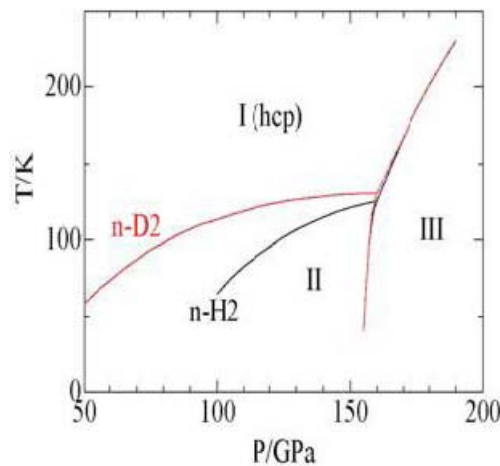


Fig. 1.12. Phase diagram for the deuterium and hydrogen, the difference between H₂ and D₂ is shown (Kawamura 2008).

For a review of targets we recommend the recent papers of Atzeni *et al* (Atzeni 2009, 2011) and (Thomas 2012) to name a few. Laser development is another highly active are of research. A

nice review of lasers in nuclear inertial fusion is offered in references (Tabak 1994, Sethian 2003, Chanteloup 2010).

Inertial fusion is mainly pursued in the USA. The path to Laser Inertial Fusion Energy (LIFE) is a four-step process:

First one was the construction and operation of a laser facility at the scale required for energy production (NIF). Second step was to demonstrate Ignition (In progress).

Next steps are: LIFE demonstration: Integration of all the technologies required for a power station (Planned for mid-2020s). Commercial LIFE fleet: Rollout of LIFE plants onto the electric grid (Late 2020s and beyond).

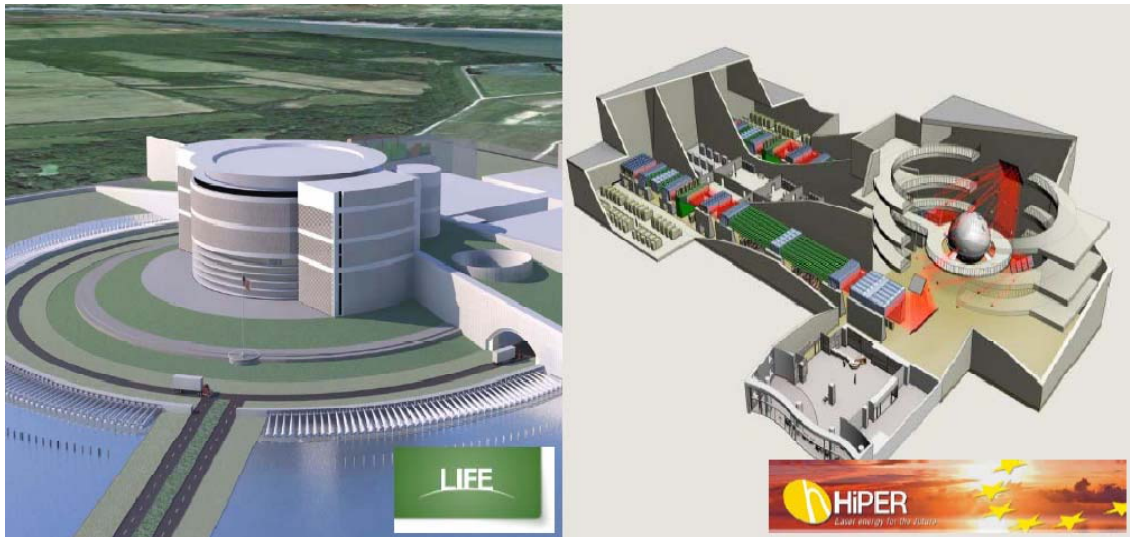


Fig. 1.13. Left) LIFE project, picture from NIF website. Right) European Inertial Confinement Fusion HiPER project. Both pictures are artist's impressions.

In the present design of LIFE the use of Li as both the breeder and coolant is foreseen. That could simplify the design which may result in higher reliability. This will be further discussed in next chapter dealing with liquid metals and breeding blanket technology.

Recently, a European collaboration has proposed the High Power Laser Energy Research (HiPER) facility, with the primary goal of demonstrating laser driven inertial fusion fast ignition. HiPER is expected to provide 250 kJ in multiple, 3ω (wavelength $\lambda = 0.35 \mu\text{m}$), nanosecond beams for compression and 70 kJ in 10–20 ps, 2ω beams for ignition. The baseline

approach is fast ignition by laser-accelerated fast electrons; cones are considered as a means to maximize ignition laser–fuel coupling.

Prior to a decision to proceed with HiPER construction the ignition scheme must be experimentally validated at full scale on an existing facility such as Laser Mégajoule (LMJ) or NIF.

In December 2010 the HiPER Executive Board made the important decision that the preferred ignition scheme for HiPER will be Shock Ignition, although other options including Fast Ignition with either electrons or protons are not excluded.

Experiments and associated numerical modeling, prior to completion of LMJ in ~2016, will be conducted using existing intermediate scale facilities including PALS (Czech Republic), PeTAL (France), Vulcan and Orion (UK), and Omega (US).

Once the modelling and experimental validations are sufficiently mature, an ignition campaign will commence on LMJ. Gain optimization experiments will follow, to underpin the commercial viability of Laser Energy [HiPER website].

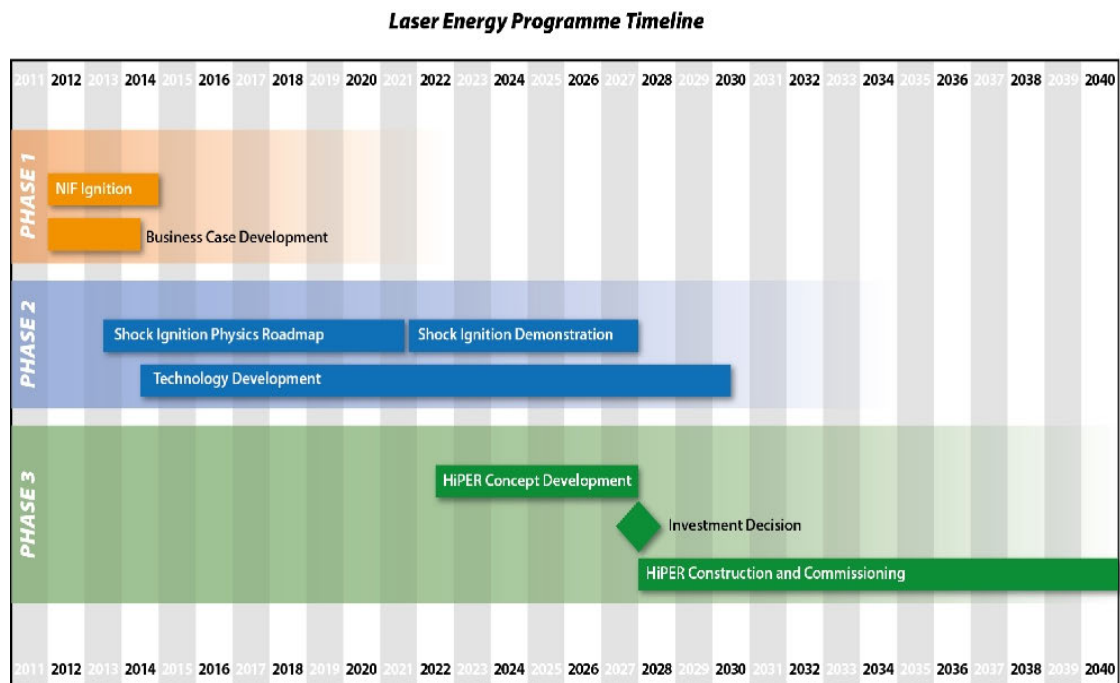


Fig. 1.14. Timeline for the proposed Laser Energy Programme [HiPER website].

Chapter 2

Liquid metals and fusion technology

Pb17Li is today a reference breeder material in diverse fusion R&D programs worldwide. One of the main issues in these programs is the problem of liquid metals breeder blanket behaviour. The structural material, constituting the blanket should meet high-performance requirements because of extreme operating conditions. The experimental data available are still scarce and sometimes the experimental uncertainty is important (Mas de les Valls 2008). Therefore the knowledge of eutectic properties like optimal composition, physical and thermodynamical behaviour or diffusion coefficients of tritium (T) are extremely necessary for current designs. In particular, the knowledge of the function linking the T concentration dissolved in liquid materials with the T partial pressure at a liquid/gas interface in equilibrium, $C_T=f(P_T)$, is of basic importance because it directly impacts all functional properties of a blanket determining: T inventory, T permeation rate and T extraction efficiency. Nowadays, understanding the structure and behaviour of this compound is therefore a real goal in fusion engineering and materials science.

In Chapter 1 we made a short introduction to nuclear fusion technologies. Here, we will shortly review the probable application of liquid metals in different parts of a nuclear fusion reactor. But not only Li-Pb system is interesting for fusion technologies. Liquid lead is used in neutron spallation sources (Henry 2008) and liquid lithium is a very promising candidate for plasma facing components (PFCs) and plasma protecting components. Recent works on the ITER and DEMO reactor projects showed that conventional technical and structural material solutions of first wall, divertor plates and other PFCs for steady state plasma burning presented serious difficulties (Verktoev 2007, Federici 2003 & 2005)

Power fusion reactor with heavy neutron flux and peak power loads cannot be realized with application of conventional solid plasma facing materials (PFM). Some problems like PFM degradation and T retention may be overcome by application of liquid metals. The best candidate is lithium as a material with low Z and low activation. What is sure is that lithium will play an important role in future nuclear fusion reactors (Evans 1978, Bloom 1990).

2.1 Liquid metals

The idea of replacing a solid first wall with a liquid wall in magnetic fusion devices was suggested by Christofilos more than four decades ago (Christofilos 1989). A review of ideas about liquid first walls can be found in (Moir 1987, 1995).

For breeding blanket designs there are mainly three candidate liquids that might meet all the required criteria, especially that of being able to breed enough tritium: Li, Flibe and Li17Pb. There are two typical formulations of FLiBe: Li_2BeF_4 and LiBeF. The first has a 10 times lower viscosity but a high melting point of 460 °C and the second has a melting point of 360°C (Sagara 1995, 1997).

Chemical and physical characteristics of lithium, especially a large liquidus range, high heat capacity and high thermal conductivity, allow lithium to be used as an effective nuclear reactor coolant. However, the corrosive properties of lithium require precautionary handling.

(1) Lithium reacts readily with water (vapor and liquid) to form hydrogen gas, a hazard under some accident conditions.

(2) Molten lithium is extremely reactive. It will burn on contact with the moist skin of personnel working with it. It also produces, upon burning, aerosols irritating to the respiratory system.

(3) Molten lithium reacts noticeably with concrete, other materials containing moisture and with many ceramic insulating materials. Lithium attacks ceramics more aggressively than sodium does.

The reactivity of Li17Pb is much less. It reacts significantly with water, carbon dioxide, and the water content of concrete but has very mild reactions with air and nitrogen. However pure lithium properties make it ideal to be used as plasma facing material and/or divertor designs.

2.1.1 Lithium divertor and plasma facing materials

Recently the 2nd International Symposium on Lithium Applications for Fusion Devices (ISLA-2011) was held at the Princeton Plasma Physics Laboratory (PPPL) with broad participation from the community working on aspects of Li research for fusion energy development. This community is expanding rapidly in many areas including experiments in magnetic confinement devices and a variety of Li test stands, theory and modeling and developing innovative approaches.

A number of unique properties of lithium determine its high potential for application for heat removal at the plasma–wall boundary:

- high latent heat of evaporation allows to redistribute efficiently the energy coming into divertor by evaporation–condensation processes,
- lithium flow from divertor region to the main vessel may be controlled by an appropriate divertor design due to efficient condensation (unlike gases),
- radiative emissivity of lithium may achieve 1000–1500 eV per one Li atom at $T_e = 20\text{--}50$ eV according to estimations of stepwise ionization process and it may be used for protection of the wall and divertor plates by radiation in disruption events and in normal conditions.

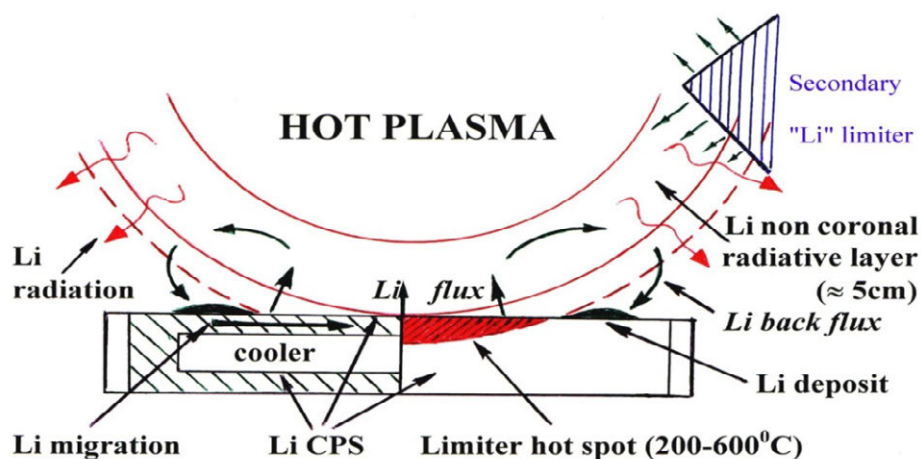
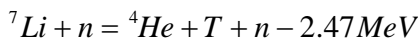
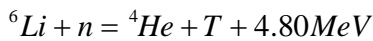


Fig. 2.1: Scheme of Li limiter concept and its interaction with tokamak plasmas (Mirnov 2009).

Early (1996) TFTR experiments showed that lithium can be successfully used as tokamak plasma facing material (PFM) and now one usually refers to ‘lithium tokamaks’ (Mansfield 1996). The Li coated tokamak vessel wall (lithiation) permits to obtain better plasma features (plasma confinement, purity, density limit) as compared with boronization. For more details about lithium PFM see (Evetikhin 2002, Verktov 2007, Nygren 2009).

2.1.2 Blanket

Deuterium is abundant in nature as about 1 part in 6500 in the hydrogen in water. Tritium does not occur naturally it is necessary to breed tritium by bombarding Li with the fusion neutrons,



The first reaction produces T by the capture of slow neutrons in ${}^6\text{Li}$, while the second produces T by inelastic scattering of fast neutrons on nuclei of the more abundant ${}^7\text{Li}$ isotope, followed by subsequent decay of the ${}^7\text{Li}$ into tritons and neutrons.

The large Pb content in Li17Pb (99.3 wt %) results in an effective neutron multiplication by the Pb (n, 2n)-reaction but this is partly compensated for by the higher ${}^7\text{Li}(n, n')T$ reaction in lithium. Li17Pb requires enriched Li to achieve a breeding ratio above unity. Overall, the breeding ratio achievable with Li17Pb with Li enriched to 90% ${}^6\text{Li}$ is slightly higher than the one in natural lithium (7.5 % ${}^6\text{Li}$) (Malang 1999).

Li17Pb has also a slight advantage compared to other breeder blankets in regard to the shielding properties but this can be compensated for by a few additional cm of shield in a lithium blanket.

Using Li-containing liquids in fusion blankets as a breeder/coolant is a very attractive option due to potentially higher blanket thermal efficiency (> 40 %) compared to solid breeder blankets. Besides utilization of different breeders (either molten salts FLiBe or FLiNaBe, or

liquid LiPb alloys or pure Li), liquid blankets can vary in many other ways depending, for instance, on: (i) cooling the breeder zone (helium-cooled, dual-coolant, or self-cooled blankets); (ii) basic flow direction (toroidal, poloidal or radial blankets); (iii) usage of insulating and structural materials, *etc.* Typical examples of liquid blankets are DCLL (dual-coolant lead-lithium), HCLL (helium-cooled LiPb), and self-cooled lithium/vanadium blankets. In spite of their attractiveness, liquid blankets have many feasibility issues associated with the nature of liquid breeders, including their high chemical activity, and interaction with the plasma-confining magnetic field that may result in various magnetohydrodynamic (MHD) effects.

Liquid metal blankets exhibit many features that make them attractive candidates for both near-term and long-term fusion applications. These advantages include:

1. Immunity to radiation damage. As liquids there are no concerns related to radiation damage lifetime.
2. Potential for tritium self-sufficiency without a beryllium neutron multiplier.

Beryllium is an expensive material and the resources are limited. The elimination of beryllium also simplifies the design options and there are no concerns with Be compatibility and radiation damage limits,

3. Tritium extraction outside blanket. Since a liquid can be circulated, it is not necessary to remove the T in-situ. This feature allows for greater flexibility for T removal options and separates the tritium removal system from the severe environment of the in-vessel components.

2.1.3 Pb-Li in the context of fusion energy

In different blanket concepts Li¹⁷Pb is foreseen as T breeder and neutron multiplier: Helium Coolant Lithium-Lead (HCLL), Water Coolant Lithium Lead (WCLL), Dual Coolant (DCLL) etc being HCLL concept selected as EU Test Blanket Module (TBM) to be tested in ITER (Norajitra 2002).



Fig. 2.2: Left) Dual Coolant Lead-Lithium (DCLL) concept. Taken from Wong *et al* (Wong 2006). Right) Cut-off view of a blanket design taken from (Wu 2007).

Much experimental and theoretical work has been done in the past years, covering many aspects of compatibility between Li17Pb and its environment. Particularly, significant results have been achieved in the field of corrosion of steels (Barker 1994), refractory metals and ceramic materials (Zhu 2009), MHD effects (Bühler 2007, Smolentsev 2008) etc. But despite of so many efforts PbLi-hydrogen isotope interaction and T extraction technology are still critical issues.

Liquid Breeder	Li	Li17Pb	Flibe	Li ₂₀ Sn ₈₀
Melting point (°C)	180	235	459	320
Density (g/cm ³)	0.48	8.98	2.0	6.0
	873K			
Li Density (g/cm ³)	0.48	0.061	0.28	0.09
	873K			
Breeding property	Good	Fairly good	Neutron multiplier required	Neutron multiplier required
Chemical stability	Active	Middle	Almost stable	Almost stable
Corrosion	Severe	Middle	HF exist, severe	?
Tritium release form	HT, T ₂	HT, T ₂	HT, T ₂ , TF	HT, T ₂

Table 2.I: Physical properties of eutectic LiPb (eutectic point to be determined) compared with other possible breeding materials.

In Table 2.1 we compare some physical properties of Li17Pb eutectic alloy, (the exact title, i.e. Li concentration is still to be determined) with other possible breeding materials as pure lithium, fluorine-lithium salts (FLiBe) and other eutectics like Li₂₀Sn₈₀. Li17Pb has fairly good breeding properties and middle chemical activity, and T release would be just T₂ and/or HT instead of TF for example when using FLiBe.

	Li	Li17Pb	Flibe	Li ₂₀ Sn ₈₀
Tritium solubility *	Very high	Very low	Very low	Middle
(atom frac Pa ^{-0.5}) (873K)	7.49x10 ⁻³	1.93x10 ⁻⁸	HT/T ₂ 1.77x10 ⁻¹¹ Pa ⁻¹ TF 1.77x10 ⁻¹¹ Pa ⁻¹	2x10 ⁻⁷ -1x10 ⁻⁵
Tritium diffusivity order (m ² /s) (873K)	Relatively high 10 ⁻⁹	Relatively high 10 ⁻⁹	Relatively high 10 ⁻⁹	Relatively high 10 ⁻⁹
Thermal conductivity	Li>Li ₂₀ Sn ₈₀ > Li17Pb > Flibe			
Dynamic viscosity	Flibe>Li ₂₀ Sn ₈₀ ~Li17Pb >Li			

Table 2.II: (I continued) Physical properties of Li17Pb compared with other possible breeding materials. T solubility and diffusivity is one of the main issues for blanket design.

2.1.4 Li17Pb physical properties

As we have seen Li17Pb present a number of advantages compared to pure Li, LiBe salts or other Li alloys. In the following section we will compare some physical properties vs temperature of Li17Pb with the corresponding values of pure Li and Pb. As we will see in Chapter 5, LiPb system is a strongly non-ideal alloy as can be seen in the excess heat capacity, resistivity and many other properties. However, some properties like density (see Figure 2.3) at the eutectic Li concentration are not very different from the linear behaviour.

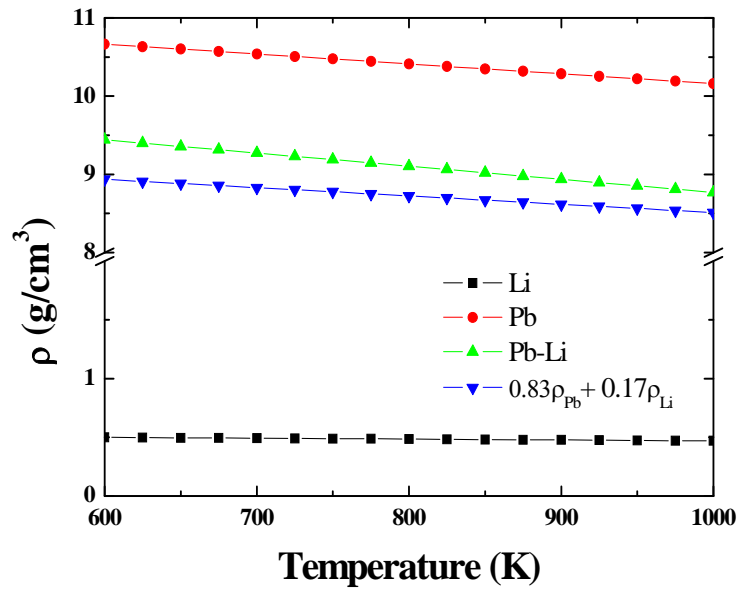


Fig. 2.3: Density of liquid Li (Ohse, 1985) and Pb (Brandes 1983, Gurvich 1991) compared to the Li17Pb (Mas de les Valls 2008). Blue triangles stand for the linear interpolation of Li and Pb densities. Note the break in the y-axis.

Interestingly, the LiPb density does not depart much from the simple interpolation (blue triangles) of both Li and Pb densities. This fact will be discussed in Chapter 5 when we will study the LiPb system in the whole range of Li concentrations.

The liquid metal (or alloy) viscosity will be another important property for engineering purposes as it will govern the fluid main properties. In engineering, the kinematic viscosity, ν , is often used, which is a ratio of the dynamic viscosity η to the liquid density ρ :

$$\nu = \eta / \rho \tag{2.1}$$

Accurate and reliable data on viscosity of liquid metals are not abundant. Some discrepancies between experimental data can be attributed to the high reactivity of metallic liquids, to the difficulty of taking precise measurements at elevated temperatures, and to a lack of a rigorous formula for calculations. All liquid metals are believed to be Newtonian liquids.

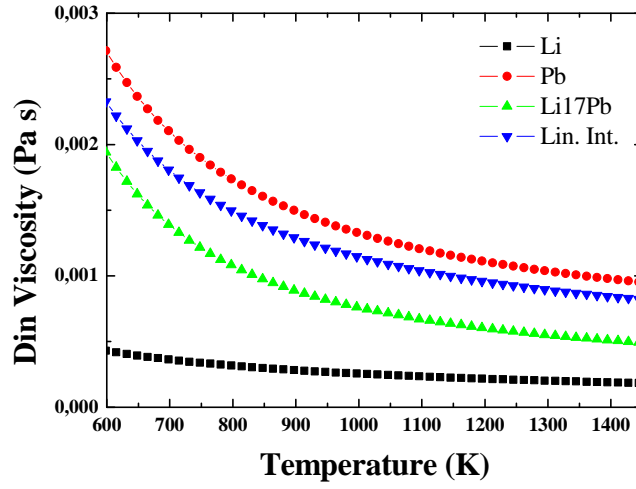


Fig. 2.4: Viscosity of liquid Li (Ohse, 1985) and Pb (Brandes 1983, Gurvich 1991) compared to the Li17Pb eutectic (Mas de les Valls 2001). Blue triangles stand for the linear interpolation.

The departure of viscosity from ideal linear behaviour ($v_{PbLi} = x_{Pb}v_{Pb} + x_{Li}v_{Li}$) can be regarded as another example of strong interaction between Li and Pb leading to short range order (SRO). Moelwyn-Hughes (Moelwyn-Hughes 1964) has proposed the following equation to calculate the viscosities for a binary liquid mixture through the enthalpies of mixing, that is

$$\eta = (x_1\eta_1 + x_2\eta_2) \left(1 - 2 \frac{\Delta H^E}{RT} \right) \quad (2.2)$$

where η represents viscosity of solution, η_i the viscosity of the pure component i and x_i mole fraction. ΔH^E is the integral molar enthalpy of mixing, R the gas constant, and T temperature in Kelvin. Eq. 2.2 can be rewritten as

$$\eta = \eta_{id} \left(1 - c_A c_B \frac{2\omega}{k_B T} \right) \quad (2.3)$$

Where ω is the interchange energy (Singh 1997)

Hence, $\eta < \eta_{id}$ for $\omega > 0$ and *vice versa*, $\eta > \eta_{id}$ for $w < 0$ corresponding to segregating demixing liquid alloys (positive SRO). Mathematical definition of SRO is given in Chapter 5 with further discussion of SRO in LiPb alloys.

Particle diffusion in fluids is an old scientific problem and of great importance in various studies, including chemistry, physics, material synthesis, and many areas in engineering (Stokes 1851, Einstein 1905, Mazo 2002). The diffusion of a solute is conventionally described by the well-known Stokes-Einstein (SE) relation,

$$D = k_B T / C \pi \eta R \quad (2.4)$$

where D is the diffusion coefficient of the solute, R the radius, and η the viscosity of the solvent. The constant C is determined by the hydrodynamic boundary condition, being 4 for the slip and 6 for the stick boundary condition, respectively.

However, if the size of the diffusing particle is not large compared to that of the solvent, the Stokes-Einstein relation is not expected to remain valid. (This will be discussed in more detail in Chapter 6)

The Stokes-Einstein relation predicts a diffusion that does not at all depend on the mass of the solute. This is completely opposite to the kinetic theory prediction. For example, the Enskog theory predicts a square root mass dependence, as given by the following expression:

$$D_E = \frac{3}{8 \rho \sigma^2 g(\sigma)} \sqrt{\frac{k_B T}{2 \pi \mu}} \quad (2.5)$$

Where μ is the reduced mass of the solute-solvent pair, σ is the diameter of the solvent, and $g(\sigma)$ is the value of the radial distribution function at contact (the x position of the first peak in $g(r)$).

But neither the kinetic theory nor the hydrodynamic theory can predict the correct mass dependence of diffusion. Clearly, the hydrodynamic and the kinetic theories describe two opposite limits of diffusion. While the first one assumes the validity of the Navier-Stokes hydrodynamics at molecular length scales, the second one tends to describe diffusion only in terms of binary collisional dynamics. While hydrodynamics assumes that the diffusion occurs via the coupling of the solute velocity with only the collective transverse current mode of the solvent, the Enskog kinetic theory neglects coupling of the solute motion to all the hydrodynamic modes. In both these pictures the diffusion due to the structural relaxation of the surrounding solvent is totally neglected.

The more recent mode coupling theory seems to interpolate between the two limits and takes into account the contributions of the structural relaxation. When the solute mass becomes significantly larger than the solvent molecules, the expression for the density contribution to friction (Bhattacharyya 1997, Bagchi 2001) leads to an inaccurate result – *it predicts an increase of diffusion with mass.*

The diffusion of hydrogen and its isotopes will be further discussed in Chapter 6.

Thermal conductivity is not accessible to our classical MD simulations. Only the estimation of the phonon contribution is possible but the main part of the conductivity will have an electronic origin.

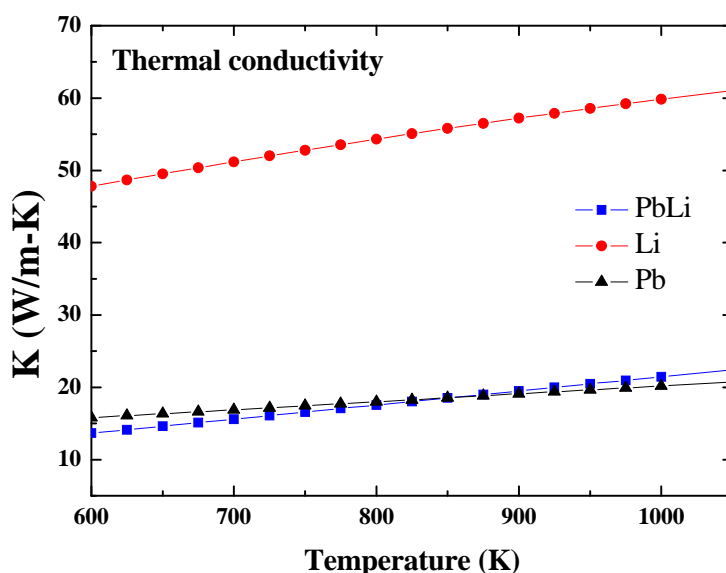


Fig. 2.5: Thermal conductivity of liquid Li (Ohse, 1985) and Pb (Brandes 1983, Gurvich 1991) compared to the Li₁₇Pb (Mas de les Vals 2008).

In next figure we show the thermal conductivity of Li17Pb compared to the pure liquid ones. As can be seen according to the experimental values of these systems the Li17Pb conductivity is almost that of the pure Pb.

The thermal conductivity, k , can be written as

$$k = \frac{n\langle v \rangle \lambda c_v}{3N_A} \quad (2.6)$$

Where n stands for the number of particles per volume, $\langle v \rangle$ represent the mean particle velocity, λ is the mean free path, c_v is the molar heat capacity and N_A is the Avogadro's number. Thermal conductivity and electrical resistivity are related by the well known Wiedemann Franz law;

$$\frac{k}{\sigma} = LT \quad (2.7)$$

Where σ is the electrical conductivity and L the Lorenz number ($2.44 \times 10^{-8} \text{ W } \Omega \text{ K}^{-2}$). Electrical resistivity is an important property to understand different magnetohydrodynamic effects in the liquid melt flow (Bühler 2007, Hongli 2008).

But using classical MD, only the phonon contribution to thermal conductivity is accessible. And for liquid metals this represents a small percent of the total conductivity (less than 10 % for most metals).

Another important physical property accessible to MD calculations is the surface tension. The surface tension, γ_0 , can be derived from the pressure tensors as:

$$\gamma_0 = \frac{1}{2} L_z \left[P_{zz} - \frac{1}{2} (P_{xx} + P_{yy}) \right] \quad (2.8)$$

The surface tension value and its temperature dependence are essential for describing surface-tension-driven flow on the liquid surface.

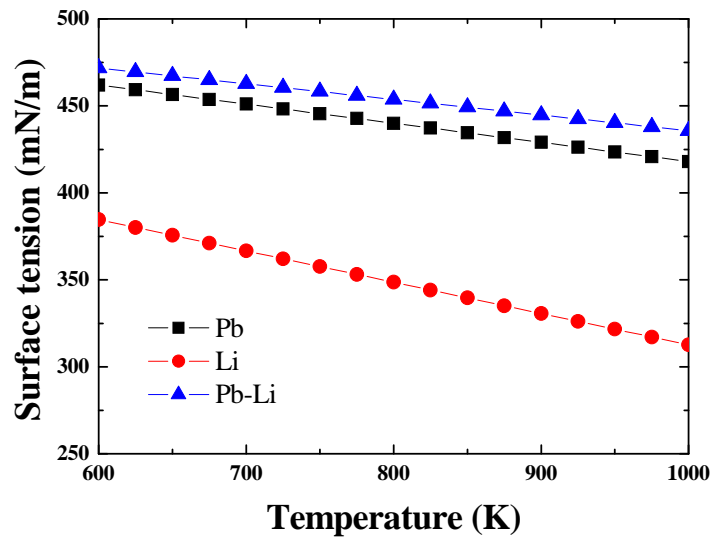


Fig. 2.6: Surface tension of liquid Li (Ohse, 1985) and Pb (Brandes 1983, Gurvich 1991) compared to the Li17Pb (Mas de les Valls 2008).

It is to be noted that two simple liquid metals do not necessarily form a simple alloy, e.g., LiPb, NaPb, etc. The electrical resistivity rises from typical simple metal values at the ends of concentration range to a very high value in between. There is clearly a profound change in the conduction electron character and the system deviates from a nearly free electron (NFE) behaviour. This will be carefully examined in Chapter 5.

2.1.5 Hydrogen isotopes inside liquid LiPb

The main motivation of our atomistic study of LiPb alloys is to study with powerful tools one of the most important unsolved problems concerning the use of liquid metals for breeder blankets; only the order of the diffusivity is known, and dispersion in solubility results depending on the technique makes the database inadequate for design purposes. Some reason seems to be the strong dependence of tritium solubility with Li concentration. This is one of the main reasons that make so important the exact determination of eutectic point in the LiPb system. (See Fig. 2.7). However, some recent results show how solubility is not so Li-concentration dependent (Karasawa 2012).

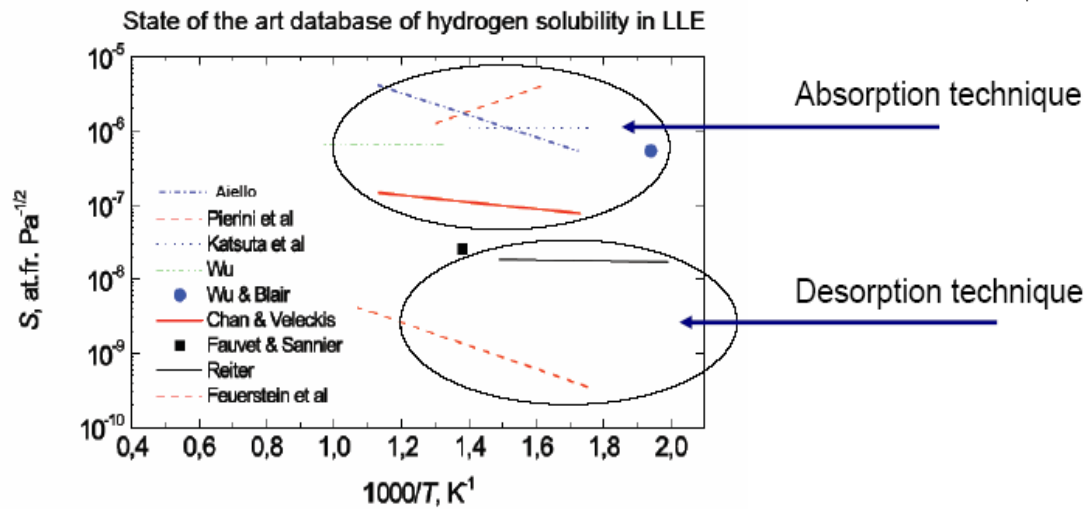


Fig. 2.7: Tritium solubility database. Scatter reflects experimental approaches and measurement techniques applied. Knowledge of dynamic transport properties (diffusion, mass transfer, interface processes) is much more limited.

Tritium recovery from lithium metal and the liquid Li17Pb alloy has been investigated using several extraction processes of gas sweeping, metal window, metal getter, etc (Pieroni 1984, 1985, Sze 1985). The sweep gas bubbling method is considered to be the most promising for the liquid Li17Pb alloys.

The extraction rate of the T from the LiPb alloys has been studied as a function of the heating temperature, the flow rates of the bubbling gas and H, contents in the sweep gas (He) (Saibene 1988, Terai 1992). However there is no data on the effect of the bubble diameters on the extraction rate, which is the key factor to design the T extraction system in the blanket and the fuel cycle of fusion reactors. The evaluation of the bubble diameters is difficult, because the bubbles are not visible in the liquid Li17Pb. It is important to develop a method to analyze the bubble diameters of the sweep gas. Based on the experimental data, empirical equations are proposed for the evaluation of the bubble diameters in liquids and examined their applicability especially for the liquid Li17Pb alloy (Mas de les Valls 2008).

Diffusion coefficient and Sievert's constants for H (D and T) has been measured but consensus is poor (Mas de les Valls 2008). Sievert's constant largely depend on the experimental technique used. As far as we are concerned the more recent experiments are given in (Edao

2011). The diffusivity of H is much closer to that of D, and the isotope effect of diffusivity between H and D is small. The solubility of D is around 1.4 times larger than that of H in the temperature range from 573 to 873 K.

2.1.6 Helium inside liquid LiPb

As far as we are concerned He solubility in PbLi is unknown. In next graph we show the He solubility in liquid Li, Pb and Li₁₇Pb. The solubilities of rare gases increase in a consistent manner with decreasing atomic radius of the rare-gas solute atom; conversely, the solubility of a given gas decrease with decreasing atomic radius of the solvent liquid-metal atom (Reed 1970).

Helium solubility inside liquid Li can be written as: $\log\chi = -7.323 - 846/T$ (K), derived from data in (Stolnick 1965) and valid from 649 to 871°C (872 to 1124 K). Solubility data for He inside liquid Pb can be found in (Shpil'rain 2007).

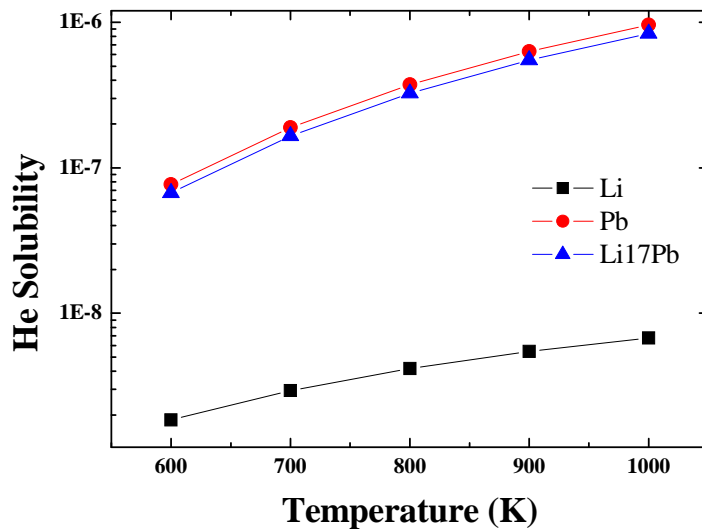


Fig. 2.8. He solubility (in mole of gas/mole of metal units) vs temperature (in K) in liquid Pb, Li and Li₁₇Pb. Data taken from (Reed 1970) and (Shpil'rain 2007), blue triangles (this work).

Assuming that the solubility of inert gases in metal melts is an additive property (Shpil'rain 2007), the following equation may be written for their solubility in a two-component Li₁₇Pb eutectic in the liquid phase:

$$x_1^{PbLi} = x_1^{Pb} y^{Pb} + x_1^{Li} y^{Li} \quad (2.9)$$

where x^{Pb} , x^{Li} and x^{PbLi} is the solubility of inert gas in liquid lead, lithium, and Li17Pb alloy per mole of gas/mole of metal, respectively; and y_{Pb} and y_{Li} denote the molar concentration of lead and lithium in the Li17Pb eutectic, respectively. Parameters for He solubilities are collected in Table 2.III.

	He-Pb	He-Li	He-PbLi
-A	4.371	-7.323	4.433
-B	1645.994	- 846	1643.84

Table 2.III. Coefficients of approximating equation $\log x_1^2 = A + B/T$.

As can be seen in Figure 2.8 the He solubility in Li17Pb is almost the same as that of pure Pb. However, the solubility and diffusivity of H, D or T could be quite different in Pb and in Li17Pb. An important issue is to understand how much it depends on the Li concentration and Li order inside the liquid alloy.

In order to have an order of magnitude for H diffusivity in Li17Pb is possible to proceed in a rough qualitatively form as proposed in (Mas de les Valls 2008). Comparison of diffusion data for H and He in Li related it with data for H in the eutectic provides such as estimation, i.e.:

$$\frac{D_{He}^{PbLi}}{D_{He}^{Li}} = \frac{D_H^{PbLi}}{D_H^{Li}} \quad (2.10)$$

The results obtained that way are summarized in the following graph.

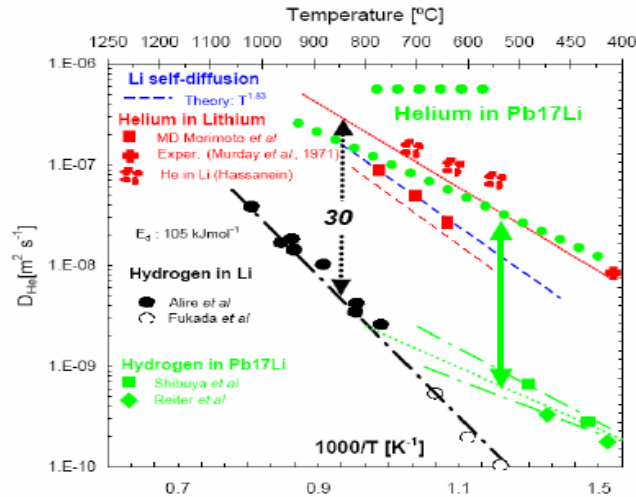


Fig. 2.9. Helium diffusivity vs $1/T$ in liquid Li_{17}Pb estimated from He and H diffusivities inside liquid Li (taken from (Mas de les Valls 2008)).

This approximation could be wrong as we will see in Chapter 6 when we study H diffusion in different liquid metals. In fact the expression (2.10) is true if we assume that the ratio of diffusivities is equal to the inverse ratio of masses as can be seen with a little of algebra. This crude affirmation is, in general, what we observed for H in liquid metals (Al, Ni and Pd) calculated with different potentials, but in clear disagreement with experimental results.

2.1.7 Helium bubbles inside liquid metals

Cavitation in fluid machinery has been a serious issue in many hydraulic applications, causing erosion of solid surfaces and resulting sometimes in destruction of structures (Arndt 1981, Karimi 1986). Cavitation in liquid mercury (Hg) is now a significant issue in the development of pulsed high-power spallation neutron sources, in which liquid Hg is bombarded by a high intensity proton beam to produce high neutron fluxes. In off beam experiments (Futakawa 2003), it was suggested that high-intensity pressure waves originating from the energy release due to spallation reactions would cause cavitation in Hg, and the associated erosion (cavitation erosion) would significantly reduce the lifetime of the target vessel in which liquid Hg flows.

In ref. (Futakawa 2008) three kinds of numerical simulations are carried out by using macro-, meso-, and microscale codes presenting another interesting example of multi-scale problem. One of the potential approaches to mitigating the cavitation erosion or preventing the cavitation

itself is to inject gas bubbles into liquid Hg. As has been demonstrated in previous studies (Carstensen 1998, Wijngaarden 1989), gas bubbles in a liquid change the dynamic and acoustic properties of the liquid and can, in some situations, act as an absorber of sound through their volume change or volume oscillation in response to pressure change. Figure 2.10 shows schematically the process.

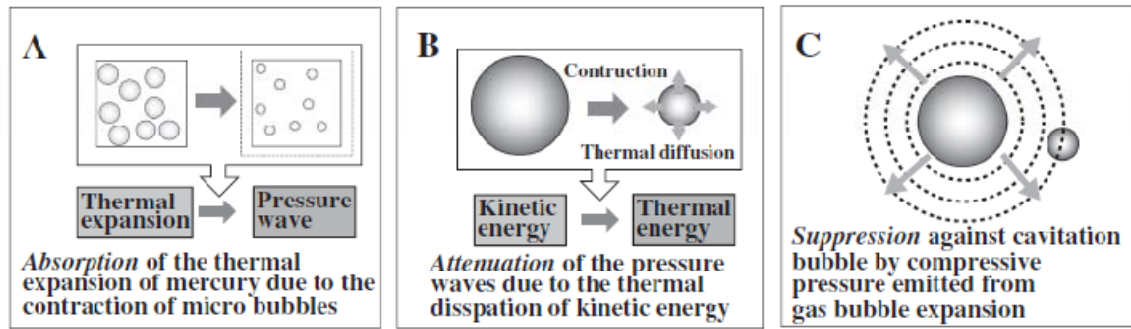


Fig. 2.10. Mechanisms of the pressure wave mitigation by bubbling (Futakawa 2008).

Helium behaviour inside liquid Pb, Li or LiPb alloys will be studied from an atomistic point of view but first will be necessary to develop the correspondent interatomic potentials (He-Li and He-Pb). The necessary *ab initio* calculations to calculate the forces etc will be explained in detail in Chapter 7. Here we stress some of the problems facing with He inside liquid metals.

An initial stage of bubble formation takes a long time compared to a typical MD-time scale, $\sim 10^{-9}$ seconds (Insepov 2007). To two processes, with different time scales have to be taken into account:

1. Slow process – formation of a critical nucleus.

This process could be studied by the kinetic theory balance equations (Frenkel 1947). However, for using this theory, we would need all the kinetic association and dissociation coefficients that should be obtained from experiment or calculated by Molecular Dynamics. The number of kinetic coefficients could be reduced by using the scaling theory (Binder 1976). Still, this would be a huge computational task.

2. Fast process – Bubble collapse and sputtering.

This part is “easy” to model by MD, typical times are about 10^{-12} sec (Insepov 2007).

The growth mechanism of cavitation bubble nuclei and the dependence with time for the growth of the mean radius using MD simulations has been investigated, for example, in (Tsuda 2008). MD simulations have been performed to investigate the microscopic dynamics of a bubble when liquids are locally heated (Okamura 2003). The bubble dynamics in that process agrees with the results of the Rayleigh-Plesset equation which describes the dynamics of a bubble in terms of macroscopic hydrodynamics, i. e. the hydrodynamic description is reliable even for microscopic bubbles (Okamura 2003). In both abovementioned studies they made use of L-J potentials (they simulated Ar, He etc). As far as we are concerned, little work has been made in the past about bubbles in liquid metals using realistic potentials.

He-Li and He-Pb potentials have to be developed. In a recent work Soldan et al presented a Li^+ -He interatomic potential (Soldan 2001). However the potential proposed in that paper means to be used to simulate the interaction of the Li ion with He atoms, but not to study He inside neutral pure lithium as we pretend [T.G. Wright private communication].

Chapter 3

Molecular Dynamics in short

In 1952 MANIAC (one of the first computers) was operational at Los Alamos after the Manhattan project. Metropolis, Rosenbluth and Teller developed the Metropolis Monte Carlo method (MC) to address the entropic free energy problem (Metropolis 1953). This paper introduced the MC technique to the solving of physical equations. It described the idea of using random numbers to project a representative subset of conformational space, whilst using the exponent of the energy as a probability filter. To use this method properly, you also need a mathematically correct random number generator. This study can be considered the beginning of computer simulations.

Few years after Alder and Wainwright (Livermore 1956) run the first molecular dynamics (MD) simulation looking at the dynamics of hard spheres (Alder 1959). And soon after Vineyard et al. (Brookhaven 1959-60) studied the radiation damage in copper (Rahman 1964). Also some few years after Rahman (Argonne 1964) studied with a Lennard-Jones (LJ) potential the dynamics of liquid Argon. An LJ potential is very accurate to describe rare gases that repel each other at very close distances and at large distances attract each other with the weak dipole-dipole interaction that goes $1/r^6$ (Lennard-Jones 1924). The interatomic potential (or potentials in a binary system) is the key of a good simulation (if the implementation of the MD code is correct). Interatomic potentials will be described in section 3.4.

MD is a powerful tool to simulate and understand all kinds of systems spanning from solids to liquids under different conditions. In this chapter we will make a very short introduction to the basis of Classical MD.

Atomistic simulations generate information at the microscopic level. The conversion of microscopic information to macroscopic observables such as pressure, energy, heat capacities, etc., requires statistical mechanics. The main idea behind using atomistic simulation is to describe system's macroscopic behaviour in terms of microscopic information and to obtain information that is not easily obtained from experiments.

3.1 Thermodynamical ensembles

Atomistic simulations are conducted under well-defined thermodynamic conditions. These conditions specify the “ensemble” of the systems (Frenkel, 1996, Greiner 1997). Atomistic simulations are commonly classified into two categories: equilibrium (EMD) and nonequilibrium (NEMD). By nonequilibrium we mean a fluid which is acted upon by an external field. This field drives the fluid away from equilibrium and, if sufficient time is available, towards a nonequilibrium steady-state (as long as the field itself is predictably well behaved). NEMD examples are radiation damage, shock waves and viscosity calculations. There are many subtleties associated with NEMD. For a more comprehensive description, see references (Evans 1984, 1990, Sarman 1998). In equilibrium atomistic simulations, the system is completely isolated from its surroundings with a fixed number of atoms, volume and constant total energy. These boundary conditions correspond to the microcanonical (NVE) ensemble in statistical mechanics. The natural ensemble is the microcanonical because Newton’s equations lead naturally to energy conservation. Unfortunately, the microcanonical ensemble does not correspond to the conditions under which most experiments are carried out. To run simulations at other non-NVE statistical ensembles we must introduce a thermostat and/or a barostat in the system. Depending on the equations of motion that describe the system of atoms, these calculations may correspond to the canonical (NVT) and/or the isothermal isobaric (NPT) ensemble in statistical mechanics. There are several schemes that have been devised to thermostat systems treated with atomistic simulations. A brief description of the thermostating methods used in this work is given in Section 3.2.2.

Independent	Dependent	Ensemble
NVE	μ PT	Microcanonical
NVT	μ PE	Canonical
NPH	μ VT	Isoenthalpic-isobaric
NPT	μ VH	Isothermal-isobaric
μ VL	NPT	Grand-microcanonical
μ VT	NPL	Grand-canonical
μ PR	NVT	Grand-isothermal-isobaric
μ PT	NVR	Generalized

Table 3.I. Different ensembles, their names and the independent and dependent properties in each case.

3.2 Molecular Dynamics

Molecular dynamics (MD) is a computer simulation method to follow the motion of particles with time by numerically integrating classical equations of motion. A general flow chart for a classical MD simulation is shown in Fig. 3.1. When an MD simulation is started for the very first time, one needs to specify the initial arrangement of the atoms in space, (starting crystal structure for example), their initial momenta and parameters that determine the interatomic potential.

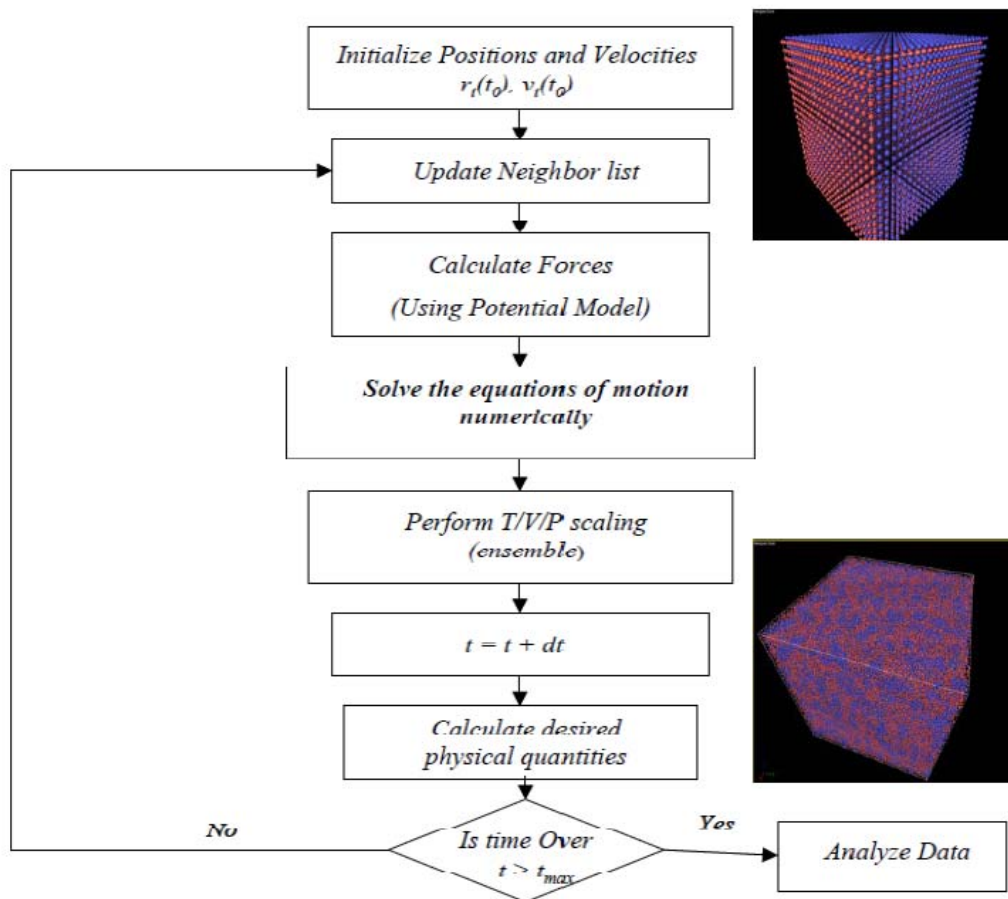


Fig. 3.1. A general flow chart for molecular dynamics simulation. Up-right corner shows an initial sample of LiPb (B2 phase). Down-right corner shows the sample in liquid phase.

The momenta in some cases need to be scaled such that they match an initial input temperature. Atoms in the system interact with each other through an interatomic potential, $\Phi(r)$. Interatomic potentials will be shortly reviewed in Section 3.4. A neighbour list allows one to reduce the number of possible interactions one needs to consider. The neighbour list is created at the beginning of the simulation and upon subsequent calls, the list gets updated automatically (see LAMMPS manual for details). Forces between particles are calculated from the gradient of the energy function. The time integration algorithms allow one to integrate the equation of motion of the interacting particles and follow their trajectory.

Knowing the positions and some of their time derivatives at time t (the exact details depend on the type of algorithm), the integration scheme gives the same quantities at a later time $t+\delta t$. For constant temperature (or pressure) simulations, atoms are also required to interact with a thermostat (or barostat). By iterating the above procedure, the time evolution of the system can be followed for long times. After a period of time the system approaches thermodynamic equilibrium and the physical properties of interest can then be calculated.

The major task of the MD simulation is to predict the time-dependent trajectories in a system of interacting particles. For this purpose, time-integration algorithms were devised to solve the equations of motion based upon truncated Taylor's expansions with respect to time. Detailed descriptions of these simulation algorithms can be found elsewhere (Burkert 1982, Hoover 1986, Rapaport, 1995, Frenkel, 1996). A nice review of methods for simulation of liquids can be found in (Allen 1987) as well as in (Ercolessi 1997).

3.2.1 Integrators

Different methods can be used to solve the classical equations of motion. Two popular integration methods for MD calculations are the velocity Verlet algorithm (Verlet 1967) and the predictor-corrector algorithms (Nordsieck 1962, Gear 1971). Both Verlet and rESPA, (for reversible reference system propagator algorithms) (Tuckerman 1992) algorithms are integrated in LAMMPS package. In Figure 3.2 we show how both algorithms are almost equivalent from a "computational cost" point of view. The simulation corresponds to the heating of a small Pb sample using the Embedded Atom Method potential (EAM) developed in (Zhou 2001).

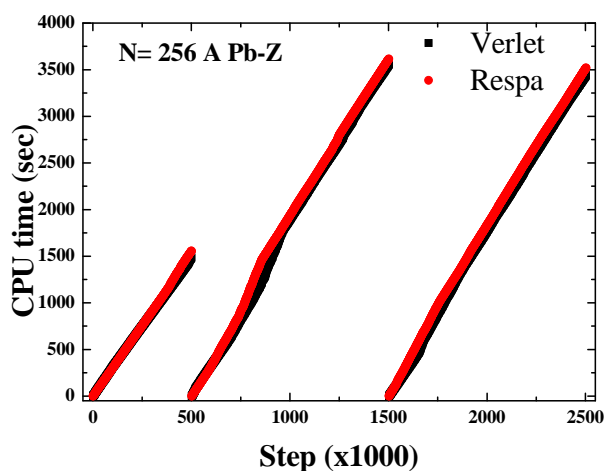


Fig. 3.2. Computer CPU time (in seconds) with two different integrators in different simulation stages (from left to right; NVE, Berendsen heating and final equilibration with N-H thermostat).

3.2.2 Thermostats

Appropriate temperature (T) control methods must be incorporated into simulations that maintain constant T . The temperature is defined by the ensemble average of the kinetic energies of all particles as:

$$\left\langle \frac{1}{2}mv^2 \right\rangle = \frac{k_B T}{2} \quad (3.1)$$

Therefore it is impossible to fix T exactly at a set point. Two techniques for T control are commonly used: (i) Direct velocity rescaling and (ii) The extended system method. Direct velocity rescaling involves resetting the velocities of the particles at each time step so that the total kinetic energy of the system remains strictly constant. They suffer the drawback that they are not time-reversible or deterministic, properties that become important in some advanced MD techniques (Hünenberger 2005). In the extended system method, the system is allowed to interact with the surrounding environment through some thermal constraints. The system may

be coupled to a heat bath to ensure that the average system temperature is maintained close to the requested temperature.

When this is done the equations of motion are modified and the system no longer samples the microcanonical ensemble. Instead trajectories in the canonical (NVT) ensemble are generated. Many different methods exist to specify the interaction between the atomic system and the environment (Hünenberger 2005). The Nose-Hoover thermostat is one such method and has been used in our MD simulations.

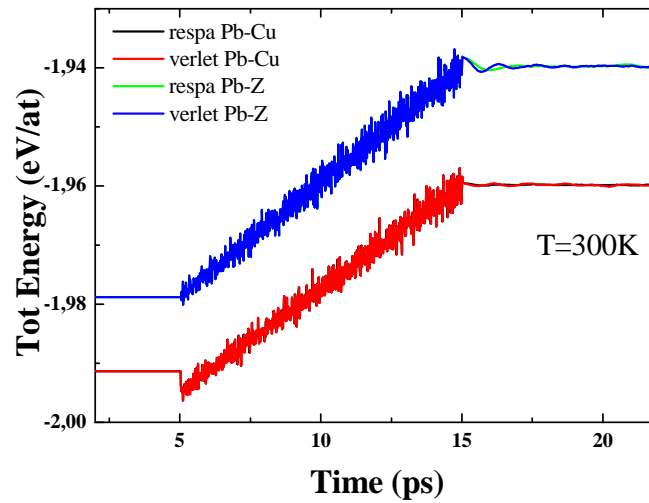


Fig. 3.3. Comparison of two different algorithms (black and green lines rESPA and red and blue ones to Verlet) in a MD run simulating the heating of a Pb sample with two different EAM potentials ((Pb) Zhou 2001) and ((Pb-Cu) Hoyt 2003).

3.2.3 Nosé-Hoover Thermostat

The Nosé-Hoover (NH) thermostat is an extended system thermostat that incorporates an external temperature reservoir into the system. The equations of motion for the system are augmented by a frictional coefficient, ξ , which couples the system dynamics to the reservoir. William G. Hoover (Hoover 1985) extended the analysis of Nosé (Nosé 1984), who proposed first such equations for the NVT ensemble, and developed the following equations for the NVT ensemble.

$$\dot{r}_i = \frac{p_i}{m}$$

$$\dot{p}_i = F_i - \xi \cdot p_i \tag{3.2}$$

$$\dot{\xi}_i = \frac{1}{Q} \left\{ \sum_{i=1}^N \frac{p_i^2}{m_i} - (f + 1)k_B T \right\}$$

where f is the degrees of freedom of the physical system (e.g. $3N$), T is the desired temperature and Q is the fictitious mass of the additional degree of freedom (reservoir). The choice of Q is critical in the implementation of this thermostat (Hünenberger 2005). The thermodynamic friction constant dynamically alters the velocities of the individual atoms such that the temperature of the system is adjusted towards the desired temperature. The NH thermostat is more complicated than other methods but it is also the best and most used thermostat today for NVT simulations.

3.2.4 Periodic boundary conditions

Despite the rapid advancement of computer power, simulating systems with more than a few million atoms at one time is still expensive. Simulations are therefore limited to systems with tens of thousands atoms on personal computers and about a billion atoms on super computers. To model a macroscopic system in terms of a finite simulation system of N particles, the concept of periodic boundary conditions (PBC) is often employed (Frenkel 1996). They are useful for simulating a part of a bulk system with no surfaces present and they have been used in all of our simulations.

Figure 3.4 illustrates the concept of PBC. The primary cell is outlined with solid lines and it represents an actual system one is interested in simulating. The primary simulated box is replicated throughout space to form an infinite lattice. Every atom in the simulation box therefore has an exact duplicate (image) in each of the surrounding image cells. A result, whenever an atom leaves the simulation cell, it is replaced by another atom with exactly the same velocity, entering from the opposite cell face. Therefore, the number of atoms, N , in the cell is conserved. Note that atoms that lie near the borders of the primary computational cell

interact with neighbour atoms across the periodic boundary. While PBC remove the effects of free surfaces, they impart image constraints on the system that must be taken into consideration when simulating defect behaviour with long-range interactions.

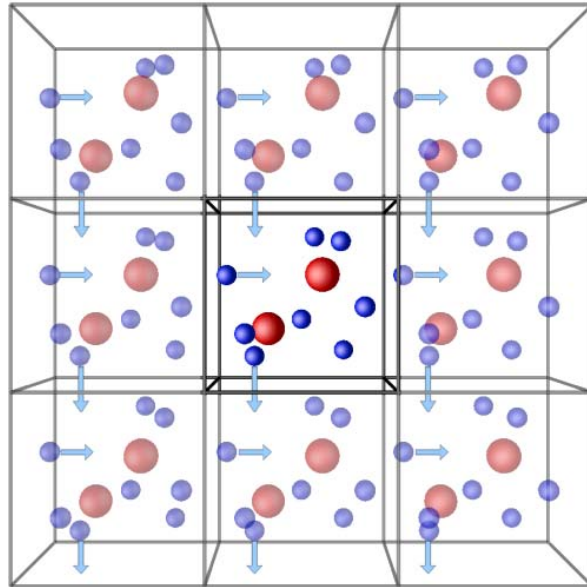


Fig. 3.4. Illustration of periodic boundary conditions in 3D.

3.3 Computational details

The MD simulations are implemented using the LAMMPS software. LAMMPS, also known as Large-scale Atomic/Molecular Massively Parallel Simulator (Plimpton 1995). Other popular MD codes are MOLDY (Refson 2000) and MDCASK (Almazouzi 1998) to name a few. The power of LAMMPS resides in the possibility of run in parallel through the Message Passing Interface (MPI) (Gropp 1999) or OpenMPI. Recently, LAMMPS is being adapted to be used on GPUs, (graphics processing unit).

First step in this work has been to establish a MD protocol for liquid metal simulations. The details of each simulation depend on the physical property or properties under study. In a few words our MD protocol can be summarized as follows:

3.3.1 Sample creation

The simulation code needs two inputs, one is the interatomic potentials giving the forces between different species and two, the initial position of atoms. Our systems are Li, Pb and mixtures of LiPb at different concentrations as well as H (at low concentration) inside metals, (Al, Ni and Pd, see Chapter 6). For Li and Pb we started in general from the crystal structure at normal conditions, i.e., fcc for Pb and bcc for Li. For LiPb mixtures we start from an fcc lattice with random distribution of Li atoms and also from a bcc B2 phase CS for LiPb in the 50-50 composition (See Chapter 5).

3.3.2 Energy minimization.

The code performs an energy minimization of the system by iteratively adjusting atom coordinates. Iterations are terminated when one of the stopping criteria is satisfied. The objective function being minimized is the total potential energy of the system as a function of the N atom coordinates.

The algorithm used for minimization is the conjugate gradient (CG) in the Polak-Ribiere version (Polak 1971) of the CG algorithm (Hestenes, 1952). At each iteration the force gradient is combined with the previous iteration information to compute a new search direction perpendicular (conjugate) to the previous search direction. The PR variant affects how the direction is chosen and how the CG method is restarted when it ceases to make progress. The PR variant is thought to be the most effective CG choice for most problems.

3.3.3 Initial heating in the microcanonical ensemble (NVE).

We perform first a short heating of the sample in the microcanonical ensemble. During the NVE integration velocities and positions of atoms are updated each timestep. N is the number of atoms, V is the volume and E is the total energy. This creates a system trajectory consistent with the microcanonical ensemble (Frenkel 2002) and serves us to check proper energy conservation (and timestep). This first stage corresponds to the first 5 ps in Figure 3.3.

3.3.4 Berendsen thermostat and barostat.

In the Berendsen temperature control scheme (Berendsen 1984), all velocities are scaled at each time step by a factor λ given by

$$\lambda = \sqrt{1 + \frac{\Delta t}{\tau_T} \left(\frac{T_0}{T} - 1 \right)} \quad (3.3)$$

Where, Δt is the time step of the simulation, τ_T is the time constant for temperature control and has to be greater than $100\Delta t$, T_0 is the desired temperature and T is the current temperature.

The Berendsen pressure control is implemented by changing all atom positions, and the system size is scaled at each time step by a factor μ given by

$$\mu = \left[1 - \frac{\beta \Delta t}{\tau_P} (P_0 - P) \right]^{1/3} \quad (3.4)$$

Where τ_P is the time constant for pressure control which should be typically greater than $100\Delta t$, P_0 is the desired pressure and P is the current pressure, b is the isothermal compressibility of the system. This type of temperature and pressure scaling gives realistic fluctuations in the temperature and pressure when large values of τ_T and τ_P are chosen.

3.3.5 Final heating and equilibration: N-H thermostat-barostat.

As final step in our MD we run a “long” constant NPT using the Nosé-Hoover thermostat (and barostat) (Nosé 1984, Hoover 1985, Martyna 1994). This creates a system trajectory consistent with the isothermal–isobaric ensemble. This is probably the more generic and the more powerful approach to the problem of thermalization. We are adding to our set of equations of

motion an additional (to positions and velocities) dynamical variable. That additional dynamical variable is a tool that either slows down or accelerates our particles in order to fluctuate appropriately around the target temperature.

These steps can be seen in Figure 3.3. During the initial heating the total energy is exactly conserved. In the second step the Berendsen thermostat increases the temperature up to the desired value (the total energy is not a conserved quantity here), and finally the NH thermostat equilibrates the system. The control of T (or P) is specified in LAMMPS with a damp parameter in time units (usually 100 timesteps for T_{damp} for example). The effect of these damp values in the final values of different properties has been benchmarked.

3.4 Interatomic Potentials

The key and soul of a MD simulation, (once all the algorithms are well implemented in the code) is the set of potentials used to describe the different interactions. When choosing potentials one should consider the following characteristics: (1) **Accuracy** (reproduce properties of interest as closely as possible). (2) **Transferability** (can be used to study a variety of properties for which it was not fit). And (3) **Computational speed** (calculations are fast with simple potentials). The choice of the interatomic potential depends on the area of intended application, there are (almost) no “good” or “bad” potentials, there are potentials that are appropriate or inappropriate for a given problem. High accuracy is typically required in Computational Chemistry, computational speed is often critical in Materials Science (processes have a collective character and big systems should be simulated for long times).

As we explained before we want to study Li17Pb alloys as we as He behavior in liquid metals and alloys but the high temperature conditions makes not easy and expensive to perform such kind of experiments so we decided to develop the interatomic potential for the relevant interactions (Pb-Li He-Pb, He-Li). This will be described in detail in Chapter 5 and 7.

The simplest classical pair potentials include the hard-sphere potential, square-well potential, and soft-sphere potential (Allen, 1987). More idealized yet still simple pair potentials include the Lennard Jones potential (Lennard-Jones 1924), Morse potential (Morse 1929, 1930), and Born–Mayer potential (Born 1932).

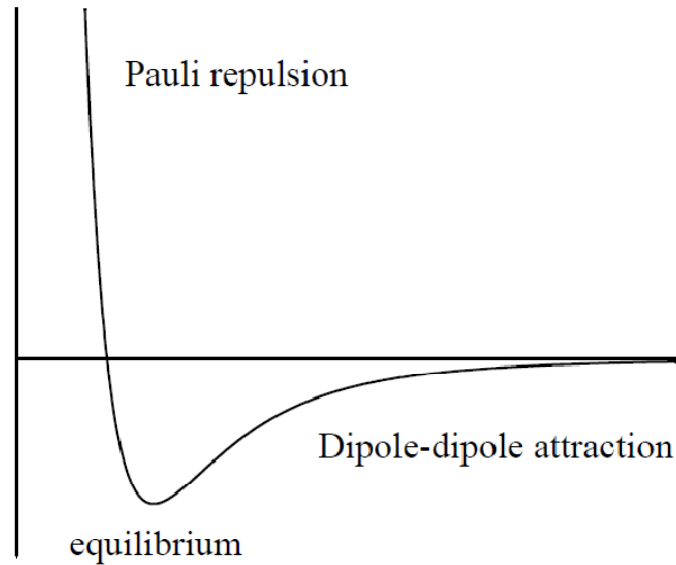


Fig. 3.5. Pair interatomic potential, $V(r)$ vs interatomic distance. Two distinct regimes depending on the distance are shown, repulsion (due to Pauli principle) and dipole-dipole attraction.

The Lennard-Jones (also known as 12-6 or simply L-J) potential is defined as

$$V(r) = 4\varepsilon \left[\left(\frac{\sigma}{r} \right)^{12} - \left(\frac{\sigma}{r} \right)^6 \right] \quad (3.5)$$

Where ε is the depth of the potential well and σ is the (finite) distance at which the interparticle potential is zero and r is the distance between the particles ($V(r) = 0$).

The term $\sim 1/r_{ij}^{12}$ - the repulsion between atoms when they are brought close to each other. Its physical origin is related to the Pauli principle: when the electronic clouds surrounding the atoms starts to overlap, the energy of the system increases abruptly. The exponent 12 was chosen on a practical basis: L-J potential is particularly easy to compute. In fact, on physical grounds an exponential behavior would be more appropriate.

The term $\sim 1/r_{ij}^6$, dominating at large distance, constitute the attractive part and describes the cohesion to the system. A $1/r^6$ attraction describes van der Waals dispersion forces (dipole-dipole interactions due to fluctuating dipoles). These are rather weak interactions, which however are responsible for bonding in closed-shell systems, such as inert gases.

The L-J potential provides a good description of van der Waals interaction in inert gases and molecular systems (Ar, Kr, CH₄, O₂, H₂, C₂H₄, etc.). Parameters are given in (Matyushov 1996). Parameters for inert gases can be also found in Ashcroft-Mermin textbook (Ashcroft 1976).

	Helium	Neon	Argon	Krypton	Xenon
ϵ (K)	10.97	42.25	143.235	201.200	282.289
σ (Å)	2.6456	2.7538	3.3472	3.5708	3.8868

Table 3.II. Potentials and parameters of the rare gas series taken from (Lombardi 2008).

Today L-J potential is also often used in simulations when the objective is to model a general class of effects and the only requirement is to have a physically reasonable potential. This is the main reason for popularity of Lennard-Jones potential. Interestingly, LJ pair potential parameters for solvents can be calculated from gas solubility data by using the scaled particle theory to calculate the work of cavity formation (Wilhelm 1971).

Morse – similar to Lennard-Jones but is a more “bonding-type” potential and is more suitable for cases when attractive interaction comes from the formation of a chemical bond. Proposed by P. M. Morse in 1930, it was a popular potential for simulation of metals that have fcc and hcp structures (Morse 1929, 1930). A fit for many metals is given in (Girifalco 1959).

$$V(r_{ij}) = \epsilon \left[\exp\{-2\alpha(r_{ij} - r_0)\} - 2 \exp\{-\alpha(r_{ij} - r_0)\} \right] \quad (3.6)$$

6-exp (Buckingham) potential – exp term (Born-Mayer) provides a better description of strong repulsion due to the overlap of the closed shell electron clouds, which is important in simulation of bombardment by energetic atoms or ions, etc (Buckingham 1938).

$$V(r_{ij}) = A \exp\left\{-r_{ij} / R_{BM}\right\} - B / r_{ij}^6 \quad (3.7)$$

Exponential term for repulsion (Born-Mayer potential) is typically used in simulations where high-energy inter-atomic collisions are involved (Born 1932).

The error in the pair-potential approximation arises from the fact that, in general, the bonds between atoms are not independent of each other. A solid described by any central-force pair interaction, such as the Lennard-Jones pair potential, has the ideal ratio of C_{12}/C_{44} of 1. So do the rare gases, which are the prototype L-J systems. However, fcc metals generally have C_{12}/C_{44} closer to 2. Some metals, like Au and Pt, have high values of C_{12}/C_{44} , between 3 and 4.

Next figure shows, schematically the different physical properties or phenomena and their relation with the different parts of a pair potential.

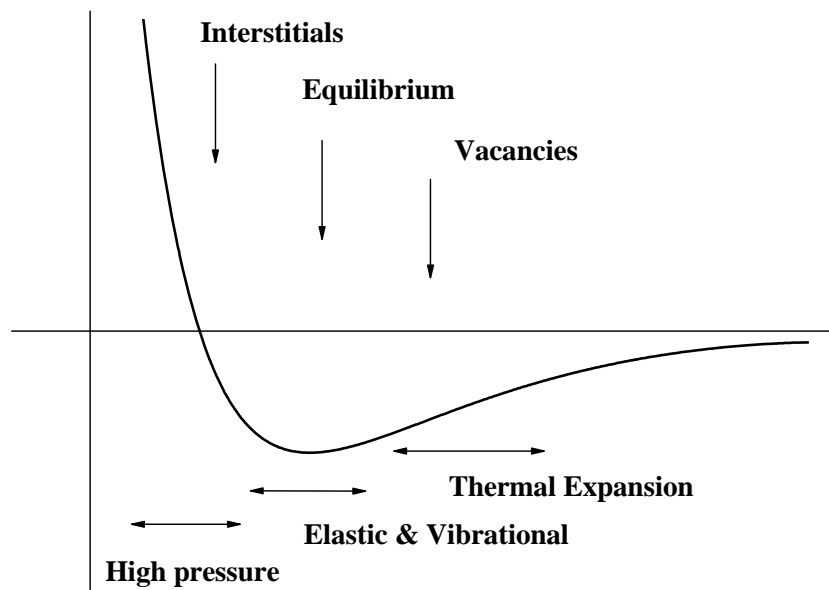


Fig. 3.6. Schematic relation of some physical properties with the interatomic potential.

Many-body effects in the interaction are present in inert gases as well and potentials more accurate than L-J have been developed for rare gases. Many body effects can account for up to 10 % of total energy. The vacancy formation energy, E_v , is significantly overestimated by pair potentials predicting $E_v \sim E_c$ where E_c is the cohesive energy, while $E_v = 0.25E_c$ for Au and $E_v = 0.33E_c$ for Cu.

Another popular method is the so called the tight binding method (TBM). The TBM, also called method of linear combination of atomic orbitals (LCAO), was originally proposed by Bloch (Bloch 1928) and later revised by Slater and Koster (Slater 1954) in the context of periodic potential problems. This method can be powerful to include magnetic properties as done by recently Paxton *et al* (Paxton 2008, 2010).

To overcome all the problems related with pair potentials several many-body approaches have been developed. The interactions between atoms can be described by a classical many-body potential like the proposed by Finnis and Sinclair (Finnis 1984), within the “glue” scheme (Ercolessi 1988), or by means of an Embedded Atom Method (EAM) potential (Daw 1983, 1984, Foiles 1985), that is the common choice today.

These methods are similar and sometimes mathematically equivalent so we will not discuss the details here. In general the three functions, the pair potential, $V(r)$, the embedding function, $F(\rho)$, and the electron density, ρ , are constructed by fitting to cohesive energy, surface energy, elastic constants, phonon frequencies, thermal expansion and melting temperature of the element under consideration. A detailed description of the Li and Pb EAM potentials used along this Thesis will be given in Chapter 4. Here we will just mention some theoretical considerations about the origin of this kind of potentials.

Within the EAM (Daw 1983, Foiles 1985), the total energy of the system is given by the sum of the single-atom energies, E_i , where

$$E_i = F[\rho_i] + \frac{1}{2} \sum_j \phi(r_{ij}) \quad (3.8)$$

with

$$\rho_i = \sum_j f(r_{ij}) \quad (3.9)$$

Here $\rho(r_{ij})$ can be viewed as the electronic density that atom i ‘sees’ due to atom j and $F[\rho_i]$ as the corresponding embedding energy of atom i when placed in the electronic density arising

from the surrounding atoms. $\Phi(r_{ij})$ can be interpreted as the effective inter-atomic potential due to electrostatic interaction as well as any modifications that the electronic response may entail.

3.5 Theory of EAM potentials

The basic theory of EAM potentials has its roots on density functional theory (DFT) and the quasy-atom concept (Stott 1980). Solution of the Schrödinger equation yields the electron density established by a given potential, and the energy is a functional of that potential. Hohenberg and Kohn (Hohenberg 1964, Kohn 1965) show the converse: that the energy is a functional of the density, and the potential is determined to within an additive constant by its electron density. Stott and Zaremba (Stott 1980) proved a useful corollary, that the energy of an impurity in a host is a functional of the electron density of the unperturbed (without the impurity) host. This result will be important in Chapter 7.

We start with the density-functional expression for the cohesive energy of a solid (Hohenberg 1964, Kohn 1965):

$$E_{coh} = F[\rho] + \frac{1}{2} \sum'_{i,j} \frac{Z_i Z_j}{R_{ij}} - \sum_i \int \frac{Z_i \rho(r)}{|r - R_i|} dr + \frac{1}{2} \iint \frac{\rho(r_1) \rho(r_2)}{r_{12}} dr_1 dr_2 - E_{at} \quad (3.10)$$

where the sums over i and j are over the nuclei of the solid, the primed sum indicates omission of the $i = j$ term, Z_i and R_i are the charge and position of the i th nucleus, the integrals are over r (or r_1 and r_2), and $r_{12} = |r_1 - r_2|$. E_{at} is the collective energy of the isolated atoms. $F[\rho]$ is the kinetic, exchange, and correlation energy functional. We can go from Eq. (3.10) to Eq. (3.8) making the following two assumptions: (1) $F[\rho]$ can be described by

$$F[\rho] = \int g(\rho(r), \nabla \rho(r), \nabla^2 \rho(r), \dots) dr \quad (3.11)$$

where g is the density and is assumed to be a function of the local electron density and its lower derivatives; and (2) the electron density of the solid can be described as a linear superposition of the densities of the individual atoms (as described in Eq. 3.9)

$$\rho_s(r) \equiv \sum_i \rho_i^2(r - R_i) \dots \quad (3.12)$$

The first approximation is motivated by studies of the response function of the nearly uniform electron gas (See EAM review (Daw 1993)). The second approximation is justified by the observation that, in many metals, the electron distribution in the solid is closely represented by a superposition of atomic densities. In addition, due to the variational nature of the energy functional, errors in the assumed density should only affect the energy to second order. It is also useful for us to define the embedding energy for an atom in an electron gas of some constant density $\bar{\rho}$ (neutralized by a positive background):

$$F_i(\bar{\rho}_i) \equiv F[\rho_i^a + \bar{\rho}_i] - F[\rho_i^a] - F[\bar{\rho}_i] \quad (3.13)$$

Semi-empirical approaches to determine the functions Φ , ρ , and F , were firstly developed by Daw, Baskes and Foiles *et al* (Daw 1983, 1984, Foiles 1985). The pair interaction between atoms of types A and B can be expressed as

$$\phi_{AB}(r) = \frac{Z_A(r)Z_B(r)}{r_{AB}} \quad (3.14)$$

where $Z_A(r)$ and $Z_B(r)$ are the effective charge of atoms A and B, respectively. They are constructed to be positive and to decrease monotonically with increasing separation distance. (Strictly speaking the requirements are not always necessary for the EAM. Some examples can be found in (Sinnott 1991)). The effective charge is computed according to (Hohenberg 1964) by

$$Z(r) = Z_0(1 + \beta r^\nu) \exp(-\alpha r) \quad (3.15)$$

Here Z_0 is the number of outer electrons of an atom. The parameters α , β and ν are determined from the bulk properties of metals, for example, the cohesive energy, surface energy, elastic constants, phonon frequencies, thermal expansion and melting temperature.

The many-atom interactions in the EAM originate with the embedding function. That is because the embedding function is non-linear for chemically active elements. This non-linearity reflects the saturation of the metallic bond by increasing the background density. This saturation of the bond can be related to the Pauli's exclusion principle. From this, one can see that the nature of the metallic bonding requires the embedding function to have positive curvature; that is, $F'' > 0$.

There are two caveats to become aware of at this point. First, the EAM will not work as well for systems where directional bonding is important, such as semiconductors and elements from the middle of the transition series (see Carlsson's review for more details (Carlsson 1990)). That review describes the relationship of the EAM to concepts of bonding in transition metals, including the saturation of bonding in metallic systems. Second, any subtleties due to Fermi-surface or band-structure effects are ignored in the EAM, so that any situations where these are important should be treated carefully.

To sum up, the limitations of the EAM are well characterized: it works best for purely metallic systems with no directional bonding; it does not treat covalency or significant charge transfer; and it does not handle Fermi-surface effects. This will be important in the study of metals under extreme conditions, i.e. high temperatures and high pressures as we will see in Appendix 1.

3.6 High pressure

Simulations of metals under high pressures (as well as particle irradiation processes for example) include short-distance interactions between atoms. At ranges, typically 1 Å, the repulsive forces, such as the Coulomb repulsion between two positively charged nuclei, become stronger than the chemical interactions between the electron shells. The short range part of a potential affects not only ballistic processes, but also the defects and melting properties of a material, and it is often added to a potential after ensuring that the equilibrium properties are correctly modeled. The most commonly used formula is the universal Ziegler-Biersack-Littmark (ZBL) potential V_{ZBL} (Ziegler 1985) which contains a pure Coulombic repulsive term that is mitigated by a screening function, $\Phi(r)$, at larger distances,

$$V_{ZBL}(r) = \frac{e^2}{4\pi\epsilon_0} \frac{Z_1 Z_2}{r} \phi(r/a) \quad (3.16)$$

Z_1 and Z_2 are the charges of the interacting nuclei, e is the elementary charge, and

$$a = \frac{0.8854a_0}{Z_1^{0.23} + Z_2^{0.23}} \quad (3.17)$$

where a_0 is the Bohr radius. The universal screening function has been constructed by fitting to the interaction energy between ions, resulting in:

$$\phi(x) = 0.181e^{-3.2x} + 0.5099e^{-0.9423x} + 0.2802e^{-0.4028x} + 0.02817e^{-0.2016x} \quad (3.18)$$

The accuracy of this potential is ~10% (Ziegler 1985). A smooth join between the high and low-energy parts is realized with, for instance, exponential or polynomial functions containing

adjustable parameters that must be fitted. The continuity of the potential functions as well as their first and second derivatives at the spline boundaries must be taken into account in the construction.

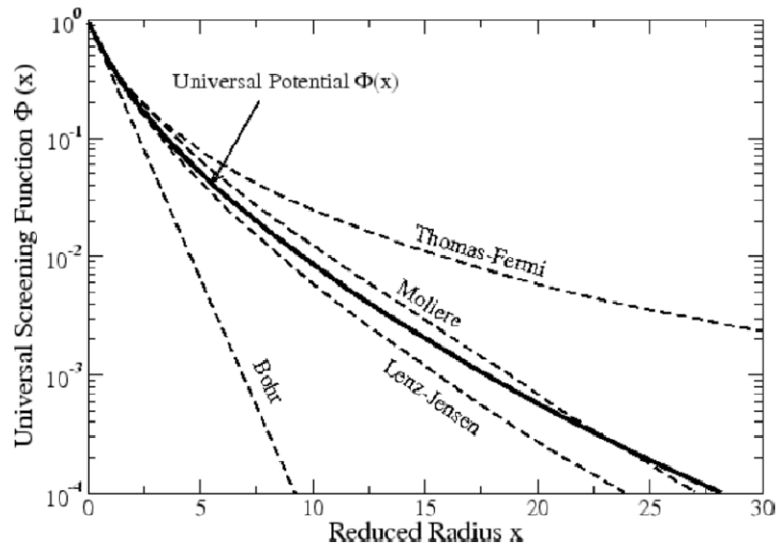


Fig. 3.7: Universal screening potential (ZBL) and other approximations. Figure taken from <http://www.iue.tuwien.ac.at/phd/wittmann/node8.html>

ZBL potentials are used in the well known SRIM-TRIM code. The ZBL potential is not the only proposed potential for high energies (see Fig. 3.7). For instance, in a typical heavy ion induced reaction, recoil velocity is about a few percent of the light speed. Stopping powers of Lindhard, Scharff and SchiØtt (LSS) seems to be more accurate than ZBL (Lindhard 1961).

The He potential used in the work of Caro and coworkers (Fe-Cr-He, Cu-Nb-He systems etc) has been modified according with the ZBL scheme. The Beck potential for He-He interaction (Beck 1968) was smoothly connected with the ZBL universal potential (Ziegler 1985) that is appropriate at high energy (short interatomic separations).

In Appendix 1 we have studied the range of applicability of Li and Pb EAM potentials studying both liquid Li and Pb under high pressures. Main conclusion is that the EAM potential can be used up to half the bulk modulus of the solid material but at higher pressures ZBL correction is necessary as expected.

3.7 Computational effort

For a given system the computational time increases as the accuracy or complexity of potentials increases. In next table we compare the computational effort in arbitrary units with different potentials, from the old L-J to recent “force field” potentials, as ReaxFF (Chenoweth 2008) and eFF (Jaramillo-Botero 2011).

	LJ	EAM	MEAM/ADP	EIM	ReaxFF	eFF	Ab initio
Time (a.u.)	1	3	12-15	~20	100	200	5000
	Noble gases	Metals	Metals with covalent bonds	Charged systems	Chemistry	Chemistry	

Table 3.III. Computational effort (schematic). Time refers to computational time in arbitrary units.

3.8 Mathematical properties of EAM potentials

EAM potentials are invariant under several transformations: In the EAM, potential functions for pure elements are invariant under the transformations (i) $\rho(\mathbf{R}) \rightarrow A \rho(\mathbf{R})$, $F(\rho) \rightarrow F(\rho/A)$ and (ii) $V(\mathbf{r}) \rightarrow V(\mathbf{r}) + 2B\rho(\mathbf{r})$, $F(\rho) \rightarrow F(\rho) - B\rho$. The two constants A and B are arbitrary and must be fixed by the external conditions.

At the same time Equation (1) is invariant with respect to the transformation

$$F[\rho_i] \rightarrow F[\rho_i] + k\rho_i \quad (3.19)$$

$$\phi(r_{ij}) \rightarrow \phi(r_{ij}) - 2kf(r_{ij}) \quad (3.20)$$

This led Johnson (Johnson 1989) to suggest that for comparison between differing embedding energies and inter-atomic potentials, ρ be chosen such that the derivative of $F(\rho_i)$ be zero at the bulk equilibrium density ρ_e . Thus in the bulk case, the structural contribution to the total energy will be entirely due to the inter-atomic potential. Such a ‘standard form’ also facilitates a natural representation for the inter-atomic potential between atoms of differing type (Johnson 1989).

Thus, this constant factor k represents or can be used as a first fitting parameter in the development of a X–Y interatomic potential and can be varied without changing the single component potentials. This will be important in our Li-Pb cross interaction potential as we will see in Chapter 5.

3.8.1 Stochastic properties of EAM model

The dynamic system of many particles possesses stochastic properties (Norman2001, 2002). It can be revealed as a cause of exponential divergence of MD calculation trajectories. An exponential trajectory divergence is a feature of the manyparticle system itself (N -equation Cauchy problem feature), not only of the MD model. In MD calculations numerical errors just initiate the divergence process.

Within the EAM model the value of dynamical memory time is estimated and is approximately equal to 7 ps (Norman 2001, 2002). Such a small value of dynamical memory time means that one could obtain two statistically completely independent trajectories from one initial condition using two different integration steps after about 7 ps of calculation. This time will be longer if the system (liquid alloys) presents short range order as we will show in Chapter 5.

Chapter 4

Atomistic molecular point of view for liquid lead and lithium.

The properties of metals in liquid state are fascinating not only from the point of view of technology development, but also from a basic science point of view. In fact, liquid iron (at high pressures) has significant importance in geophysics, being the main constituent of Earth's liquid core (Shen 2004) and many other terrestrial planet cores. For instance recent investigations (Yoder 2003) indicate that the Martian core could be entirely liquid.

As we have seen in Chapter 2, fluid metals are considered as ideal candidates for high temperature working fluids because they have high latent heats of vaporization and high heat transfer coefficients. For example, metallic fluids such as molten sodium, having similar density and viscosity to water, find application as coolant in nuclear reactors (Mansur 2004). Spallation is an established technique for the production of high intensity fluxes of neutrons. Liquid metal targets for spallation sources have several advantages such as the mean density of the target not decreases by the presence of a coolant and they do not suffer from radiation damage extending the lifetime of the facility (Appleton 1995).

Nowadays, understanding the structure and behavior of liquid metal alloys is a real goal in nuclear engineering and materials science. To that end, the use of MD simulations represent a unique tool, able to relate structural correlations and molecular behavior with thermodynamic properties of any material in the framework of engineering design. Moreover, MD of liquid Li and Pb, represent the basic pillar of a multiscale modeling methodology able to relate molecular properties and physical phenomena inside a fluid at the atomic scale (up to several million atoms), with macroscopic behavior in terms of complex fluid theory.

The MD study reported in this chapter is, to our knowledge, the first work in the literature attempting to model metals like Pb or Li at the atomic scale in liquid phase. We test the predictions in the liquid phase under different thermal conditions of the Pb and Li Embedded Atom Method (EAM) potentials existing in the literature (Zhou 2001, Belaschenko 2009). In addition, our work represents a first step in order to develop a LiPb alloy potential for classical MD simulations, able to capture the physics underlying the properties of the eutectic mixture, in concentrations and temperatures of interest for Nuclear Fusion technology (Fraile 2013).

4.1 Methodology

Molecular Dynamics by means of EAM potentials constitutes a powerful methodology to describe both dynamical and structural properties of liquid metals. The EAM is a commonly used representation for the energy that overcomes the volume dependent limitation of pair-potentials by adding a term for the energy to embed an atom in the background electron density of its neighbors. The EAM has proven particularly good at modeling bulk and defect properties (energy, structure) of metals and alloys. For example, many MD and Monte Carlo simulations have been performed using the EAM to model such phenomena as surface reconstruction (Foiles 1986), crack growth (Baskes 1988) and grain boundary structure (Merkle 1990). More details about EAM theory are given in Chapter 3. In next section we will describe in detail the potentials used to simulate Li and Pb.

Within the framework of the EAM theory, the total internal energy of the system of N atoms is described as the energy required to embed these N atoms into the homogeneous electron gas caused by surrounding atoms plus a correction of energy from two-body interactions. Thus this total energy can be expressed as:

$$E_i = \frac{1}{2} \sum_{i,j,i \neq j} \phi_{ij}(r_{ij}) + \sum_i F_i(\rho_i) \quad (4.1)$$

Where Φ_{ij} represents the pair energy between atoms i and j separated by r_{ij} , and F_i stands for the embedding energy to embed an atom into a local site with electron density ρ_i . ρ_i can be calculated using

$$\rho_i = \sum_{j,j \neq i} f_j(r_{ij}) \quad (4.2)$$

With $f_j(r_{ij})$ the electron density at the site of atom i arising from atom j at a distance r_{ij} away. Thus one can assume that the atomic electron density also follows an exponential form

$$f(r) = f_e \exp[-\chi(r - r_e)] \quad (4.3)$$

Where f_e is a scaling constant, r_e is the equilibrium nearest distance, and χ is an adjustable parameter that must be determined. In obtaining additional functions of the EAM, a caution should be kept in mind; that is, the embedding function should have positive curvature. This ensures that the bond strength decreases with increasing coordination.

In general, the parameters that describe a particular EAM potential are determined by minimizing the root-square deviation between calculated and experimental thermodynamic data, usually consisting of a set of elastic constants, the vacancy formation energy (E_{vf}), the equilibrium lattice constant (a_0), and the cohesive energy (E_c).

4.1.2 EAM potential for Pb

We have used the EAM potential proposed by Zhou *et al* (Zhou 2001). The functional form for this potential is already implemented in the LAMMPS package (Plimpton 1995). In this case, the pair energy between atoms, takes the following expression.

$$\phi(r) = A \frac{\exp\left(-\alpha\left(\frac{r}{r_e} - 1\right)\right)}{1 + \left(\frac{r}{r_e} - k\right)^{20}} - B \frac{\exp\left(-\beta\left(\frac{r}{r_e} - 1\right)\right)}{1 + \left(\frac{r}{r_e} - \lambda\right)^{20}} \quad (4.4)$$

Where r_e is the equilibrium spacing between nearest neighbors, A, B, α , β , are four adjustable parameters, and k, λ are two additional parameters for the cut off.

The electron density function is taken with the same form as the attractive term in the pair potential with the same values of β and λ , i.e.,

$$f(r) = \frac{f_e \exp\left(-\beta\left(\frac{r}{r_e} - 1\right)\right)}{1 + \left(\frac{r}{r_e} - \lambda\right)^{20}} \quad (4.5)$$

To have embedding energy functions that can work well over a wide range of electron density, three equations to separately fit to different electron density ranges, $r < r_n$, $r_n \leq r_0$ and $r_0 \leq r$ are used. The use of $r_n = 0.85r_e$ and $r_0 = 1.15r_e$ where r_e is the equilibrium electron density, can ensure that all equilibrium properties are well fitted in the electron density range $r_n \leq r < r_0$.

For a smooth variation of the embedding energy, the following equations are required to match values and slopes at their junctions. These equations are listed as follows:

$$F(\rho) = \sum_{i=0}^3 F_{ni} \left(\frac{\rho}{\rho_n} - 1\right)^i, \quad \rho < \rho_n, \rho_n = 0.85\rho_e \quad (4.6)$$

$$F(\rho) = \sum_{i=0}^3 F_i \left(\frac{\rho}{\rho_e} - 1\right)^i, \quad \rho_n \leq \rho < \rho_0, \rho_0 = 1.15\rho_e \quad (4.7)$$

$$F(\rho) = F_e \left[1 - \ln\left(\frac{\rho}{\rho_e}\right)^\eta \right] \left(\frac{\rho}{\rho_e}\right)^\eta, \quad \rho_0 \leq \rho \quad (4.8)$$

EAM – Pb					
r_e	3.499723	K	0.425877	F_1	0
f_e	0.647872	Λ	0.851753	F_2	0.921049
ρ_e	8.906840	F_{n0}	-1.419644	F_3	0.108847
A	8.468412	F_{n1}	-0.228622	H	1.172361
B	4.516486	F_{n2}	0.630069	F_e	-1.440494
A	0.134878	F_{n3}	-0.560952		
B	0.203093	F_0	-1.44	Σ	12

Table 4.I. Parameters to define the EAM potentials for Pb (Zhou 2001).

Table 4.I shows the sixteen parameters appearing in these equations (Zhou 2001). Generally, in computer simulations, the potential function and its first derivatives with respect to atomic coordinates should be continuous at all geometries of the system. This can be accomplished by forcing the atomic electron density, $f(r)$, and pair potential, $\Phi(r)$, and their first derivatives $f(r)'$ and $\Phi(r)'$ to go smoothly to zero at a cutoff distance using a cutoff function.

4.1.3. EAM potential for Li

In the case of Li, we decided to use the approach of D. Belashchenko (Belaschenko 2011, 2012) that we implanted in LAMMPS format by homemade codes. Note that in our calculations, we found that the potential parameters are valid for calculating basic properties of lithium such as lattice constant, cohesive energy, density and heat capacity, when the cutoff distance is taken to be larger than $1.5a_0$ [third-nearest neighbor (NN)].

In a similar manner than for Pb, three fitting functions $F(\rho)$, $f(r)$ and $\rho(r)$ are used in the procedure for the calculation of our EAM potential.

$$f(r) = p_1 \exp(-p_2 r) \quad (4.9)$$

the embedding potential is defined in different regions as

$$F(\rho) = a_1 + c_1(\rho - \rho_0)^2 \text{ at } \rho_1 < \rho < \rho_6 \quad (4.10)$$

$$F(\rho) = a_i + b_i(\rho - \rho_{i-1}) + c_i(\rho - \rho_{i-1})^2 \quad (4.11)$$

At $\rho_i < \rho < \rho_{i-1}$ ($i=1, 2, 3, 4, 5$)

$$F(\rho) = [a_6 + b_6(\rho - \rho_1) + c_6(\rho - \rho_1)^2] \left[2 \frac{\rho}{\rho_s} - \left(\frac{\rho}{\rho_s} \right)^2 \right] \quad (4.12)$$

at $\rho < \rho_5$

and

$$F(\rho) = a_7 + b_7(\rho - \rho_0)^m \text{ at } \rho \geq \rho_6 \quad (4.13)$$

The parameters used to define this set of equations are described in Table 4.II.

Li – EAM					
ρ_1	3.0450	a_4	-0.859314	\mathbf{b}_7	0.006520[r]
ρ_2	1.2200	a_5	-0.808846	c_1	0.043000
ρ_1	0.900	a_6	-0.776842	c_2	2.000000
ρ_2	0.849	a_7	-0.881043	c_3	-1.090000
ρ_3	0.700	a_{10}	-0.8809	c_4	1.300000
ρ_4	0.480	\mathbf{b}_1	0 [*]	c_5	-0.515400
ρ_5	0.420	b_2	-0.008600	c_6	0.000000
ρ_6	1.100	b_3	-0.248600	c_7	0.018130
a_1	-0.880900	b_4	0.056600	r_0	1
a_2	-0.880470	b_5	-0.808846	m	1.5
a_3	-0.872754	b_6	-0.551400	σ	7.5

[*] condition of continuity of functions $F(r)$ and $dF(r)/dr$ at $r = r_i$.

Table 4.II. Parameters to define the EAM potentials for Li. Li parameters a, b and c are expressed in eV (from Refs (Belaschenko 2011, 2012)).

The pair potential, in this case, is defined in two parts as in (Belaschenko 2012). For $r > 2.45$,

$$\varphi(r) = k_1 + k_2 \frac{1}{r} + k_3 \frac{1}{r^2} + k_4 \frac{1}{r^3} + k_5 \frac{1}{r^4} + k_6 \frac{1}{r^5} \quad (4.14)$$

and for $r \leq 2.45$,

$$\varphi(r) = k_1 + k_2(2.45 - r) + k_3(\exp[k_4(2.45 - r)] - 1) \quad (4.15)$$

At $r = 2.45 \text{ \AA}$, the potential and its first derivative are continuous: $\varphi(r) = 0.252868 \text{ eV}$ and $f(r) = -d\varphi(r)/dr = 0.897320 \text{ eV/\AA}$. The set of parameters k_i are given in Table 4.III.

	$r > 2.45$	$r \leq 2.45$
k_1	-1.6153	0.252868
k_2	32.9193	0.15252
k_3	-245.8304	0.38
k_4	840.2178	1.96
k_5	-1368.3812	-
k_6	905.6236	-

Table 4.III. Parameters to define Li pair potential (in eV) as defined in Eq's (14) and (15). From Ref (Belaschenko 2012), distance, r , in \AA .

Next figure shows the pair potentials, $\varphi(r)_{\text{Pb}}$ and $\varphi(r)_{\text{Li}}$, of the EAM potentials employed all along this work.

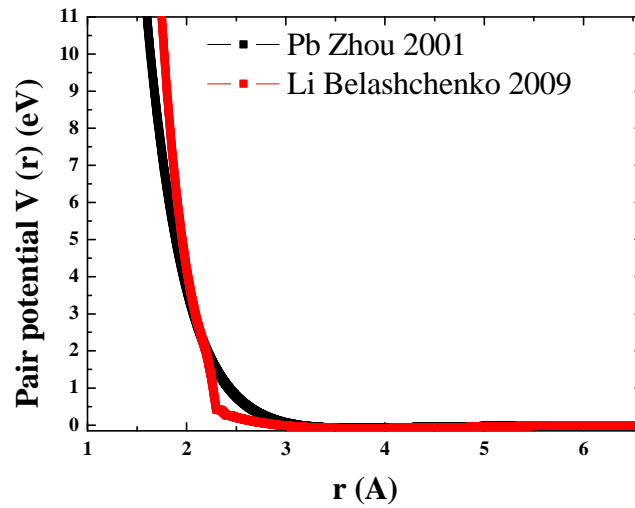


Fig. 4.1. Pair potentials for Pb and Li following references (Zhou 2001, Belaschenko 20011).

4.2 Computational details

Samples for Pb and Li ranged in size from 10,000 up to 100,000 atoms. They were canonically generated, energy minimized and equilibrated. We have tested size effects in our results and adopted sizes that minimize them. For example, a Pb sample of 5,000 atoms was checked to be equivalent to an equivalent one 10 times bigger in size. Periodic boundary conditions (PBC) were imposed to minimize surface and edge effects.

MD simulations were carried out using the parallel code LAMMPS (Plimpton 1995). Integration algorithms of Verlet and rESPA were benchmarked. The integration time step, Δt , used for the heating and equilibrating phases was 10^{-4} ps. In the production phase we used a Δt of 10^{-4} - 10^{-5} ps and we always tested in both cases a proper convergence. Average length of simulation time in production stage (equilibrium) was around 50 ps.

Trajectories in the canonical ensemble (NVT) were generated after 5 ps of heating by coupling our system to a Berendsen thermostat (Berendsen 1984), and ulterior equilibration and production phases by means of a Nosé-Hoover chain (Martyna 1992). For some more details of the employed techniques see Chapter 3.

4.3 Results. Validation of Li and Pb EAM potentials

An accurate interatomic potential for MD simulations (EAM-type in our present case) must be able to provide a good representation of dynamics, thermodynamics and structural properties of the target material under the conditions of interest.

Moreover, in order to develop future alloy potentials (like PbLi, Pb-He, Li-H) with exceptional value for Nuclear Fusion Technology, the pure element's potentials have to provide accurate descriptions of their properties.

The main goal of the validation of these lead and lithium potentials for future use in alloy simulations, is the reproduction of liquid phase thermal properties, or diffusion and transport phenomenology under conditions frequent in Nuclear Technology. Therefore, we present in this section, MD simulations extracting the main properties expected from these two elements in such scenario.

4.3.1 Study of static properties

As a first test, simple but critical, we have calculated what we would like to denote as static properties of our systems: cohesive energy and lattice parameter, for Pb and Li at 0 K. Doing that, we obtain the values represented in Figure 4.2 for Pb and Li respectively. Our values are in good agreement with the experimental data reported in the works of (Toloukian 1970, (Brandes 1983, Dewaele 2007, Xie 2008). Note that the experimental values reviewed from these works, are $E_c(\text{Pb}) = -2.03$; $a(\text{Pb}) = 4.9095 \text{ \AA}$ and $E_c(\text{Li}) = -1.63$; $a(\text{Li}) = 3.355 \text{ \AA}$.

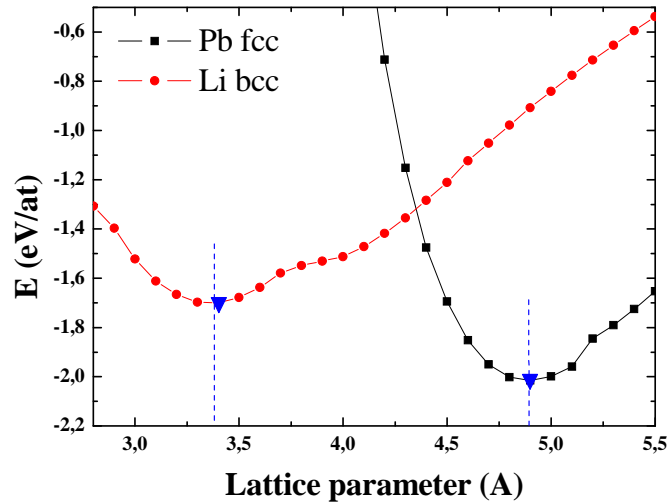


Fig. 4.2. Energy (in eV/at) of pure elements Pb and Li (in fcc and bcc structures respectively) vs lattice parameter, a_0 . The minimum corresponds to the cohesive energy. The experimental values of cohesive energy y-axis and lattice parameter (x-axis) are represented by triangles.

Our agreement is not surprising, since the cohesive energy is one of the physical properties used to adjust the parameters that define the potential, in particular the atomic electron-density. The cohesive energy is a measure of the cohesion of the atoms and should be therefore comparable to the sublimation energy. A good reproduction of this value is critical if we like that our potentials reproduce properly structural properties at any temperature.

4.3.2 Lindemann criterion

According to the Lindemann melting criterion (Lindemann 1910), a solid melts when the ratio of the mean amplitude u of the atomic thermal vibrations to the distance d_{NN} between the nearest neighbors reaches a certain critical value, L , identical for all substances,

$$\sqrt{\langle u^2(T_m) \rangle} = \delta d_{NN} \quad (4.16)$$

where L is the Lindemann constant. The pressure dependence of T_m is usually estimated under the assumption that the constant L is almost invariable along the melting curve $T_m(p)$.

A simple way to understand Lindemann law is to take a 10 % of the lattice parameter at equilibrium and calculate the energy necessary to have such vibrations (red lines in next figure). This can be better seen graphically in Fig 4.3, and is equivalent to consider $\delta = 0.1$ for every material. For Pb (fcc), $E_c = -2.01469$, $\{a=4.89433 \text{ \AA}\}$ then to have $0.1 \times 4.894 = 0.4894$ one needs to increase the energy in around 0.1 eV.

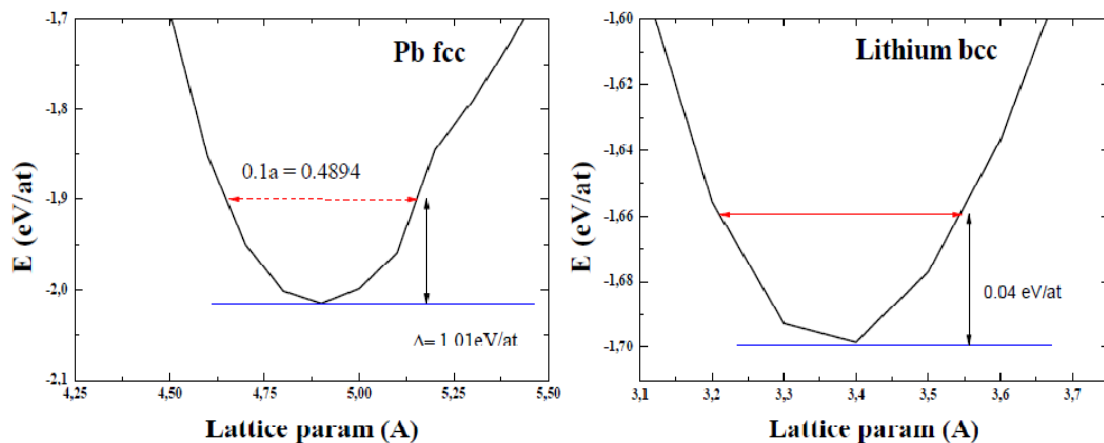


Fig. 4.3.Left) Melting of Pb using Lindemann criterion; $T_m(\text{Pb}) = 0.114 \text{ eV/at} / 8.61710\text{e}5 \text{ eV/K} \rightarrow 1322 \text{ K}$. Experimental melting point is 600 K. Right) Same calculation for Li; $T_m(\text{Li}) = 0.04 \text{ eV/at} / 8.61710\text{e}5 \text{ eV/K} \rightarrow 464 \text{ K}$. Experimental melting point is 453 K.

But if we take into account more accurate calculations like the presented in (Shapiro 1970) treating the frequency spectrum analytically by means of the moment trace method (Montreaux 1942) we will see that 0.1 is not universal but changes slightly from one material to another depending on the CS for example. In fact, 0.1 is quite correct for Li, (the value given in (Shapiro 1970) is 0.0116) but not for Pb as we have seen in previous picture. For fcc Pb the value given in (Shapiro 1970) is 0.067. With this value in mind the result is much better (700 K)

4.3.3 Structural properties

Molecular Dynamics simulations of a liquid metal are able to provide a rich view of the existing interactions between fluid particles, information about self diffusion coefficients, interaction of secondary of third NN atoms within the fluid, or the molecular basis of corrosion phenomena induced by the liquid metal in contact to a wall material.

Structural order and distribution of particles within a fluid are frequently well described by the pair-correlation function $g(r)$. This quantity is related to the probability of finding the center of a particle a given distance from the center of another particle. For short distances, this is related to how the particles are packed together. Therefore, it is a good magnitude to study if we want to test the accuracy of a molecular potential at structural level.

Diffraction experiments yield $I(q)$, the coherent intensity per atom as a function of the momentum transfer, $q = 4\pi\sin\theta/\lambda$, where λ is the wavelength of the radiation and θ is half the angle between the primary and diffracted beams. The total structure factor $S(q)$ is obtained from $I(q)$ according to $S(q) = I(q)/\langle b^2 \rangle$. $\langle b^2 \rangle = \sum c_i b_i^2$ where c_i and b_i are the atomic concentration and the coherent scattering amplitude of the i species respectively.

Total structural factor is related to pair distribution function as

$$S(q) = 1 + 4\pi\rho \int_0^{\infty} r^2 [g(r) - 1] \frac{\sin(qr)}{qr} dr \quad (4.17)$$

and

$$g(r) = 1 + \frac{1}{2\pi^2\rho} \int_0^\infty q^2 [S(q) - 1] \frac{\sin(qr)}{qr} dr \quad (4.18)$$

Where ρ is the atomic density $\rho = N/V$. And the pair-correlation function is generally defined as:

$$g(r) = \rho^{-2} \left\langle \sum_i \sum_{j \neq i} \delta(r_i) \delta(r_j - r) \right\rangle = \frac{V}{N^2} \left\langle \sum_i \sum_{j \neq i} \delta(r - r_{ij}) \right\rangle \quad (4.19)$$

Our calculations using the implementation of EAM potentials for Li and Pb, are in very good agreement with experimental results. As can be seen in Figure 4.4 and 4.5, the radial distribution function $g(r)$ for both Pb and Li, matches very well the experimental results reported by Waseda in his classic textbook and also in website (Waseda 1980) in the liquid phase, at different working temperatures of interest in Nuclear Technology. The statistical error bars are the size of the symbols.

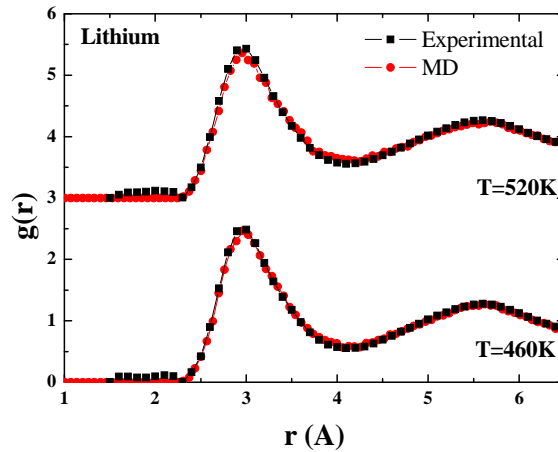


Fig. 4.4. Lithium $g(r)$ calculated (red circles) compared with experimental results (black squares) at $T=460$ and 520 K. In both cases an excellent agreement between MD simulation – experiment in the radial distribution of the liquid phase is obtained. (Experimental data from (Waseda 1980)).

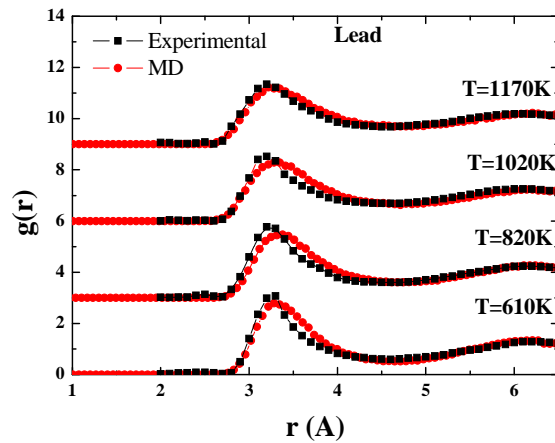


Fig. 4.5. Lead $g(r)$ calculated (red circles) compared with experimental results (black squares) temperature ranging from $T = 610$ K to $T = 1170$ K. (Experimental data from (Waseda 1980)).

Alternatively, we have also paid attention computed the static structure factor $S(Q)$, the Fourier transform (FT) of $g(r)$, and can be compared with data obtained from neutron diffraction experiments. Has to be noted that this $S(Q)$ curves are not calculated as a FT of the $g(r)$ curves, but as a result of applying the Debyer code [Debyer website] to our MD output. The agreement shown in Figures 4.6 and 4.7 confers this quantity a strong importance in the validation of EAM potentials for both liquid metals.

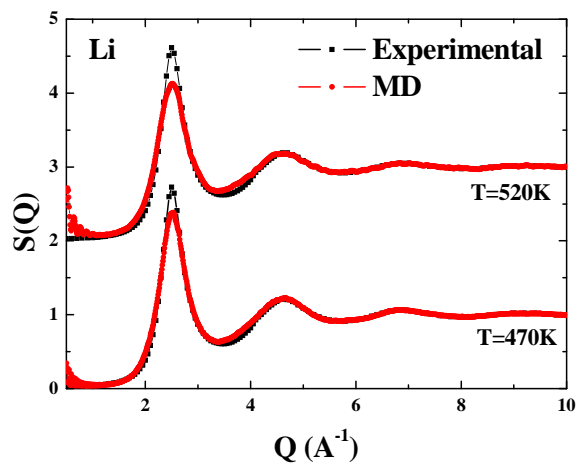


Fig. 4.6. Lithium $S(q)$ calculated (circles) compared with experimental results (triangles) at $T = 460$ and 520 K. (Experimental data from [Waseda website]).

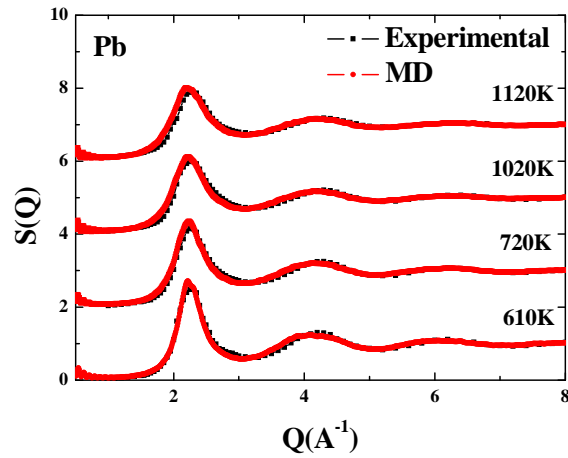


Fig. 4.7. Lead $S(q)$ calculated (circles) compared with experimental results (triangles) at temperatures ranging from 610 to 1120 K. (Experimental data from [Waseda web]).

An additional validation of the potential can be obtained by studying density and thermal expansion.

Density of the liquid, ρ , at melting point is correctly represented by the EAM potentials we are studying. For Li the experimental value is 0.53 g/cm^3 and our MD result is 0.51 g/cm^3 . For Pb the agreement is also very good, being the experimental value 10.96 g/cm^3 and our MD result is 10.64 g/cm^3 . Also the variation with temperature, $\partial\rho/\partial T$, gives an excellent agreement with experimental results. For Li the experimental value is $-8.6 \times 10^{-5} \text{ g/cm}^3\text{K}$ (Ohse 1985) and our MD simulations gives -9.6×10^{-5} . For Pb the agreement is even better, being $-0.003 \text{ g/cm}^3\text{K}$ both experimentally (Gurvich 1991) and in our MD runs.

In conclusion, the agreement between the properties calculated with these two potentials and the experimental data for different structural and correlation properties, certifies the adequacy of both potentials to describe the properties of cooling and breeding materials (liquid metals) in Nuclear Technology.

4.4 Thermodynamic properties

Thermodynamic properties are critical in industrial applications of liquid metals, since they are essentially used as cooling and breeding materials. PbLi is promising candidate as breeder material for nuclear fusion but also, for instance, Pb and PbBi are proposed as coolants for Generation IV fission reactors. See ref (Mansur 2004) and references therein for a review.

As test of thermodynamic properties we calculated the specific heat at constant pressure, C_p , by the derivative of enthalpy H . Enthalpy shows a jump when the sample melts but this jump does not correspond with experimental melting point as usual. See figure 4.8 and 4.9.

In order to determine the melting point, T_m , the free energy calculation of both solid and liquid phase is needed. Then, both curves will cross at a certain temperature that corresponds to T_m . Doing that, we obtain 580 ± 25 K for Pb while the experimental result is 600 K. For Li our estimation is about 453 ± 25 K and the experimental value is 450 K (See Fig. 4.13). First, in the next section, we will present some of the intermediate results along with the details of the free energy calculations. A detailed explanation can be found in (Ogando-Arregui 2002).

4.4.1 Free energy calculations

In this section we focus in the predictions of the free energy and melting temperature for both potentials. Description of the solid-liquid phase transition is the main step in modeling these systems and crucial for further extrapolation of thermal conductivity, diffusion and alloys properties. In next graphs the MD heating cooling cycles are shown. Figure 4.8 shows the enthalpy jump at a certain temperature, usually higher than the experimental melting point. Figure 4.9 shows the same jump, now in the volume of the sample. Blue dashed lines represent the experimental melting temperature of both elements. Enthalpy data will be used in the H vs Temperature fit needed in Eq. 4.20.

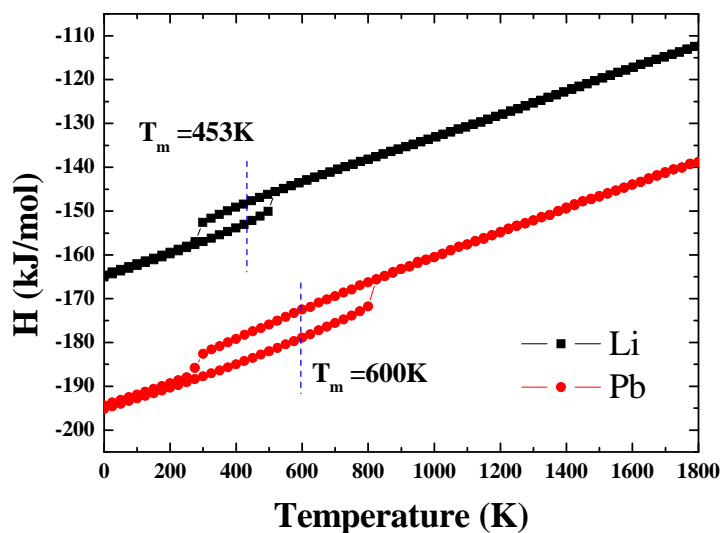


Fig. 4.8. Enthalpy, H , in eV/at, for both Pb and Li calculated in a MD run. The jump in H corresponds to the melting of the sample, but not with the melting temperature.

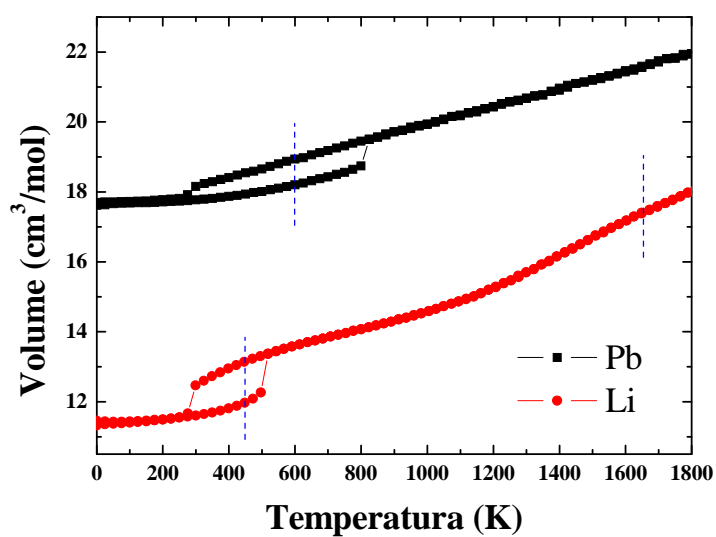


Fig. 4.9. Volume, V , in cm^3/mole , for both Pb (black) and Li (red) calculated in a MD run. The jump in V corresponds to the melting of the sample, but not with the melting temperature.

Calculating free energies involves the computation of the partition function by integrating over the entire phase space of a system with a large number of degrees of freedom. For empirical

Hamiltonians, an almost direct calculation of the free energy is possible and is the approach taken in this work. We write the Gibbs-Duhem equation

$$f(T) = f(T_0) \frac{T}{T_0} - T \int_{T_0}^T \frac{h(\tau)}{\tau^2} d\tau \quad (4.20)$$

where $h(\tau)$ is the enthalpy per particle. The coupling-constant integration method, or switching Hamiltonian method, (Ciccotti & Hoover 1986) is used to calculate $f(T_0)$.

$$f(T_0) = f_w(T_0) + \Delta f$$

$$\Delta f = \frac{1}{N} \int_0^1 \left\langle \frac{\partial H}{\partial \lambda} \right\rangle d\lambda = \frac{1}{N} \int_0^1 \langle U - W \rangle_\lambda d\lambda \quad (4.21)$$

where $f_w(T_0)$ is the free energy of the reference system at T_0 temperature. The integration is carried over the coupling parameter, λ , varying between 0 and 1, and $\langle \dots \rangle$ is the average over a canonical ensemble, or a time average on a (T, V, N) MD simulation.

For the solid phase it is customary to take as reference system a set of Einstein oscillators.

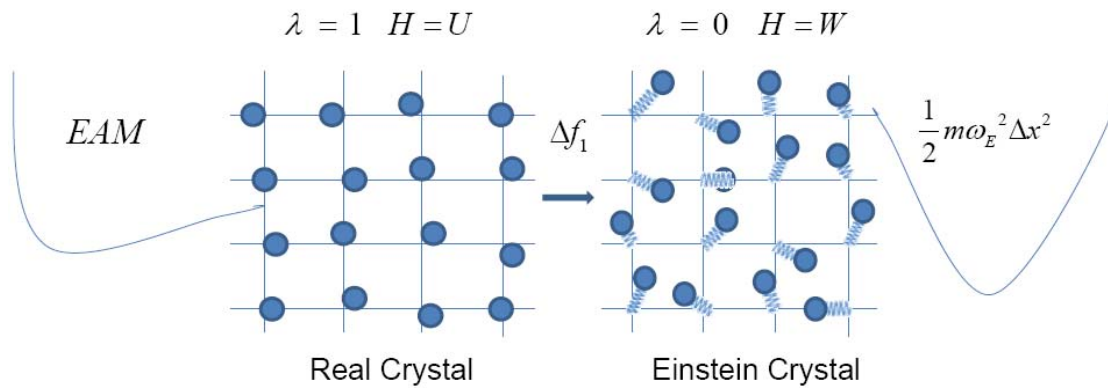


Fig. 4.10. Schematic representation of switching Hamiltonian technique in solid phase.

4.4.2 Solid / Einstein

In the Einstein approximation, the vibrational density of states of a solid is approximated by a sum of delta functions centered on the local atomic vibrational frequencies.

For a perfect crystal (with cubic or higher symmetry), all frequencies are equal to ω_0 . The time-averaged spatial distributions of atom positions in the harmonic solid consist of Gaussian functions of the form

$$\left(\frac{\alpha}{\pi}\right)^{3/2} = \exp(-\alpha(r_i - r_i^0)^2) \quad (4.22)$$

centered on the average atomic positions r_i^0 , where

$$\alpha = m\omega_0^2 / (2k_B T) \quad (4.23)$$

m is the atomic mass, and $k_B T$ is the thermal energy. The classical vibrational contribution to the free energy can then be written as

$$A_v = \frac{3}{2} N k_B T \ln \left[\frac{\alpha \Lambda^2}{\pi} \right] \quad (4.24)$$

where Λ is the thermal wavelength

$$\Lambda = h / (2\pi m k_B T)^{1/2} \quad (4.25)$$

4.4.3 Liquid / Ideal gas

For the liquid, the usual reference system W is an ideal gas at the same temperature and volume of the EAM sample. We change Hamiltonian from a real liquid to an ideal gas in two steps. The process to switch from U to W involves an intermediate step to avoid particle overlap during the integration. First, we compute the free-energy difference between the true system with potential U (the EAM potential) and a system with a repulsive potential W_L that can be a soft spheres potential, a Buckingham potential for example (Bukingham 1938).

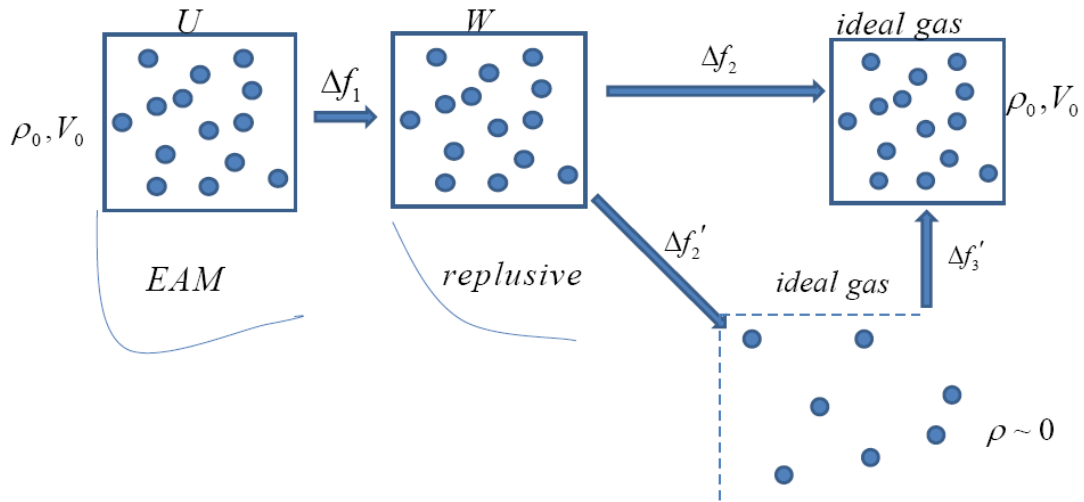


Fig. 4.11. Schematic representation of switching Hamiltonian technique in liquid phase.

In this work, we use $W_L=0.1U_{\text{rep}}$, where U_{rep} is the pair potential part of the EAM energy.

As in the solid phase, the integration is carried over the coupling parameter λ varying between 0 and 1. The system is kept at the constant volume V_0 , that equilibrated the U Hamiltonian at temperature T_0 and $P=0$. Therefore, the free-energy change for a pure element due to the switch is given by Δf_1 , as in the second line of Eq. (2). The second step is also double: a reversible expansion of the repulsive gas, now at V_0 and high pressure, to reach the dilute limit (where it becomes identical to the ideal gas), followed by a reversible compression of the ideal gas, to recover the initial density or volume. The change in free energy due to both processes is

$$\Delta f_2 = k_B T_0 \int_0^{\rho_0} \left[\frac{P}{\rho k_B T_0} - 1 \right] \frac{d\rho}{\rho} \quad (4.26)$$

where $\rho_0 = N/V_0$ is the particle density. After the process represented by Eq. (4.26) has taken place we end up with an ideal gas at (T_0, ρ_0) , whose free energy f_{id} is known,

$$f_W^{liq}(T_0, \rho_0) = f_{id}(T_0, \rho_0) = k_B T_0 [\ln(\rho_0 \Lambda^3) - 1] \quad (4.27)$$

Where Λ is the thermal wavelength as defined before (Eq. 4.25). Then, the free energy of the liquid phase is calculated as the sum

$$g_L(T_0) = \Delta f_1 + \Delta f_2 + f_W^{liq}(T_0, \rho_0) \quad (4.28)$$

Fig. 4.12 (Left) gives us the value of Δf_1 and integration of Fig 4.12 (right) that of Δf_2 . For a more detailed description of this method see (Frenkel 1996).

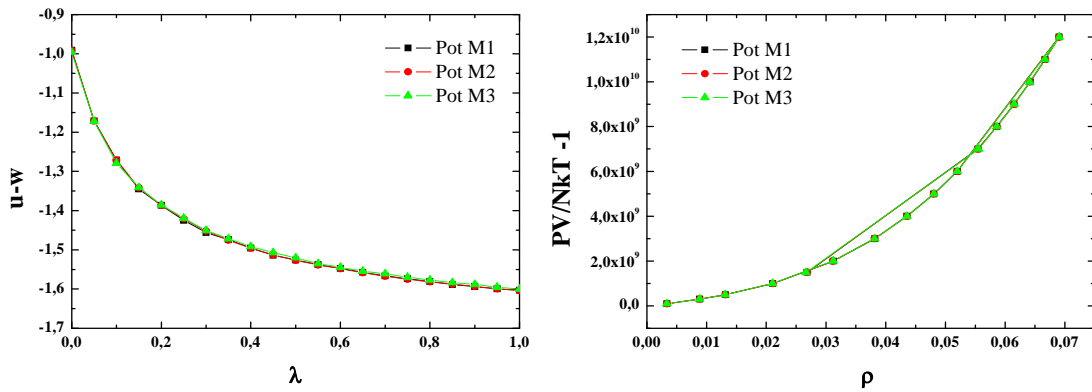


Fig. 4.12. Liquid runs. Left), liquid switch vs λ , right), volume expansion vs density. Three different potentials are used. Results in liquid switch are almost potential independent.

Equation (4.20), with Eqs. (4.21) and (4.28), give the free energies of the solid and liquid phases of pure elements as a function of temperature. The melting temperature of a system can be obtained as the crossing point between the solid and liquid phase prediction of the free energy

variation as a function of temperature. As can be seen in Figure 4.13, we obtain an excellent agreement between experimental data and our Molecular Dynamics prediction in both systems.

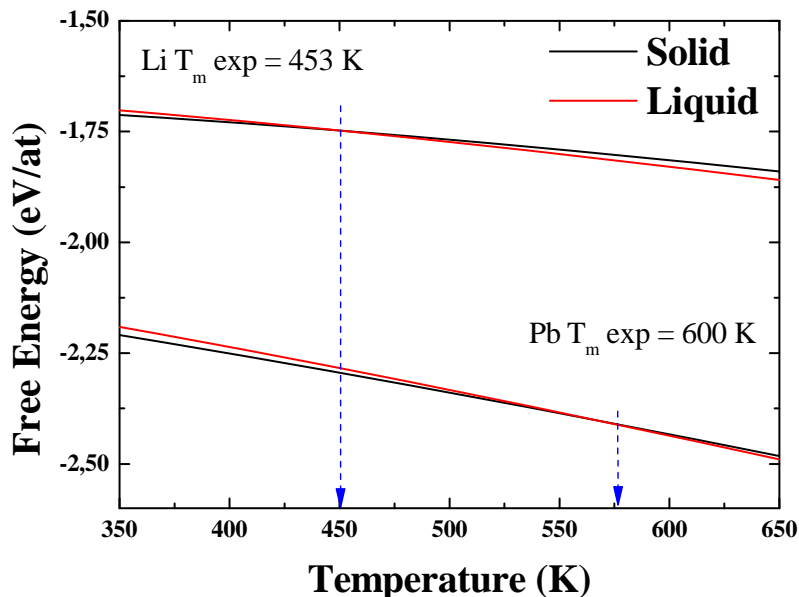


Fig. 4.13. Free energies vs temperature for pure Li (up) and Pb (down) in solid (black lines) and liquid (red lines) phase. Crossing point of both correspond to T_m . The blue dashed lines are a guide to the eye.

Experimental values are 453 K and 600.6 K for Li and Pb respectively, and our calculated values are 450 K and 575 K for Li and Pb as shown in figure 4.13.

Moreover, we can also calculate volume and enthalpy change at melting, ΔV and ΔH respectively, and compare with the proper experimental values (Ohse 1985, Gurvich 1991).

In the case of Pb, values agree fairly well with the experiment. Volume change in our simulations is about a 3.8 % while experimentally is expected about 3.6%. In addition, the change in enthalpy (heating) is 5.5 kJ/mole while the experimental value is 4.8 kJ/mole. The result depends on the way we arrive to the final state, i.e, heating or cooling. Cooling the sample from a higher temperature down to the final one the values are: $\Delta H= 5.4$ kJ/mole and $\Delta V =2.5$ %. For Li, results depend more on the simulation size. Volume change in our simulations is about a 10.0 % while the experimental one is 1.6 %. The change in enthalpy is (heating) 4.5 kJ/mole while the experimental value is 3.0 kJ/mole. In cooling mode, the results are: $\Delta H= 4.5$ kJ/mole and $\Delta V =6.5$ %.

4.5 Entropy of Melting

Entropy of melting is defined as the difference between entropy in liquid and solid phase, $\Delta S_m = (S_{liq} - S_{sol})$, and equals the enthalpy jump divided by the melting temperature, $\Delta H_m / T_m$. The value of this entropy of melting is constant for all simple metals and is equal to 8.8 J/K-mole.

$$\Delta S_m = (S_{liquid} - S_{solid}) = \frac{\Delta H_m}{T_m} \approx 8.8 JK^{-1} mol^{-1} \quad (4.29)$$

Again, this is a critical magnitude that we can use to evaluate both Pb and Li EAM potentials in this range of thermodynamics conditions (liquid phase in Nuclear Systems conditions)

If we calculate ΔH_m from our MD runs and melting temperature, T_m , from free energy evaluation as described in section 4.3.1, we obtain ΔS_m (Pb) = 9.1 (± 0.5) and ΔS_m (Li) = 10.0 (± 0.8). For lead our MD calculated value agrees well with the experiment (difference is less than 5 %). For lithium ΔS_m is overestimated in the simulation (about a 14 %) due to a too large jump in enthalpy (and volume) when the metal melts.

4.6 Liquid-Liquid Phase transitions

First-order structural phase transitions are common in crystalline solids, whereas first-order liquid-liquid phase transitions (that is, transitions between two distinct liquid forms with different density and entropy) are exceedingly rare in pure substances (Young 1991, Ponyatovsky 1992). A single-component liquid may have more than two kinds of isotropic liquid states and the transition between these different states is called ‘‘liquid-liquid phase transition’’ (Poole 1997, Brazhkin 1997). It is one of the most interesting challenging problems in the field of liquid science. Today, growing indications for first-order transitions in liquids have come from analysis of their physical properties and from computer simulations (Harrington 1997, Debenedetti 1997).

4.6.1 Pb high temperature: transition around 1000 K

A liquid-liquid (LL) phase transition is possible in Pb around 1000 K according to density, viscosity and magnetic susceptibility (Fig 4.14) measurements carried out by Hu *et al* (Hou 2006). The exact temperature depends on the physical properties as shown in Table 2 in the same paper. LL transition has been suggested experimentally (Grimsditch 1984, Biermann 1998) and theoretically (Harrington 1997) to occur in some one-component (P, S, C) and a few multiple component systems, for example in PbBi alloys (Li 2006).

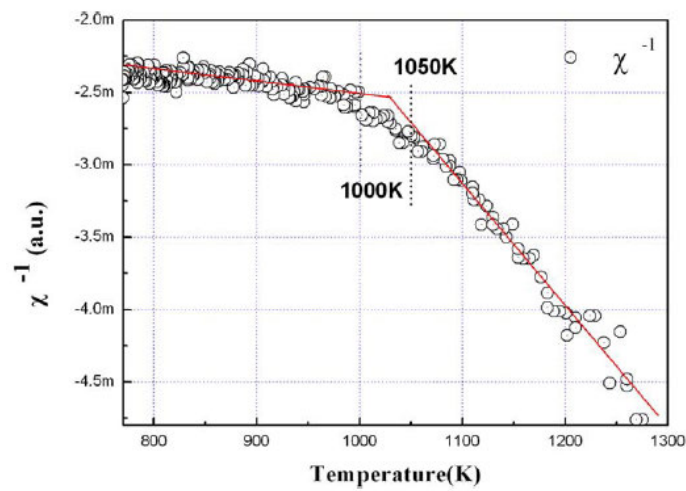


Fig. 4.14. Reciprocal of Pb magnetic susceptibility versus temperature during cooling process (Hou 2006).

In order to study that transition a detailed structural analysis has been made. Magnetic susceptibility is not accessible with CMD but additional information on the structural features of the system can be obtained by calculating the Wendt–Abraham parameter (Wendt 1978).

$$r^{WA} = \frac{g_{\min}(r)}{g_{\max}(r)} \quad (4.30)$$

and the translational order parameter (Tanaka 1998).

$$\xi = \int_0^{r_0} |g(r) - 1| dr \quad (4.31)$$

Where, $g_{\max}(r)$ and $g_{\min}(r)$ represent the main maximum and the first minimum in the radial distribution function, respectively, and r_0 is the distance at which the structural features of the system cease to be considered, i.e the cutoff used in our MD simulations.

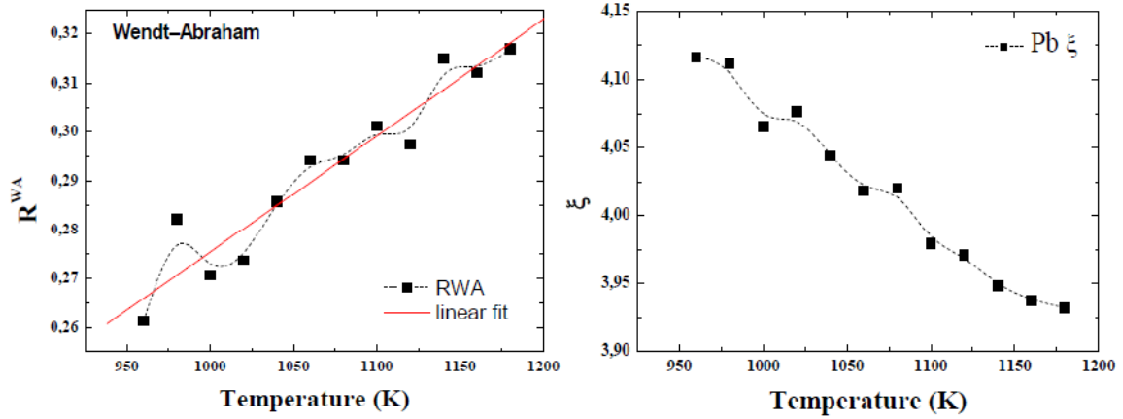


Fig. 4.15. Left) Wendt Abraham parameter, R^{WA} , vs temperature in liquid Pb. Red line represents a linear fit and dashed line is a guide to the eye. Right) Translational order parameter vs temperature in liquid Pb.

A decrease in the value of r^{WA} indicates an increase in the role of two-particle structural clusters in the system, which can appear, e.g., during the densification of the system and can characterize its transition into a crystalline or amorphous phase. An increase in the ξ value points to the development of structural ordering in the system. However, in our liquid Pb simulations we did not find clear evidence of LL phase transition (See Figure 4.15) although the results are not definitive.

Wendt Abraham and translational parameters will be further used in our study of the properties of LiPb around the eutectic composition (Fraile A. *et al*, to be published).

4.7 Conclusions

Classical Molecular Dynamics simulations via EAM potentials have showed to be a powerful tool to simulate and understand liquid metals, in our particular case, Pb and Li. Our results prove the validity of these potentials and provide useful structural and thermodynamic data in conditions of interest to Nuclear Fusion technology. Reported figures are in agreement with experimental results available in the literature. In addition, our work represents a base methodology for the extrapolation of liquid Pb and Li properties into regions of temperature and composition where direct experimental measurements either do not exist, or are not accessible.

Moreover, we have tested that our particular choice constitutes a solid base for the development of a future PbLi alloy potential (Chapter 5).

The main results presented in this Chapter have been recently accepted in *Journal of Nuclear Materials* (Fraile 2013).

Different parameters to quantify liquid structures have been analyzed in order to understand the Pb LL phase transition. The use of those parameters could represent an interesting tool to study liquid Li₁₇Pb (eutectic) alloys. This will be further explored in chapter 5.

Chapter 5

LiPb interatomic potential

5.1 The road to LiPb cross potential

Most of times liquid metals are classified as a prototype of simple liquids, but even in the simplest monatomic case, metallic fluids are actually two-component systems. The interplay between electron and ions, indeed, is an intrinsic aspect of liquid metals (Scopigno 2005). Nevertheless some aspects of pure elements in liquid phase can be described with simple hard sphere (HS) models. Binary mixtures are, in some occasions, ideal mixtures and most of its properties are linear interpolation of the physical properties of the pure constituent elements. As we will soon see, this is not all the case of LiPb system, being Li and Pb two very different metals in terms of mass, electronegativity and chemical properties.

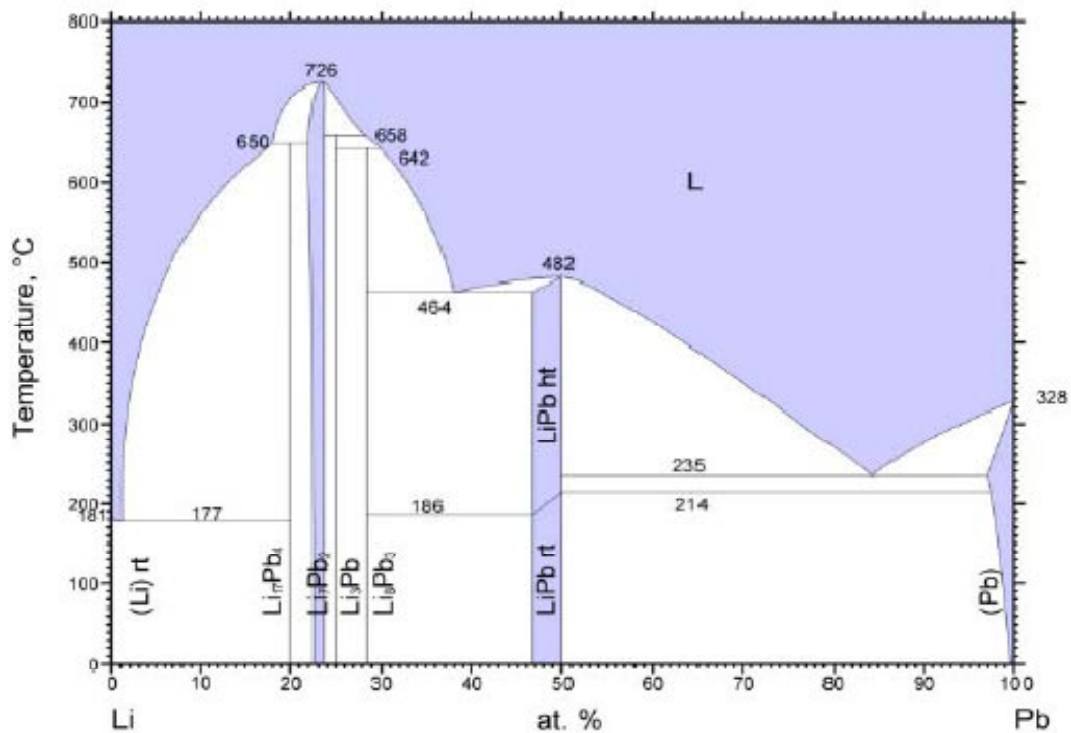


Fig. 5.1. Experimental phase diagram for LiPb system (Okamoto 1993).

The experimental phase diagram is showed in Fig. 5.1. LiPb alloys are a complex compound forming system and several inter-metallic compounds like $\text{Li}_{17}\text{Pb}_4$, Li_7Pb_2 , Li_3Pb and LiPb are present. We are interested mainly in the lead rich part of the phase diagram and more precisely in the eutectic composition so we do not need by now to know much more about the Li rich compounds. A detailed thermodynamic analysis of their radically different chemistry can be found in (Hubberstey 1992, 1997).

To our best knowledge only one pair potential for PbLi has been reported in the literature (Bazhirova 2008). In that study inter-atomic interactions are described by a many-particle potential for Pb, Li from the set of EAM type potentials suggested in (Lim 1992, Li 1998). Based on the approach from (Landa 2000) they modified the density and embedding functions from:

$$\rho(r) \rightarrow C\rho(r), \quad F(\rho) \rightarrow F(\rho/C) \quad (5.1)$$

This transformation does not change the Hamiltonian itself but permit to vary the cross-Pb–Li pair interaction function by changing constants C for each atom type:

$$\phi_{\text{PbLi}}(r) = \left(\frac{\rho_{\text{Pb}}}{\rho_{\text{Li}}} \phi_{\text{Li}}(r) + \frac{\rho_{\text{Li}}}{\rho_{\text{Pb}}} \phi_{\text{Pb}}(r) \right) \quad (5.2)$$

Then they calculate static structure factor $a(K)$ as a functional depending on C_{Li} and C_{Pb} . Fitting to experimental data on $a(K)$ from (Ruppertsberg 1975) they found that the best correspondence was reached at the values of constants $C_{\text{Li}} = 0.7$, $C_{\text{Pb}} = 0.9$.

5.1.1 Pb-Li. Effective representation.

Both potentials are in our case quite different if we compare for example the embedding functions. In order to mix them in an inter-atomic potential for the cross interaction Li-Pb we should first use the so called effective representation (Caro 2005). By doing this one minimizes the nonlinear contribution of the embedding term.

We start with a preparation of the two pure element potentials in a way that is adequate for our purpose, that is, the effective representation with normalized densities, which for $\alpha = A; B$ reads

$$\begin{aligned}\rho_\alpha &= \rho_\alpha^0 / \zeta_{\alpha,eq}^0 \\ F_\alpha(\zeta_\alpha) &= F_\alpha^0(\zeta_\alpha^0) - F_\alpha^{0,\prime}(\zeta_{\alpha,eq}^0) \zeta_\alpha^0 \\ V_{\alpha,\alpha}(r) &= V_{\alpha,\alpha}^0(r) + 2F_\alpha^{0,\prime}(\zeta_{\alpha,eq}^0) \rho_\alpha^0(r)\end{aligned}\tag{5.3}$$

where the superscript ⁰ stands for original, $\zeta_{\alpha,eq}^0$ for the density on a lattice site at equilibrium,

$$\zeta_{\alpha,eq}^0 = \sum_{j \neq i} \rho_{\alpha i}(r_{ij}^{eq})\tag{5.4}$$

and the prime \prime for derivative. These transformations do not alter the properties of the pure elements but have the advantage of minimizing the contribution of the embedding term to the formation energy of the alloy, as is discussed below, and allow us to combine potentials for pure elements coming from different authors with eventually very different and unrelated magnitudes of the densities.

Total energy at 0K for a pure element with a defined crystal lattice can be calculated analytically. The distances for the fcc lattice are, in function of the lattice parameter are:

$$r_{1fcc}(a) = \frac{a\sqrt{2}}{2}, r_{2fcc}(a) = a, r_{3fcc}(a) = a\sqrt{\frac{3}{2}}, r_{4fcc}(a) = a\sqrt{2}, r_{5fcc}(a) = a\sqrt{3} \quad (5.5)$$

And for the bcc lattice:

$$r_{1bcc}(a) = \frac{a\sqrt{3}}{2}, r_{2bcc}(a) = a, r_{3bcc}(a) = a\sqrt{2}, r_{4bcc}(a) = a\frac{\sqrt{11}}{2}, r_{5bcc}(a) = a\sqrt{3} \quad (5.6)$$

Then total density $\rho(a)$ must be calculated like,

$$\rho_{pb}(a) = 12\psi(r_1(a)) + 6\psi(r_2(a)) + 24\psi(r_3(a)) + 12\psi(r_4(a)) + 8\psi(r_5(a)) \quad (5.7)$$

Where ψ is the electron density in EAM formalism. And equally for lithium

$$\rho_{Li}(a) = 8\psi(r_1(a)) + 6\psi(r_2(a)) + 12\psi(r_3(a)) + 24\psi(r_4(a)) + 8\psi(r_5(a)) \quad (5.8)$$

Now total energy for lead in an fcc lattice is:

$$E_{tot(pb)} = F(\rho(a)) + 6\phi(r_1(a)) + 3\phi(r_2(a)) + 12\phi(r_3(a)) + 6\phi(r_4(a)) + 4\phi(r_5(a)) \quad (5.9)$$

And for lithium,

$$E_{tot(Li)} = F(\rho(a)) + 4\phi(r_1(a)) + 3\phi(r_2(a)) + 6\phi(r_3(a)) + 12\phi(r_4(a)) + 4\phi(r_5(a)) \quad (5.10)$$

The numbers multiplying the pair potential are the number of nearest neighbours divided by 2.

In the next figures the plot of these energies vs the lattice parameter is shown. The minimum gives the lattice parameter and the cohesive energy in the equilibrium. In table 5.1 we summarize the results for Pb and Li in fcc and bcc.

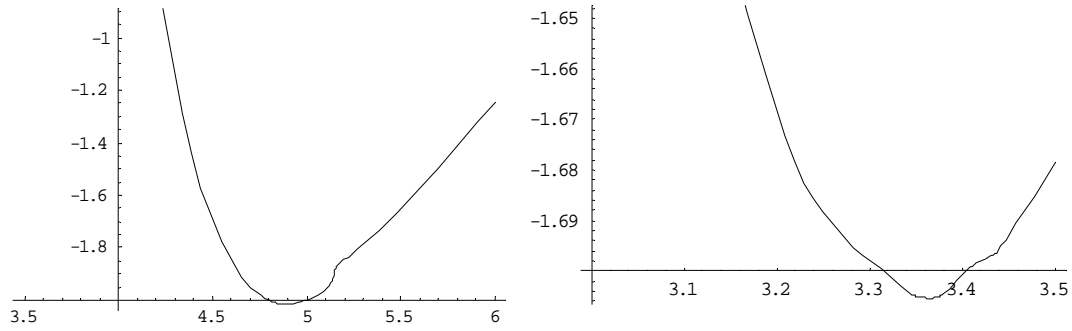


Fig. 5.2. Minimum in the total energy (y axis) for lead (left) and lithium (right) calculated from original EAM potentials (Zhou 2001, Belashchenko 2009), x axis is distance in Å.

	FCC		BCC	
Element	E_c (eV/at)	a_0 (Å)	E_c (eV/at)	a_0 (Å)
Pb	-2.014	4.894	-1.97	3.78
Li	-1.675	4.21	-1.705	3.3648

Table 5.I. Calculated cohesive energy, E_c , and lattice parameter, a_0 , for Pb and Li in fcc and bcc phases. All values have been calculated using Pb and Li EAM potentials in the effective representation. The results are exactly the same that those obtained with the original potentials.

5.1.2 Mixing energy calculation (theory)

The difference between the enthalpy of a mixture (our LiPb system) and the sum of the enthalpies of its components (at the same pressure and temperature) is the mixing enthalpy (or mixing energy), that we will denote as ΔH . Deviations from ideality can be described by the use of activity coefficients.

First we define the linear interpolation of the pure element lattice parameters as a function of composition;

$$L_{id(fcc)}(x) = xa(Pb)_{fcc} + (1-x)a(Li)_{fcc} \quad (5.11)$$

$$L_{id(bcc)}(x) = xa(Pb)_{bcc} + (1-x)a(Li)_{bcc} \quad (5.12)$$

And the same for the cohesive energies;

$$E_{cid(fcc)}(x) = xE_c(Pb)_{fcc} + (1-x)E_c(Li)_{fcc} \quad (5.13)$$

$$E_{cid(bcc)}(x) = xE_c(Pb)_{bcc} + (1-x)E_c(Li)_{bcc} \quad (5.14)$$

and then we can define our mixing energy target (at 0 K, G_{0K}) for both fcc and bcc structures, as a polynomial function, for example;

$$G_{0K(fcc)}(x) = \sum_n a_{n-fcc} x^n \quad \text{and} \quad G_{0K(bcc)}(x) = \sum_n a_{n-bcc} x^n \quad (5.15)$$

With n running from 0 to 4.

now we just define the Li-Pb cross potential as:

$$V_{mix}^0(r) = \frac{1}{2}(\Phi_{Pb}(r) + \Phi_{Li}(r)) \quad (5.16)$$

and

$$\Phi_{PbLi}^0(x, h) = hV_{mix}^0(r) \quad (5.17)$$

Now we calculate the disordered total energy “disutot” per atom for an alloy with composition x using the standard EAM for alloys both for fcc and bcc phases:

$$U_{fcc}^{dis-TOT}(a, x, h) = x \left(F_{Pb} \sum_{n=1}^5 N_{NN}^i x \Phi_{Pb}^0 r_n^{fcc}(a) + (1-x) \Phi_{Li}^0 r_n^{fcc}(a) + \left(\frac{1}{2} \left(\sum_{n=1}^5 N_{NN}^i x V_{Pb}^0 r_n^{fcc}(a) + (1-x) V_{PbLi}^0 r_n^{fcc}(a) \right) \right) \right) +$$

$$(1-x) \left(F_{Li} \sum_{n=1}^5 N_{NN}^i x \Phi_{Pb}^0 r_n^{fcc}(a) + (1-x) \Phi_{Li}^0 r_n^{fcc}(a) + \left(\frac{1}{2} \left(\sum_{n=1}^5 N_{NN}^i x V_{PbLi}^0 r_n^{fcc}(a) + (1-x) V_{Li}^0 r_n^{fcc}(a) \right) \right) \right)$$
(5.18)

and the same for bcc

$$U_{bcc}^{dis-TOT}(a, x, h) = x \left(F_{Pb} \sum_{n=1}^5 N_{NN}^i x \Phi_{Pb}^0 r_n^{bcc}(a) + (1-x) \Phi_{Li}^0 r_n^{bcc}(a) + \left(\frac{1}{2} \left(\sum_{n=1}^5 N_{NN}^i x V_{Pb}^0 r_n^{bcc}(a) + (1-x) V_{PbLi}^0 r_n^{bcc}(a) \right) \right) \right) +$$

$$(1-x) \left(F_{Li} \sum_{n=1}^5 N_{NN}^i x \Phi_{Pb}^0 r_n^{bcc}(a) + (1-x) \Phi_{Li}^0 r_n^{bcc}(a) + \left(\frac{1}{2} \left(\sum_{n=1}^5 N_{NN}^i x V_{PbLi}^0 r_n^{bcc}(a) + (1-x) V_{Li}^0 r_n^{bcc}(a) \right) \right) \right)$$
(5.19)

and then we define the enthalpy of mixing as the difference between the calculated mixing energy and the ideal mixing one, i.e.

$$\Delta H_{fcc}(x, h) = U_{fcc}^{dis-TOT}(L_{id(fcc)}, x, h) - E_{c_{id(fcc)}}(x)$$
(5.20)

$$\Delta H_{bcc}(x, h) = U_{bcc}^{dis-TOT}(L_{id(bcc)}, x, h) - E_{c_{id(bcc)}}(x)$$
(5.21)

now we can calculate the minimum between this functions and the target using mathematica as

FindMinimum [(DeltaHfcc[0.5, h] - G0Kfcc[0.5])², {h, 0.5}]

FindMinimum [(DeltaHbcc[0.5, h] - G0Kbcc[0.5])², {h, 0.5}]

and also

$$\text{FindMinimum} \left[\left(\text{DeltaHfcc}[c, h] - \text{GOKfcc}[c] \right)^2 + \left(\text{DeltaHbcc}[c, h] - \text{GOKbcc}[c] \right)^2 \right]$$

and then, we can calculate the value of the polynomial that makes this difference minimum. This polynomial is written in the last line of the EAM-cd potential. This way we can create different potentials changing the weight of the fcc or bcc disordered ΔH etc.

5.1.3 Cut-off

Generally, in computer simulations, the potential function and its first derivatives with respect to atomic coordinates should be continuous at all geometries of the system. This can be accomplished by forcing the atomic electron density $f(r)$ and pair potential $\phi(r)$ and their first derivatives $f'(r)$ and $\phi'(r)$ to go smoothly to zero at a cut-off distance using a cut-off function. To assure that we can also make use of a Fermi function defined as

$$F_F(r_c) = 1 / (1 + \exp((r - (r_0 - r_1)) / d)) \quad (5.22)$$

This function is 1 up to r equal some value close to the cut-off, r_0 , and then tends quickly to 0. For example, if we want the cut-off be 6.5 Å, we can choose $r_0=6.4$, $r_1=0.1$ and $d=0.01$. Then, we can multiply every function for this Fermi one having new functions that go smoothly (and the derivatives too) to zero.

5.1.4 Pb-Li cross potential

Instead of using $g(r)$ of a particular composition as a target to create the potential for the cross interaction we will use the mixing enthalpy curve of the alloy to create an EAM potential composition dependent (eam/cd) (Caro 2005). The concentration-dependent embedded atom method (CD-EAM) is a powerful model for atomistic simulation of concentrated alloys with arbitrarily complex mixing enthalpy curves.

Very few experimental data are available about the mixing energy of the LiPb alloys in the literature. The most recent one is the thermodynamic study carried by Gasior and co-workers on (Gasior 2001) using the electromotive force method.

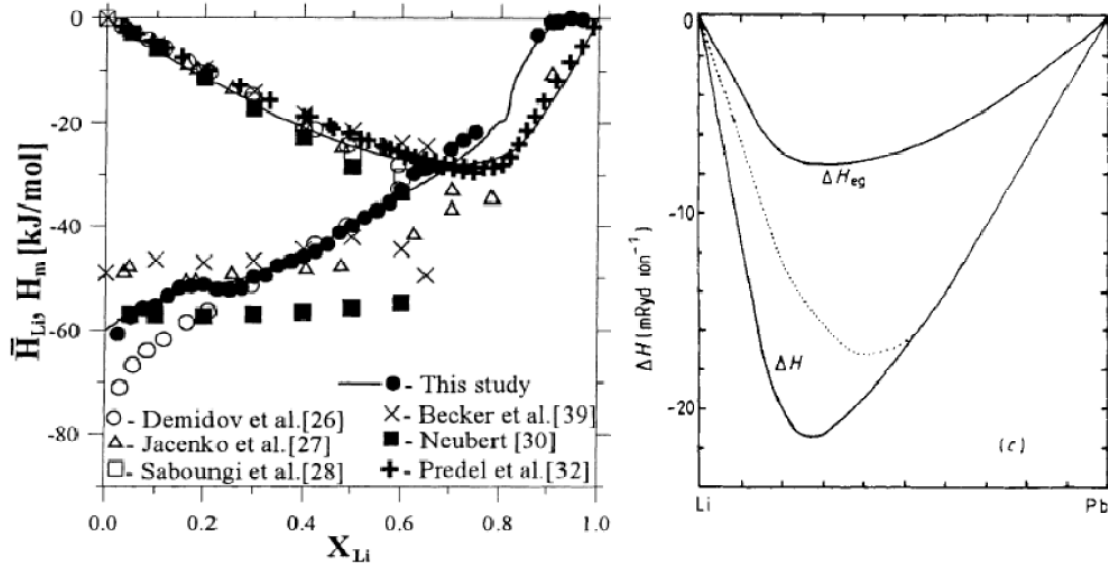


Fig. 5.3. Left) Experimental partial enthalpy of Li and the integral enthalpy of mixing for the Li-Pb liquid alloys (Gasior 2001) at 800 K. Right) Measured heat of formation ΔH (Ruppersberg 1976) and electron-gas contribution ΔH_{eg} at $T = 1000$ K (Hafner 1984).

We do not have experimental data for the solid alloy so we will use as first approximation a negative mixing energy symmetric with concentration and with the same order of magnitude to that of the liquid. As first target function we used simply: $\Delta H = (-80) * x * (1-x) * 0.010$ (eV/at).

Now we create a pair potential that minimizes the difference of the calculated mixing energy and the target both in fcc and bcc phases. We do not know the crystal structure of every single alloy Li_xPb_{1-x} so we used here simple the interpolation of both lattice parameters, i.e. $a(Li_xPb_{1-x}) = a_{Pb} - xLi(a_{Pb} - a_{Li})$ (as defined in Eq. 5.11 and 5.12) being x the concentration of Li and a_{Pb} and a_{Li} the corresponding lattice parameter for the pure elements in the corresponding fcc or bcc phase. The eam/cd format has a line at the end with the coefficients of the polynomial expression ($h = a + bx + cx^2$). Of course this potential could be improved in many ways.

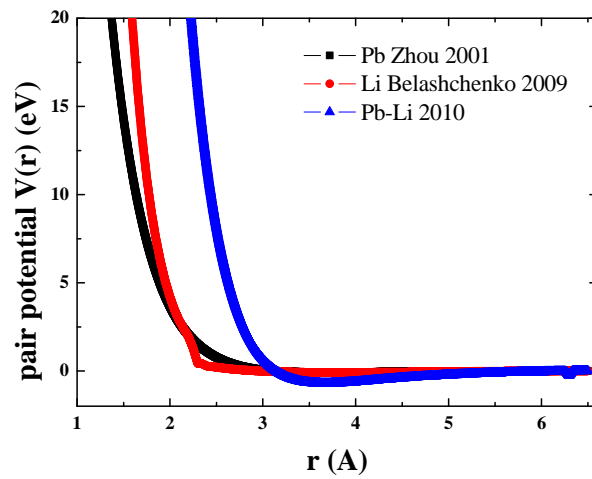


Fig. 5.4. EAM potentials. Pair potentials vs interatomic distance in Å.

Figure 5.5 show the results after using the EAM/cd without reading the polynomial parameters. Then, the contribution of the embedding function to the enthalpy of mixing of LiPb alloys should be exactly zero.

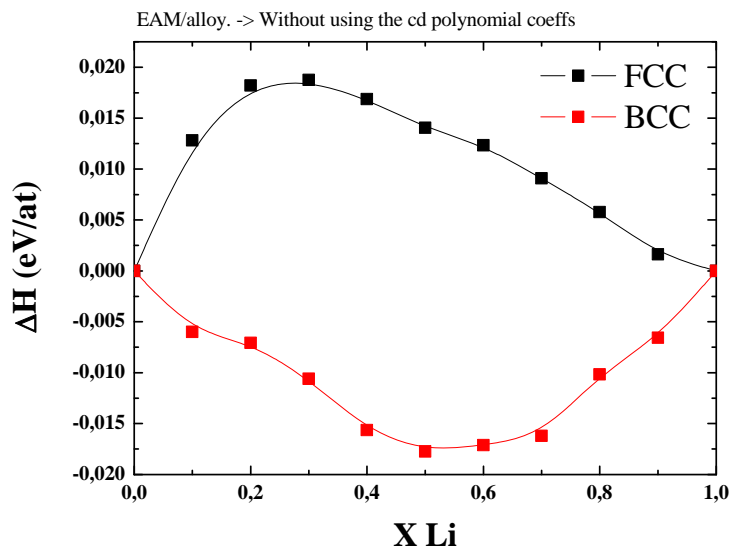


Fig. 5.5. Contribution of the embedding function to the enthalpy of mixing of LiPb alloys. Ideally it should be exactly zero.

5.1.5 Enthalpy of mixing

Enthalpy of mixing is easily calculated from MD runs. As first choice we started from a simple polynomial of grade four negative enthalpy being Li-Pb a compound forming system. The calculated ΔH with that initial potential gave wrong results with a crossing from negative to positive values at high lithium concentrations. Next, we used as target the experimental curves shown in figure 5.3 (and 5.6). Except when noted MD runs are cooling runs. Here we present some preliminary results to illustrate the method.

Using different targets we obtained different potentials or different versions that we called pot. v1, v2 etc or just pot. 1, 2, etc. The curve used as target took in account the energies of formation of some compounds as described in (Hubberstey 1975) and shown in Table 5.V.

Potential 5 seems to give good fitting of the experimental enthalpy of mixing according with (Gasior *et al* 2001). One point to be noted is that our MD results have been obtained in cooling runs because some compounds have melting points (or decomposition temperatures!) higher than 800 K (See phase diagram in Fig 5.1). The statistical error bars are the size of the symbols. If we compare now ΔH at 1000 K with experimental results from (Ruppersberg 1976), as can be seen in Fig. 5.6 (Right) now pot. 4 gives better results than pot 5. In next sections we will see how these differences affect other properties.

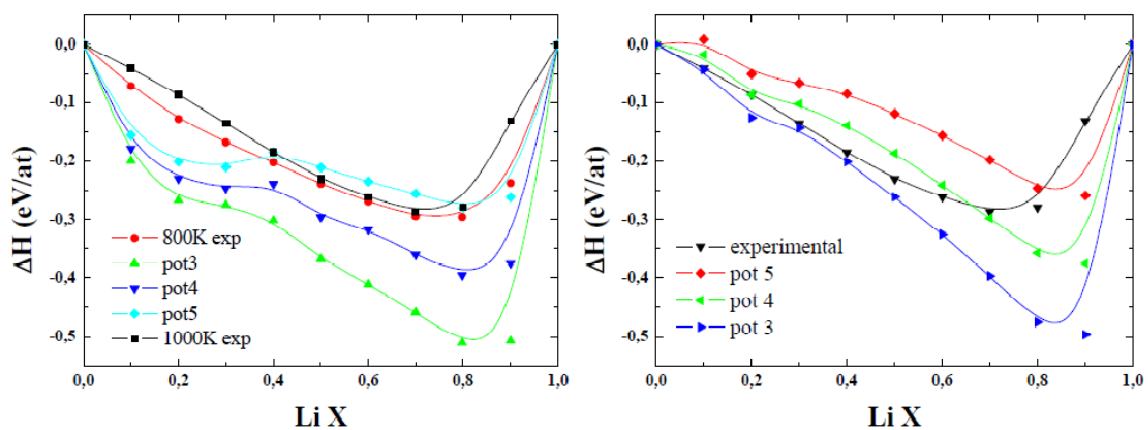


Fig. 5.6: Left) Calculated ΔH at $T = 800$ K compared with experimental data (Gasior 2001). Right) **5.7:** Calculated ΔH at $T = 1000$ K compared with experimental data (Ruppersberg 1976).

5.1.6 Potentials, Polynomials and Targets

To understand a little bit better the somewhere trial-and-error process of fitting enthalpies we show in the next two figures the different targets used as well as the different polynomials obtained. These polynomials will be important if we try to determine the eutectic point with some of these potentials. (One more paper is in progress dealing with different methods to determine the eutectic point in LiPb phase diagram (Fraile 2013)). Left part of Fig 5.7 shows the targets used to create potentials v2 to v5 respectively and right part show the polynomials needed to fit enthalpy of mixing calculated with our potential, to the target.

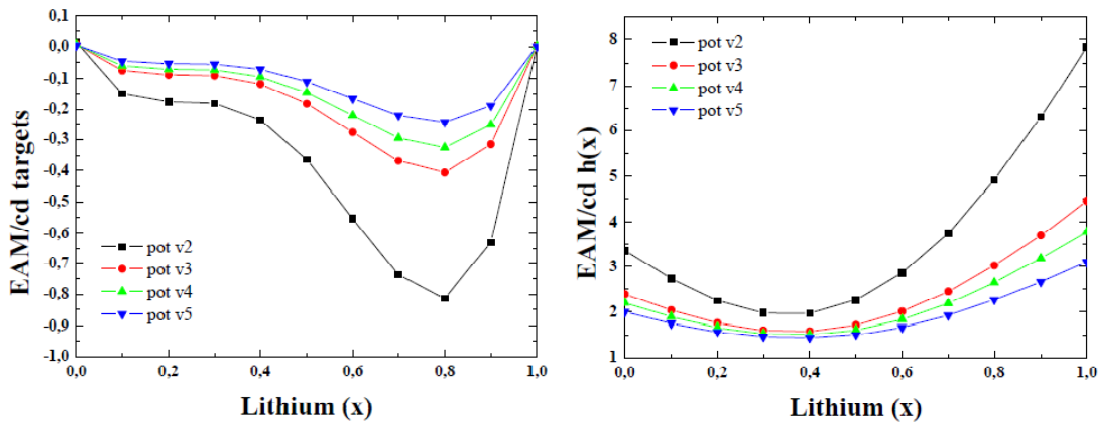


Fig. 5.7. Left) Targets for LiPb EAM/cd potentials. Right) Polynomials obtained with the targets shown in left picture.

5.1.7 Heat capacity

Heat capacity at constant volume, C_v , can be calculated from the energy oscillations as:

$$C_v = \frac{1}{k_B T^2} \left(\langle E^2 \rangle - \langle E \rangle^2 \right) \quad (5.23)$$

But experimental heat capacity values are usually measured at constant pressure, C_p . These two quantities are related by the well know relation $C_p - C_v = VT\alpha^2/\beta_T$ where α is the coefficient of thermal expansion and β_T is the isothermal compressibility. If we calculate the enthalpy of the system, defined as $H = U + pV$ where U is the internal energy of the system, p is the pressure at the boundary of the system and its environment, and V is the volume of the system, then we can easily calculate C_p .

$$C_p = \left(\frac{\partial H}{\partial T} \right)_p \quad (5.24)$$

Li17Pb volume change and enthalpy change at melting results are close to the expected values. The experimental value is $\Delta H_f = 5.8$ kJ/mole and our simulation gives $\Delta H_f = 5.3$ kJ/mole. See next figure. Two simulations (using pot 5) are shown to check size effects, with 2048 and 13500 atoms respectively. Note: Eutectic point is still under discussion but in our simulations of eutectic LiPb we will use 17 % of Li as eutectic concentration except when noted.

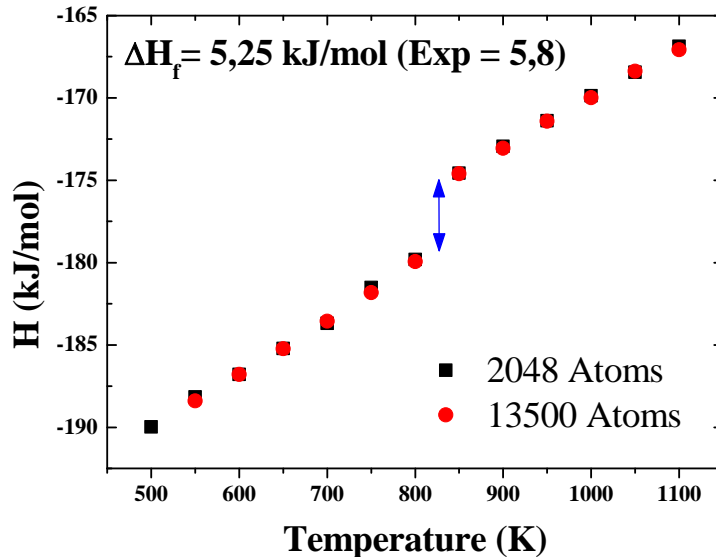


Fig. 5.8 Calculated enthalpy of Li17Pb from two different MD simulations. (Black squares 2048 atoms, red circles 13500). Blue arrow signals the enthalpy jump at melting.

From the slope of this H vs T curve one can obtain the heat capacity at constant pressure, C_p , of Li_{17}Pb . Calculated C_p , gives good agreement with the experimental value as can be seen in Fig. 5.9. It is to be noted that C_p values (or temperature dependence) are different with different potentials something that we will see is not always true if we look at the structural properties.

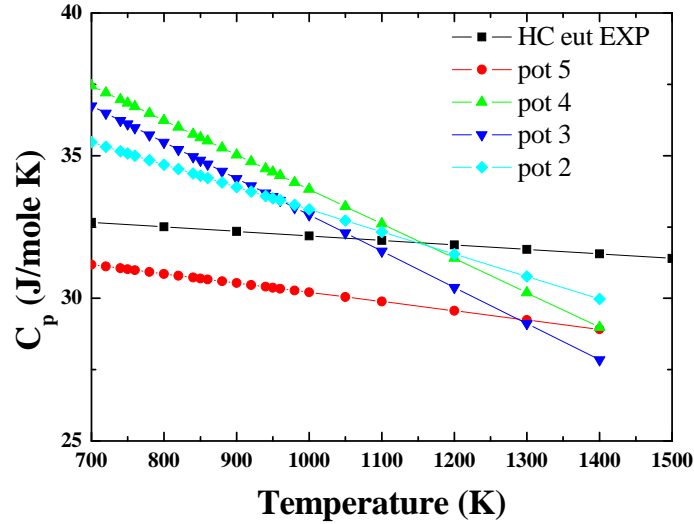


Fig. 5.9: Calculated heat capacity of liquid Li_{17}Pb using different potentials compared to experimental data (Mas de les Valls 2001). MD heating runs with T ranging from 900 to 1400K.

5.1.7.2 Heat capacity in LiPb system.

Little is known about the heat capacity C_p , of liquid alloys and its variation with composition and temperature (Bergman 1985). From the thermodynamic point of view, the positive excess specific heat is the most important indicator of the existence of chemical short range order (CSRO or just SRO hereinafter) in liquid alloys.

In next figure we compare the C_p of LiPb systems calculated with potentials 4 and 5 with experimental data found in (Saar 1987). As can be seen the MD results roughly follow the ideal behaviour signalled by violet dashed lines.

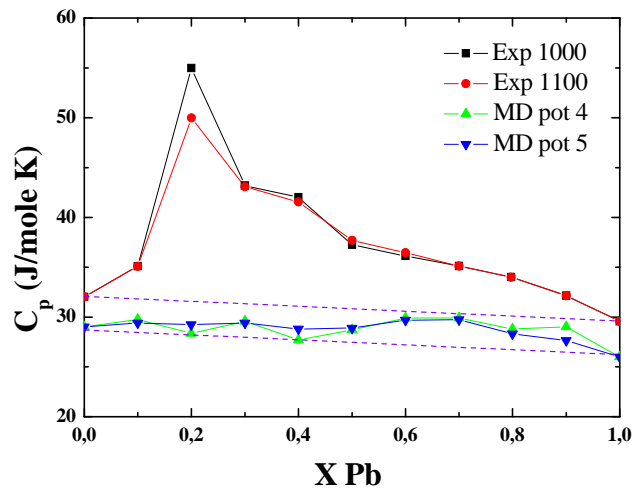


Fig. 5.10. Heat capacity of LiPb system using two different potentials (pot4 and pot5) compared with experimental data (Saar 1987).

5.1.8 Density of LiPb system:

In next figure we compare density of LiPb systems calculated with potentials 4 and 5 with experimental data available in (Saar 1987). MD simulations has been carried out with 4000 atoms and size effect has been checked.

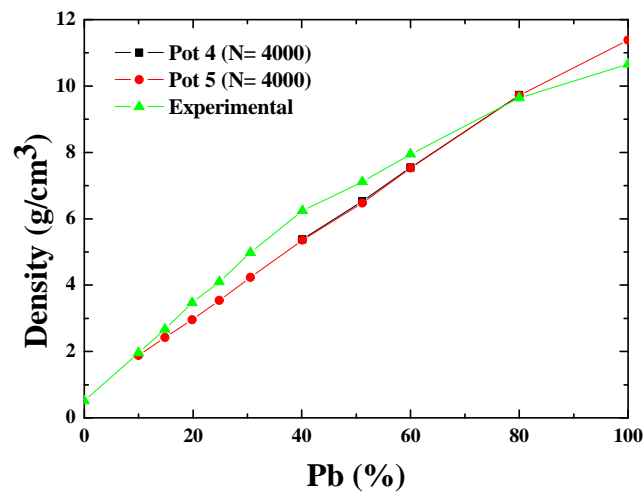


Fig. 5.11. Calculated density of Li-Pb system from MD simulations. (N = 4000 atoms) compared with experimental values (green triangles) taken from (Saar 1987).

All those calculations have been made from MD cooling runs as explained before. The overall agreement is good (error is about 10%). The dependence of SRO and compound forming effects is not yet clear.

5.1.9 Volume

We can also compare predicted volume from our MD ($T = 1000$ K, cooling runs) simulations with experimental results taken from (Saar 1987). Again, possible size effect has been checked. With $N = 13500$ atoms, the sample is big enough and size effects are not important. In a similar way as before, the volume of our simulated LiPb systems (See Figure 5.12) almost present an ideal linear behavior (Vegard's rule) while experimentally LiPb system shows a clear volume contraction at 80 % of Li concentration.

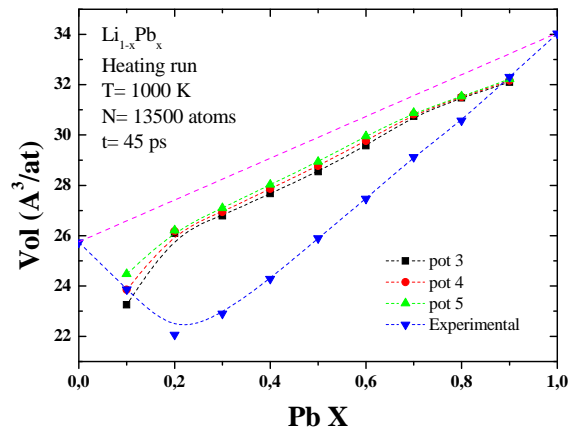


Fig. 5.12. Calculated volume of $\text{Li}_{1-x}\text{Pb}_x$ compounds with 3 different potentials. MD heating run, $N=13500$ atoms, total simulation time 45 ps. Experimental data from (Saar 1987).

5.1.10 Eutectic

If we focus now in the eutectic concentration, namely Li₁₇Pb, we will see how Potential-5 gives good thermodynamic results in the eutectic. In Fig. 5.15 the calculated density with Pot-5 is shown and compared to experimental values according to (Mas de les Valls 2001). As can be

seen the overall agreement is quite good (error is about 5 %) and the dependence with temperature (dp/dT) is almost exactly the same.

The result shown in figure 5.13 is encouraging but can be misleading. Density is not a good property to compare different potentials. In fact the result is almost the same with potentials 3, 4 and 5. (See Fig 5.13). This is important because it means that different potentials, that give different thermodynamics, can give almost indistinguishable structural properties hence the structural properties of liquids should not be a target to create potentials. See (Figure 5.9) heat capacity results of liquid LiPb eutectic with different potentials. C_p vs T is different depending on the potential employed, while density is almost identical.

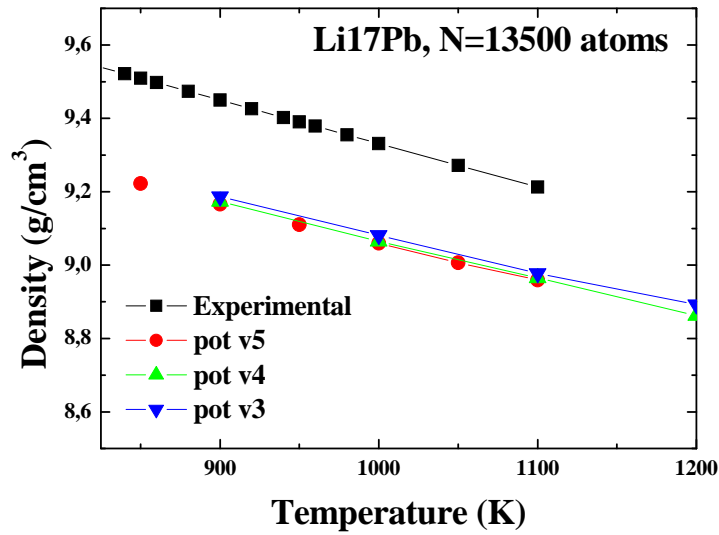


Fig. 5.13. Calculated density of Li17Pb from MD simulations ($N = 13500$) compared with experimental values (black).

5.1.11 Structural properties

As we advanced in Chapter 4, (Eq. 4.19) the pair-correlation function is generally defined as:

$$g(r) = \rho^{-2} \left\langle \sum_i \sum_{j \neq i} \delta(r_i) \delta(r_j - r) \right\rangle = \frac{V}{N^2} \left\langle \sum_i \sum_{j \neq i} \delta(r - r_0) \right\rangle \quad (5.25)$$

where ρ is the atomic density $\rho = N/V$. The radial distribution function $RDF(r)$, given by

$$RDF(r) = 4\pi r^2 \rho_0 g(r) \quad (5.26)$$

can be integrated to obtain the average number of neighbouring atoms in a coordination shell:

$$\bar{n} = \int_{r_1}^{r_2} RDF(r) dr = 4\pi \rho_0 \int_{r_1}^{r_2} g(r) r^2 dr \quad (5.27)$$

where r_1 and r_2 are the distances corresponding, for example, to consecutive minima in $g(r)$ \rightarrow the deeper the minima, the more robust the delimitation of atomic shells. The average number of atoms in the first (i.e. innermost) shell is often called the coordination number. It should be noted that there is often some confusion about the meaning of the coordination number.

Firstly, it does not mean that every atom in the structure has this number of atoms around it; the coordination number is an average - hence it is quite reasonable to have a non-integral number. Secondly, the definition of the limits of the first shell in equation (5.27) is somewhat arbitrary and various methods for quoting coordination numbers are often used, e.g. integrating to the first minimum in $g(r)$, fitting and integrating peaks in $g(r)$ (see, e.g. Waseda 1980, Pings (1968).

Temperature (K)	r_1 exp (Å)	r_1 MD	r_2 exp	r_2 MD	r_2/r_1 exp	r_2/r_1 MD
573	3,52	3,28	6,67	6,21	1,89	1,89
593	3,55	3,28	6,72	6,14	1,89	1,87
653	3,60	3,28	6,81	6,21	1,89	1,89
673	3,56	3,34	6,89	6,14	1,93	1,83

Table 5.II. Main results for Li17Pb total $g(r)$. Comparison between MD and experiments (Mudry 2008), all distances in Å.

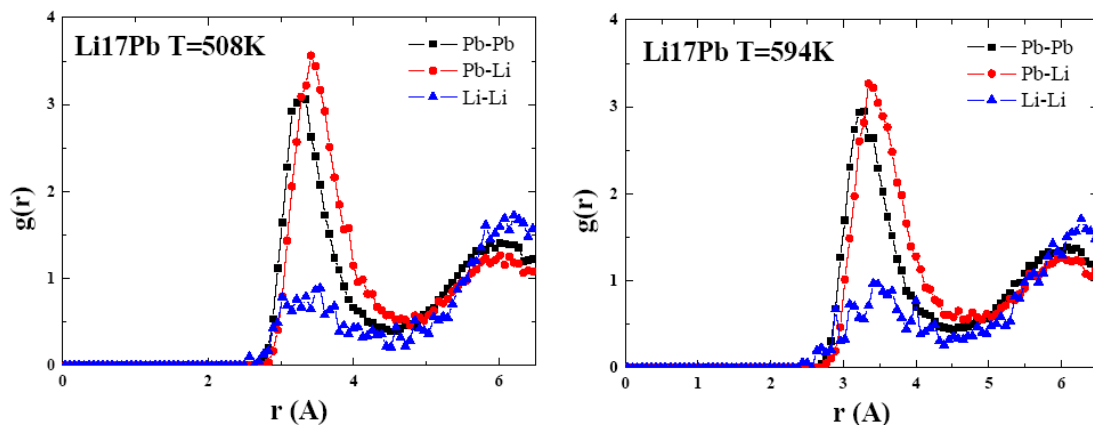


Fig. 5.14. Partial $g(r)$ calculated from MD cooling runs at $T = 508$ K (left) and $T = 594$ K (right).

Table 5.II collects the results of total pair distribution, $g(r)$ function for Li17Pb obtained using pot 5 and those presented in (Mudry 2008). As can be seen in both tables, the positions r_1 and r_2 are a little bit different while the ratio, r_1/r_2 agrees very well with the experimental value.

Figures 5.14 show the partial distribution functions, $g_{ij}(r)$ at two different temperatures, namely 508 K (left) and 594 K (right). Numerical results are collected in Table 5.III.

$g_{ij}(r)$	T(K)	Exp $r_1(\text{Å})$	MD $r_1(\text{Å})$	Error (%)
Pb-Pb	508	3.55	3.35	<10
	593	3.54	3.28	<10
Pb-Li	508	2.79	3.41	25
	593	2.77	3.35	25
Li-Li	508	2.40	3.3 (3.02?)	35 (<10)
	593	2.76	3.47 (2.89?)	35 (<10)

Table 5.III. Main results for Li17Pb eutectic partial $g(r)$'s. Comparison between MD and experiments (Mudry 2008). $r_{1 \text{ Pb-Li}}$ and $r_{1 \text{ Li-Li}}$ does not match the experimental results.

With all those results the potential 5 (for example) could be considered good enough to simulate Li17Pb system. However let see first what happen at higher Li concentrations.

5.1.12 $\text{Li}_{50}\text{Pb}_{50}$

As before, when we compared density results for eutectic concentration (See figure 5.13), now, in liquid $\text{Li}_{50}\text{Pb}_{50}$ potentials v5, v4 and v3 give almost the same result. The dependence with temperature ($d\rho/dT$) is almost exactly the same. Interestingly the v2 potential, which is far from giving good results looking at the enthalpy curves (figures 5.6) is giving now the best result for the LiPb liquid density. This however is again not guarantee of having a good description of the liquid for that concentration as we will see soon.

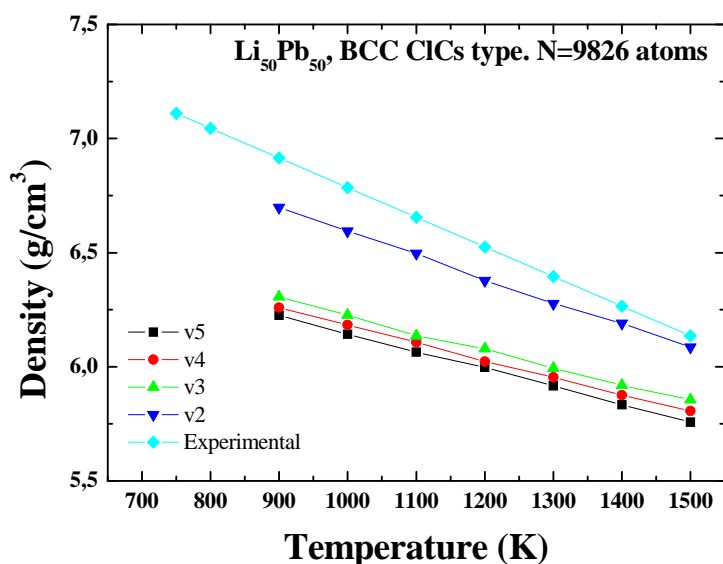


Fig. 5.15. Calculated density of $\text{Li}_{50}\text{Pb}_{50}$ from MD simulations ($N = 13500$) compared with experimental values (cyan) taken from (Saar 1987).

Again, both potentials v3, v4 and v5 are almost giving the same results looking at the density of liquid $\text{Li}_{50}\text{Pb}_{50}$ while C_p results for the eutectic are different, and enthalpy curves are different as well. This reinforces what was said before; different potentials, that give different thermodynamics, can give almost indistinguishable structural properties and structural properties should be taken with care as target for interatomic potentials.

5.1.13 Structural factors

We can also compare with *ab initio* investigations (Senda 2001). Overall agreement is good for both compounds. However all these calculations are somewhere blind to the real structure of the liquid as we will see when we study segregation and SRO. In next figure we compare partial distribution functions (as defined in Chapter 4, Eq. 4.18 and 4.19) of liquid $\text{Li}_{50}\text{Pb}_{50}$ and $\text{Li}_{80}\text{Pb}_{20}$ with the results reported in (Senda 2001). Temperature is fixed to 1075 K and 805 K for the liquid $\text{Li}_{80}\text{Pb}_{20}$ and $\text{Li}_{50}\text{Pb}_{50}$ alloys, respectively.

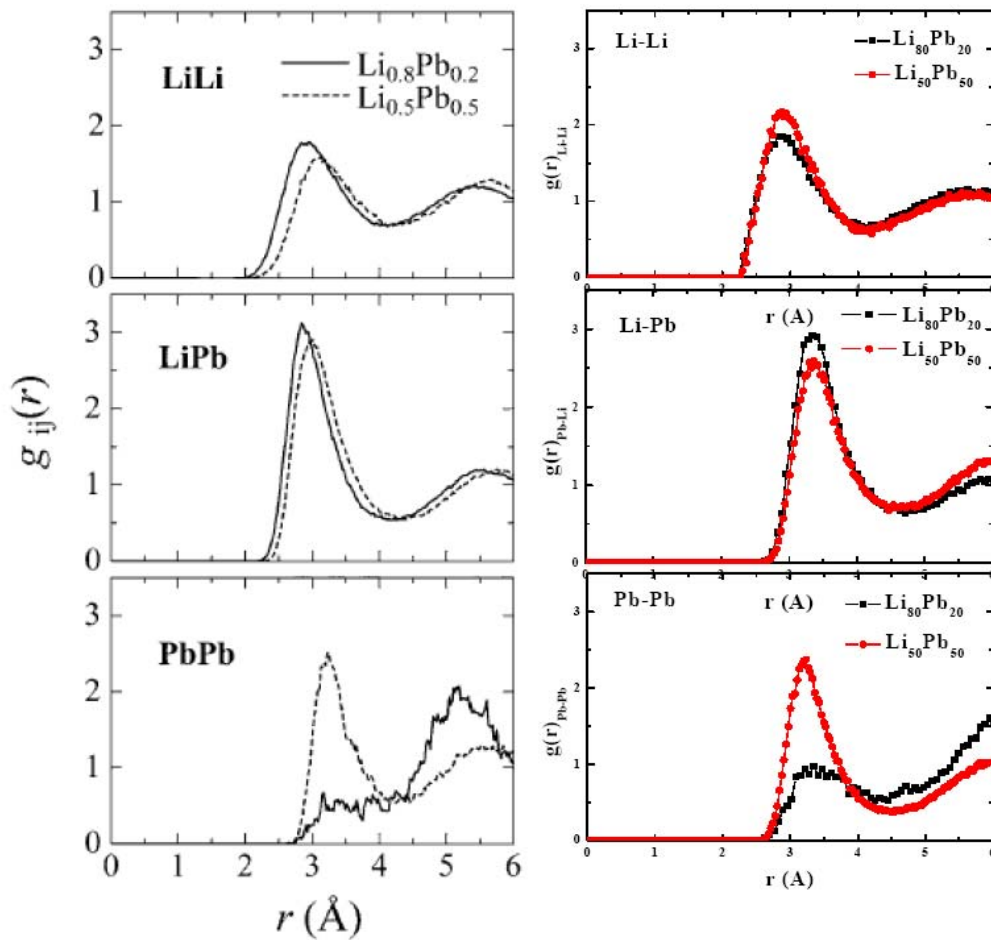


Fig. 5.16. RDF $g_{\text{LiLi}}(r)$, $g_{\text{LiPb}}(r)$ and $g_{\text{PbPb}}(r)$ for the liquid $\text{Li}_{0.8}\text{Pb}_{0.2}$ (solid line - black) and $\text{Li}_{50}\text{Pb}_{50}$ (broken line - red) alloys. Left graphs taken from (Senda 2001).

5.1.14 Problems: segregation

In order to get a quantitative measure of the chemical order we consider the coordination numbers defined as

$$n_{ij} = 4\pi \frac{Nc_j}{V} \int_0^{R_{ij}} g_{ij}(r) r^2 dr \quad (5.28)$$

It is well known that these quantities suffer for some arbitrariness in the definition of the upper limit of the integral. (R_{ij} is chosen as the position of the first minimum of the corresponding $g_{ij}(r)$). This is important in the case of alloys since four coordination numbers can be defined according to the chemical nature of the pairs. The Warren-Cowley (Cowley 1950, Warren 1969) short range order (SRO) parameter for the first neighbor shell, $\alpha_1^{(i)}$, is a simple way of displaying the short range order in the alloy. It is defined as

$$\alpha_1^{(i)} = 1 - \frac{n_{ij}}{x_j(n_{ii} + n_{ij})} \quad (j \neq i = 1,2) \quad (5.29)$$

where n_{ij} is the number of j-type particles around an i-type particle, within a sphere of radius R_{ij} . We will use this definition (Eq. 5.29) of SRO hereinafter. However, coordination numbers are strongly influenced by the concentration of the mixture and chemical order does not always appear clearly. Therefore, various parameters have been proposed in the literature to allow a quantitative description of the chemical order in a mixture. Another one is the so called local mole fraction method

$$x_s - 1 = \frac{n_{11}}{n_{11} + n_{12}} + \frac{n_{22}}{n_{22} + n_{21}} - 1 \quad (5.30)$$

since it is independent of the concentration. If the system exhibits complete chemical disorder, $x_s-1=0$, while it becomes positive with homocoordination (it tends to 1 when both components are immiscible) and becomes negative with heterocoordination and compound forming.

5.1.15 Pot-4 and Pot-5 comparison

Let us now compare potentials 4 and 5 looking at the SRO predictions, for a liquid $\text{Li}_x\text{Pb}_{1-x}$ alloys at 1000 K, in all Li concentration range (x from 0.1 to 0.9 in 0.1 Li concentration steps, $N=13500$ atoms). As shown in Fig 5.17 SRO values are positive (segregation) for intermediate Li concentration (40-70%). The values are slightly negative, indicating slight tendency toward heterocoordination for low and high Li concentrations (10 - 30% and 80 - 90%).

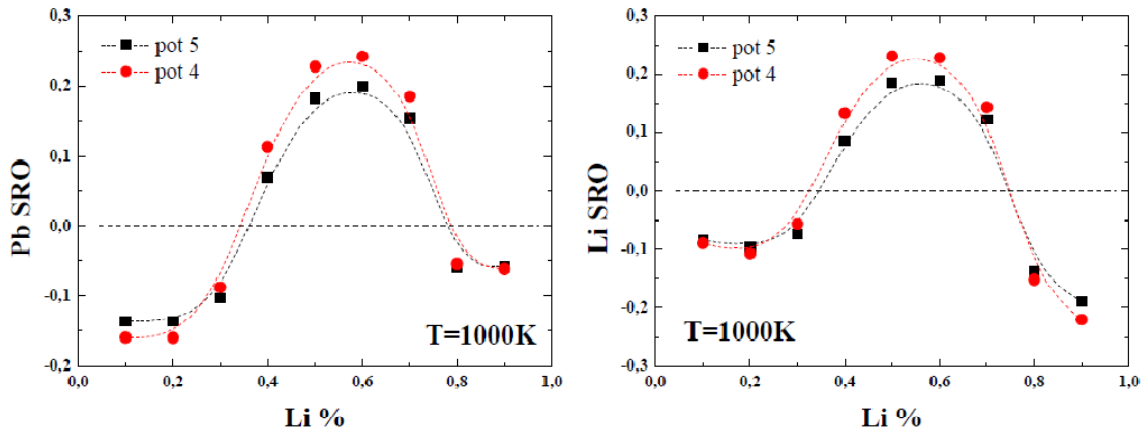


Fig. 5.17. Left) Pb SRO in LiPb system calculated using potentials number 4 and 5. Right) Li SRO.

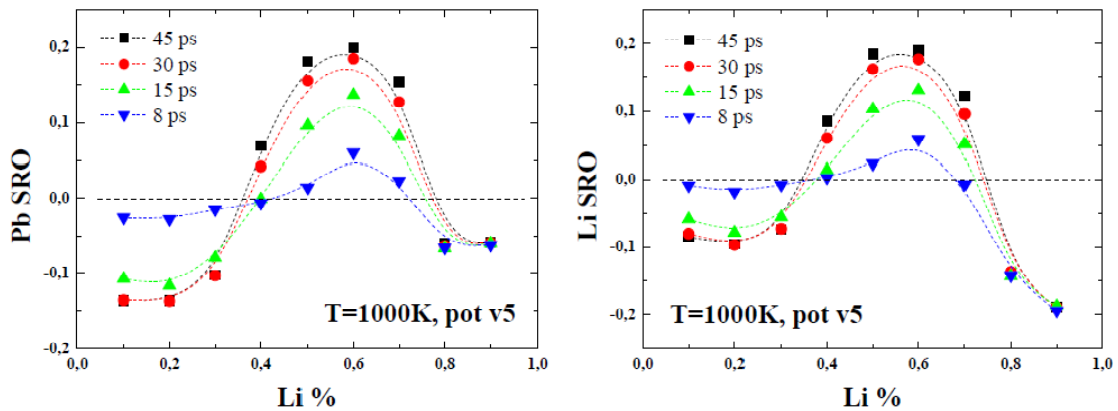


Fig. 5.18. Left) Pb SRO in LiPb system calculated using potential 5 at several simulation times, 8 ps 15 ps 30 ps and 45 ps as labelled. Right) Li SRO in LiPb system.

What is important in the last graphs (Fig. 5.18) about SRO is to note that short time simulations will give results far from equilibrium from a chemical point of view, i. e., the system is still evolving. Then, one has to take into account that apart of thermodynamic properties as temperature or pressure one should look at SRO time evolution to be sure about equilibrium properties *according to the potential employed*. Figure 5.19 shows the temporal variation of Li SRO for different Li concentrations in liquid $\text{Li}_x\text{Pb}_{1-x}$ systems at 1000 K.

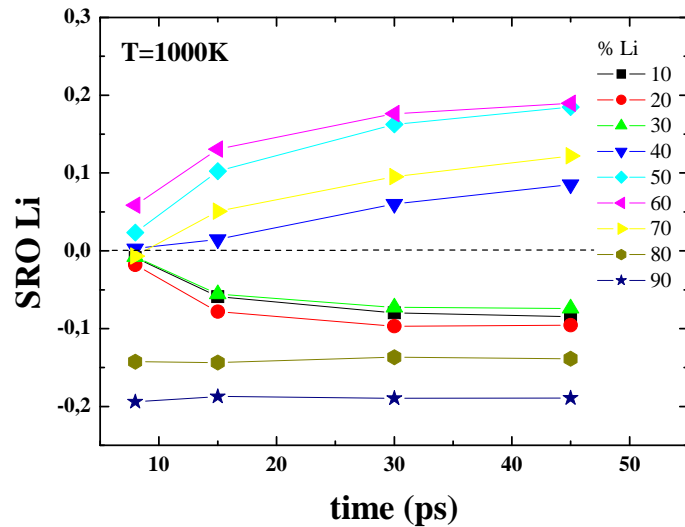


Fig. 5.19. Li SRO values calculated from MD runs data for nine different LiPb systems at four different times. ($T = 1000 \text{ K}$ and $N = 13500$ atoms, potential number 5)

Another important benchmark is to check size effects on the calculated SRO. As can be seen in Figure 5.20 SRO can depend on the initial random configurations, i.e. initial seeds for random velocities creation and random Li substitution in Pb fcc lattice (see LAMMPS manual) if the sample is not big enough (or if the simulation is not long enough). If $N = 13500$ or bigger, then SRO does not change more than a 5 % with different initial configurations.

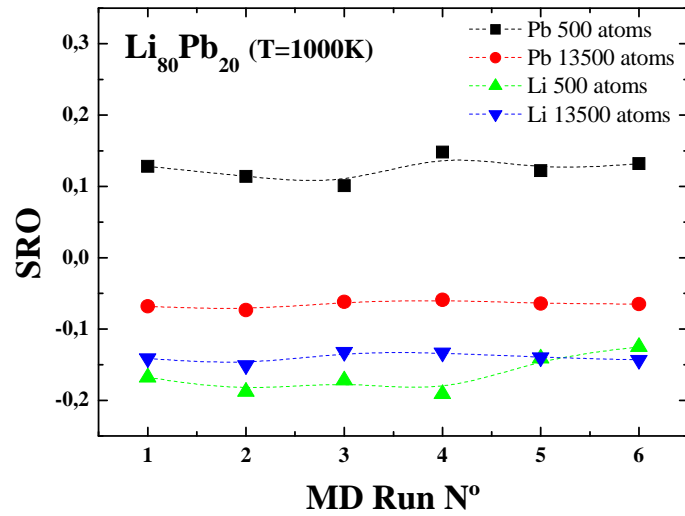


Fig. 5.20. Calculated SRO for $\text{Li}_{80}\text{Pb}_{20}$ at $T = 1100 \text{ K}$ for two different size simulations ($N = 500$ and $N = 13500$). In black fcc Pb SRO, in red Li SRO.

The meaning of positive SRO or homocoordination is better shown in next section. A simple visualization of the systems shows two different regions, one Pb rich and another one Li rich like a water and oil mixture. The system presents segregation while experimentally both metals are miscible. The results for potential 4 are very similar and are not shown for brevity sake.

5.1.16 (Visual) Segregation

In this subsection we will make use of the open visualization tool (Ovito) (Stukowski 2010) to observe the aspect of our sample after melting. As can be seen in the following figures, at first sight some homocoordination, is to say demixing or segregation can be adverted. Figure 5.23 correspond to a small simulation ($N = 2662$ atoms) of $\text{Li}_{50}\text{Pb}_{50}$ heated up to 1300 K starting from a bcc B2 phase. Figure 5.23 demonstrate that positive SRO is not a size effect.

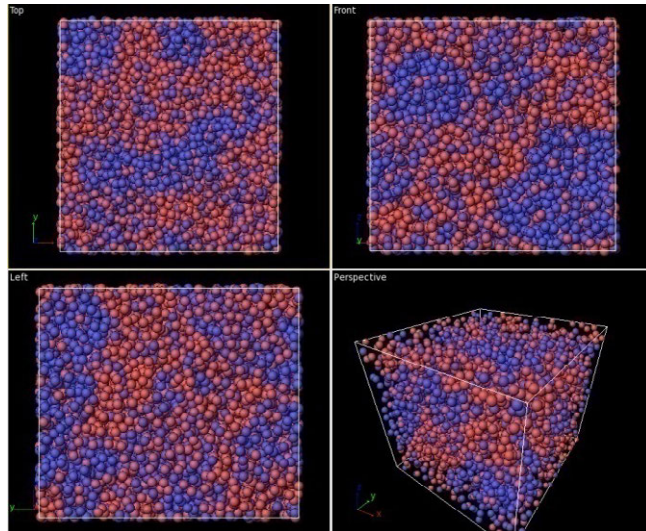


Fig. 5.21. Snapshot after a MD heating run up to 1300 K of a $\text{Li}_{50}\text{Pb}_{50}$ sample starting from a bcc lattice CICs type. System shows homocoordination.

In next figure we show a result obtained after a long simulation (total time 50 ps) of a big sample ($N = 500000$ atoms) using 100 processors in the “Finis Terrae” supercomputer (Centro de Supercomputación de Galicia, CESGA).

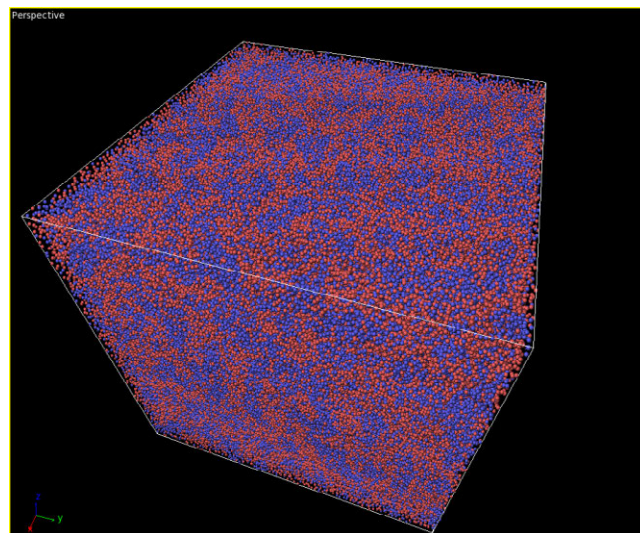


Fig. 5.22. Snapshot after a MD heating run up to 1300 K of a $\text{Li}_{50}\text{Pb}_{50}$ sample starting from an fcc lattice ($N = 500000$). System still shows homocoordination.

Next figure summarize the calculated SRO values for LiPb liquids at different concentrations with different sample sizes.

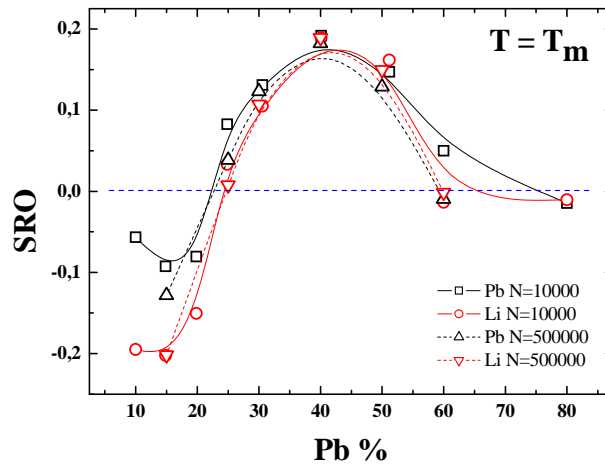


Fig. 5.23. Calculated SRO for LiPb system at liquidus temperature for two different size simulations ($N = 10000$ and $N = 500000$). In black Pb SRO, in red Li SRO.

5.1.17 Understanding segregation

The system minimizes energy segregating in two phases, one rich in lead and one rich in lithium as can be explained by the shape of the energy of mixing used as target. See next figure. For example, a $\text{Li}_{40}\text{Pb}_{60}$ (long red arrow) liquid will segregate in a mixture of two subsystems, one will be Pb rich (left red arrow) and another one Li rich (right red arrow).

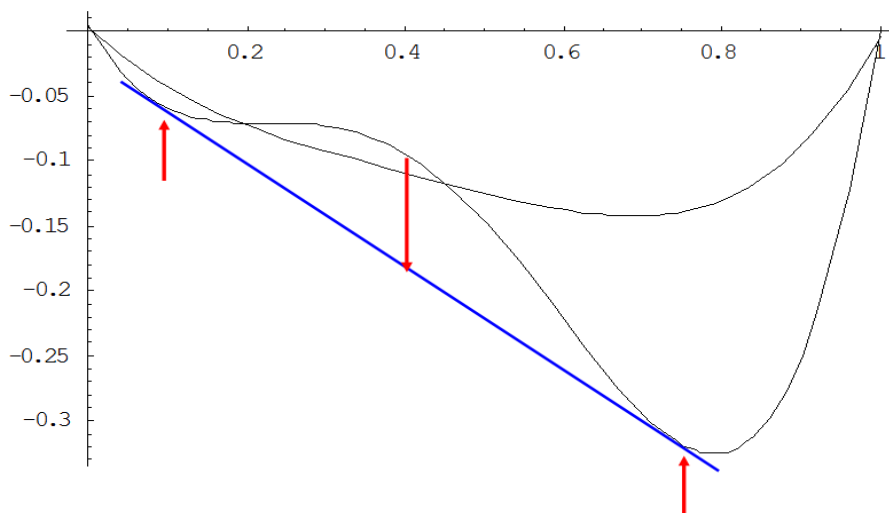


Fig. 5.24. A $\text{Li}_{40}\text{Pb}_{60}$ alloy “artificially” segregates in two “phases”, one rich in Li (around 75% Li +Pb) and another one rich in Pb (10 % Li +Pb).

We define now a new target and include in it also the energy of the LiPb compound (50% concentration) in the B2 phase (bcc CICs type). What is important here is that the new potential that gives an energy for LiPb (5050) in ordered phase (B2) lower than the solid solution. (We can check running MC simulations that the liquid 5050 system will solidify in and ordered bcc phase CICs like)

5.1.18 Li₅₀Pb₅₀ crystal structure:

According to H. Okamoto 1993 (ASM alloy Phase Diagram centre website) LiPb has two different crystal structure (CS) of LiPb in the solid phase. At room temperature CS is the hR6 (Pearson Symbol) R-3m (Space group) and at high temperature (T > 200 °C) CS is a bcc cubic like the CICs one (cP2, Pm-3m). The values of density, volume and cell parameters are listed in the following table.

	Pearson Symbol Space Group	Density (g/cm ³) Volume (nm ³)	Cell parameters (Å)
rt (0<T<200 °C)	hR6	8	a= 4.9872 α = 90
	R-3m	0.13329	b= 4.9872 β = 90 c= 6.1882 γ = 120
ht (200<T<482°C)	cP2	7.71	a= 3.586 α = 90
	Pm-3m	0.04611	b= 3.586 β = 90 c= 3.586 γ = 90

Table 5.IV. Crystal data for Li₅₀Pb₅₀ compound (Zalkin 1957) at two different temperature ranges, room temperature (rt), and high temperature (ht).

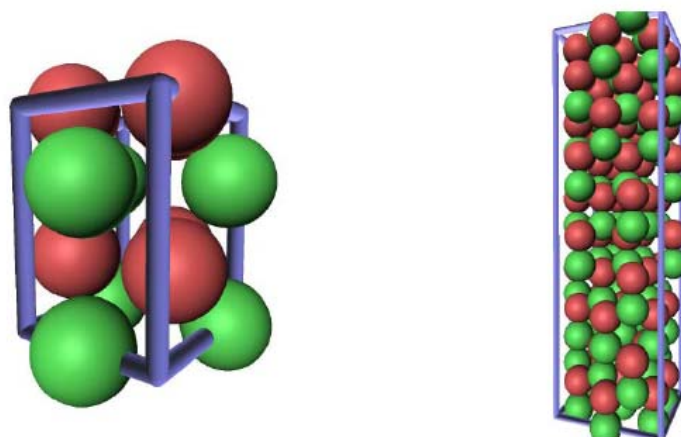


Fig.5.25. LiPb CS: Left at high temperature ($T > 200\text{ }^{\circ}\text{C}$) CS is a bcc cubic like the CICs one (cP2, Pm-3m). At room temperature CS is the hR6 (Pearson Symbol) R-3m (Space group).

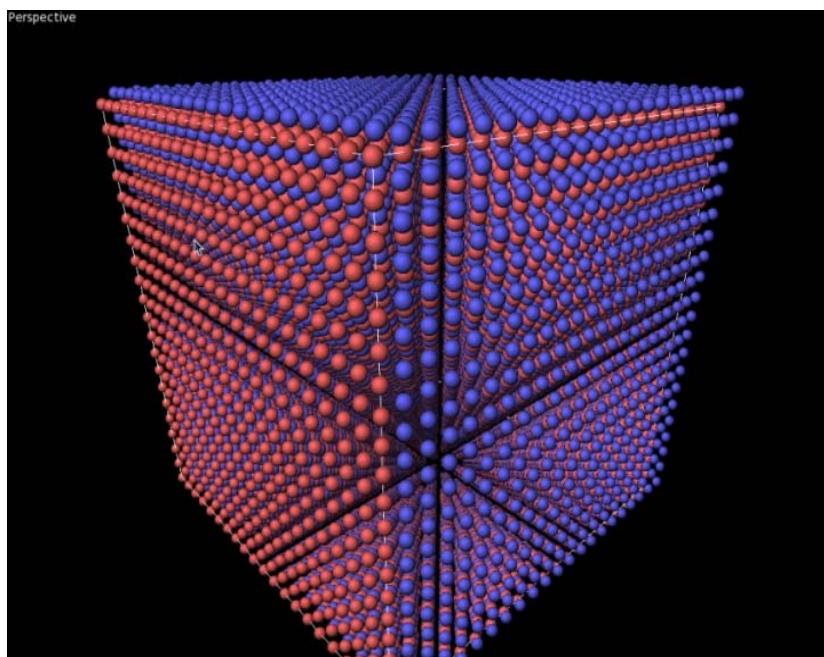


Fig. 5.26. Sample for LiPb B2 phase (CICs-like) visualized with OVITO (Stukowski 2010).

$\text{Li}_{50}\text{Pb}_{50}$ has a well known crystal structure in solid phase. Nevertheless, final results in liquid phase are almost independent on the initial crystal structure, bcc CICs type or just fcc with random substitution of Pb by Li ones. In the next figures can be seen how calculated partial $g(r)$'s are almost the same at two different temperatures above melting point.

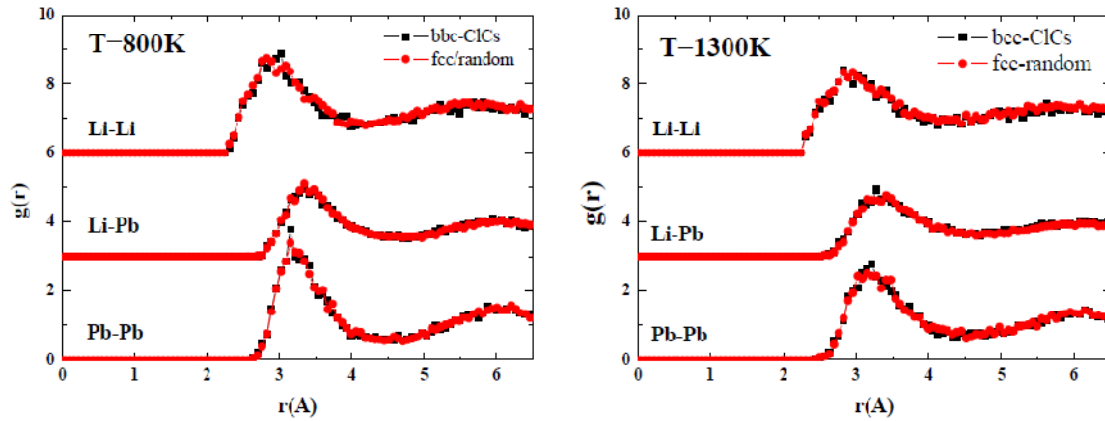


Fig. 5.27. Partial RDFs of $\text{Li}_{50}\text{Pb}_{50}$ at 800 K (left) and 1300 K (right) starting from two different initial CS; In red the results using an fcc lattice with random substitution of Pb atoms and in black the same with a bcc lattice CICs type. From up to down, Li-Li, Li-Pb and Pb-Pb partial $g(r)$, as indicated in the figures.

5.2 A Brand New Potential

5.2.1 $\text{Li}_{50}\text{Pb}_{50}$ cohesive energy and lattice parameter in the target

In order to get rid of the segregation problems a new potential has been developed adding as one more fitting parameter the cohesive energy of the LiPb in the B2 phase.

PbLi (5050) CS is the B2, CsCl type. The B2 structure has a primitive cubic Bravais lattice with two atoms per unit cell. In the binary compounds, the unit cell contains one atom of each type and so we can consider the lattice to consist of two interpenetrating simple cubic lattices, a and b , each of which contains atoms of only one type under conditions of perfect order at 0 K. Over the last years, there have been many papers dealing with different aspects of binary and ternary B2 compounds (Zhou 2011).

Table 1
 Li_xPb_y phases; melting/decomposition temperatures and free energies of formation

Phase	x_{Li}	M.Pt. (K)	$\Delta_f G^\circ$ (kJ mol ⁻¹)
LiPb	0.500	755 ^a	-60
Li_8Pb_3	0.727	915 ^b	-377
Li_3Pb	0.750	931 ^b	-137
Li_7Pb_2	0.778	999 ^a	-316
$\text{Li}_{22}\text{Pb}_5$	0.815	923 ^b	-791

^a Congruently melting.

^b Peritectically decomposing.

Table 1. Cohesive energy per atom (in eV) for ordered solid alloys in two competing structures

Alloy	Body-centered tetragonal	CsCl-like structure
LiPb	2.325	2.415
NaPb	1.910	1.895
KPb	1.835	1.545

Table 5.V. Left) Table 1 from (Hubberstey 1997). Right: Table 1 from (Molina 1998). Both papers give the same cohesive energy for LiPb in bcc B2 phase.

The experimental lattice parameter for the B2 phase is 3.586 Å (Zalkin 1957, 1958) and the cohesive energy -2.415 eV/at (Hubberstey 1997) that also correspond to the calculated with *ab initio* techniques (Molina 1998).

Naively is easy to think that the nearest neighbors are alternated, i.e., if we start sitting in a Pb atom first NN are Li, second NN are Pb etc.. But this is not correct! First NN is the other kind of atom (\neq), but next two NN are the same kind of atom that the initial one ($=$). This can be better seen in figure 5.30.

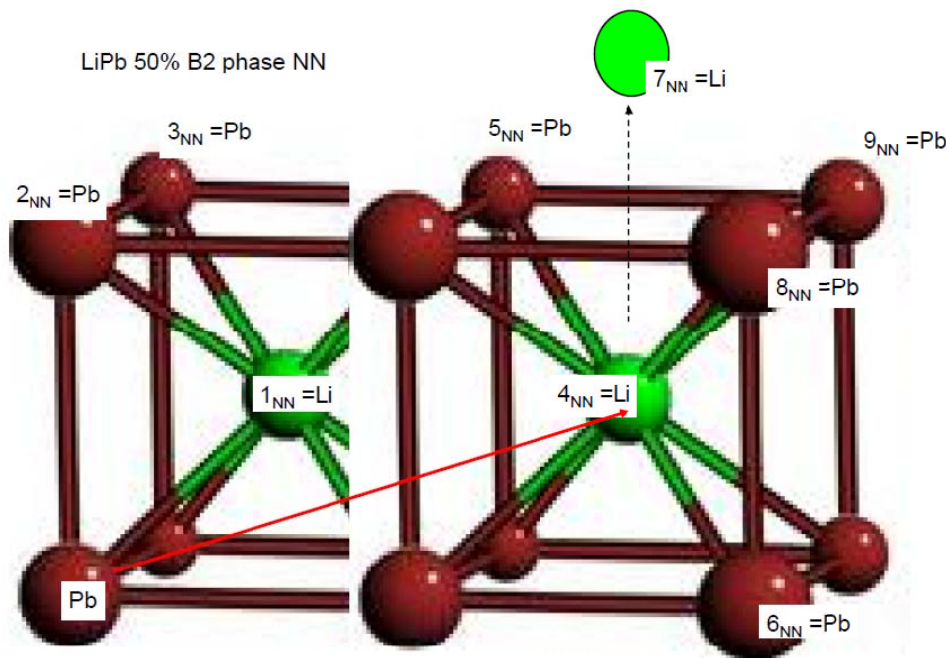


Fig. 5.28. $\text{Li}_{50}\text{Pb}_{50}$ CS and nine first nearest neighbours. 1, 4 and 7 are different (\neq). The others are equal to the origin atom ($=$).

Next table summarizes the distances, number of NN total number of atoms in shell I, Σ^T , and type of atom (= or \neq). Figure 5.29 was made as double checking in order to assure that the created CS was the desired one.

NN	$r \text{ x}(a_0)$	N	$\Sigma^T i_{\max}$	Type
1	$(\sqrt{3})/2$	8		\neq
2	1	6	14	=
3	$(\sqrt{2})$	12	26	=
4	$(\sqrt{11})/2$	24	50	\neq
5	$(\sqrt{3})$	8	58	=
6	2	6	64	=
7	$(\sqrt{19})/2$	24	88	\neq
8	$(\sqrt{5})$	24	112	=
9	$(\sqrt{6})$	24	136	=

Table 5.VI. B2 phase. Distances (in lattice parameter, in a_0 units), number of nearest neighbours and atom type, different (\neq) or same (=) as “origin one”.

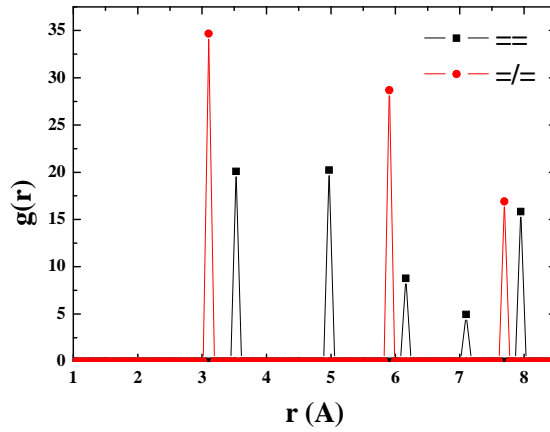


Fig. 5.29. $\text{Li}_{50}\text{Pb}_{50}$ Partial radial distribution functions (with $a = 3.5 \text{ \AA}$). The $g(r)$ peak positions and number of NN are given in table 5.VI.

With the numbers given in table 5.6 for NN and type of atom the energy of the B2 phase can be written as

$$E_{B2} = 0.5 \times \left\{ \begin{aligned} &F_{Pb}(8(\phi_{Li}(r_1))) + (6(\phi_{Pb}(r_2))) + (12(\phi_{Pb}(r_3))) + (24(\phi_{Li}(r_4))) + \\ &(8(\phi_{Pb}(r_5))) + (6(\phi_{Pb}(r_6))) + (24(\phi_{Li}(r_7))) + (24(\phi_{Pb}(r_8))) + (24(\phi_{Pb}(r_9))) + \\ &\frac{1}{2} \left((8V_{PbLi}(r_1)) + 6V_{Pb}(r_2) + 12V_{Pb}(r_3) + 24V_{PbLi}(r_4) + 8V_{Pb}(r_5) + \right. \\ &\left. \frac{1}{2} \left(6V_{Pb}(r_6) + 24V_{PbLi}(r_7) + 24V_{Pb}(r_8) + 24V_{Pb}(r_9) \right) \right) \end{aligned} \right\} +$$

$$0.5 \times \left\{ \begin{aligned} &F_{Li}(8(\phi_{Pb}(r_1))) + (6(\phi_{Li}(r_2))) + (12(\phi_{Li}(r_3))) + (24(\phi_{Pb}(r_4))) + \\ &(8(\phi_{Li}(r_5))) + (6(\phi_{Li}(r_6))) + (24(\phi_{Pb}(r_7))) + (24(\phi_{Li}(r_8))) + (24(\phi_{Li}(r_9))) + \\ &\frac{1}{2} \left((8V_{PbLi}(r_1)) + 6V_{Li}(r_2) + 12V_{Li}(r_3) + 24V_{PbLi}(r_4) + 8V_{Li}(r_5) + \right. \\ &\left. \frac{1}{2} \left(6V_{Li}(r_6) + 24V_{PbLi}(r_7) + 24V_{Li}(r_8) + 24V_{Li}(r_9) \right) \right) \end{aligned} \right\} \quad (5.31)$$

5.2.2 Fitting potential procedure

In the low radius regime we assume that the PbLi-mix potential will be essentially correct so we fit our new potential to a new sum of splines only for $r > 2.5 \text{ \AA}$ for example. As can be seen in next graph the new potential matches correctly the V_{mix} potential in this point.

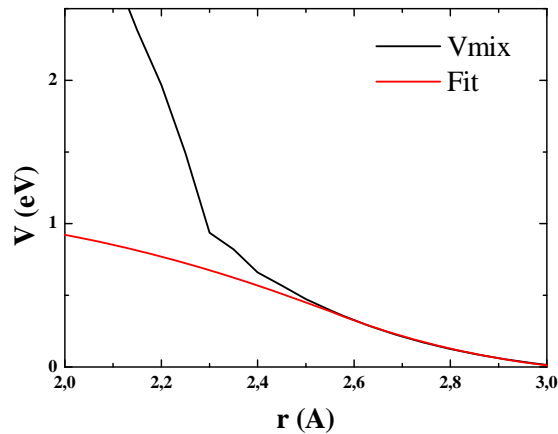


Fig. 5.30: Match between our fitted potential (red line) and the original (black line) for very short distances ($r < 2.5 \text{ \AA}$).

Depending on the definition of E_{B2} the resulting potential can be very different and, of course depending on the “fitting parameters”. Next figure shows different unrealistic potentials that can be obtained with uncareful choice of targets and weights.

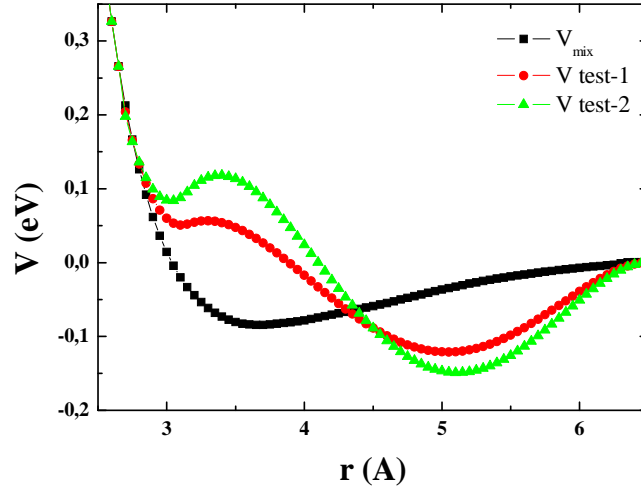


Fig. 5.31. Different potentials obtained with two different definitions of energy in B2 phase compared with the average of Pb and Li pair potentials, V_{mix} .

The current fitting procedure considers $V_{\text{PbPb}}(r)$, $V_{\text{LiLi}}(r)$, $F_{\text{Pb}}(\rho)$, and $F_{\text{Li}}(\rho)$ as given from the pure elements; the only unknown function is then the cross-pair interaction $V_{\text{LiPb}}(r)$ which contains the fitting parameters, $\{a_i\}$. This is given the common form of a piece-wise cubic polynomial possessing some n_k knots at (chosen) positions r_i ,

$$V_{\text{LiPb}}(r) = \sum_i^{n_k} a_i H(r_i - r)(r_i - r)^3 \quad (5.32)$$

where $H(x)$ is the Heaviside unit step. All potentials are imposed to reach up to the 5th neighbours shell, implying a host of three-body terms to be dealt with.

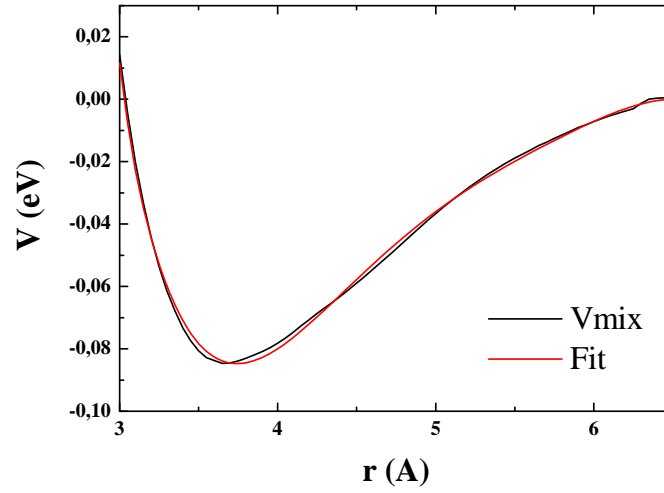


Fig. 5.32. Fit of V_{mix} to a sum of splines. In black the average of Pb and Li pair potentials V_{mix} , and in red the fitting function.

As target we use a Redlich-Kister expansion (Saunders 1998) for mixing energies, ΔH ,

$$\Delta g(x, T) = x(1-x) \sum_{p=0}^n L_p(T) (1-2x)^p \quad (5.33)$$

As far as we are concerned there are no data about ΔH for LiPb at 0 K. However, ΔH is in general independent of temperature (and in fact ΔH is very similar both at $T= 800$ K (Gasior 2001) and $T= 1000$ K (Ruppersberg 1975) so we can suppose ΔH at 0 K will have a similar shape that those reported for the liquid system. Also importantly, inflexion points in mixing enthalpy target can lead to segregation, i.e. positive values for short range order (SRO) parameter, in order to minimize total energy (See figure 5.24). In figure 5.33 we present the enthalpy of mixing calculated with new potentials M1, M2 and M3 (M for Madrid). The cohesive energy of LiPb in B2 phase, is also used as a target. The orange square represent the result obtained with potential M1 that as we will see gives the best results in different properties.

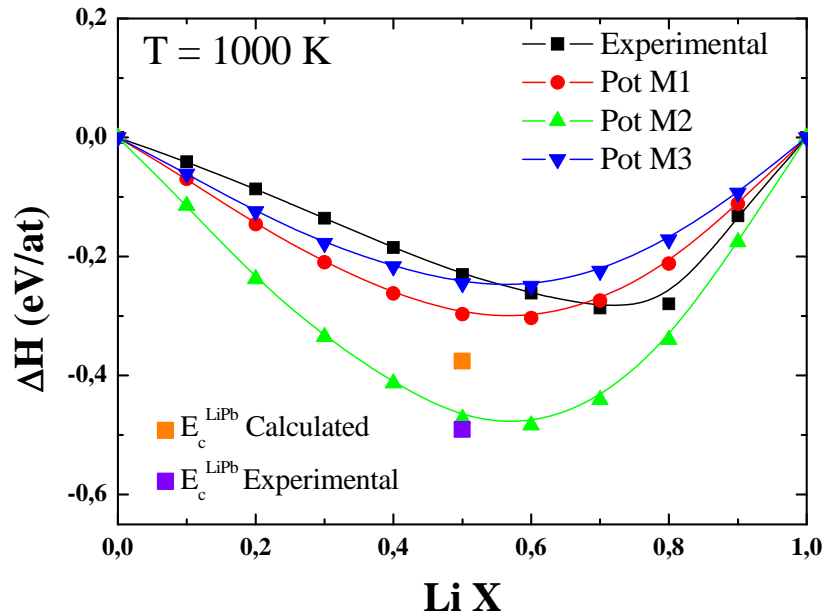


Fig. 5.33. Enthalpy of mixing vs Li concentration. Experimental values taken from (Ruppersberg 1975), MD results as labelled. Cohesive energy of LiPb in B2 phase, (purple square) is also used as a target. Orange square represent the result obtained with potential M1.

In order to ensure that the potential will give correct thermodynamic properties we also use as a target the cohesive energy and lattice parameter of LiPb compound. This compound has two different CS in solid phase (Zalkin 1957). At low temperature ($T < 200 \text{ }^\circ\text{C}$) CS is the “hexagonal” hR6 and at high temperature ($200 < T < 482 \text{ }^\circ\text{C}$) CS is bcc CICs-like, i. e. two simple cubic structures interpenetrating (see Table 5.IV for details). What is important here is to have a smaller cohesive energy in the solid ordered phase compared to the disordered (liquid) one. That way, we will have correct melting point of this compound and hopefully (how we will see) correct phase diagram description.

The work of Ruppersberg and Eager (Ruppersberg 1975) shows that Li–Pb alloys manifest a preference to an unlike atom arrangement leading to a short-range order in the alloy. In a recent work (Mudry 2008) atomic distribution in the $\text{Pb}_{83}\text{Li}_{17}$ eutectic seems to be significantly affected by the Li_4Pb associates. These chemically ordered structural units (also called Zintl ions) are randomly distributed in Pb “matrix”.

In the theoretical work of Anusionwu (Anusionwu 2005) the influence of the strong heterocoordination tendency of the Li–Pb liquid alloy on its surface properties is studied using a statistical thermodynamic model based on compound formation and that based on the layered structure near the interface. In addition to the already mentioned Li_4Pb compound formed in the liquid alloy, the study shows that the compound Li_3Pb also has a profound influence on the thermodynamic properties of the liquid alloy.

5.2.3 Short Range Order

Now we do not have positive SRO (except when Li concentration is very high, >80%). Experimentally, as far as we are concerned, there is only one experimental study (Ruppersberg 1982) that gives an estimation of SRO for LiPb alloys, and they gave $\text{SRO} < 0$ (around -0.2) for high Li concentrations (between 40 and 80 %), but they admit that their calculations contain a lot of uncertainties (See Table 2 in (Ruppersberg 1982)).

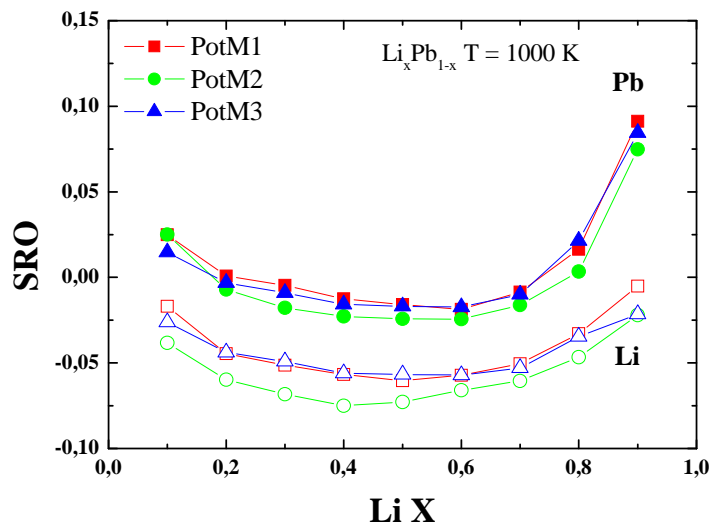


Fig. 5.34. SRO values vs Li concentration calculated with new potentials. As can be observed now SRO is not positive for intermediate Li concentrations (See figures 5.19-20 and 5.25).

5.2.4 Structural properties

In figure 5.35 we present the structure factor $Q(S(Q)-1)$ curves of liquid Li17Pb at 775 K (500 °C). Experimental data have been taken from (Ruppersberg 1975) and MD results are shown with two different potentials. It is noteworthy that different potentials can yield to different thermodynamic properties but almost identical structural properties at certain compositions.

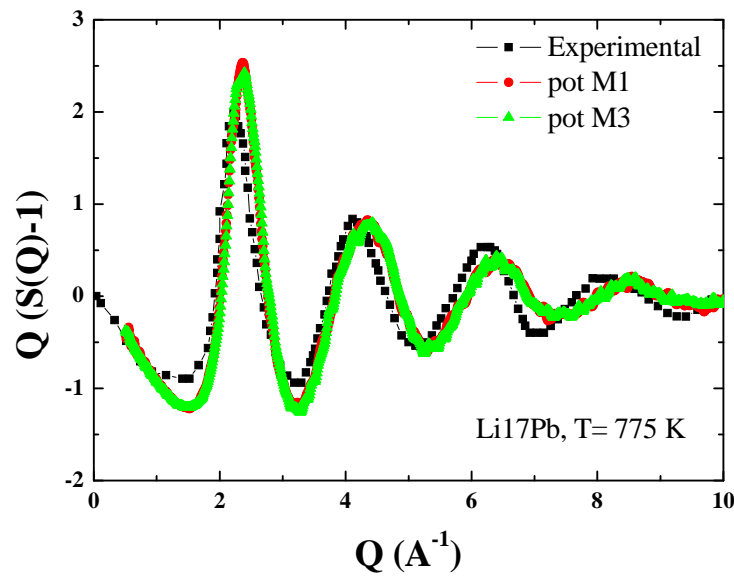


Fig. 5.35. $Q(S(Q)-1)$ of liquid Li17 at $T = 775$ K. Black squares are the experimental data (Ruppersberg 1975) red circles and green triangles represent calculated data with pot. M1 and M3 respectively.

The partial pair distribution functions, $g_{ij}(r)$, are not shown for brevity sake, and are very similar to the presented previously in figures 5.14 (a) and (b). The positions of the first peak, r_1 , calculated with two different EAM/alloy potentials (M1 and M3) are summarized in next table.

Having satisfactory agreement between the structure factor calculated by MD and the experimental one, a similarly good agreement would be expected in density. Indeed, our density calculations give very good results in a wide temperature range from 500 to 1200 K (see Fig 5.36).

$g_{ij}(r)$	T (K)	Exp r_1 (Å)	r_1 (Å) MD Pot M1	Error %	r_1 (Å) MD Pot M3	Error % (New)	EAM/cd r_1 (Å)	Error % (Old)
PbPb	508	3.55	3.28	< 10	3.28	< 10	3.73	< 10
	593	3.54	3.28	< 10	3.28	< 10	3.67	< 10
PbLi	508	2.79	2.95	<10	3.02	<10	3.02	25
	593	2.77	2.75	< 5	3.02	< 5	2.95	25
LiLi	508	2.40	2.95	< 10	2.89	< 10	3.05	35
	593	2.76	2.95	< 10	2.89	< 10	2.9	35

Table 5.VII. Partial $g(r)$ peaks with Pot. M1. The results are as good as or better than the obtained with previous potentials (last column). General agreement is better than 10% of error in first peaks position.

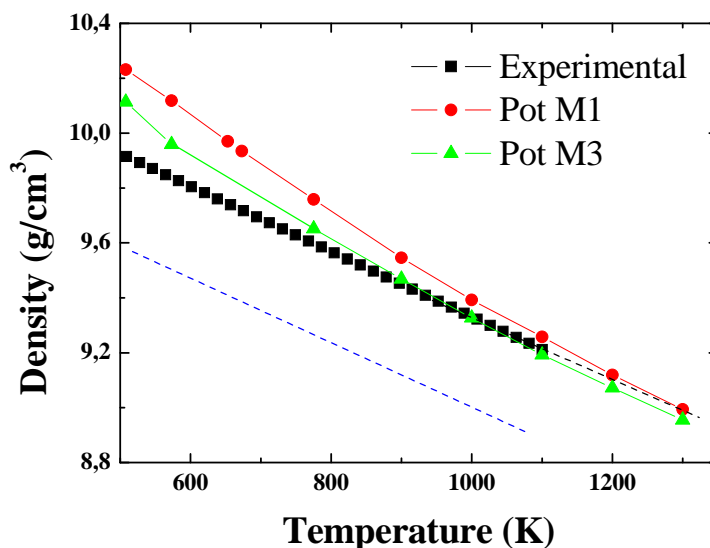


Fig. 5.36. Density of liquid eutectic calculated with potentials M1 and M3 (red circles and green triangles respectively). Black squares are the experimental data taken from (Mas 2008). Blue dashed line represents the result with Pot.5 (See figure 5.13).

To finish with eutectic properties we have analyzed lithium self diffusion in liquid Li₁₇Pb. Diffusivity is explained somewhere in detail in Chapter 6 so we will not repeat here definitions and methods. The calculated values from MD simulations can be compared to the theoretical estimation reported in (Mas de les Valls 2008). Our values are of the same order of magnitude but some slightly different temperature dependence (Fraile *et al*, to be published).

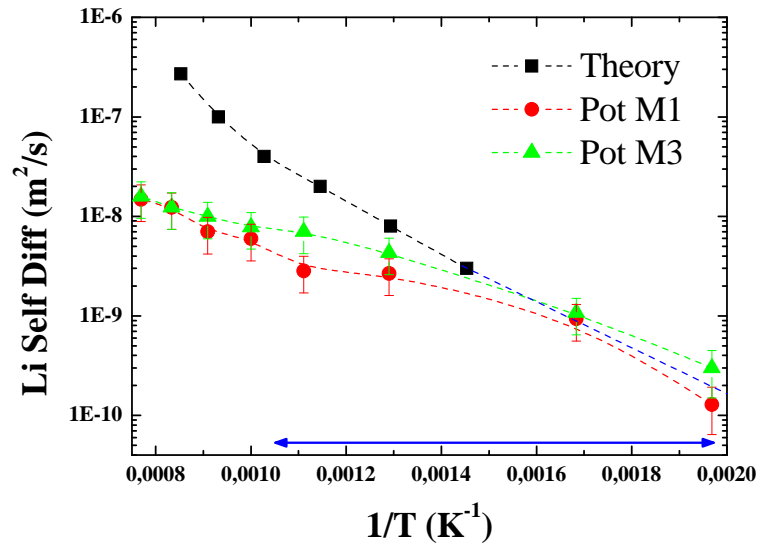


Fig. 5.37. Li self diffusion in Li17Pb calculated with potentials M1 and M3 as labelled. Black squares taken from (Mas de les Valls 2008). Blue dashed line stands for the interpolation of theoretical data. Blue arrow denotes the working temperature window in breeder blankets.

Note: Li17Pb working temperatures window comes determined by the structural materials choice restrained by corrosion limits under eutectic flowing conditions (velocities between mm/s for pure breeding concepts and m/s for self-coolant ones). Thermal windows typically assumed range between eutectic points, 550 °C, case of ferritic-martensitic steel, or 700 °C, assumed *SiCf/SiC* corrosion limit in flowing Li17Pb (Mas de les Valls 2008).

5.2.5 Volume contraction

Let us now examine the whole LiPb system. Experimentally, a volume contraction is observed around 80% of Li (Saar 1987) sometimes claimed to be due to some kind of Li₄Pb compound formation still present in liquid phase. If we plot liquid Pb_xLi_{1-x} volume (at a certain temperature, here 1000 K in cooling run) vs Li concentration we observe the same contraction almost at the expected Li concentration. Compare Fig. 5.38 to Fig. 5.12, the improvement reached with these new potentials is evident.

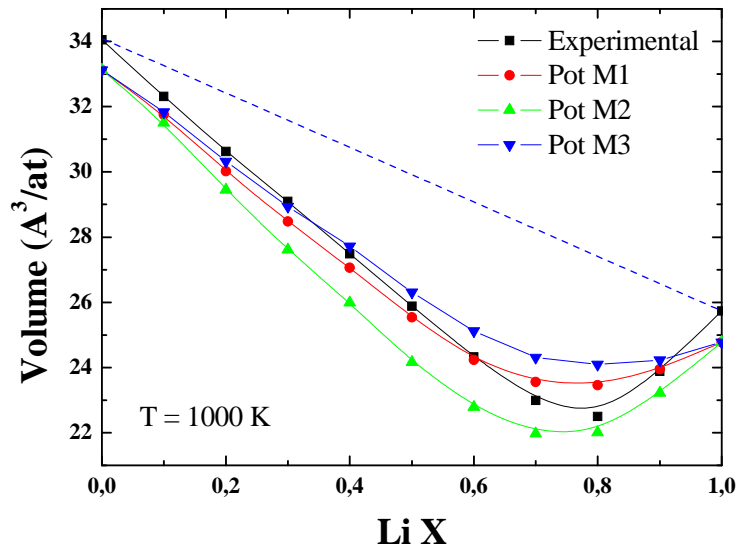


Fig. 5.38. Volume contraction in liquid LiPb system. The system departs from ideal behavior (blue line). Experimental data from (Saar 1987). MD values calculated with three different potentials M1, M2 and M3 as labelled.

5.2.6 Heat capacity

If we move to thermodynamics, another important deviation from ideal solution is observed in the heat capacity, C_p , (Saar 1987). In next figure we present our C_p results compared to the experimental data reported in (Saar 1987). Surprisingly, our interatomic potential gives a different C_p result depending on the Li concentration, and the dependence with concentration resembles the experimental curve. A positive excess heat capacity is a hint of positive SRO, i.e. homo-coordination. However, in our MD simulations the mixtures are almost random distributions, with SRO values close to zero independently of the Li concentration (and increasing slightly at high Li concentrations, up to values around 0.1 for Pb atoms). Again, if we compare figures 5.39 and 5.10 the improvement is noticeable.

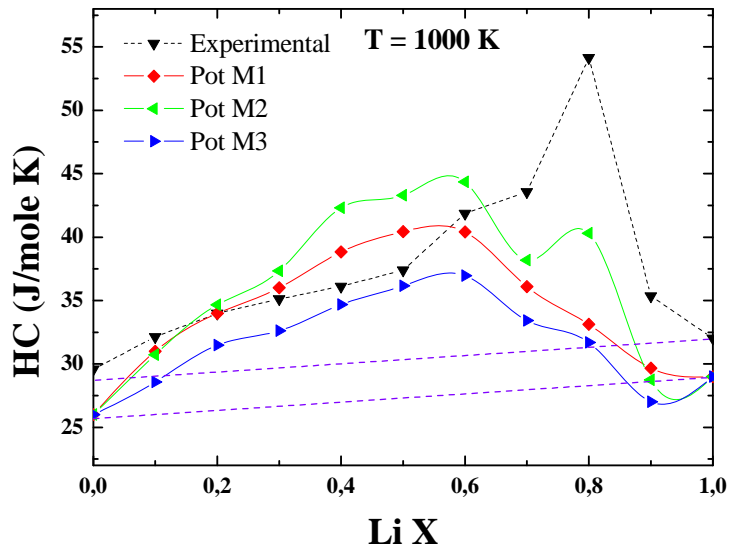


Fig. 5.39. Liquid LiPb alloys at 1000 K. Experimentally, C_p present a strong departure from ideality (violet dashed line). Remarkably the MD results also present similar behaviour.

5.2.7 Structure factors and neutron diffraction theory

Information on the microscopic dynamics of liquid metals can be obtained using acoustic spectroscopy and scattering experiments (Copley 1975, Scopigno 2005). The latter include inelastic X-ray scattering and inelastic neutron scattering.

Structural properties of higher Li concentration alloys are trickier. Next figure summarizes our MD results compared to available experimental results. It has to be noted that X-Ray scattering (red squares) and neutron scattering results (black squares in Fig 5.40) are clearly different. Our MD results both with EAM/cd potentials (red line) or EAM/alloy potentials (blue and green squares) are similar and resemble better the neutron scattering data. Again we can see how different potentials give very similar results regarding the structural properties, not only for low Li concentrations but also for intermediate Li concentrations (50 %).

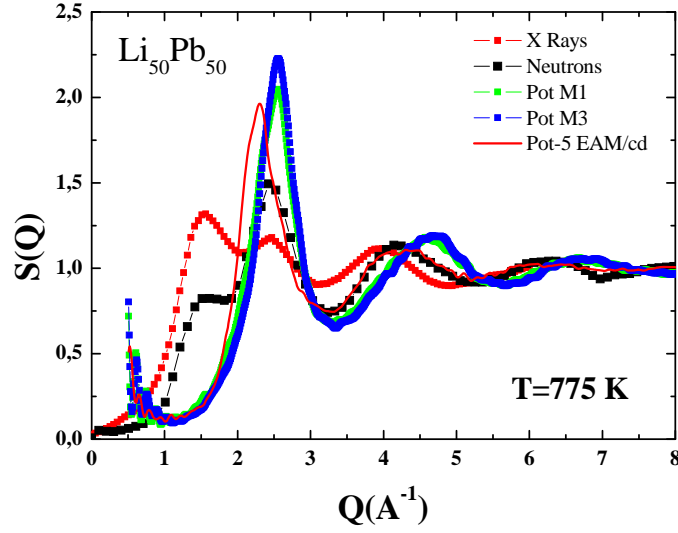


Fig. 5.40. Liquid total structure factor $S(Q)$ of $\text{Li}_{50}\text{Pb}_{50}$ at 775 K. X-Ray scattering (red squares) and neutron scattering results (black squares). MD results: EAM/cd pot.5 (red line) or EAM/alloy potentials (blue and green squares).

Let us pause here to mention some important result of neutron diffraction theory in order to understand the structural properties of metals and alloys. The total structure factor $S(q)$ of an alloy is related to three sets of partial structure factors: the Ashcroft-Langreth (Ashcroft 1967), the Faber-Ziman (Faber 1972) and the Bhatia-Thornton (Bhatia 1970) partial structure factors (referred as AL, FZ and BT hereinafter). The relations between them are given by Waseda's book (Waseda 1980). The total structure factor is related to the BT partial structure factors $S_{NN}(q)$, $S_{NC}(q)$ and $S_{CC}(q)$ by:

$$S(q) = w_{NN}S_{NN}(q) + w_{NC}S_{NC}(q) + w_{CC}S_{CC}(q) \quad (5.34)$$

where the weight factors are written versus the concentrations c_1 , c_2 and the neutron scattering lengths b_1 , b_2 by:

$$w_{NN} = \frac{(c_1b_1 + c_2b_2)^2}{c_1b_1^2 + c_2b_2^2}, \quad w_{NC} = \frac{2(c_1b_1 + c_2b_2)(b_1 - b_2)}{c_1b_1^2 + c_2b_2^2} \quad \text{and} \quad w_{CC} = \frac{(b_1 - b_2)^2}{c_1b_1^2 + c_2b_2^2} \quad (5.35)$$

Coherent and incoherent scattering cross sections (in barns) for pure Pb and Li (99.05% ${}^7\text{Li}$, 0.95% ${}^6\text{Li}$) are summarized in Table 5.VIII. The different cross sections are supposed to be k independent. Note that $b_1 = 11,11$ for Pb and $b_2 = 0,66$ for Li (Ruppertsberg 1975), then the weight factors for different concentrations are collected in Table 5.IX.

	b_{coh}	b_{incoh}	$b_c + b_i$
Pb	11,11	0,3	11,31
Li	0,66	0,8	1,46

Table 5.VIII. Coherent and incoherent scattering cross sections (in barns) for Pb and Li according to (Ruppertsberg 1975).

	$\text{Li}_{17}\text{Pb}_{83}$	$\text{Li}_{30}\text{Pb}_{70}$	$\text{Li}_{40}\text{Pb}_{60}$	$\text{Li}_{50}\text{Pb}_{50}$
w_{NN}	0,887	0,73499	0,64694	0,5592
w_{NC}	1,895	1,92617	1,9511	1,98593
w_{CC}	1,025	1,26197	1,47107	1,76321

Table 5.IX. Weight factors defined in Eq.s (5.34) for eutectic composition and some Li-Pb alloys using only the coherent cross sections given in Table 5.VIII.

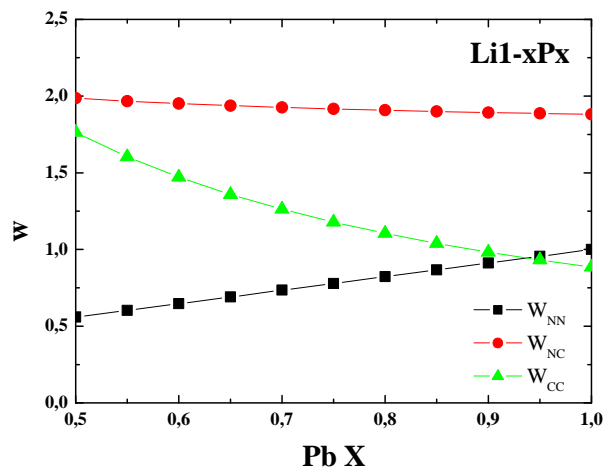


Fig. 5.41. Weight factors, w , in $\text{Li}_{1-x}\text{Pb}_x$ alloys vs Pb concentration, x , (right part of LiPb phase diagram).

The BT partial structure factors have each a clear physical meaning. The partial structure factors $S_{NN}(q)$, $S_{NC}(q)$ and $S_{CC}(q)$ indicate respectively the topological, the size and the chemical effects. They are expressed as functions of the FZ partial structure factors $a_{ij}(q)$ ($i, j = 1, 2$) by:

$$S_{NN}(q) = c_1^2 a_{11}(q) + 2c_1 c_2 a_{12}(q) + c_2^2 a_{22}(q) \quad (5.36)$$

$$S_{NC}(q) = c_1 c_2 (c_1 (a_{11}(q) - a_{12}(q)) - c_2 (a_{22}(q) - a_{12}(q))) \quad (5.37)$$

$$S_{CC}(q) = c_1 c_2 (1 + c_1 c_2 (a_{11}(q) + a_{22}(q) - 2a_{12}(q))) \quad (5.38)$$

The FZ partial structure factors, $a_{ij}(q)$, are connected to the partial pair correlation functions $g_{ij}(r)$ by:

$$g_{ij}(r) - 1 = h_{ij}(r) = \frac{1}{2\pi^2 \rho_0 r} \int_0^\infty q (a_{ij}(q) - 1) \sin(qr) dq \quad (5.39)$$

where ρ_0 is the average number density.

In case of heterocoordination, the chemical effect appears in the partial structure factors $a_{11}(q)$ and $a_{22}(q)$ by a positive prepeak and by a negative prepeak in $a_{12}(q)$. The prepeaks cancel in $S_{NN}(q)$ and in $S_{NC}(q)$ but are magnified in $S_{CC}(q)$. If the two species have very close sizes in the alloy then $S_{NC}(q)$ may be approximately zero. If the size of the components ions do not change in the alloy then it is possible to replace $S_{NN}(q)$ by a linear combination of the structure factors $S_1(q)$ and $S_2(q)$ of the two pure metals:

$$S_{NN}(q) \approx c_1 S_1(q) + c_2 S_2(q) \quad (5.40)$$

These different assumptions lead to consider that the chemical effect appears mainly in the partial structure factor $S_{CC}(q)$. The Fourier transform of $S_{12}(q)/(c_1 c_2)$ is given by:

$$\frac{1}{2\pi^2 \rho_0 r c_1 c_2} \int_0^\infty q \left(\frac{S_{CC}(q)}{c_1 c_2} - 1 \right) \sin(qr) dq = g_{11}(r) + g_{22}(r) - 2g_{12}(r) = \frac{g_{CC}(r)}{(c_1 c_2)^2} \quad (5.41)$$

The quantity $g_{11}(r) + g_{22}(r) - 2g_{12}(r)$ is linked to the difference between the homo-coordination, characterized by $g_{11}(r) + g_{22}(r)$ and the hetero-coordination characterized by $2g_{12}(r)$ and indicates the nature of the chemical order in the first nearest neighbours shell.

Bhatia and Thornton (Bhatia 1970) define for a binary system an alternative set of partial structure factors, $S_{NN}(q)$, $S_{CC}(q)$ and $S_{NC}(q)$, describing, respectively, the distributions of atomic number density, of concentration and the correlation between the two. The measured total interference function $F(q)$ can be expressed in terms of Bhatia–Thornton (BT) partial structure factors as

$$F(q) = \langle b \rangle^2 S_{NN}(q) + [\bar{b}_1 - \bar{b}_2]^2 S_{CC}(q) + [\langle b \rangle (\bar{b}_1^* - \bar{b}_2^*) + \langle b \rangle^* (\bar{b}_1 - \bar{b}_2)] S_{NC}(q) - (c_1 \bar{b}_1^2 - c_2 \bar{b}_2^2) \quad (5.42)$$

where c_1 and c_2 are the atomic concentrations and $\langle b \rangle = c_1 \bar{b}_1 - c_2 \bar{b}_2$ $\langle b \rangle = c_1 b_1 + c_2 b_2$ is the overall average scattering length. Fourier transformation leads to the BT partial pair-distribution functions $g_{NN}(r)$, $g_{CC}(r)$ and $g_{NC}(r)$.

The BT and FZ formalisms are connected by simple linear combinations involving only the concentrations c_1 and c_2 of the two species (e.g. Cusack (1987)):

$$\begin{aligned} S_{NN}(q) &= c_1^2 S_{11}(q) + 2c_1 c_2 S_{12}(q) + c_2^2 S_{22}(q) \\ S_{CC}(q) &= c_1 c_2 (1 + c_1 c_2 (S_{11}(q) + S_{22}(q) - 2S_{12}(q))) \\ S_{NC}(q) &= c_1 c_2 (c_1 (S_{11}(q) - S_{12}(q)) - c_2 (S_{22}(q) - S_{12}(q))) \end{aligned} \quad (5.43)$$

where the coefficients differ slightly from those for the r-space functions:

$$\begin{aligned}
 g_{NN}(r) &= c_1^2 g_{11}(r) + 2c_1 c_2 g_{12}(r) + c_2^2 g_{22}(r) \\
 g_{CC}(r) &= c_1 c_2 (g_{11}(r) + g_{22}(r) - 2g_{12}(r)) \\
 g_{NC}(r) &= c_1 (g_{11}(r) - g_{12}(r)) - c_2 (g_{22}(r) - g_{12}(r))
 \end{aligned}
 \tag{5.44}$$

The number–number partial structure factor, $S_{NN}(q)$, concerns the sites of all the scattering nuclei without regard to the chemical species decorating those sites and therefore represents the ‘colour-blind’ scattering cross-section, i.e. $S_{NN}(q)$ would be measured directly if both chemical species had the same average (i.e. coherent) scattering length. The concentration-concentration partial structure factor, $S_{CC}(q)$, describes the ordering of the two chemical species with respect to the sites specified by $S_{NN}(q)$. When there is a preference for like or unlike neighbours at a given distance, corresponding positive or negative peaks will appear in $g_{CC}(r)$, respectively.

For an ideal (solid or liquid) solution, in which the two chemical species mix randomly without volume change or heat of mixing, all three FZ partial structure factors are equal and hence $S_{CC}(q) = c_1 c_2$, i.e. constant. Conversely, any q-dependence in $S_{CC}(q)$ indicates non-ideal substitution between the two species. Note that if the sample is a ‘zero alloy’, having $\langle b \rangle = 0$, then $S_{CC}(q)$ is measured directly in a diffraction experiment. The real-space counterpart of $S_{NC}(q)$, namely $g_{NC}(r)$, describes the correlation between sites and their occupancy by a given chemical species. If the sample is an ideal solution then there is no correlation between site and chemical species, so that $S_{NC}(q) = 0$ and therefore all q-dependence in $F(q)$ (and hence all structural information) is contained in $S_{NN}(q)$.

5.2.8 $\text{Li}_{50}\text{Pb}_{50}$ $S(Q)$

Density of LiPb alloys in the right part of phase diagram is correctly described by our interatomic potentials (see volume vs Li concentration in Figure 5.38). Why is the total structure factor $S(q)$ so different from the experimental one?

The number–number partial structure factor, $S_{NN}(q)$, defined in Eq. (5.36) concerns the sites of all the scattering nuclei without regard to the chemical species decorating those sites and therefore represents the ‘colour-blind’ scattering cross-section, i.e. $S_{NN}(q)$ would be measured directly if both chemical species had the same average (i.e. coherent) scattering length. But coherent scattering cross sections for lead and lithium (99.05 % ^7Li , 0.95 % ^6Li) are very different, $\sigma_{\text{Pb}} = 11,11 \text{ b}$ and $\sigma_{\text{Li}} = 0,66 \text{ b}$ respectively (Ruppertsberg 1975).

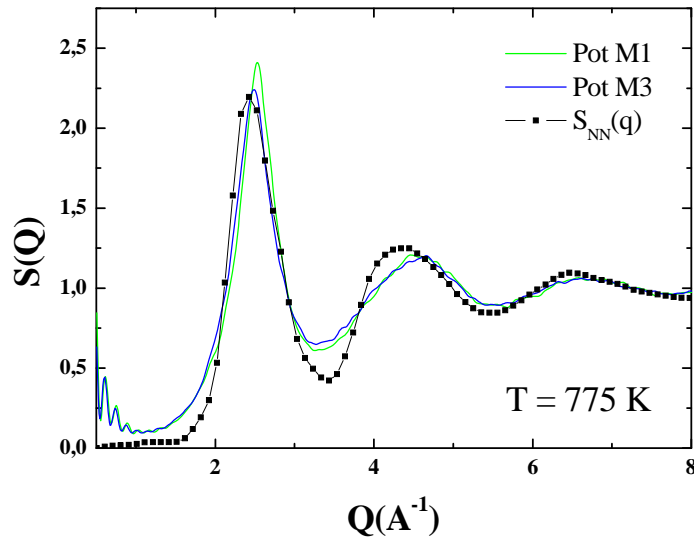


Fig. 5.42. Total structure factor, $S(q)$, of $\text{Li}_{50}\text{Pb}_{50}$ alloys at **775 K** calculated from MD simulations (green and blue lines (pot M1 and Pot M3)) compared to $S_{NN}(q)$ taken from (Ruppertsberg 1982).

Generally speaking, $S_{NN}(q)$ describes the distance correlation between particle-density fluctuations and is normalised to modulate about one.

$S_{NC}(q)$ is related to the corresponding correlation between particle-density and concentration fluctuations. It modulates about zero and becomes identical to zero for equal global surroundings of particles 1 and 2. This corresponds to the case of a strictly substitutional alloy ('Keating case' for liquids) of equal-size atoms which in addition have to perform thermal vibrations of the same amplitude. An experiment for which $\langle b \rangle = c_1 b_1 + c_2 b_2 = 0$ yields $S_{CC}(q)$ directly because the terms S_{NN} and S_{NC} in equation (1) vanish. This happens for the neutron diffraction pattern of Li_4Pb prepared from the isotope ^7Li and natural lead. $S_{CC}(q)$ describes the correlation between concentration fluctuations. It oscillates about $c_1 c_2$ and becomes identical to $c_1 c_2$ for strictly substitutional alloys if the atoms 1 and 2 are distributed at random.

Next figure show the $\text{Li}_{50}\text{Pb}_{50}$ $S(q)$ at **775 K** calculated from MD simulations with Pot M1 and Pot M3 compared to theoretical hard-sphere curve with hard-sphere diameter $\sigma = 2.8 \text{ \AA}$ and packing fraction $\eta = 0.43$ (Ruppersberg 1982).

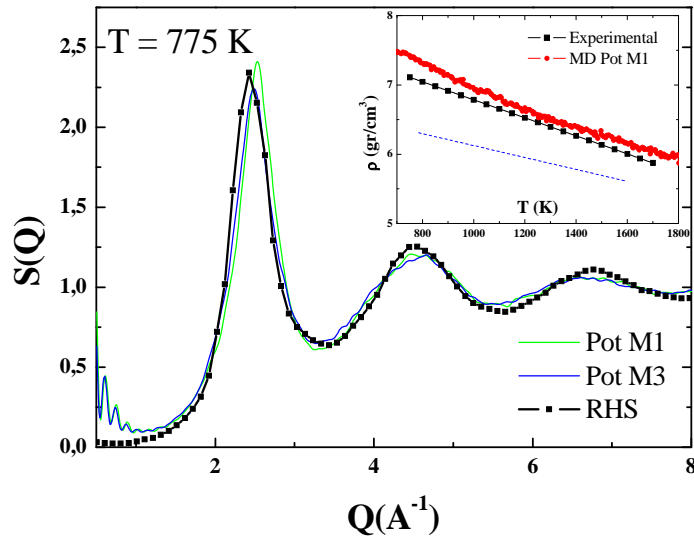


Fig. 5.43. $S(q)$ of $\text{Li}_{50}\text{Pb}_{50}$ alloys at 775 K calculated from MD simulations green and blue lines (Pot M1 and Pot M3) compared to theoretical hard-sphere curve (Ruppersberg 1982). **Inset** shows liquid $\text{Li}_{50}\text{Pb}_{50}$ density vs T . Red squares represent the values obtained with MD. Black squares are the experimental values (Ruppersberg 1976). Blue dashed line stands for the results shown in Fig. 5.15.

Liquid Pb structure is “hard-sphere like” according to (Waseda 1980), thus LiPb system seems to be governed by, Pb, the heaviest atom ($m_{\text{Pb}} \sim 30m_{\text{Li}}$) when Li concentration is low (eutectic for example) and up to 50 % of Li concentration, presenting a HS structure. This is not surprising since even in the 50-50 concentration Li represents less than 4 % of the total mass. In next figure the total pair distribution functions is shown. As can be seen the curves change little up to Li concentrations around 30 or 40 % with both potentials, the old EAM/cd version (Pot-5) and our best EAM/alloy potential, Pot M1. With the first one the first peak broadens and shift x-position towards lower radius decreasing height as well. With Pot M1 the x-positions (r_1 and r_2) moves to the left but the shape of the curve remains almost invariant.

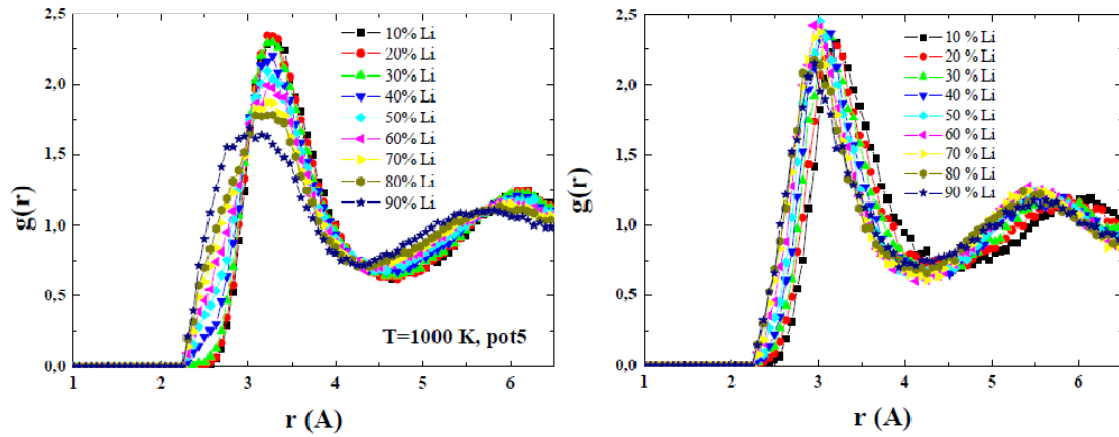


Fig 5.44. Total pair distribution functions of liquid LiPb alloys ($T = 1000$ K) as labelled. Left) results with EAM/cd Pot-5. Right) Results with Potential M1.

5.2.9 SRO Analysis

It is important to mention that EAM potentials present some limitations. For example charge transfer is simply neglected in this kind of potentials (both EAM/cd or EAM/ally). And charge transfer will be important when we are dealing with alloys of two different metals like Li and Pb having so different chemical properties. One just has to look at the electronegativity as mentioned in Chapter 2. To illustrate this fact, next figure show the density charge according to *ab initio* calculations (Senda 2000).

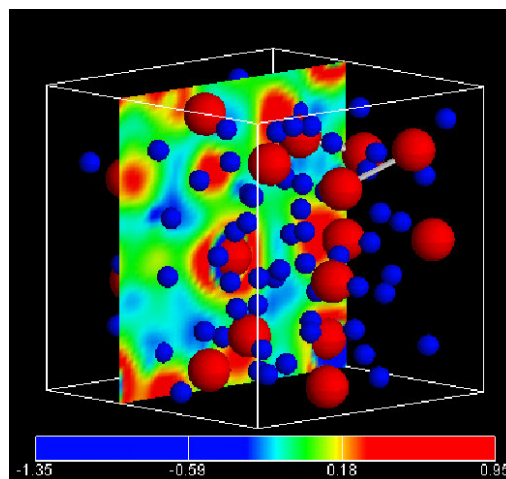


Fig. 5.45. The difference of the electron-density distribution for the ionic configuration of the liquid $\text{Li}_{80}\text{Pb}_{20}$ alloy from the linear combination of the atomic valence-electron-density distribution. The Li and Pb ions are drawn as blue and red balls, respectively (Senda 2000).

Another evidence of negative SRO is the departure of eutectic viscosity from linear interpolation of Li and Pb viscosities; $\eta < \eta_{id}$ as can be seen in Fig. 2.4 (Chapter 2).

If we calculate the ordering potential as defined in (Pasturel 1985)

$$\phi_{CC}(r) = c_1 c_2 (\phi_{11}(r) + \phi_{22}(r) - 2\phi_{12}(r)) \quad (5.45)$$

where 11 stands for Pb-Pb, 22 for Li-Li and 12 for Li-Pb interactions, then the ordering potential is deeper for the 50-50 concentration (see Fig. 5.46). This fact suggests that SRO will present a maximum at this concentration that is roughly what we observe in figure 5.34.

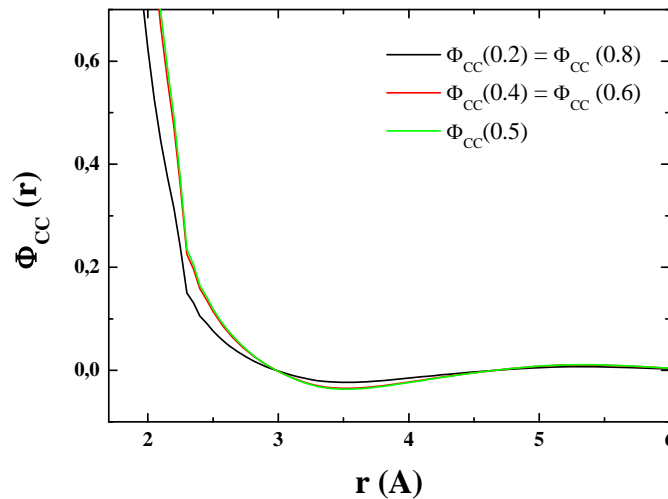


Fig. 5.46. Ordering potential, ϕ_{CC} , is symmetric by definition \rightarrow SRO will be also symmetric!?

To further understand the SRO properties of LiPb system we tempted to use EIM (embedded ion method) potentials as tool to calculate trends on SRO depending on the difference on electronegativity (Zhou 2011). With those potentials SRO is negative for example in liquid LiF, however those potentials for alkaline salts in general are not good enough to describe the properties of single elements like Li in solid or liquid phase.

5.2.10 Eutectic point

Many questions remain unclear around eutectics (Kalashnikov 1997). Here we shortly present some ideas in order to determine the eutectic concentration according to our MD simulations. To that end we have simulated 6 different eutectic LiPb systems, with concentrations ranging from 14% to 19% in liquid phase, (temperatures ranging from 800 K to 1600 K). Cell size was 13500 atoms in total and the final configuration was in equilibrium (after 50 ps). To summarize we can see that SRO decreases when lithium content increases and there is no clear evidence of some anomaly in this trend around eutectic point.

As was advanced in Chapter 4, Wendt Abraham and translational parameters (see definitions in Section 4.6) could be used in our study of the determination of the eutectic in the LiPb phase diagram. However there is no clear maximum or minimum signalling the eutectic point (Fraile A. *et al.*, to be published).

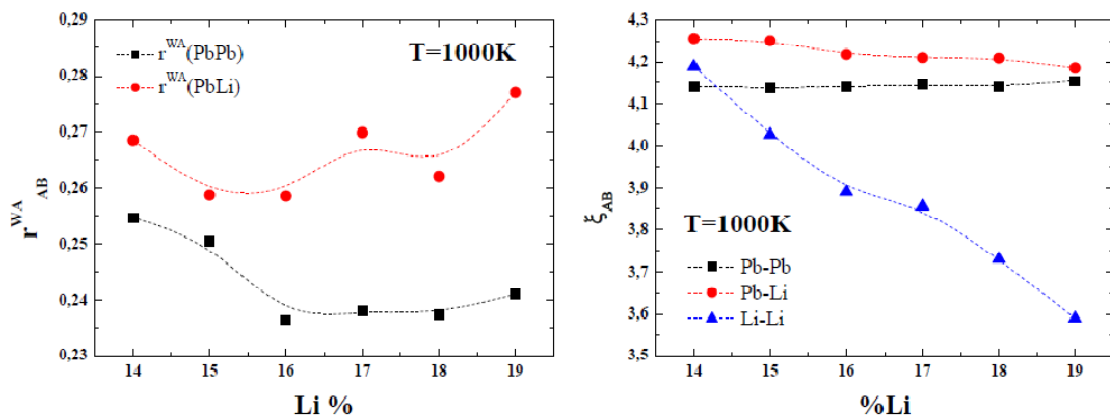


Fig 5.47. Left) Partial, Wendt–Abraham Parameter, r_{AB}^{WA} , for LiPb alloys close to the eutectic point at T=1000 K. Right) Partial translational parameter, ζ , for LiPb alloys close to the eutectic point at 1000K.

We studied the ratio between kinetic energy and potential energy, KE/PE, for all the mentioned alloys and there is not clear difference between them as can be seen in figure 5.48 (Left). That ratio gives an idea of the disordering velocity of the system. As one more example we defined the critical temperature, T_c , of our system as that temperature where SRO equals zero (SRO tends to 0 when T increases). Then, if we represent that T_c vs Li concentration again, a minimum seems to appear around 17% of Li. See right part of next figure.

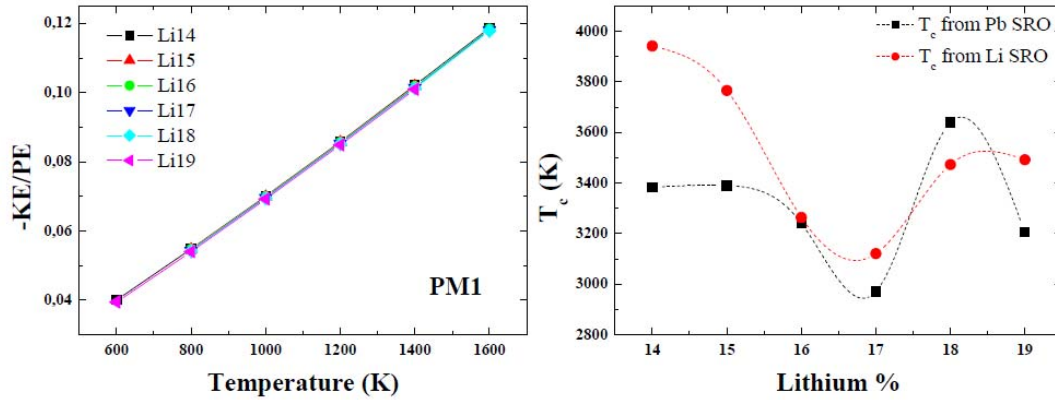


Fig 5.48. Left) KE/PE ratio for six different LiPb eutectics vs temperature. Right) Critical temperature vs Li concentration calculated from Li and Pb SRO in the melt.

Many other properties could be studied in detail around the eutectic concentration as Li diffusivity, SRO etcetc. However it has to be noted that some results can be potential dependent.

5.2.11 Phase Diagram

Now, to finish this Chapter we discuss our results regarding the phase diagram. Our EAM/alloy potential has been created to give the correct thermodynamic properties of $\text{Li}_{50}\text{Pb}_{50}$ system. Indeed, the melting point calculated after careful determination of the free energies as described in Chapter 4 gives an acceptable value for the melting point. The results are shown in Fig 5.49. Melting point predicted by this calculation is 720 ± 25 K while the experimental melting point is 755 K. Free energies of the disordered LiPb compounds for $\text{Li} < 50\%$ has been calculated, as well as the free energies of solid and liquid fcc-Pb+Li with Li concentration ranging from 1 to 5%. The common tangent method will be applied (Christian 1965, Atkins 1990). However, the problem is complex and a detailed understanding of SRO in the liquid will be needed in order to construct the phase diagram. For this reason the work is still under progress.

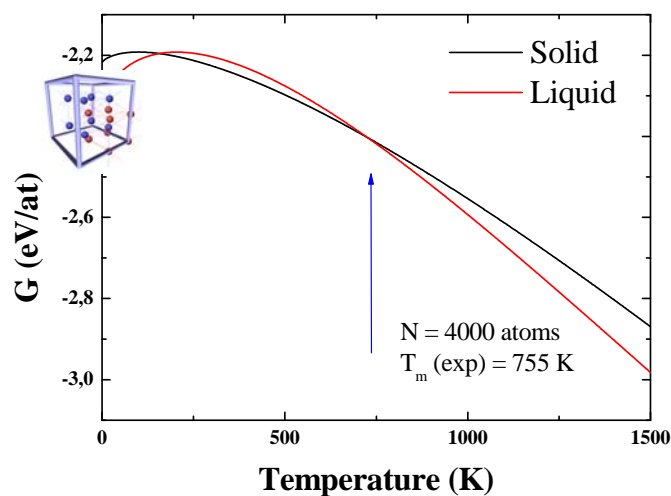


Fig 5.49. $\text{Li}_{50}\text{Pb}_{50}$ (B2) free energies calculated with potential M1: Melting point is very close to the experimental value, MD = 720, Exp 755 K.

The calculation of phase diagram is currently under construction and discussion. Figure 5.50 shows a simple estimation based on enthalpy/volume jump. Interestingly for low Li concentrations we observe a clear decrease in the melting temperature, as expected. Main results shown in this Chapter will be published in a forthcoming paper (Fraile 2013).

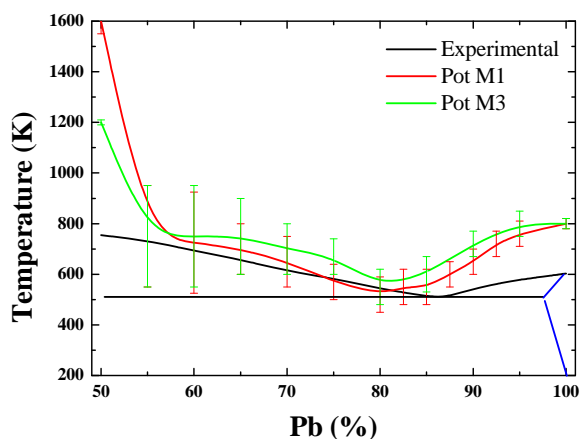


Fig 5.50. Pb-rich part of LiPb phase diagram; Red and green lines represent a simple the estimation from MD heating cycles. Black lines represent the experimental phase diagram according to (Okamoto 1993).

Other methods like to determine melting like two-phase coexistence (Ladd 1977 1978, Alfè 2002) are being explored. A comparison review of different methods using MD can be found in (Zhang 2012).

5.3 Conclusions

In summary we have developed a new LiPb interatomic potential. Our MD simulations gave good match of many structural, thermodynamic and dynamic properties around the eutectic concentration. This is not so difficult to accomplish and different potentials can lead to very similar structural properties but different thermodynamic ones so a careful examination of different physical properties is mandatory.

Higher Li concentrations showed more difficult to describe by a simple EAM/alloy potential due to possible charge transfer between Li and Pb ions. The difference observed between calculated structural properties compared with experiments can be explained in terms of the Batia-Thorton theory. The main results described in this chapter will be submitted to Phys. Rev. B.

A realistic interatomic potential like the proposed one would be useful to simulate several problems of scientific and technological interest like solidification process and the study of cooling ratio effect in the solid structure of the alloy, determination of the optimal composition for eutectic behavior etc.

Introduction of a third kind of atom (He and/or H) in the system is being studied. This, for example, will permit to study the solubility of tritium (or helium) in LiPb eutectic alloy *in silico*.

Chapter 6

Hydrogen in liquid metals

Although the study of hydrogen in metals dates back over a century (Graham 1866, Fukai 1985, 1989), our understanding of these systems is not fully satisfactory. The studies on the interplay of all possible mechanisms of mass transport at the interface of liquid metal-gas systems are of a topical interest, from a scientific and a technological point of view. Here we present hydrogen diffusivity calculations in three different H-metal systems, namely Pd-H, Ni-H and Al-H, by means of classical molecular dynamics simulation (CMD). Four different interatomic potentials are used but no important differences in the general trends are observed. We compare the hydrogen diffusivity values with available experimental data when possible and, as a rule, our MD calculations are at least one order of magnitude below the experimental value. Some explanations are discussed in the frame of diffusion theories in liquids.

Interest in understanding the physics of hydrogen in metals and alloys has been continuously increasing for many reasons. On one side there are the practical uses of metal-hydrogen systems such as: storage of hydrogen for clean energy purposes, catalyzers, or absorption of nuclear radiation.

On the other, there are unwanted effects on the materials properties caused by small amounts of H dissolved in metals, such as embrittlement, crack propagation, and corrosion. There is extensive literature dealing with these issues, ranging from first-principles calculations to engineering applications (see for example, (Fukai 1985, 1989). It is well known that H induces embrittlement in metals such as Fe, Al alloys and intermetallic compounds (Hirth 1980, Albrecht 1979). As explained in Chapter 2, diffusion of hydrogen is also important in plasma facing materials (PFM).

The diffusional properties of hydrogen interstitials in metals are unique for several reasons. They are influenced, or even controlled by, quantum and tunneling effects since H is the lightest

of all elements. The fact that H has the highest possible isotopic mass ratios of all elements leads further to large - and experimentally well observable - isotope effects in diffusion.

The importance of H diffusion in liquid metals is important for many technological reasons. Hydrogen has high solubility in most liquid metals, which can usually induce defects in the solidified metal as porosity, property reduction structure (e.g. hydrogen brittleness), etc. (Fukai 1985, 1989, Jong 2011) Recently, the high solubility of hydrogen is being used positively to produce an ordered porous new material called GASAR (Karpov 2007), (see figure 6.1).

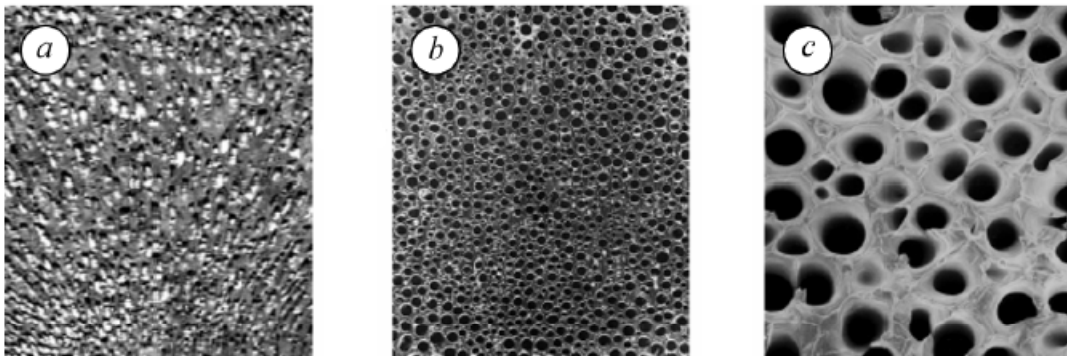


Fig. 6.1. Taken from Ref. (Karpov 2007). Structures of gasars: (a) longitudinal section, (b) transverse section ($\times 5$), (c) image in the scanning electron microscope ($\times 20$).

And, as we know (see Chapter 2), also liquid metals are envisaged as good candidates for breeder modules in future nuclear reactors (T production), being Li17Pb one of the most promising candidates because of its low chemical activity and good breeding ratio (Edao 2011).

In a recent paper the diffusion mechanism of H in Li-Pb is proposed (Masuyama 2009). The authors claim that hydrogen in liquid lithium-lead seems to be stabilized near Li atoms by the binding interaction of Li-H. After breaking the interaction at a certain moment, hydrogen moves into the cloud of Pb atoms and migrates for a short time; subsequently, it binds to another or the same Li atom. However, *ab initio* simulation presents several difficulties to understand a dynamics process as H diffusivity. Simulation time has to be long and size effects in the small cells generally used in *ab initio* simulations could be important. Hydrogen diffusivity is not reported (Masuyama 2009). Also important, according to (Jiang 2011) the electronic structure of liquid metal dominates the H solubility; the larger the effective charge density of the metal, the higher the hydrogen solubility.

6.1 Computational details

In this chapter we will make use of three different interatomic potentials for H-metal system. First we will use the EAM/alloy potential for Pd-H developed by Zhou and co-workers (Zhou 2008) and the EAM/alloy potential for Al-Ni-H developed by (Angelo 1995). Secondly we will calculate hydrogen diffusion in liquid aluminium using the more advanced angular dependent potential proposed by Apostol and Mishin (Apostol 2010). Our goal is not to judge that any particular potential is "the best" because the best interatomic potential may depend on the problem being considered. Details about EAM formalism can be found elsewhere (Baskes 1988, 1992, Foiles 1989) and also in Chapters 3 and 4.

Molecular dynamics computer simulation method, based on n-body interatomic potentials, has become an established tool in materials science to evaluate many properties. Most of the EAM potentials were originally proposed for solid-state calculations, however these potentials have been shown to predict the thermodynamic properties of liquids Au and Ag fairly accurately (Bogicevic 1997) and in our recent work also of Li and Pb (Fraile 2013).

Details of the molecular dynamics technique can be found elsewhere (Frenkel 1996). First, we melted an fcc (both Pd, Ni and Al are fcc in normal conditions) structure to obtain an initial configuration (i.e., the positions and velocities of the particles) at the chosen pressure P and temperature T , and performed a canonical MD simulation using the Nosé-Hoover constant-temperature technique (Martyna 1992). See Chapter 3 and references therein for details about thermostats etc.

The constant-pressure MD simulations tend to overestimate the values of self-diffusion constants due to large density fluctuation (Hakkinen 1989). However we did not find important differences in NPT and NVE runs when the sample is big enough and simulation times are large. (Fluctuations in density are in all cases less than 1% of the average value).

In simulating hydrogen in transition metals like nickel, palladium and/or aluminum, one is faced with two questions: (i) can one find adequate potentials? (ii) are quantum effects important?. Most of MD simulations available in the literature deal with H embrittlement, (swelling, blistering, flaking etc) in metals (Jong 2011). Very little simulation work has been done on

hydrogen in liquid metals... The same holds for experimental results. Most work has been done in solid metals (Cao 1997) while little work is published on liquid metals.

The question of quantum effects is trickier, because there is at present no simple and reliable way of estimating quantum corrections to dynamical quantities such as the diffusion in liquids. However, since the vibrational frequency of hydrogen in palladium is about 16 THz (Drexel 1976) (13.5 according to (Dhawan 1981)) and around 18 for nickel and 23 for aluminum, (see Table III in (Dhawan 1981)), which corresponds to a temperature of about 750 K, and since we shall be mainly interested in temperatures above melting point (> 1800 K for Pd and > 900 K for Al), we expect that quantum effects will be of minor, though probably not negligible, importance. One expects quantum effects to be dominant when the temperature T is low compared with these values (Wimmer 2008). For example, quantum corrections for the diffusion of H in solid Al between 650 and 850 K by using Wigner and Eckart tunneling methods have been studied in a recent paper [EPAPS web]. It is estimated that the omission of tunneling effects introduces insignificant (less than 2 %) errors to the computed lattice diffusivity of H in the considered range of T . Therefore, should we believe that quantum effect will be negligible in the liquid phase?

	θ_D (K)	$\hbar\omega_H$ (eV)	$\hbar\omega_H/K_B$ (K)	E_a (eV)	E_a+E_S (exp) (eV)
Al	428	0.097	1125.6	0.073	0.26
Ni	450	0.075	870.3	0.112	0.409
Pd	275	0.056	649.8	0.05	0.52

Table 6.I. Some parameters used in this study. Debye temperature, vibrational frequencies of H-M system and activation energies taken from (Dhawan 1981).

We will test three different potentials in order to gain some insight about the differences in H behavior depending on the model. First we have computed the Hydrogen diffusivity in liquid palladium using the EAM potential developed by (Zhou 2008). In second place we repeat the same calculation for hydrogen dissolved in nickel and aluminum using the potential described in (Angello 1995). And finally we repeat H-Al calculations making use of the most advanced EAM/ADP potential (Apostol 2010). In Appendix A-B-C we report some previous benchmarks in order to asset the availability of these potentials to simulate the liquid melts.

It is known since 1866 that Pd can absorb large amounts of H (Graham 1866). In fact the ability of absorbing hydrogen is common in all metals although metals differ on how much hydrogen can be absorbed in a given situation. The hydrogen diffusion coefficient in solid metallic amorphous alloys is dependent on concentration, because of the presence of structural sites possessing different levels of potential energy for H localization and diffusion (Birnbaum 1972). In liquids we will have not these structural sites so diffusion is expected to be less concentration dependent (always concentrations of H are small).

6.2 Results

In figure 6.2 we show the calculated values of Pd self diffusivity and H diffusivity between T_m (1850 K) and 2750 K. The blue line represents the expected H diffusivity estimated by simple kinetic considerations.

$$\frac{D_A}{D_B} = \left(\frac{m_B}{m_A} \right)^{1/2} \quad (6.1)$$

Is to say, the diffusion of H would be just as $D_H = D_M \sqrt{m_M}$ where m_M stands for the mass of the host metal.

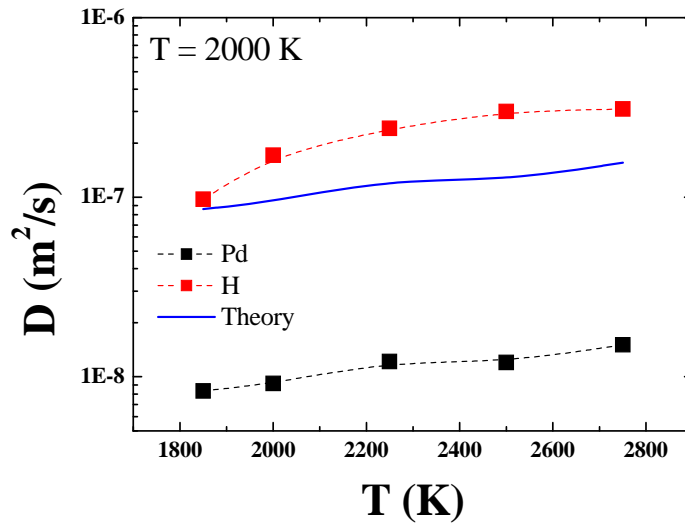


Fig. 6.2. Diffusivity values for H in Pd compared with host metal self-diffusivity (black squares). H diffusivity (red triangles) is close to the calculated (blue) following Eq. 6.1.

Figure 6.3 shows the calculated values of Ni self diffusivity and H diffusivity between T_m (1728 K) and 2750 K. Here H data are somewhere larger than the predicted by our simple model. However experimental data (reported in (Sacris 1970)) shows that our MD results are well below the measured ones.

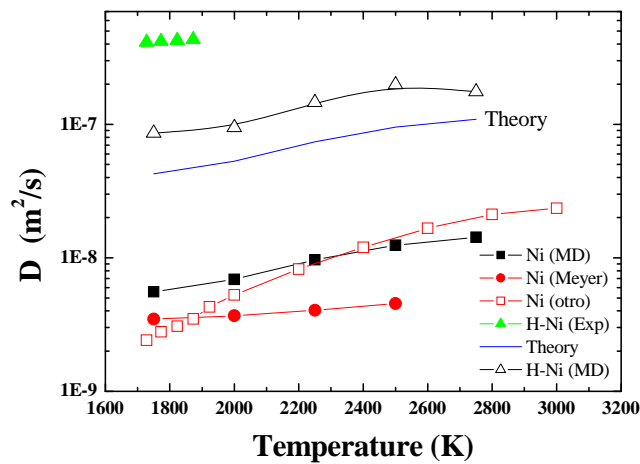


Fig. 6.3. Diffusivity values for H in Ni compared with host metal self-diffusivity (black squares). H diffusivity (black triangles) is close to the calculated (blue = Eq 6.1). Green triangles represent the experimental data (Sacris 1970).

Figure 6.4 shows the calculated values of Al self diffusivity and H diffusivity between T_m (980 K) and 2000 K. Here H data (with two different potentials) lay almost exactly around the predicted by our simple model. However, again experimental values (Eichenauer 1974) are much higher (on order of magnitude!).

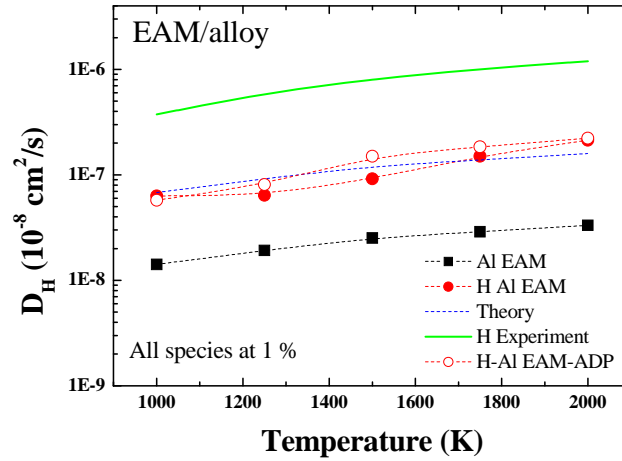


Fig. 6.4. Diffusivity values for H in Al compared with host metal self-diffusivity (black squares). H diffusivity (red circles) is very close to the calculated (blue). Green line represents the experimental data (Eichenauer 1974).

Isotope effects, simulated by changing just the mass of the particle gives approximately the expected relation $D_H(T) = D_D(T)/\sqrt{2} = D_T(T)/\sqrt{3}$. This simple result will lead our further analysis of H diffusivity in the melt.

6.4. Discussion

In a liquid metal, hydrogen (or any other light species) diffusivity will be governed by the collision frequency of the atoms forming the host metal. Therefore it is tempting to think that, in average, the final H diffusivity will depend little on the details of the H-Metal interaction, or if

concentration is low (as in our simulations), the H-H interactions. The simplest model to estimate the hydrogen D would be $D_H = D_M^* \sqrt{m_M}$, i.e, like in Eq. (6.1) considering H like an “isotope” of the studied metal. In next figure (fig. 12) we show how this idea, even if it is simple, is fairly accurate.

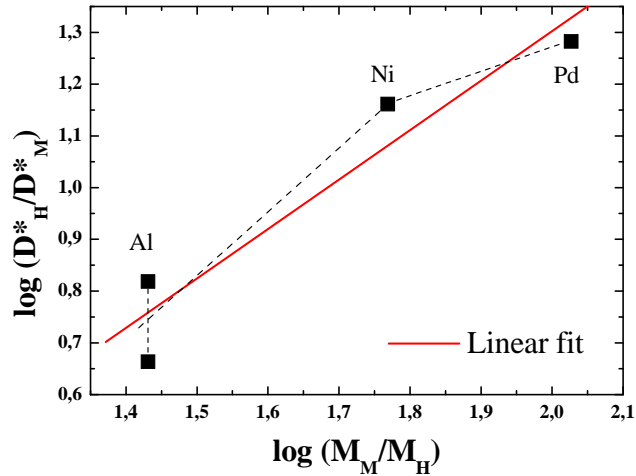


Fig. 6.5. log-log plot of hydrogen diffusivity values divided by the host metal self diffusivity vs the mass ratio m_M/m_H . The slope value is ~ 0.9 , and not ~ 0.1 as reported in (Bearman 1981).

To our best knowledge only hydrogen diffusion data is available for Al. Experimentally, hydrogen diffusion coefficient, (in m^2/s) is $D_{H-Al} = 3.8 \times 10^{-6} \exp(-2315/T)$ (Eichenauer 1974). i.e. one order of magnitude higher than our MD results.

We have found H diffusion values in liquid metals only for nickel, silver and copper (Sacris 1970). If we compare these values with the predicted taking into account the metal self diffusivity (experimentally determined or calculated by MD simulations) we can see that H diffusivity is around one order of magnitude higher than the predicted by this simple model.

It is a widely accepted viewpoint that the solved H in solid metals dissolves at the interstitial sites of the metallic crystal structure, and the solubility is determined by the radius ratio of the hydrogen atom to the metallic atom. The smaller the atom radius ratio, the higher the hydrogen solubility (Wagner 1971). However, according to the experimental results, the solubility of hydrogen in some liquid metals is low as in the zinc melt (Manchester 2000), although the

radius of H atom is much smaller than that of any metallic atom (Lange 1985). Hence, the atom radius effect might not be the determining factor in determining the H solubility in liquid metals. Aside from the atom radius effect, the electron interaction between hydrogen and metals is another important factor that should also be considered in the H solubility problem.

In a neat atomic fluid where the particle mass m_1 is changed to m_2 the pure mass effect on the self-diffusion coefficient D can be represented formally by the inverse square root law $D(m_2)=D(m_1)(m_2^*)^{-0.5}$ with the mass ratio $m^*_2= m_2/m_1$ (Hirschfelder 1964, Tyrrell 1984). A more realistic expression could be something like the developed by Thomaes and Itterbeek relating the mutual diffusivities in two binary systems with a common solvent (Thomaes 1959).

$$\frac{D_B}{D_A}(T) = \left(\frac{\varepsilon_{AB}}{\varepsilon_{AA}} \right)^{1/2} \left(\frac{r_{AB}}{r_{AA}} \right) \left(\frac{m_A}{m_B} \right)^{1/2} \quad (6.2)$$

Where ε_{AB} and ε_{AA} are effective interaction parameters of hydrogen and host metal respectively. And the distance parameter r_{AB} is taken as the arithmetic average of the pure component values: $r_{AB} = \frac{1}{2}(r_{AA} + r_{BB})$. The ratio of the apparent hard sphere radius for hydrogen to that for a metal atom in liquid metals can be assumed to be equal to the ratio of screening lengths.

Isenberg (Isenberg 1950) and others (Oriani 1967) have shown that hydrogen is believed to dissolve in metals (both in normal and transition metals) as a proton and an electron by giving up its electron to the collective electron gas of the metal. The positive charge of a proton, as for a metal ion, is subsequently screened by a local excess electron density. As proposed by Ziman, the screened metal ion and screened proton may be considered to be pseudoatoms if the radii are properly chosen.

The characteristic screening length for a metal ion (λ_M) is, in one simple form, given by the well known Thomas-Fermi approximation, (March 1968) *i.e.*,

$$\lambda_M = \frac{1}{2} a_0^{1/2} \left(\frac{\pi M}{3n_M N_0 d_M} \right)^{1/6} \quad (6.3)$$

where a_0 is the Bohr radius, M , d , and n_M are the atomic weight, density, and the number of valence electrons per atom, respectively, of the metal in question. Following Mott's theory

(Mott 1958) the screening length for a proton may be given by the same equation except that the difference between n of hydrogen ($n_H=1$) and the metal is substituted for n_M .

Normal and transition metal melts can be regarded as hard sphere fluids, and that a hard sphere corresponds to a screened neutral pseudoatom, the radius of which may be determined by a small multiple of the screening length. In order to evaluate, for Eq. 6.2, the ratio of the apparent hard sphere radius for hydrogen to that for a metal atom in liquid metals, it is assumed that this ratio is equal to the ratio of screening lengths. It is further assumed that the latter ratio is equal to the ratio of the minus one-sixth power of the effective number of s electrons per metal atom in the liquid (n_M) to the difference between n_M and the number of s electrons of hydrogen, namely one. Thus, the value of r/a_M in Eq. 6.2 is given by

$$\frac{a_H}{a_M} = \frac{2r}{a_M} - 1 = \frac{\lambda_H}{\lambda_M} = \left(\frac{n_M}{1 - n_M} \right)^{1/6} \quad (6.4)$$

For $n_M \neq 1$. For $n_M = 1$ a_H is taken to be equal to a_M .

	Z	M	r_{HS} (Å)	r_M/r_H (model)	r_M/r_H (Jiang)	r_M/r_H (Emi)	$\epsilon_{AB}/\epsilon_{AA}$
Pd	46	106.42	2.77	1.9	1	1	1 ± 0.2
Al	13	26.98	2.90	1.8	?	1	1 ± 0.2
Ni	28	58.7	2.53				

Table 6.II. Some parameters used in this study. $\epsilon_{AB}/\epsilon_{AA}$ is the hydrogen to metal atomic ratio of various typical hydride-forming metals. r_{HS} values from (Protopapas 1973)

To check the assumption we have modified “*ad hoc*” our Pd-H potential to calculate the change of diffusion this way. We multiply the Pd-H pair potential by an arbitrary constant, k , making deeper or shallower the potential. The effect can be better seen in figure 6.6. This way we can see how we can increase in a factor 2 the order of diffusivity of H in Pd just making the interaction less attractive. But the trend saturates around this value so seems not possible to achieve further improvement by this simple “one-constant”-method. It would be possible to change the shape of the H-Metal interaction making much more repulsive the pair potential, but it goes without saying that this would change other properties correctly described by the original potential.

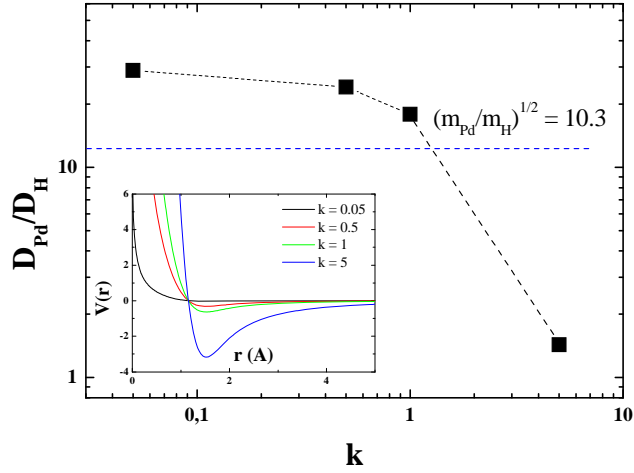


Fig. 6.6. Diffusivity values for H in Pd at $T = 2250$ K vs “screening” constant, k . Inset shows the pair potentials Pd-H (being $k = 1$ the original (Zhou 2008)).

According to some models (Jiang 2011) and (Emi 1970), as reflected in Table 6.II, some of the ratios r_M/r_H and $\epsilon_{AB}/\epsilon_{AA}$ in Eq. 6.2 are not far from unity so one could expect experimental results closer to the MD calculated ones that, as we have seen, are close to our simple model theory. Hence there is not simple explanation for the disagreement between MD and experiments.

6.5 Conclusions

H diffusion in liquid metals seems to be not as simple as a classical molecular dynamics study suggest. In an oversimplified point of view the main results point to some simple kinetic behavior of H diffusion, i.e. H diffusivity values are given by the host metal self diffusivity multiplied by some mass ratio factor.

Some questions arise. Can be quantum effects important in liquid metals? Can be quantum diffusion important at temperatures high above the Debye temperature of the host metal? H move like an isolated atom or is more likely some ionization-recombination behavior?

The diffusional properties of hydrogen in metals is likely to be influenced, or even controlled, by quantum and tunneling effects since hydrogen is the lightest of all elements. But the quantum effects seem to be really important at low temperatures, as shown in figure 6.7.

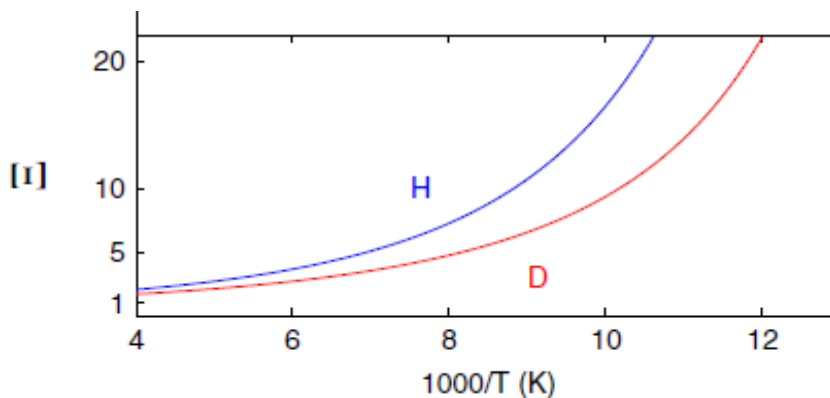


Fig. 6.7. Quantum effects dominate when Ξ is much larger than 1, but are important over the entire temperature range (Jardine 2010).

A fundamental limitation of classical molecular dynamics, of course, is that atoms actually obey quantum mechanical as opposed to classical equations of motion. Zero-point motion, quantum interferences, quantized energy levels, and tunneling are absent in classical MD. Unfortunately, a fully QM version of molecular dynamics for systems of many degrees of freedom is not likely to be practical in the near future, so classical mechanical molecular dynamics will continue to be the workhorse for many years to come.

This work continues in several ways. Some ab initio calculations of H-Al system are in progress but will be not presented in this Thesis. The main results were presented in the recent TNT 2012 (Trends on Nanotechnology International Congress) in Madrid, in an oral presentation.

Appendix A: Structure of liquid metals

Here we report some previous benchmarks in order to asset the availability of this potential to simulate the liquid M+H system.

First test any potential should pass to be considered reliable to simulate a liquid metal is to correctly describe the structure by mean of the pair distribution function (and/or its Fourier transform, the total structure factor). The average local structure around Pd atoms in liquid Pd at

1850 K, is represented by the pair distribution function, $g(r)$, and is compared, in Fig. 4 with our MD result. The liquid phase $g(r)$ (red circles) is in agreement with the diffraction measurements of liquid Pd performed by Waseda and Ohtani (Waseda 1975) (black line).

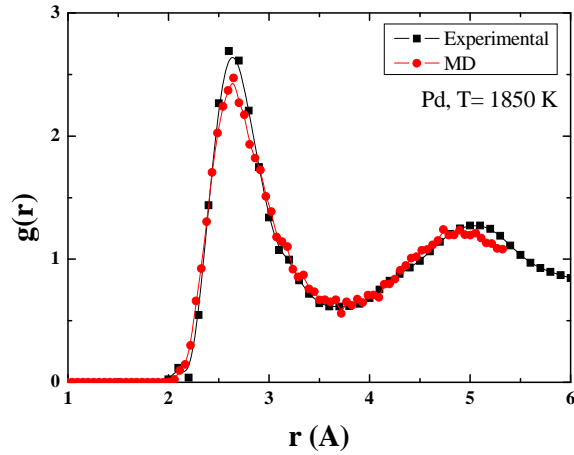


Fig. A1. Calculated pair distribution function of liquid Palladium ($T = 1850$ K) compared to the experimental data from (Waseda 1975).

We calculated the structural parameters through a series of isobaric-isothermal simulations at 1725 K and 2025 K. Figure A.2 shows our MD results compared to the available experimental data $g(r)$ curves.

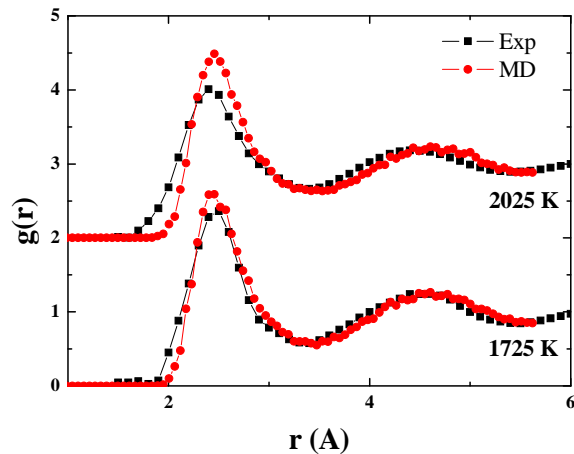


Fig. A2. Calculated pair distribution function of liquid Nickel at 1750 K and 2025 K compared to the experimental data from (Waseda 1975).

Examination of Fig.A3 shows that as the temperature increases, the peaks and valleys of the structure factor broaden, the peaks losing intensity and the valleys becoming shallower. This phenomenon is due to the increase in random thermal motion of the ions with temperature.

Following Waseda (Waseda 1975), liquid aluminum belongs to the simplest case of liquid metal; i.e. It presents a Hard-sphere-like structures with symmetric first peaks of both the static structure factor $S(q)$ and pair correlation function $g(r)$. In Figure A3 we can see that the ADP potential shows a better agreement with experimental curves at low temperature, but at high temperature (1300 K) the agreement seems to be better using the simple EAM potential.

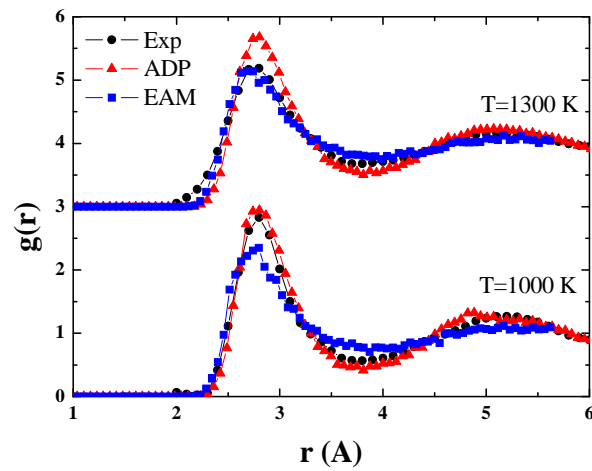


Fig. A3. Calculated pair distribution function of liquid aluminum (1000 K and 1300 K as labelled) compared to the experimental data from (Waseda 1975).

Structural properties of liquid Al has been checked twice by doing the calculation of $S(Q)$ in a similar way as explained in Chapter 4. As can be seen in next figure the ADP potential gives much better results if we compare with Waseda data. $S_1(Q)$ stands for the y-value of $S(Q)$ at the first peak.

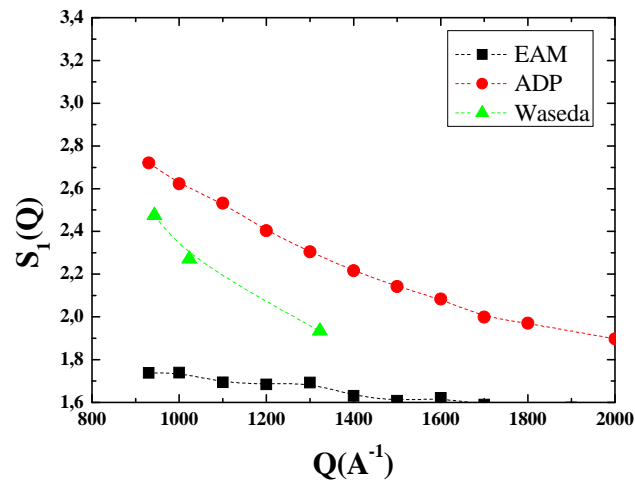


Fig A4: $S_1(Q)$ values calculated using MD simulation with two different potentials (EAM and ADP) compared with experimental results (Waseda 1975).

Also we can compare Al heat capacity from our MD simulations with experimental data from (Forsblom 2005). Simple EAM potential give results very similar to the calculated by Ercolessi et al (using a different EAM potential). The HC calculated with ADP potential is in a very good agreement with experimental results.

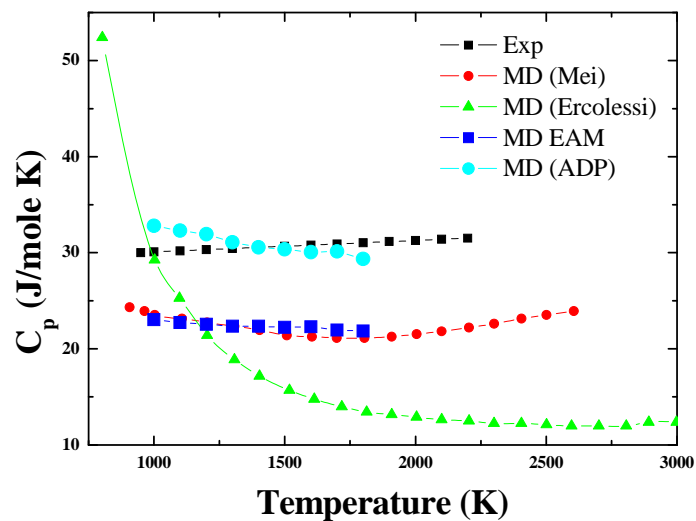


Fig A5: Heat capacity, C_p , values calculated using MD simulation with two different potentials (EAM and ADP) compared with experiment and other MD results from (Forsblom 2005).

Appendix B: Liquid metal diffusivities

We report here on the host metal self-diffusivities and compare, when possible, with experimental values. As far as we are concerned there are no available data on liquid palladium self diffusivity so we can only check our simulation by comparison of the MD results reported in (Ahmed, 2004). Red line represents the exponential fit. Fitting results are: $D_0 = 4.7 \times 10^{-8} \pm 1.1 \times 10^{-8} \text{ m}^2/\text{s}$ and $Q = 240 \pm 46 \text{ meV}$.

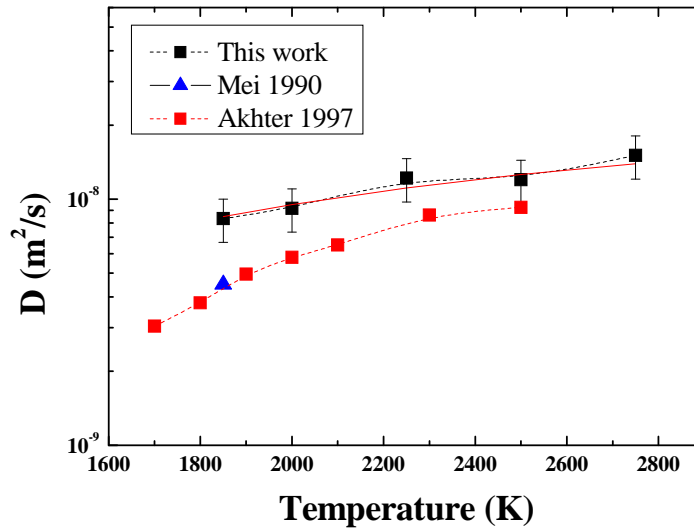


Fig. B1. Self diffusion of pure Pd compared to MD results (black squares). Blue triangle and red squares correspond to the MD results from (Ahmed 2004, Mei 1990).

Arrhenius diffusion parameters for each potential. The units of Q are meV and of D_0 are $10^{-5} \text{ cm}^2/\text{s}$. Our MD results are (T from 1750 to 2750 K) $D_0 = 84.5 \times 10^{-5} \text{ cm}^2/\text{s}$ (± 11) and $Q = 419$ (± 27) that agree well with the values reported in (Demmel 2011) using the same potential ($D_0 = 56.0 \text{ cm}^2/\text{s}$ and $Q = 364 \text{ meV}$ for T from 1750 to 2000 K). If we do the fit in the same range of temperatures then our results are $D_0 = 62 \times 10^{-5} \text{ cm}^2/\text{s}$ and $Q = 380 \text{ meV}$.

For liquid aluminum we can test our MD results with the recent neutron diffraction work of Demmel and co-workers (Demmel 2011). Both potentials give good results (see fig. B2) and interestingly the temperature dependence predicted by the ADP potential is almost identical to the reported experimentally.

The mentioned fits to an Arrhenius behavior are given as an example. However an Arrhenius temperature behavior of the diffusion coefficient is more an exception than a rule (Faber 1972, Nachtrieb 1976). *Still*, this form of representation is quite common and seems to be “the accepted law in most of the literature”. The use of the Arrhenius formula in liquid metals should have been abandoned long ago (Bogicevic 1997).

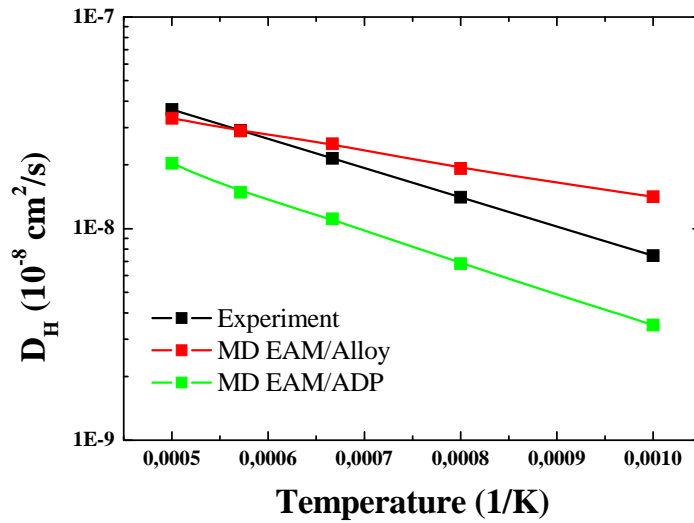


Fig. B2. Self diffusion of pure Al. Experimental data (black line) from recent neutron diffraction experiments (Demmel 2011). MD simulations (red and green symbols).

Self diffusion of pure metals can also be fitted to an Arrhenius-type temperature dependence. Demmel reported an activation energy $E_a = 274 \pm 4$ meV and the prefactor is $D_0 = 179 \pm 11 \times 10^{-5} \text{ cm}^2/\text{s}$. Our MD results yield $D_0 = 120.84 \pm 11 \times 10^{-5} \text{ cm}^2/\text{s}$ and $E_a = 310 \pm 13$ meV. As well as in (Becker 2010) previous MD simulations the overall diffusion coefficients are smaller than the experimental values (which might be related to different temperatures between simulation and experiment). The activation energy agrees well with the simulation.

Appendix C: Short Range Order

Previous computer experiments on Lennard Jones (L-J) liquids were done with much larger mass differences and different mass dependencies were deduced, e.g., $D(m_1)/D(m_2) = (m_2/m_1)^{-\mu}$, where $\mu < 0.1$ (Bearman 1981). However in those experiments concentrations of lighter element are high, and sometimes equimolar. Here we can not always run such a simulations without observe segregation, (sometimes artificial?). When we simulate a Hydrogen-rich Pd-H or Ni-H mixture the system is almost a random solution for any given concentration. (See figure C1).

Contrary, if we run a rich hydrogen simulation of liquid aluminium (5 to 20% of H for example) we can observe a strong homo-coordination tendency. This happens with both Al-H potentials.

A common way to quantify segregations tendencies is using the short range order (SRO) parameter (See Chapter 5 for definition). SRO values tend to 1 as we increase H concentration. This can be seen clearly in figures C1 and C2.

In a recent work (Harvey 2010) several Metal-H systems are analyzed from a thermodynamic point of view. Their model takes into account the effect of SRO on the configuration contribution to the mixing entropy of the solution as a function of the change in the Gibbs energy of the quasi-chemical first nearest neighbor pair reaction:

$$(H-H)_{pair} + (Al-Al)_{pair} = 2(Al-H)_{pair} \Delta g_{AlH} \quad (6.6)$$

where Δg_{AlH} is the nonconfigurational Gibbs-energy change for the formation of two moles of Al-H pairs. A negative value of Δg_{AlH} for reaction (Harvey 2010) indicates that the equilibrium is shifted to the right, resulting in negative SRO (hetero-coordination). However, a positive value of Δg_{AlH} implies that H-H and Al-Al pairs are favored (SRO > 0, i.e. homocoordination). Both cases represent SRO phenomena and may affect the atomic configuration of the liquid. In their work they gave a negative value for Al-H system ($\Delta g_{AlH} = -6516.58 - 0,544T$, in J/mole) so SRO should be negative.

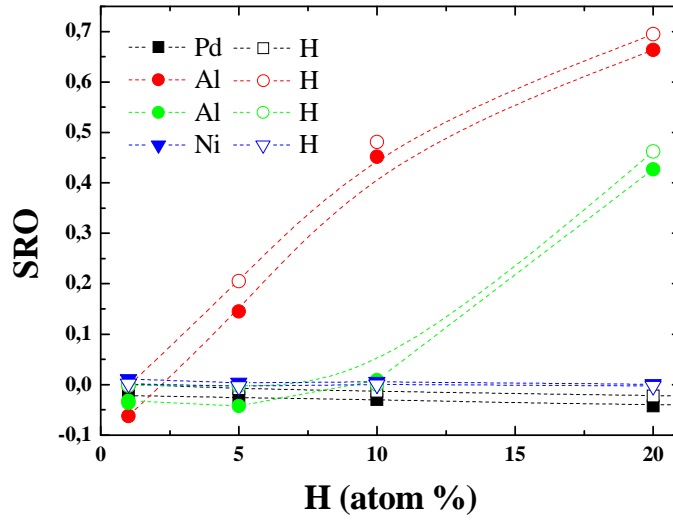


Fig. C1. SRO values dependence with H concentration (in atom %) for Pd-H and Al-H systems. Pd-H and Ni-H systems are almost a random solution independently of H concentration while Al-H system rapidly shows segregation.

In Table 6.5 we show some parameters of interest in H-Metal systems. As can be seen ΔH_s is positive for all metals studied here so SRO should be negative. As can be seen the effective charge is quite different in the studied metals.

	Z	mass	Density (m. p.)	ϵ	ΔH_s	ΔS	Q_{eff}
H	1	1.008	0.07	2.20	-	-	0.712
Al	13	26.98	2.375	1.61	+0.70	-6	1.792
Ni	28	58.69	7.81	1.91	+0.17	-6	2.43
Pd	46	106.42	10.38	2.20	+0.10	-7	3.21

Table 6.III. Some parameters used in this study. Density at melting point units are gr/cm^3 , ϵ is the electronegativity (Pauling scale). ΔH_s is the enthalpy of solution of hydrogen in the metal in the low concentration limit (Fukai 1993).

Next figure illustrates positive SRO in liquid H-Al system when H concentration is high ($> 15\%$). As can be seen, hydrogen (yellow atoms in fig C2), forms bubbles inside liquid Al in our simulations. Fig. C2 was obtained after simulation using EAM/alloy potential (Angelo 1995) but similar result was obtained with the ADP potential.

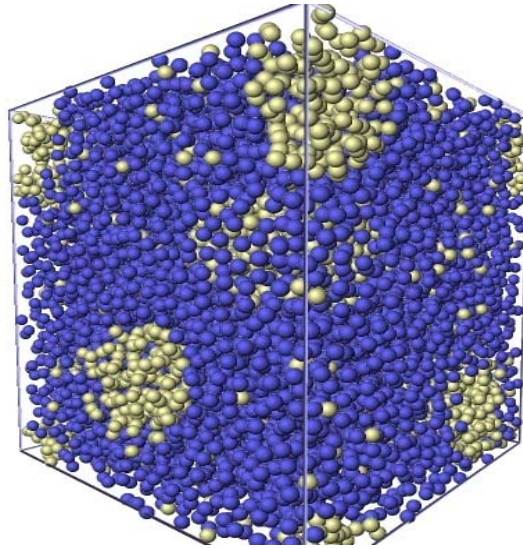


Fig. C2. SRO evidence in Al-H system (using EAM/alloy (Angelo 1995)). Yellow balls represent H atoms while blue ones represent Al ones. Here the H concentration is high (20%) for clarity sake.

This positive SRO is not expected but could be used to simulate high porosity materials as shown in figure 6.1. We could run an Al+H simulation and after reaching this stage we can delete H atoms and quench (i.e. cool down quickly) the system to have polycrystalline Al with high porosity.

Appendix D: Literature Review

Next figure show a summary of results from different authors. As can be seen H diffusivity in metals is high above the simple theoretical calculation proposed by Eq. 6.1. This literature review supports our intuition and basic conclusion. In short, classical MD seems to underestimate the H diffusivity in liquid metals.

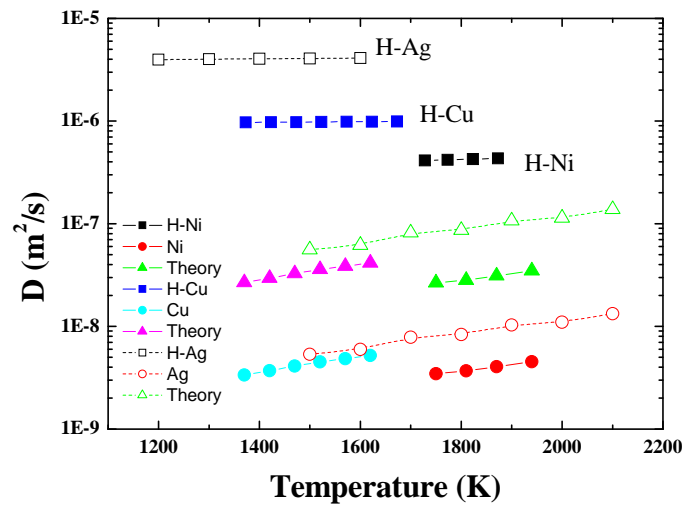


Fig. D1. Hydrogen diffusivity in liquid metals. Experimental data taken from (Sacris 1970). Self diffusivity of pure metals taken from MD results in reference (Ahmed 2004). Experimental data for liquid Cu and Ni taken from (Meyer 2008).

If we represent D_H/D_M at a certain temperature well above melting point (see Figure D2) for divided by the ratio of masses we can see clearly that, in general there is an order of magnitude between our simulations (black squares) and experimental values (red circles).

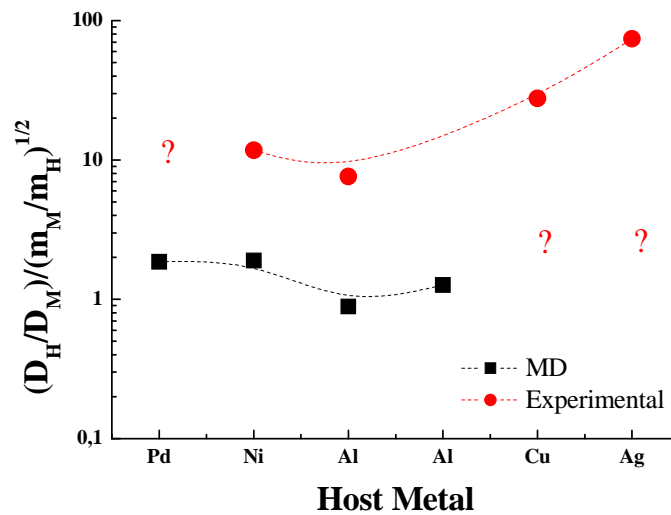


Fig. D2. Ratio of H diffusivity in liquid metals divided by the host metal self-diffusivity. Black squares stand for our MD results, red circles are experimental data taken from the abovementioned references.

Chapter 7

Ab initio calculations of Helium inside Lithium and Lead

The properties and behavior of light atoms in dense metals are important in several applications, ranging from H storage to H and He embrittlement of materials. Therefore helium inside metals has been widely studied in the past for nuclear reasons (Stoller 1988, Victoria 2000, Caro 2007).

In tokamaks with high-temperature plasmas the first wall is subject to a flux of light ions ($=10^{19}$ - 10^{22} ions $\text{cm}^{-2}\text{s}^{-1}$) with energy spectrum ranging from 1 to 100 eV (Ullmaier 1983). Evaluation of the mechanical effects induced by the presence of those species in the metal structure is one of the main tasks in the development of fusion reactor materials. Several mechanisms are responsible for the presence of light ions and atoms in structural material, among them the implantation of particles in a direct interaction of plasma with exposed surfaces and their production in the bulk region through neutron induced reactions.

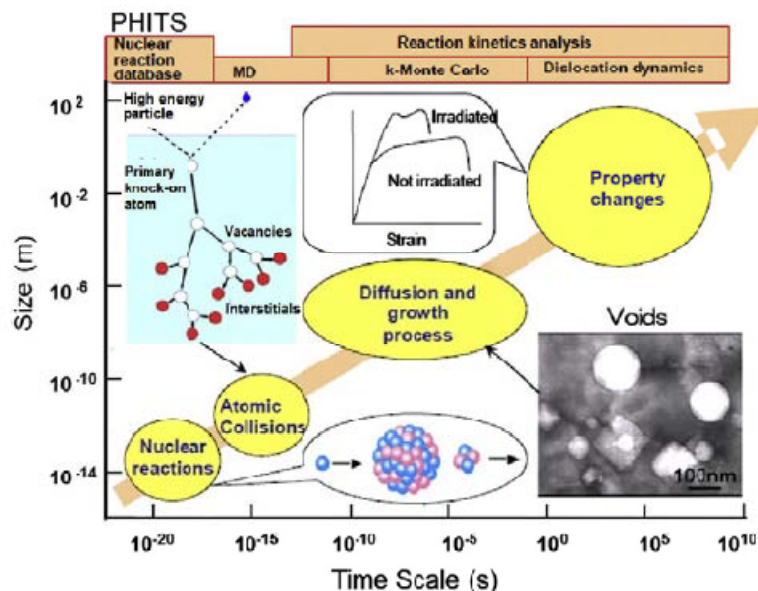


Fig. 7.1. Multi-scale model from nuclear reaction to property change due to irradiation (Kawai 2011).

The case of He is of major significance: the observed growth of He bubbles and their segregation into lattice defects, such as grain boundaries and dislocations, lead ultimately to severe embrittlement (Ullmaier 1986-92), blistering and swelling (Erents1973, Singh 1992), with consequent loss of mechanical properties of the irradiated materials.

Helium in liquid mercury is another important issue in the development of pulsed high-power spallation neutron sources, in which liquid mercury is bombarded by a high intensity proton beam to produce high neutron fluxes.

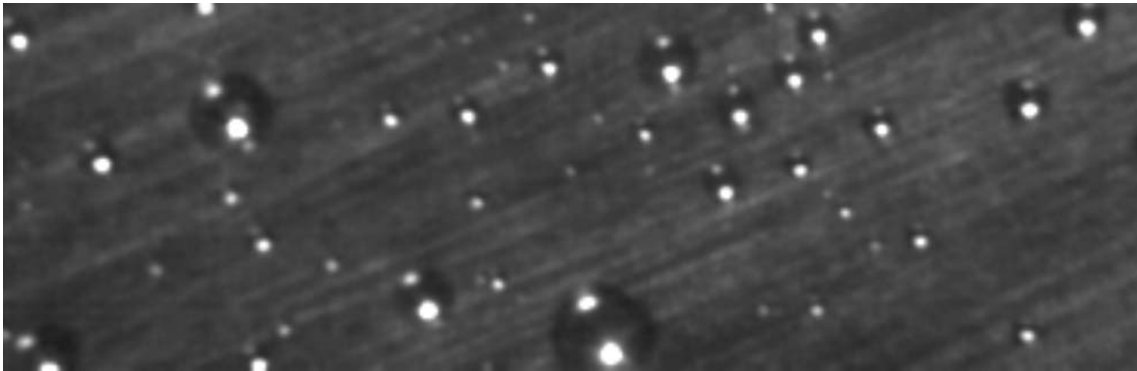


Fig. 7.1b. He bubbles in liquid mercury observed through a glass window placed on the surface of the mercury. The height of this image corresponds to 1.62 mm (taken from (Ida 2007)).

7.1 Introduction

The idea to study He inside Li and Pb does not respond to the necessity of studying He diffusion or mobility in Li, Pb or LiPb alloys after irradiation. To clarify the mechanism of the He bubble nucleation process in liquid metals from a molecular point of view, MD simulations are suitable tools. Hence, the main goal of this *ab initio* calculations is to create a forces database to be fitted with a He-Pb and/or He-Li interatomic potential using the so called force matching method (FMM) proposed by Ercolessi and Adams (Ercolessi 1994).

As we have seen in previous Chapters, analytic EAM potentials are typically fit to experimental data for a small number of properties, cohesive energy bulk modulus etc. When constructing an empirical potential, it is beneficial to include first-principles force data in addition to experimental data because it provides for a more accurate and transferable potential. The force-matching method proposed in (Ercolessi 1994) offers an alternative way to construct potentials.

Generating accurate potentials using the force-matching method is an optimization problem in a high-dimensional space. The EAM functions are parameterized by cubic splines, and the program POTFIT (Brommer 2006-07) optimizes the spline knots using a combination of simulated annealing and conjugate-gradientlike algorithms. Once the He-Pb and He-Li potentials are created we will construct a ternary potential with the LiPb potential proposed in Chapter 5, hence to study He nucleation and cavitation inside liquid Li₁₇Pb would be possible.

The nucleation rate can be directly estimated by the MD simulation, and the formation free energy and critical nucleus can be estimated by the MD and MC simulations. MD study of the gas bubble and cavity formation in simple bulk liquids is a well studied area of statistical mechanics (Blander 1975, Oxtoby 1992). Classical nucleation theory (CNT) has been reviewed in (Blander 1975).

The MD method has been used to calculate the homogeneous cavitation rate pressure dependence in liquid lead under negative pressure near the liquid spinodal (Insevpov 2007). The considered cavities contain only metal atoms, i.e. without any light ions or atoms of He or any other element. Such simplification of the model is based on the calculation results that the total energies, pressure tensors, and surface tensions of the cavities do not drastically change if helium atoms were placed inside the cavity, due to a weak interaction of helium with lithium. In any case they conclude that their results are not in agreement with the simple classic nucleation theory approach. Also they claim that is not clear if this discrepancy can be attributed to the shortcomings of the potential or the kinetic model deployed. The method presented gives the possibility of the direct calculation of the cavitation rate.

Not only would be interesting to study the behavior of He inside Li₁₇Pb. Another important issue is the interaction of H (or its isotopes) with He bubbles. It is known that impurities such as H and He interact strongly with dislocations in metals and what is more important; the synergetic effect of both H and He atoms is now being studied (Li 2012). In the same way, would be very interesting to develop a ternary potential for Pb-He-H or Li-He-H and study both He bubbles inside a liquid metal (Pb or Li) and the interaction of H with He bubbles in this medium. See ref (Donnelly 1985) for a review of pressure bubbles inside metals.

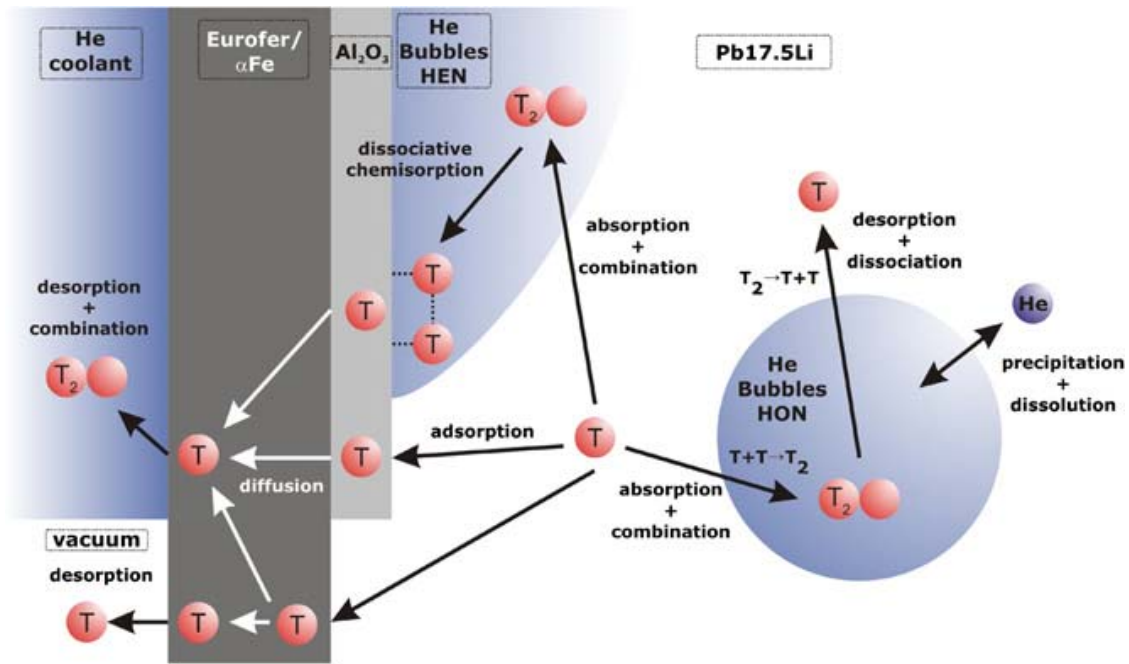


Fig. 7.2. Schematic representation of the importance of He bubbles inside liquid metals in breeder blanket design. (taken from (Fradera 2011)).

7.1.1 He potential (Morisita He-He potential)

The He potential for our proposed ternary Pb-Li-He potential need not to be developed. Rare gases in metals produced by nuclear reaction or by ion implantation are essentially insoluble hence tend to precipitate and to form bubbles. The pressure in these bubbles is about some GPa and hence the Ziegler-Biersack-Littmark correction (Biersack 1982) for high pressures is needed as explained in Chapter 3. The Beck potential for He-He interaction was smoothly connected with the ZBL universal potential that is appropriate at high energy (short interatomic separations).

The helium-metal interaction is described by a fully repulsive potential, $V(r) = \Gamma \exp(-\gamma r)/r$ where r is the distance between the helium and a lattice atom. For example, in the He-Ni interaction, the potential parameters determined by Melius *et al* are: $\Gamma = 45.9$ eV, and $\gamma = 2.03$ Å⁻¹ (Melius 1978). Several authors use as a good description of He-Metal interaction a pairwise potential in the form of Lennard-Jones function (see Chapter 3, Eq. (3.5)). We will discuss further the suitability of L-J potentials for H-Metal at the end of the Chapter.

7.2 Computational details

In order to obtain the force and energetic data that are needed to improve the interatomic potentials developed in the present work, first principles electronic structure simulations based on Density Functional Theory (DFT) (Hohenberg 1964) were performed.

For that purpose, the Kohn-Sham equations (Kohn 1965) have been self-consistently solved using a plane-wave basis set with the standard projector augmented wave (PAW) pseudopotentials (Blöchl 1994), as implemented in the Vienna *Ab initio* Simulation Package (VASP) (Kresse 1993; -96; -99). The exchange-correlation functional assumed was the PBE (Perdew-Burke-Ernzerhof, (Perdew 1996)) parameterization of the GGA (Generalized Gradient Approximation). We initially performed calculations for pure bcc Li with one *s* valence electron and pure fcc Pb with 14 valence electrons, in order to check the reliability of our computational procedure and concurrently provide a comparison to other calculations and experiment. Careful convergence checks were performed to find the optimum k-point meshes and planewave cutoff energies (505 eV for bcc Li and 264 eV for fcc Pb) sufficient for convergence of energy differences. Brillouin zone sampling followed the Monkhorst-Pack scheme (Monkhorst 1976). Volume relaxations were subsequently carried out using the standard conjugate-gradient algorithms present in VASP to find the optimal lattice constants (3.51 Å for Li and 5.02 Å for Pb), that compare well with the experimental values.

The supercell approach with periodic boundary conditions was used to simulate point defects as well as the corresponding pure phases of the same size. Forces were computed according to the Hellmann-Feynman method (Hellmann 1937, Feynman 1939), as implemented in VASP. Volume and ionic relaxations were performed as above, with accuracy in the forces better than 0.02 eV. The Brillouin Zone (BZ) integrations during the relaxation runs were done using a Methfessel-Paxton scheme (Methfessel 1989) with a smearing of $\sigma=0.2$ eV, that gives good results for metals. Once the relaxation was completed, accurate total-energy calculations, better than 10^{-6} eV, were carried out without smearing following the tetrahedron method with Blöchl corrections (Blöchl 1994). Series of these total-energy calculations were also computed for the non-relaxed supercells.

In a simulation using periodic boundary conditions the strain field created by one defect inside a supercell will possibly interact with its image strain fields. This is the well known size effect that can only be minimized, never completely eliminated, using as large supercells as possible. Due to the limited computational resources available, we had to restrict ourselves to 3x3x3

supercells in the case of Pb. On the other hand, elemental Li has a much lower atomic number and less valence electrons than Pb, so we could use up to 5x5x5 supercells for lithium. Since Pb is a heavy atom, electrons are relativistic and the spin-orbit interaction becomes more important than the effect of electron repulsion. Thus, non-relaxed Pb supercell calculations were repeated including spin-orbit coupling (SOC) in a non-collinear magnetic structure setting. Using the nonmagnetic calculations that we had from the previous step, we set the spin quantization axis in parallel to the z direction, meaning that the magnetic field is now parallel to that direction. As spin-orbit coupling couples the spin to the crystal structure, we are able to find the spin and orbital magnetic moment components separately, along the (0 0 1) direction, something that is simply not possible without SOC. By comparing the energies for different orientations the magnetic anisotropy can be determined, but we have not gone that far: our aim was simply to check if the inclusion of magnetism and spin-orbit coupling affected the energetics and forces of the system. Since it makes not sense to further relax the structures, we have only carried out the accurate total-energy calculations as outlined above, albeit the global energy break condition for the electronic self-consistent loop is an order of magnitude smaller, 10^{-5} eV. When calculating local magnetic moments, it is important to introduce atomic radii to find the local projections on the atomic orbitals. The values adopted throughout this work are the recommended ones, 1.23, 1.47, and 0.93 Å for Li, Pb, and He, respectively, which correspond approximately to their metallic radii, except for He, a noble gas for which we take its Pauling ionic radius.

In the present Chapter the relative stabilities of single He defects in Li (bcc) and Pb (fcc) metals are investigated. The interstitial He formation energies at the tetrahedral and octahedral positions are calculated. Furthermore, the electronic density of states (DOS) and charge density difference of He atom and its first neighbor Pb are analyzed to address the effects of magnetism on the relative stabilities of He defects in bcc Pb. Charge transfer is studied by means of Bader analysis (Bader 1990) and compared with the raw results obtained with VASP.

7.3 Methodology

A single He defect consists of a substitutional or interstitial He atom. Pb crystallizes in the fcc structure under normal conditions. Li crystal structure at 0 K is somewhere under discussion (Orlov 2001) but here will consider it to be bcc. In fact, Li crystallizes at low temperatures in

the close-packed 9R and fcc phases (Linn 1986), and the bcc phase appears only at temperatures of about 100 K.

In both bcc and fcc structures all the substitutional sites are equivalent, while there are two possibly interstitial sites, i.e., tetrahedral and octahedral positions. These interstitial sites are illustrated in Fig. 7.3: a and b for bcc structures and c and d for fcc structures, respectively.

A substitutional defect has 8 nearest neighbors at $0.866a_0$ in a bcc structure, while it has 12 nearest neighbors at $0.707a_0$ in an fcc structure. The tetrahedral interstitial has four nearest neighbors at $0.559a_0$ in a bcc structure and four nearest neighbors at $0.433a_0$ in an fcc structure. The octahedral interstitial has six nearest neighbors, with two of them located at $0.5a_0$ and four of them at $0.707a_0$ in a bcc structure, while it has six nearest neighbors at $0.5a_0$ in an fcc structure.

It is clear that for both bcc and fcc structures the substitutional site has the largest free volume, followed by the octahedral site, but the tetrahedral site has the smallest one. Since He has a closed-shell electronic structure and bonding interaction is small, He is expected to occupy defect sites in the order of largest free volume, namely, substitutional sub, octahedral octa, and tetrahedral tetra in both bcc and fcc structures.

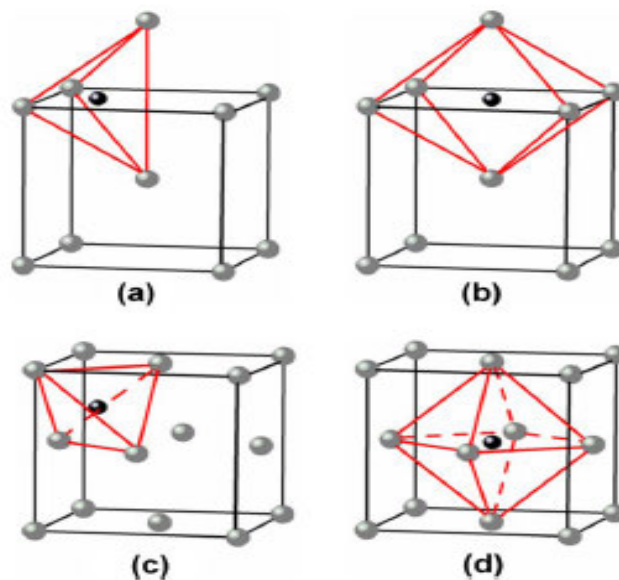


Fig. 7.3. High symmetry interstitial sites in a bcc structure, (a) tetrahedral and (b) octahedral, and in an fcc structure, (c) tetrahedral and (d) octahedral.

The relaxation energy of a crystal is determined as a difference between the total energy of a crystal before and after relaxation. The relaxation volume is determined similarly. In order to be

comparable, the formation energies of He interstitial and substitutional defects are defined for the same initial atomic configuration that is a perfect bcc crystal with an isolated He atom. The formation energy of He interstitial is

$$E_{\text{int}}^f = E_{N_m, \text{He}} - NE_m - E_{\text{He}} \quad (7.1)$$

where N is the number of metal atoms in the initial and final supercells, E_m is the energy per atom of the perfect bcc lattice, and E_{He} is the energy of an isolated He atom. Creating a He substitutional defect causes also a creation of a vacancy. The formation energy in this case is

$$E_{\text{sub}}^f = E_{(N-1)m, \text{He}} - (N-1)E_m - E_{\text{He}} - E_{\text{vac}}^f \quad (7.2)$$

where E_{vac}^f is the formation energy of a vacancy. The binding energy of a He atom to a vacancy is defined straightforward as the energy difference between interstitial and substitutional positions,

$$E_{\text{bind}} = E_{\text{int}}^f - E_{\text{sub}}^f \quad (7.3)$$

Here E_{He} is the energy of the He atom alone. The value we have used is $E_{\text{He}} = 0.01432$ eV (Gonzalez 2012) calculated by first principles using PAW pseudopotentials and GGA approximation for exchange and correlation functional. E_{vac}^f is the formation energy of a vacancy. The values used for the pure elements are 0.58 eV for Pb (Lee 2003) and 0.77 eV for Li (Yuan 2003).

7.4 Results

7.4.1 Formation Energies

The cohesive energy of the pure elements from our *ab initio* calculations are -1.89557 eV for Li, and -3.6558 eV for Pb without SOC and -4.205 eV for Pb taking into account SOC. The results obtained with these values in mind and using equations 7.1 - 7.3 are collected in Table 7.I.

	Pb+He (eV/at)			Li+He (eV/at)	
	Unrelax	Unrelaxed	Relaxed	Unrelaxed	Relaxed
	NSOC	SOC	NSOC		
Oct	-0,02212	-0,66172	-0,72682	1,28828	0,34018
Sub	-2,96792	-2,56662	-1,95392	0,42461	-0,37539
Tetra	1,32788	0,68958	-0,62252	1,28818	0,33228

Table 7.I. Summary of formation energies of high symmetry He interstitials in Pb and Li.

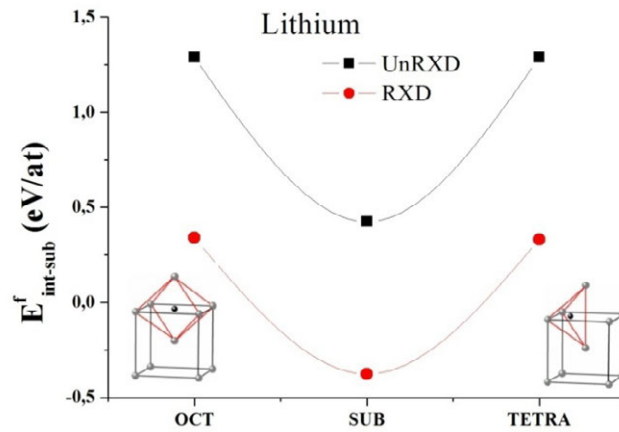


Fig. 7.4. He defects inside pure lithium (bcc) for two different scenarios, unrelaxed (black squares) and relaxed (red circles).

After atomic relaxation the formation energy decreases significantly due to the change in the charge densities but the order of site preference for the He interstitials does not change. It is assumed that the relative stability of a He defect in a bcc structure is associated with the available free volumes of the defect sites, generally following the order of substitutional, octahedral, and tetrahedral positions (Zu 2007), however we do not see any difference between the octahedral and tetrahedral interstitials.

The substitutional position is also the most stable site for all the fcc metals considered according to several studies (Zu 2009). Furthermore, the octahedral He interstitial is energetically more favorable than the tetrahedral interstitial in fcc Pb as observed in Ag and Pd. Interestingly the formation energies of He interstitials at the tetrahedral and octahedral positions are almost the same once SOC is taken into account while the substitutional position remains the most favorable one.

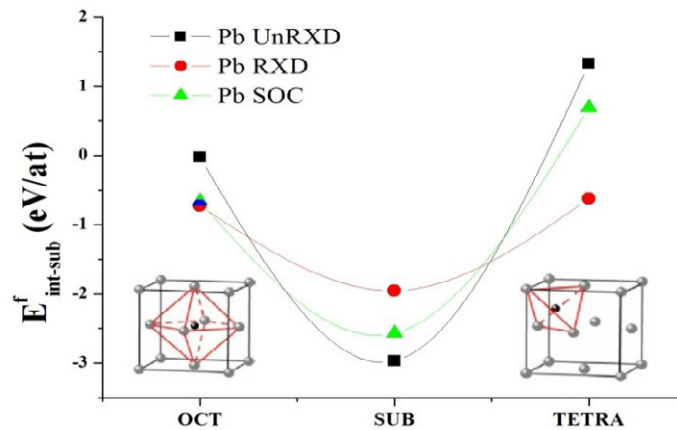


Fig. 7.5. He defects inside pure lead (fcc) for the three different studied scenarios; unrelaxed (black squares), relaxed (red circles) and (unrelaxed) taking into account SOC (green triangles).

Pb is not magnetic enough to induce a magnetic moment in the He atom. In fact only in the tetrahedral position of He, Pb shows a small magnetic moment, -0.020 and $-0.026 \mu_B$ for the x and y projections (μ_x and μ_y) and smaller, only $-0.008 \mu_B$, for μ_z .

Pb+He	Magnetic Moment (μ_B) Unrelaxed			
	Pb (μ_x, μ_y, μ_z)			He
Oct	0.0	0.0	0.0	0.0
Sub	0.0	0.0	0.0	0.0
Tetra	-0.020	-0.026	-0.008	0.0

Table 7.II. Magnetic moment components, μ_i , for Pb and He atoms. Pb values are the average of the first nearest neighbors.

To understand better the effect of SOC in the calculations we can compare the results of He inside Ni (see (Zu 2009) Table V) and Fe ((Seletskiaia 2005), Table II). He total magnetic moment is equal zero in both Ni and Fe (as well as in Pb) for the substitutional case, and different values spanning from 0.01 to 0.02 μ_B in the other cases. In both Ni and Fe this value increases after relaxation.

In table 7.III we collect the calculated volumes for the studied interstitials and also the volumes of pure Pb and Li for comparison sake. Note that the difference in both Pb and Li volumes per atom change in the unrelaxed case is just due to the addition of an atom to the equation, is to say, we are now dividing the total volume between 108 and 109 atoms, and 250 and 251 atoms for Li. As can be seen the relaxation process cell expand the Pb cell ($\Delta V > 0$) in all the He configurations, being the expansion smaller for the substitutional case. For Li the situation is quite different and now, relaxation contracts ($\Delta V < 0$) the cell, more notably in the substitutional configuration.

	Pb				Li		
	Unrelaxed	Relaxed	SOC	ΔV (%)	Unrelaxed	Relaxed	ΔV (%)
Octa	31.43	31.85	31.41	1.3363	21.54	20.32	-5,6638
Sub	31.70	31.96	31.70	0.8202	21.62	20.38	-5,7354
Tetra	31.41	31.95	31.41	1.7192	21.54	20.33	-5,6174
Pure	31.70				21.62		

Table 7.III. Volume per atom (in \AA^3) for pure Pb, Li, and He interstitials, before and after relaxation, and taking into account SOC.

When an impurity is implanted to a crystal, it changes the crystal volume. This change is determined as the difference between the volume of the crystal containing an impurity and the pure-crystal volume and is called the excess volume. Table 7.III lists the excess volumes which helium atoms contribute to the Pb and Li lattices.

The coordination polyhedrons in the fcc (also in hcp) structures are regular polygons; in this case, the tetrahedrons are half in volume as the octahedrons. It follows that, when the impurity atom is placed in the tetragonal interstitial site, the Pb unit cell increases (the shape being unchanged) to a greater degree than in the case of the octahedral coordination.

The volumes of the octahedral interstitial sites in the bcc lattice are twice as large as those of the tetrahedral ones. However, the coordination polyhedrons in the bcc structure are not regular: the tetrahedron edges differ in length (one edge is a and five edges are $a\sqrt{3}/2$) and the octahedrons are strongly flattened in a direction, although their edges have the same length.

These specific features of the coordination polyhedrons of the bcc lattice lead to the fact that larger non-metallic atoms can implant to the tetrahedral interstitial sites than atoms implanted to the octahedrons. In our case, this circumstance is manifested in the fact that the helium atom located in the octahedral interstitial site increases the Pb unit cell volume to a greater degree than the helium atom located in the tetrahedral interstitial site.

7.4.2 Charge transfer

In this section we described the charge transfer observed between Metal and He atoms. Pure elements, Li and Pb, unrelaxed total charge values are 0.253 and 8.605 respectively (in atomic units). Total charge of He unrelaxed corresponds to the He interstitial average. Note that the calculated value agrees with the value given in ref (Seletskaja 2005). However the value of effective charge for Pb is roughly half the value obtained in our calculations.

Lithium: The results without relaxation show almost the same charge for Li and He in both octahedral subs and tetrahedral positions. If we examine the relaxed values we note that there is not charge transfer in the substitutional case. For the Oct. and Tetra positions the Li charge

diminish in 0.15 (atomic units) and that of He augments in 0.2 a.u. These results are graphically presented in Fig. 7.6.

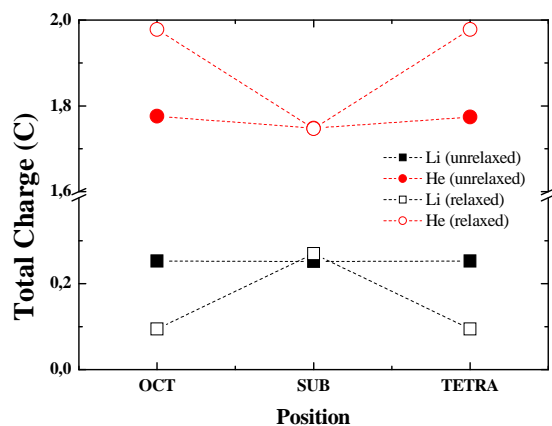


Fig. 7.6. Helium atom and Li total charge relaxed and unrelaxed as labelled. Note the break in the y axis.

Lead: In the three initial Pb-He configurations studied, before relaxation the total charge is not the same as we found in Li. After relaxation we do not observe charge transfer in the substitutional case as expected. Somewhat surprising, in the octahedral interstitial the total charge of surrounding Pb atoms Pb remains constant while that of He atom decreases in 0.5 units. In the tetrahedral interstitial the Pb diminishes 3.2 units and that of He increases in 0.25.

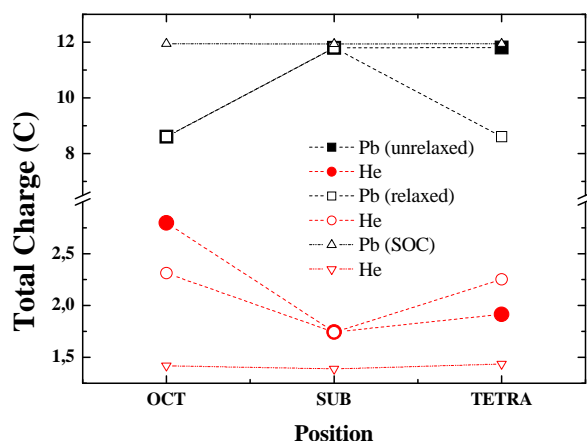


Fig. 7.7. Helium atom and Pb total charge relaxed and unrelaxed as labelled. Note the break in the y axis.

When calculations are carried out with SOC there is no charge transfer. (The simulation is too expensive so the system is not relaxed). Interestingly the results for octahedral position of He are different compared to the unrelaxed situation, while not in for the sub and tetra.

7.4.3 Charge character

Lithium: In the Li-He configurations before relaxation Li charge is 45 % p and 55 % s and that of He is 100 % s. After relaxation, the substitutional case seems the more stable again and Li charge does not change. In both octahedral and tetrahedral interstitials Li charge became more p-like (50 %) and less s-like (50 %). In other words, there is a change in the character of the Li atoms around the He atoms in octahedral and tetrahedral positions ($s \rightarrow p$), almost absent in the substitutional case. At the same time the s-character of the charge of He atom decreases in ~2 %.

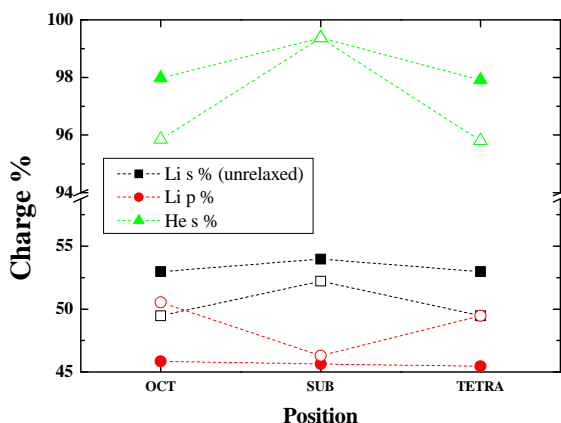


Fig. 7.8. Helium atom (green triangles) and Li charge character (unrelaxed). Dashed lines are just guides to the eye. Note the break in the y axis.

Lead: Before relaxation the total charge of Pb atoms is 82 % d, 12 % s and 6 % p for both substitutional and tetrahedral He but 95 % d, 5 % s and less than 1.0% p in the octahedral position. After relaxation the character of Pb atoms becomes almost totally d-like (95 %) in the octahedral and tetrahedral configurations. In the substitutional configuration, after relaxation, the character of Pb charge and that of the substitutional He atoms remains almost constant,

pointing again to the fact that the substitutional position is the most favorable. Some decrease of the s character of the He atom is correct according to the results shown in (Trioni 1998).

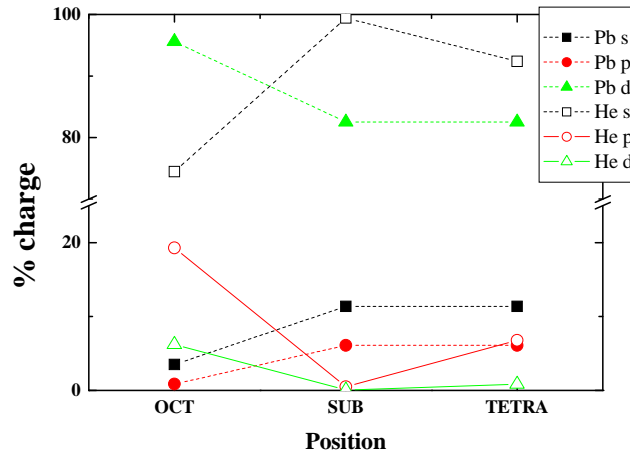


Fig. 7.9. Helium atom and Pb charge character unrelaxed. Note the break in the y axis.

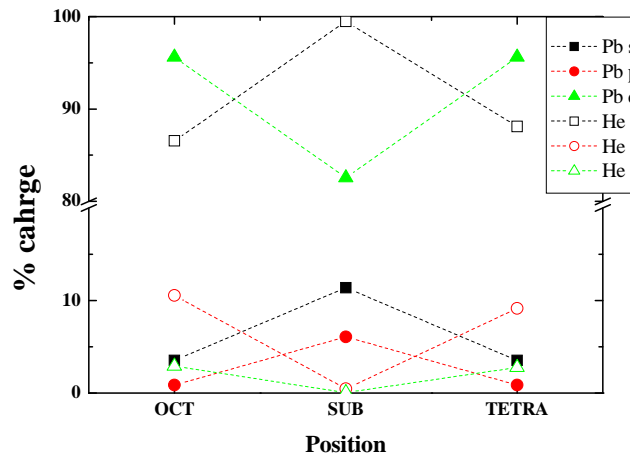


Fig. 7.10. Helium (open symbols) atom and Pb (closed symbols) charge character (s, p and d, black, red and green respectively) after relaxation. Note the break in the y axis.

Lead-Helium: He charge is s-type in a 75% for the octahedral position, 100 % for the substitutional one and about a 97% for the tetrahedral interstitial in the unrelaxed configurations. After relaxation, in the octahedral and tetrahedral positions is in both cases 86% s-type and 12% p-type while in the substitutional case does not change. Then the charge transfer

differs in both tetrahedral and octahedral configurations, decreasing the s character of the first and increasing the s character of the second.

Figure 7.11 shows one the most important results shown in the work of Zaremba and Kohn; Y-axis represents the electronic density corresponding to the metallic state in a direction perpendicular to the surface and through the center of the atom in the vicinity of a He atom. According to (Zaremba 1977), in general, some charge transfer from the host metal atoms to the interstitial He exist (metal charge density decreases around the He impurity). This is what we observe both for Li and Pb.

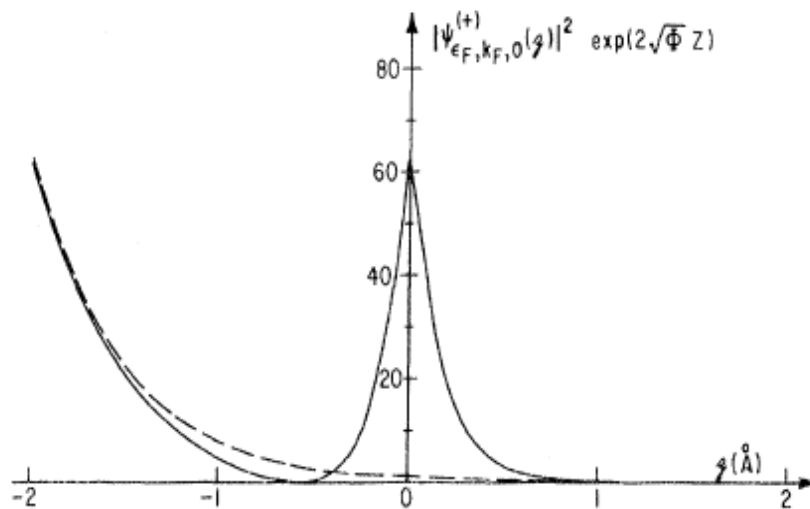


Fig. 7.11. Charge density of the metallic electrons in the vicinity of the helium atom. The dashed curve is the unperturbed metallic density. (taken from (Zaremba 1977)).

In a more recent paper (Trioni 1998), is possible to find similar results that also point in the same direction. In their paper, Trioni and co-workers study He (and Ne) in the vicinity of an Ag-like jellium metal surface by *ab initio* calculations. Next figure show the variations of the 1s level of a He atom close to a metallic surface. As we have seen in previous figures we observe a s-character decrease in the tetrahedral He interstitial but an increase in this character for the Octahedral He atom.

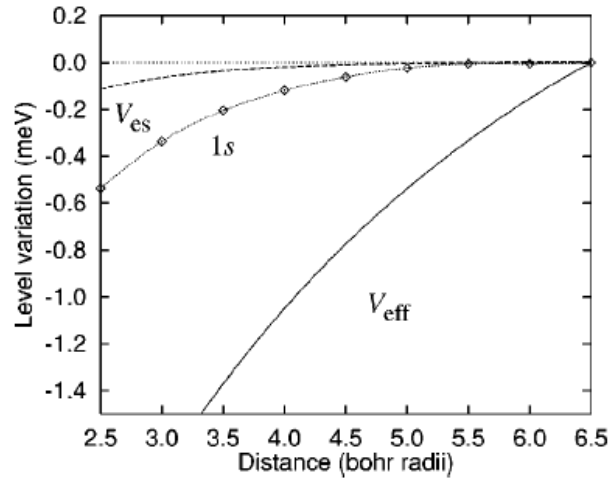


Fig. 7.12. (Fig. 3 in Trioni 1998). The variations of the $1s$ level (line with diamonds) of a He atom, of the bare metal electrostatic potential V_{es} (dashed line), and of the bare metal effective potential V_{eff} (solid line) as functions of the atom jellium edge distance.

7.4.4 Density of States of He (inside metals)

In the following we analyze the electronic structure of the various He defects and hosts in an attempt to understand what underlies He site-preference order in the different studied metals. Figure 7.13 shows the total DOS of a He interstitial at tetrahedral, octahedral and substitutional positions inside bcc-Li. The position of the Fermi level relative to the peaks in the density of states (DOS) determines the occupation of the states and the nature of bonding (Pentcheva 2002). It can be seen from Fig. 7.13 that the interaction of tetrahedral and octahedral He interstitials with its neighbor Li atoms gives almost identical DOS of He atoms at the Fermi level which indicates the similar bonding at the tetrahedral and octahedral sites.

Right part of Fig 7.14 shows the s,p-projected DOS of the Li atoms close to the He interstitials, as well as Fig 7.13 shows the s,p,d-projected DOSs of the He defects. The changes in both s and p DOS of the Li atoms near the He octahedral and tetrahedral positions are more significant than that of the Li atoms near the He substitutional position, which means that the hybridizations between the Li atom and the octahedral and tetrahedral He atom are stronger than that between the Li and the substitutional He.

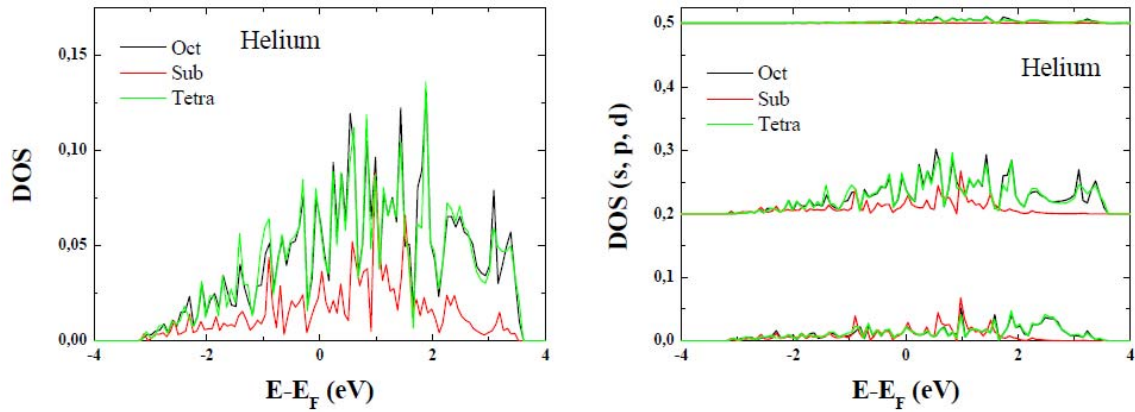


Fig. 7.13. Total (left) and projected DOS (right) of He inside Li after relaxation. The units are number of states/unit cell. p and d DOS are shifted upwards +0.2 and 0.5 units for clarity. Octahedral (black line), substitutional (red) and tetrahedral (green).

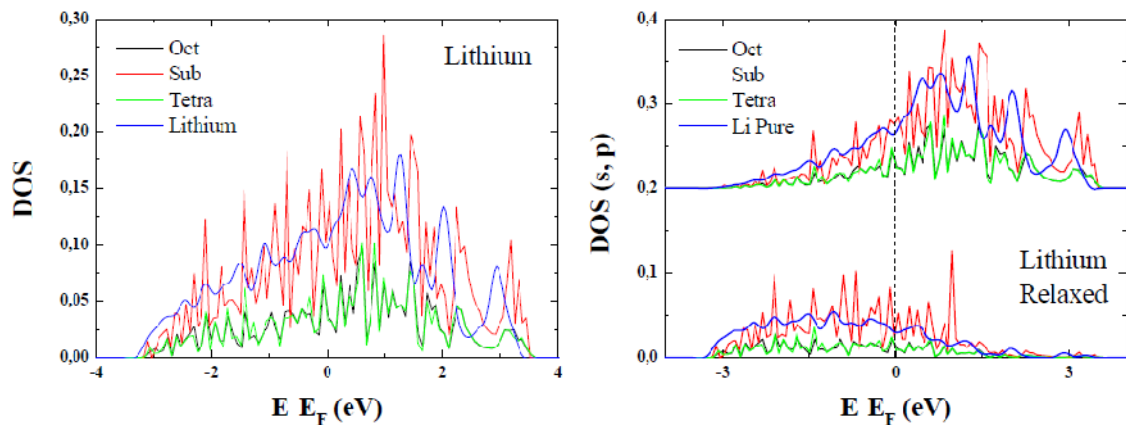


Fig. 7.14. Total (left) and projected DOS (right) of Li with different interstitials after relaxation; octahedral (black line), substitutional (red), tetrahedral (green) and pure Li (blue line).

Similar conclusions can be subtracted from the partial DOS (shown in figure 7.13 and 7.14 - left). Again the tetrahedral and octahedral positions present very similar s, p and d DOS.

Figure 7.15 shows the total and partial DOS of a He interstitial at tetrahedral, octahedral and substitutional positions inside fcc Pb. It can be seen from Fig. 7.15 that the interaction of octahedral He interstitial with its neighbor Pb atoms leads to a lower DOS of He atoms at the Fermi level than that of the tetrahedral interstitial, which indicates the stronger bonding at the octahedral interstitial site.

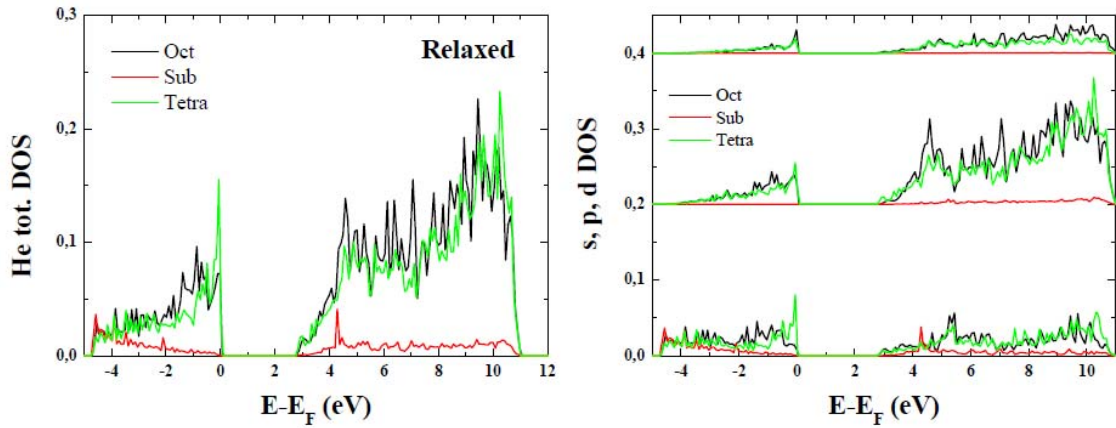


Fig. 7.15. Total (left) and partial (right) DOS of He inside Pb after relaxation for three different configurations; octahedral (black line), substitutional (red) and tetrahedral (green). p and d-DOS are shifted upwards +0.2 and 0.5 units for clarity.

Figure 7.16 shows the total and partial DOS of a pure Pb (blue lines) compared to the Pb DOS of surrounding atoms of He interstitials (at tetrahedral, octahedral and substitutional positions).

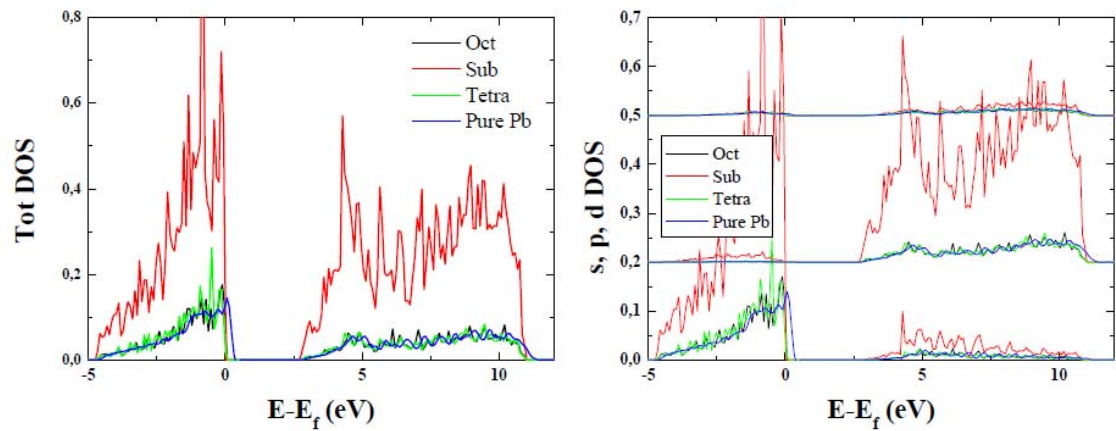


Fig. 7.16. Total (left) and partial (right) DOS of Pb after relaxation with three different He interstitial; octahedral (black line), substitutional (red) and tetrahedral (green). Partial p- and d-DOS are shifted upwards +0.2 and 0.5 units for clarity.

If we compare He DOS and Li DOS (Fig. 7.13 and 7.14 respectively) one immediate fact is that both DOS are similar in shape. Now if we compare both figures with their respective He inside Pb and Pb with He interstitials, (Fig 7.15 and 7.16) first thing to note is that again both DOS are similar, but now, a clear gap in the DOS is present in both He and Pb. The first is another evidence of hybridization while the second is not well understood.

If we now compare Pb DOS with SOC vs Pb without SOC results (unrelaxed in both simulations) we observe the following: substitutional DOS are similar below the Fermi energy but well above the Fermi energy the DOS of Pb with SOC broadens. Looking at the tetrahedral and octahedral interstitials a decrease in the DOS is clear up and down the Fermi energy. The gap in between is almost equal in both SOC and no-SOC calculations. Again DOS above the Fermi Level broadens towards higher energies.

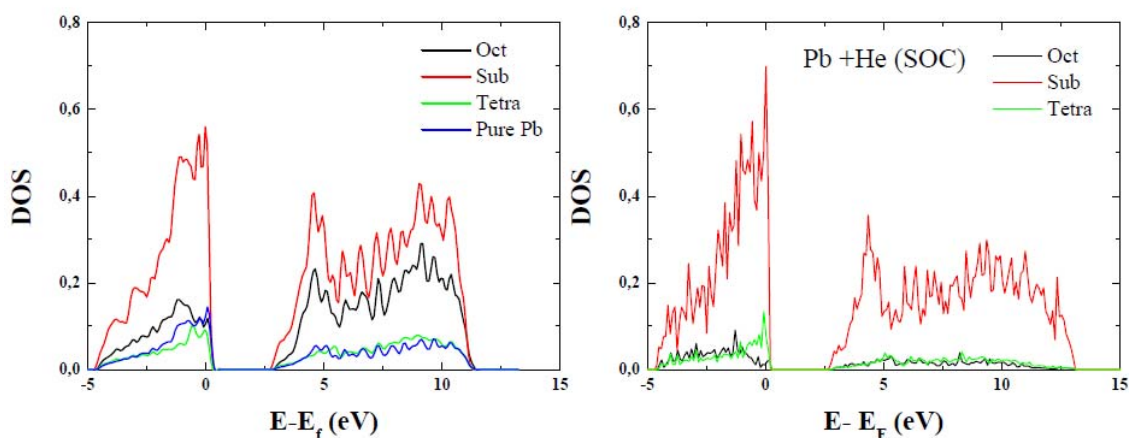


Fig. 7.17. Total DOS of Pb before relaxation without SOC (left) and with SOC (right) and with three different He interstitials; octahedral (black line), substitutional (red) and tetrahedral (green). Blue line stands for the pure fcc Pb DOS.

7.4.5 Bader analysis

The properties of chemicals and materials are often described in terms of charge transfer between atoms and the presence of ionic charges or electric multipoles on atoms or molecules. Accurately describing these complex interactions is difficult, but it can also be challenging to rationalize the calculated energetics. One powerful technique for doing this is to decompose properties of the molecule or material into contributions from the individual atoms. Bader suggested an elegant way to do this partitioning (Bader 1990). His idea was to use the charge density to divide space within molecular systems into atomic (Bader) volumes.

Bader analysis (Henkelman 2006, Sanville 2007, Tang 2009) uses what are called zero flux surfaces to divide atoms. A zero flux surface is a 2-D surface on which the charge density is a minimum perpendicular to the surface. Typically in molecular systems, the charge density reaches a minimum between atoms and this is a natural place to separate atoms from each other.

Besides being an intuitive scheme for visualizing atoms in molecules, Bader's definition is often useful for charge analysis. For example, the charge enclosed within the Bader volume is a good approximation to the total electronic charge of an atom. The charge distribution can be used to determine multipole moments of interacting atoms or molecules. Bader's analysis has also been used to define the hardness of atoms, which can be used to quantify the cost of removing charge from an atom.

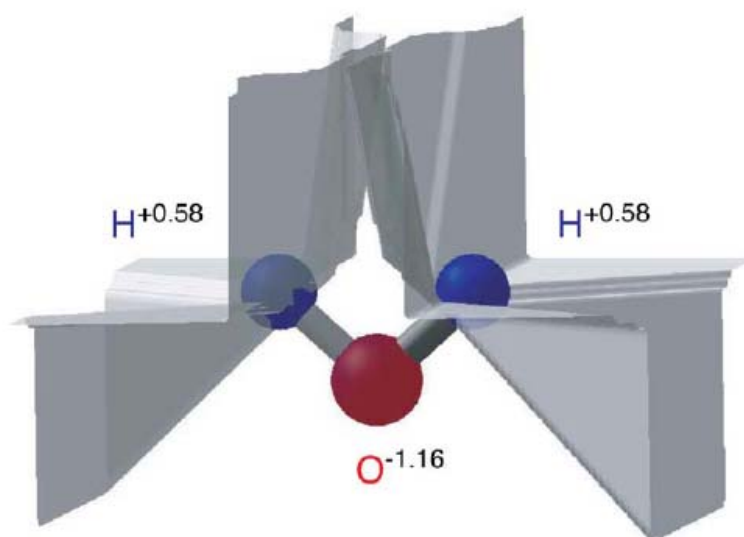


Fig. 7.18. Dividing surfaces separating the oxygen and hydrogen Bader regions in a water molecule. The integration over the Bader regions indicates that 0.58 e are transferred from each hydrogen atom to the oxygen atom (taken from (Henkelman 2006)).

We have used a program for doing Bader's analysis on a charge density grid. The program [<http://theory.cm.utexas.edu/bader/>] can read in charge densities in the VASP CHGCAR format, (also the Gaussian CUBE format). The program outputs the total charge associated with each atom, and the zero flux surfaces defining the Bader volumes.

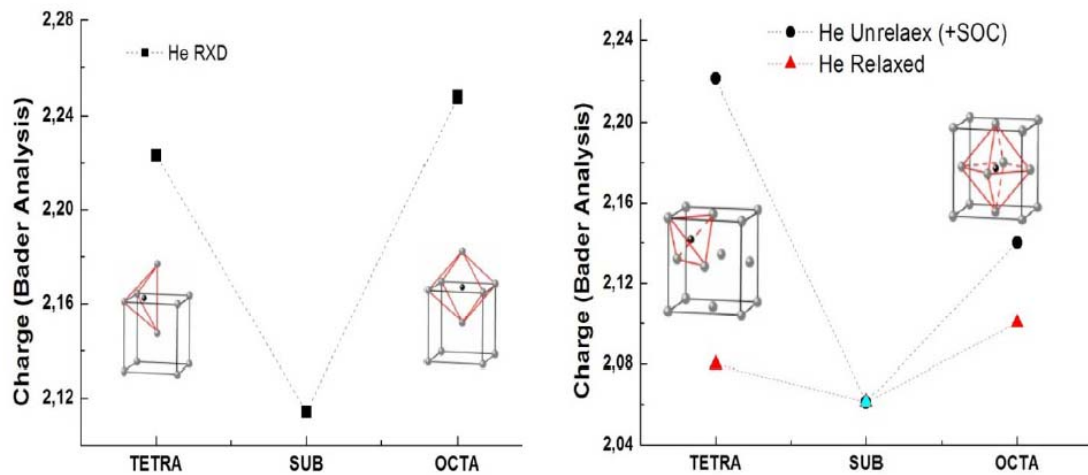


Fig. 7.19. He charge inside Li (left) and Pb (right) after relaxation calculated using Bader analysis. Dashed lines are just guide to the eye.

For Li-He (Fig.7.19 left), the Bader analysis after relaxation gives the same results that those of the unrelaxed system, while some small charge transfer was observed from raw data. Total charge around the He atoms is lower for the substitutional case (as well as in section 7.4.2) and almost equal in the octahedral and tetrahedral interstitials.

Now, for the Pb-He system (Fig 7.19 right), the results after and before relaxation are different (note that for Li-He the results were almost the same). Total charge around He atom is slightly lower in the substitutional case and approximately the same for octahedral and tetrahedral positions. During relaxation the value of this charge diminishes in 0.14 for the tetrahedral interstitial and 0.03 for the octahedral.

7.4.6 Charge Visualization

Valence charge density distribution reveals the features of the atomic bonds (Pentcheva 2002). Figure 7.20 shows the changes in the charge densities produced by the He octahedral and tetrahedral defects in the relaxed and unrelaxed structures with magnetism, as well as in unrelaxed structures without magnetism.

Vaspview does not give useful information if we just plot the output CHGCAR from Vasp. However if we subtract the pure Pb charge to some Pb-He configuration we will observe some

clear differences. For example in next figure we show this difference for Pb plus one He tetrahedral interstitial. The lines represent contours of equivalent charge density.

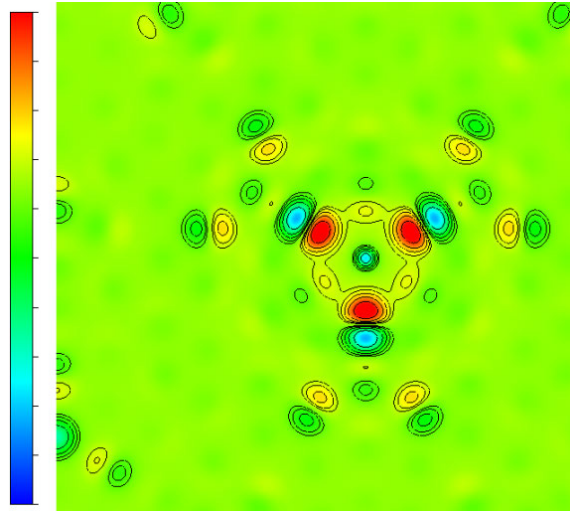


Fig. 7.20. Schematic illustration of the difference in charge of pure Pb and Pb with an He interstitial in tetrahedral position.

He atom in tetrahedral position inside a 3x3x3 Pb fcc cell. "contour plot" after subtraction of pure Pb CHGCAR. View along [111] plane, with vectors [1 -1 0] and [1 1 -2] parallel to (1 1 1) plane (and perpendicular to the [1 1 1] axis, and hence between them. Red and blue represent increase and decrease of charge with respect to green color that would be zero in this cut.

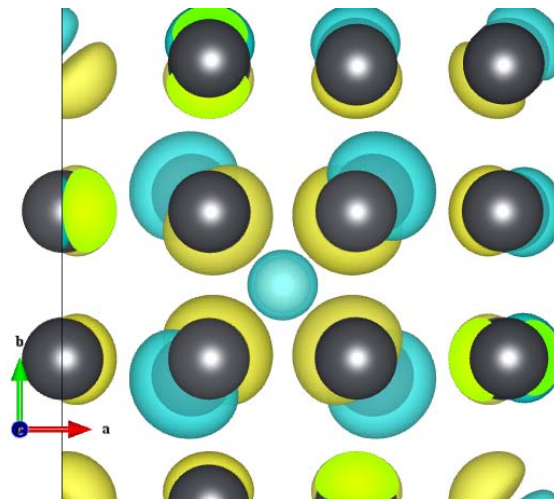


Fig. 7.21. Schematic illustration of the difference in charge of pure Pb and Pb with a He interstitial in tetrahedral position. Yellow color represent the s "orbitals".

All the reported results up to now manifest how helium substantially perturbs the electrons of a host metal and also can distort its lattice.

Polarizability, usually denoted as α_0 , is the measure of the change in a molecule's electron distribution in response to an applied electric field. Polarizabilities determine the dynamical response of a bound system to external fields. Hence we can understand the different charge transfer described before in terms of this property. As we can see in Table 7.IV, the Li polarizability is much higher than that of Pb (about 3 times) what could explain the different charge transfer observed in both cases. In fact, charge transfer in Pb+He system is about a 25 % (See Section 7.4.2) significant but less important than in Li+He system where charge transfer is around 60 %.

Element	Total charge (Unrelaxed)	Effective charge (2)	r_s (1)	Atomic diameter (Å) (2)	α_0 (a.u.)
Li	0.253	?	3.28	?	164
Pb	8.605	4.0	3.24	3.48	47
He	1.7(7)	1.7	?	2.70	1.38

Table 7.IV. Total charge of He and host metals according to this work. (2) Some relevant data: effective charge (Shpil'rain 2007), polarizability, α_0 , (Mitroy 2010). (1) electronic density, r_s , (Zaremba 1977).

7.4.7 Forces

The main purpose of this work is to give a representative atomic-scale description of the phenomena induced by the presence of helium atoms on the surrounding host lattice and to calculate the forces between both Li and Pb with He. We have calculated the forces created by the introduction of a He atom inside a Li and Pb cell, as mentioned above, in the three more simple configurations. Other possibilities are shown in figure 7.22 for a bcc lattice. The work could be continued in that direction.

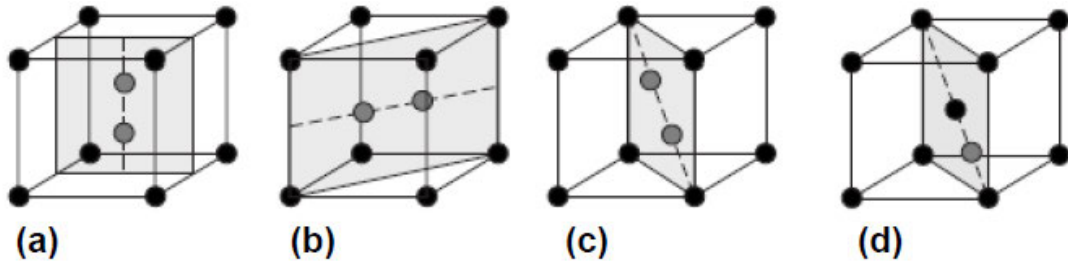


Fig. 7.22. Schematic illustration of the (a) $\langle 100 \rangle$ dumbbell, (b) $\langle 110 \rangle$ dumbbell, (c) $\langle 111 \rangle$ dumbbell and (d) $\langle 111 \rangle$ crowdion, in a bcc CS.

The details of force matching method will not be reproduced here and can be found in the original paper of Ercolessi and Adams (Ercolessi 1994) and in many others (Li 2003). A detailed explanation of the errors in the different fitting methods can be found in (Fellinger 2010). In next figure we show an example of force fitting taken from (Izvekov 2004).

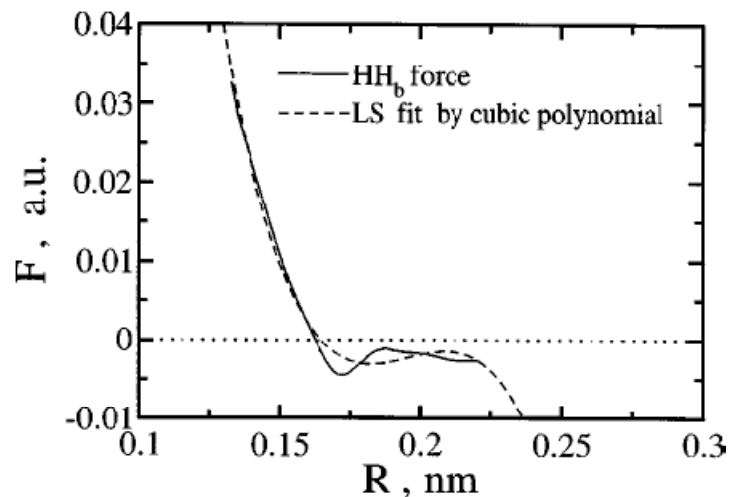


Fig. 7.23. Example of force fitting taken from (Izvekov 2004); intramolecular component of the HH effective force field (solid line) and least-squares fit using a cubic polynomial (dashed line).

This is intended as a means to properly compute the Kanzaki forces (Kanzaki 1957, Simonelli 1994) and the defect formation volumes. When applied to some perfect harmonic forces, Kanzaki forces produce the same displacements as the defect, so that they can be thought to represent the forces with which the defect interacts with its neighboring atoms. For us, they will allow a better fit of the interatomic potentials for Li-He and Pb-He that is the ultimate aim of our work.

7.5 Conclusion

To summarize, we have determined some elementary properties of He in Pb and Li by *ab initio* calculations. The most stable configuration for He in interstitial configuration is the substitutional one both in fcc Pb and bcc Li. For lithium both tetrahedral and octahedral interstitial are similar energetically. For Pb the octahedral position is slightly favoured. Our spin-orbit coupling calculations suggest that the magnetism in fcc Pb affects the formation energy of He interstitials but does not alter their relative stabilities. Charge transfer and hybridization effects are being carefully examined.

SOC calculations are important because relativistic effects are necessary to explain the fcc structure of Pb. Indeed, a non-relativistic simulation predicts that Pb is more stable in the diamond structure than in the fcc structure (Christensen 1986). However SOC simulations are much more expensive from a computational point of view and some further calculations (relaxation of Pb+He systems) are still necessary before draw our conclusions and publish the results.

The simulations presented in this chapter are the first step to develop a ternary interatomic potential for LiPb+He classical molecular dynamics simulations. He interaction with both Li and Pb will be mainly repulsive as expected. However taking into account spin orbit coupling in the Pb simulations could give a different set of forces leading ultimately to a different potential.

Appendix 1

Exploring the limits of classical molecular dynamics.

Liquid Li and Pb under high pressure

This Appendix is a continuation of the Li and Pb EAM potentials validation. In Chapter IV we presented the results of our simulation of liquid Li and Pb under normal conditions. Here we will present a study of the suitability and limits of application of EAM potentials for the simulation of liquid metals under high pressures. The main results were presented in the “New insights on metals under extreme conditions” International Congress, in Paris on December 13th to 15th of 2012.

A1 Introduction

Materials at high pressures occur at the centers of planets and in stars and in both natural and man-made explosions. In fact, liquid metals like iron (at high pressures) has significant importance in geophysics, being the main constituent of Earth’s liquid core (Shen 2004) and many other terrestrial planet cores. Recent investigations (Yoder 2003) indicate that the Martian core could be also entirely liquid. Silicate melts and glasses under pressure are of geological interest for understanding physical and thermo-dynamic behaviours of magmatic liquids under the Earth’s crust and mantle (Matsui 2003).

High pressures may also be applied to small laboratory samples in a controlled manner using devices such as the diamond anvil cell (DAC). The static pressure applied in a DAC is a

continuously variable parameter which can be used for systematic studies of the properties of solids as a function of the interatomic distances (Holzapfel 1996).

We pause to mention some facts about Li and Pb pertinent to this study. Li, as well as all alkali metals, was considered in the past a “simple” metal and its electronic properties well described by the nearly free electron (NFE) model. Lithium adopts the body centered cubic (bcc) form at ambient conditions. The first high-pressure phases for alkali metals are known to have the face-centered cubic (fcc) structure (Olinger 1983). At still higher pressures, they possess complex crystal structures, unexpected for elemental solids (Xie 2008). Lead is also highly compressible, and should, therefore, exhibit phenomena that for other substances are typically seen at higher P . A transition to the hcp structure occurs at 14 GPa and a further transition to the bcc structure is observed around 110 GPa ((Mujica 2003) and references therein).

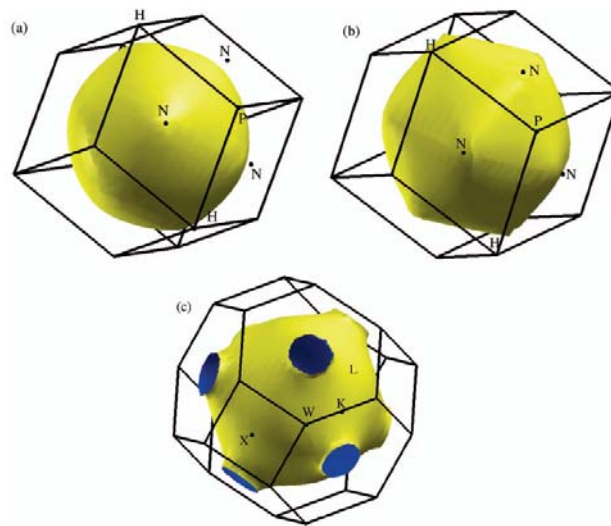


Fig. A1. Fermi surface of bcc lithium at (a) equilibrium and (b) $P=8$ GPa and fcc at (c) $P=30$ GPa. Taken from ref (Rodriguez 2006).

The $\text{bcc} \rightarrow \text{fcc}$ transition in alkali metals has been attributed to $s \rightarrow d$ electrons transfer for K, Rb, and Cs, and $s \rightarrow p$ electrons transfer for Li (Rodriguez 2006). The spheroidal Fermi surface at equilibrium becomes increasingly distorted under pressure and at 8 GPa, corresponding to the experimentally observed bcc-fcc transition, contacts the Brillouin zone boundary at the bcc Γ_N point. At 30 GPa the Fermi surface shows increasing necks along Γ_L and, develops an extended nesting along several directions, which becomes the origin of profound modifications on its physical properties (Rodriguez 2006).

A2 Computational details

MD methods have been extensively exploited to obtain static and dynamic properties of simple liquid metals. The accuracy of the classical MD simulations relies on the ability of the model used in these simulations to reproduce either experimental data or the results of *ab initio* calculations. The embedded atom model (EAM) potential (Daw 1983, Foiles 1985) has often been found to successfully describe the thermodynamics and transport properties of liquid metals in several works (Foiles 1985, Bogicevic 1997) to name a few. However, the limitations of the EAM potentials are well known: it works best for purely metallic systems with no directional bonding; it does not treat covalency or significant charge transfer; and it does not handle Fermi-surface effects (Daw 1993).

The MD study reported here attempts to validate two interatomic potentials for metals like Pb or Li under high pressures. We test Pb and Li EAM potentials existing in the literature (Belaschenko 2009, Zhou 2001). Previously both potentials have shown to describe fairly well both liquid metals under normal conditions (see Chapter 4 and Ref. (Fraile 2013) for details).

As explained before, MD simulations were carried out using the parallel code LAMMPS (Plimpton 1995). The integration time step Δt used for the heating and equilibrating phases was 10^{-4} ps. In the production phase we used a Δt of 10^{-5} ps and we always tested in both cases a proper convergence. Average length of simulation time in production stage (equilibrium) was around 50 ps. In this work, *NPT* (constant number of particles together with constant pressure and temperature) simulations were performed. Periodic boundary conditions were applied. To obtain a desired average pressure P and temperature T , the Hoover algorithm was used to form the Nosé-Hoover thermostat and barostat for the equations of motion (Martyna 1992). Langevin (dissipative) dynamics has been used as well and results are found to be almost identical for liquids. See Chapter 3 for further details.

A3 Results; Validation of the Li and Pb EAM potentials

A solid model interatomic potential for MD simulations (EAM -type in our present case) must be able to provide a good representation of dynamics, thermodynamics and structural properties of the target material under conditions relevant for technology.

Size effects have been checked. Simulations results are exactly the same with 2,000 atoms and 16,000 atoms. From the output volume at different final pressures bulk modulus can be easily calculated. The bulk modulus, B, can be formally defined by the equation:

$$B = -V \frac{\partial P}{\partial V} \quad (\text{A.1})$$

where P is pressure, V is volume, and $\partial P/\partial V$ denotes the partial derivative of pressure with respect to volume. The inverse of the bulk modulus gives a substance's compressibility, χ_T , i.e. ($\chi_T = -1/V)(\partial V/\partial P)$.

We have carried our several MD simulations at different pressures. The system has been carefully equilibrated at 300 K and pressure ranging from 0 to 10 GPa.

	Experimental (300 K)		MD	
	B	B'	Heating	Cooling
Pb	44.8	4.87-5.74	49.2	39.5
Li	11.2	3.62	24.4	11.6

Table A.I. Experimental bulk modulus (Ashcroft 1976), B, (in GPa) and its derivative, B', and MD results using Pb and Li EAM potentials described above (T = 300 K).

According to Olinger (Olinger 1983) the bulk modulus reported in (Swenson 1966) was calculated from piston displacement measurements up to 2.0 GPa. They found that Lithium bulk modulus and its pressure derivative are 11.2 GPa and 3.60. Therefore we have calculated B applying pressures up to 2 GPa. In fact a non linear behavior is found in volume when applying higher pressures, both in Li and in Pb.

The heating result for Pb agrees well with the experimental value while the cooling result underestimates the value. The structure of Pb in our cooling simulations is not anymore an fcc structure but some disordered one. For lithium, our result in bcc phase (heating) is wrong, being more than twice the correct value. The result for Li in amorphous phase (cooling result) agrees well with the experimental result. It has to be taken in mind that the Li potential was developed to simulate liquid lithium and is not expected to work well in solid-crystal simulations. In the best case it could work to simulate amorphous lithium [Belaschenko private communication].

A3.1 Bulk modulus in liquid phase

We have found sound speed data for liquid lithium in (Yokoyama 2001). In a fluid, the bulk modulus, B , and the density, ρ , determine the speed of sound, c , (pressure waves), according to the Newton-Laplace formula

$$c = \sqrt{\frac{B}{\rho}} \quad (\text{A.2})$$

Solids can also sustain transverse waves: for these materials one additional elastic modulus, for example, the shear modulus is needed to determine wave speeds. We have used Eq. (A.2) to calculate bulk modulus and compare with the results of our MD simulations. Pb data has been taken from (Mustafin 1983). Main results are summarized in next figure.

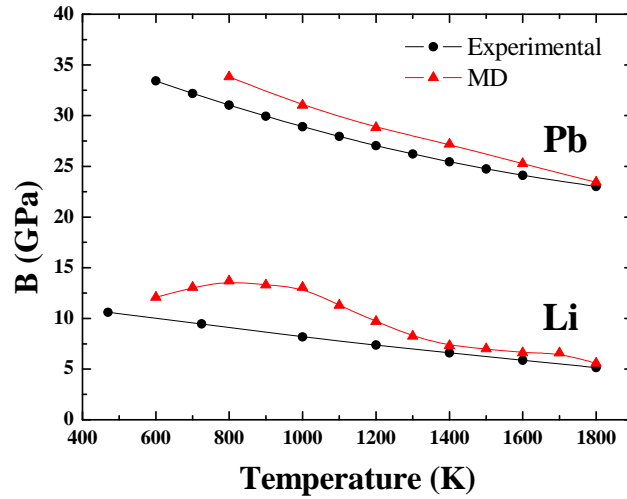


Fig.A2: Bulk modulus for liquid Li and Pb at different temperatures. The experimental values of Pb are taken from (Mustafin 1983). Li experimental values have been calculated from (Yokoyama 2001) using Eq (A.2).

As can be seen in Fig A2, our Pb results match fairly well the experimental data. However the Li MD results show an anomaly at low temperature (800 to 1100 K) whose origin is not yet clear.

A3.2. Structural properties

Liquid structures are defined by means of the pair distribution function, $g(r)$, and/or the total structure factor $S(q)$. The relation between both quantities is the Fourier Transform ($g(r) \rightarrow \text{TF} \rightarrow S(q)$ and *vice versa*). Details can be found elsewhere (Waseda 1980). Our calculations of Li and Pb pair distribution function, $g(r)$, using the EAM potentials under normal conditions, have proved to be in very good agreement with experiment (see Chapter 4).

Here we compared the calculated $g(r)$'s at different pressures and temperatures, with available *ab initio* calculations. As far as we are concerned no experimental results have been published.

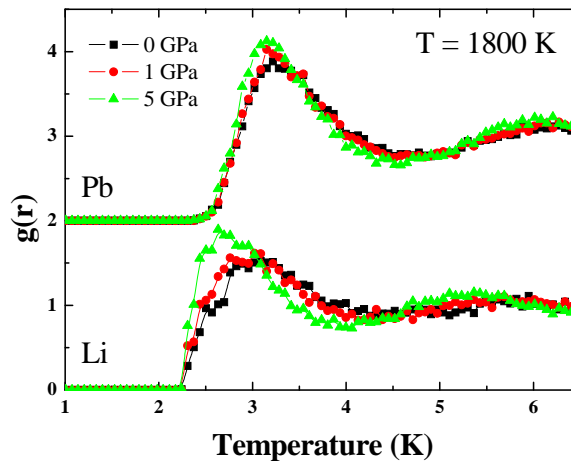


Fig. A3. Lithium and lead (shifted 2 units upwards) $g(r)$ at different pressures (0, black squares, 1 GPa red circles, 5 GPa green triangles) at $T = 1800$ K.

Figure A3 shows the Li and Pb at different pressures. The smooth radial distribution functions shown in Fig. A3 are characteristic of a liquid state. As the pressure increases, the $g(r)$ peaks become more distinctly separated, indicating increase of a structuring in liquid, more clearly in Li than in Pb.

However, the position of the first peak moves to lower r while in the recent work of Yang *et al* (Yang 2010) the shape of the RDF does not change up to 10 GPa, indicating uniform compression at low pressure. In their simulations at higher pressures the first peak broadens and the height decreases slightly, a feature not observed in our Li simulations.

Next figures show pair distribution functions for Li and Pb. For Li we can compare with *ab initio* calculations up to 20 GPa. The results are similar for pressure up to 5 GPa but quite different for 20 GPa as can be seen in Fig. A4.

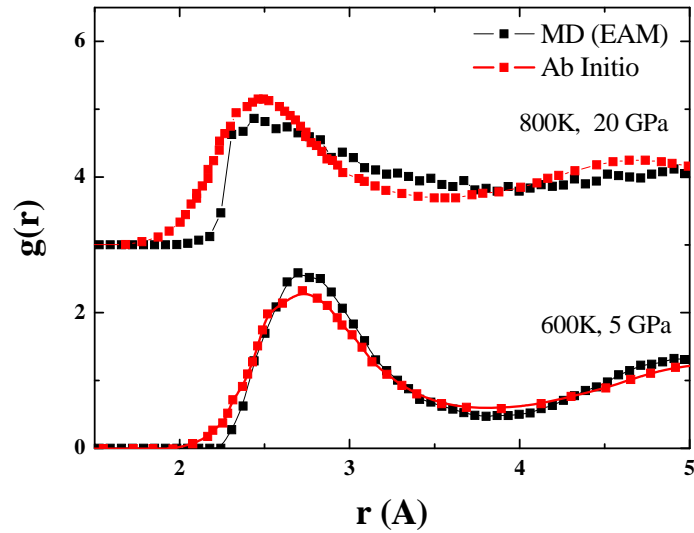


Fig. A4. Lithium $g(r)$ at high pressures and high temperatures as labelled. Red line represents the same result from *ab initio* calculations taken from Yang *et al* (Yang 2010).

For Pb we have not found low pressure $g(r)$ experimental or *ab initio* data. In the *ab initio* calculations of (Cricchio 2006) high temperature and high pressure is reported.

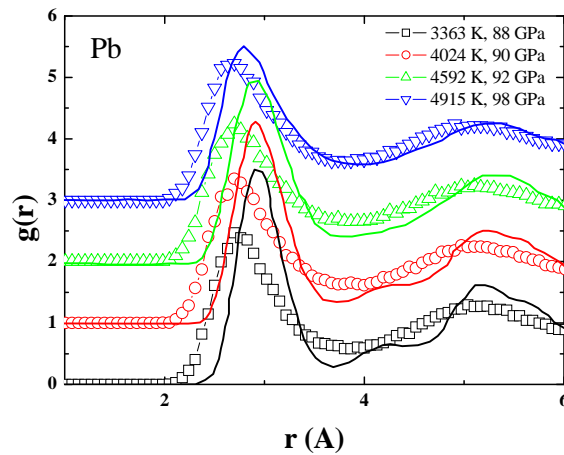


Fig. A5. Lead $g(r)$ at very high pressures and high temperatures as labelled. Symbols are our MD data and lines represent the same result from *ab initio* calculations (Cricchio 2006).

In next figure we show our MD results confronted to the $g(r)$ curves reported in (Cricchio 2006). The structure in our simulations seems to be similar but denser than the *ab initio* calculations as can be deduced from the shifting of the first peak to lower radius.

A3.4. Uniform compression model

In next figure we examine the classical theory of liquid metals as proposed in (Waseda 1980). According to Waseda an increase of k_2/k_1 ratio (or r_2/r_1) indicates that a liquid is no longer a simple isotropic liquid but that the local structural environment is becoming more anisotropic. Linear fit values in fig. A6 are: $A = 1.94$ and $B = -0.00334$ for Pb ($T = 1800$ K) and $A = 1.961$ and $B = 0.00062$ for Lithium ($T = 1700$ K). This result agrees with the first principles studies of (Yang 2010). In their work they show that below 30 GPa the ratio k_2/k_1 is nearly constant (~ 1.90), close to the value of 1.86 expected for a simple liquid metal (Waseda 1980) where the local potential interaction is isotropic (Hansen 1986). If the ratio k_2/k_1 is constant then the same can be said of the r_2/r_1 ratio that is the result we show in Fig. 5.

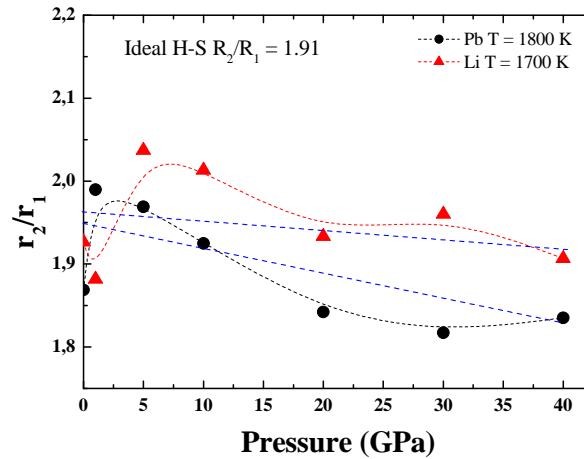


Fig. A6. r_2/r_1 ratio for liquid Pb and Li at different temperatures (Pb 1800 K, black circles and Li 1700 K red triangles) and pressures up to 40 GPa (Dashed blue lines are linear fits).

Experimental measurements have revealed that compressions of liquid alkali metals are almost uniform, whereas those of liquids that have covalent components in bonding are mostly anisotropic (Waseda 1980). For covalent liquids, the volume dependence of the nearest-

neighbour distance deviates from $(V/V_0)^{1/3}$ behaviour (V being the molar volume and V_0 being the molar volume at zero pressure) and changes in coordination play important roles. In some elements, different types of volume dependence of the nearest neighbour distances are observed in different pressure ranges.

Uniform compression is observed in simple metallic liquids (alkali metals). Various degrees of deviation of r_1 from the uniform compression model are observed in not-simple liquid metals. Compression of the low dimensional structures is mainly due to closer packing of the structural units.

Next figures shows $r_1/r_{1(0)}$ for Li and Pb. If the liquid is compressed uniformly, $r_1/r_{1(0)}$ follows a relation of $r_1/r_{1(0)} = (V/V_0)^{1/3}$. The relation is indicated by a blue dashed line in both figures. Applied pressure ranges from 0 to 60 GPa. Li follows the uniform compression model up to 20 GPa (around twice its bulk modulus). Interestingly Pb departs from uniform compression at low pressures, 5 GPa at low temperature (1000 K) and 20 GPa for high temperatures (1800 K).

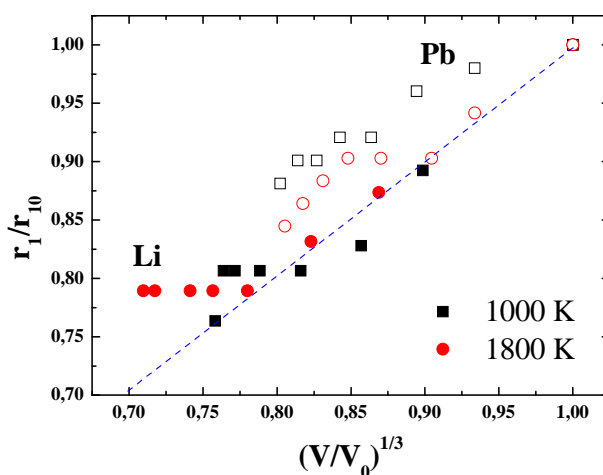


Fig. A7. Volume dependence of nearest-neighbour distance, r_1 , for liquid Li (full symbols) and Pb (open symbols). Volume, V , and r_1 are normalized by values at atmospheric pressure, V_0 and $r_{1(0)}$, respectively, and $(r_1/r_{1(0)})$ is plotted as a function of $(V/V_0)^{1/3}$.

While the liquid structure of many metallic elements is described by a simple hard-sphere-like structure with coordination number of 9–11, that of some metallic elements shows deviations from the simple structure. Elements that have covalent bonds and open-packed crystalline structures, such as three-dimensional network (group IV elements), layer (group V) and chain (group VI) structures, melt into liquids that are characterized by low coordination numbers.

Covalent characters in the bonding remain in the liquid state for those elements. In fact, these liquids are poor metals or semiconductors.

Further increase of pressure often induces a structural phase transition. In general, elements that have open-packed crystalline structure transform toward dense-packed structure through successive pressure-induced phase transitions: coordination number, CN, increases at the transitions. For example, Si transforms from diamond structure (CN = 4) to the β -tin structure (CN = 6), orthorhombic phase (CN = 6), simple hexagonal structure (CN = 8), orthorhombic phase (CN = 10, 11), hexagonal close-packed structure (CN = 12) and face-centred cubic structure (CN = 12), see for example (Yao 2012) and references therein.

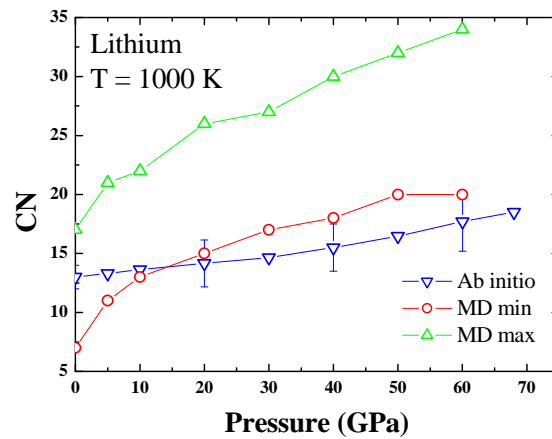


Fig. A8. Maximum and minimum coordination number (CN) of lithium atoms at high pressures ($T = 1000$ K) compared to *ab initio* calculations (Yang 2010).

The electronic structure also changes under pressure and a non-metal to metal transition usually takes place. Not only covalent solids, but also some metallic elements, exhibit pressure-induced structural transitions. In exceptional cases, a decrease of the coordination number is observed in a high-pressure phase [30]. Figure A.8 show the CNA analysis of our MD simulations compared to the *ab initio* calculations taken from (Yang 2010).

As has been anticipated in the introduction, both Li and Pb present several phase transitions under high pressure. Here we present some simple tests in order to check the ability of both potentials to “see” that phase transitions. The system is equilibrated at a certain temperature and

then pressure is increased in several steps, with enough time to allow the system reach equilibrium. Needless to say, this is not a thoroughly study of phase transitions. However, the main result, roughly, is that, in both cases, the system orders in the expected crystal structure at high pressures.

A3.5. Liquids under high pressure

Alkali metals are usually considered as simple metals because of the simple electronic structure with just one conduction electron outside the closed-shell configurations. The NFE model is known to be a good approximation to describe their electronic properties due to the weak interaction between valence electrons and ionic core under ambient conditions. However, under high pressure, the NFE description of alkali metals fails as evidenced by the complex sequence of phase transitions (Xie 2008). Lithium presents a structural phase transition (from bcc to fcc lattice) at high pressures (Olinger 1983), exactly at 7.5 GPa. The other alkali metals having the bcc structure at low pressure transform to an fcc modification, Na at 65 GPa, K at 11.5 GPa, Rb at 7 GPa, and Cs at 2.3 GPa, respectively ((Xie 2008) and references therein).

To analyse the liquid structure we can make use of the common neighbour analysis (CNA) method (Honeycutt 1987, Cleveland 1999). The CNA algorithm performs a simple geometric analysis of the first shell of nearest neighbours around a reference atom. One by one, the arrangement of atoms within a certain distance between itself and one of its nearest neighbours is analysed. The number of next neighbours and the arrangement of the common neighbours with each of them can then be compared with the situation in perfect crystal structures. This method is implemented in OVITO (Stukowsky 2008). For an extension of the CAN method to binary system see (Lümmen 2007).

Pb crystallizes in the fcc structure under normal conditions. A first transition to the hcp structure is observed at 14 GPa (Takahashi 1969). At about 110 GPa a further transition to the bcc structure is observed (Vanderborgh 1989, Mao 1990). In both cases the volume reduction is very small and there is a large region of phase coexistence, consistent with a very small enthalpy difference between the phases over a large pressure interval.

In Figure A9 we present the CNA analysis at 2000 K vs pressures for Li and Pb (MD cooling runs and $N = 5000$ atoms). A clear jump in the number of atoms in an fcc structure takes place around 7 GPa, as expected. Regarding the Pb CNA analysis does not show a clear change from fcc to hcp order at low pressure. It has to be noted that the fcc and hcp CS differ only in the third and next NN and, for Pb, the energies are very similar. Some ordering to a bcc structure takes place around 100 GPa.

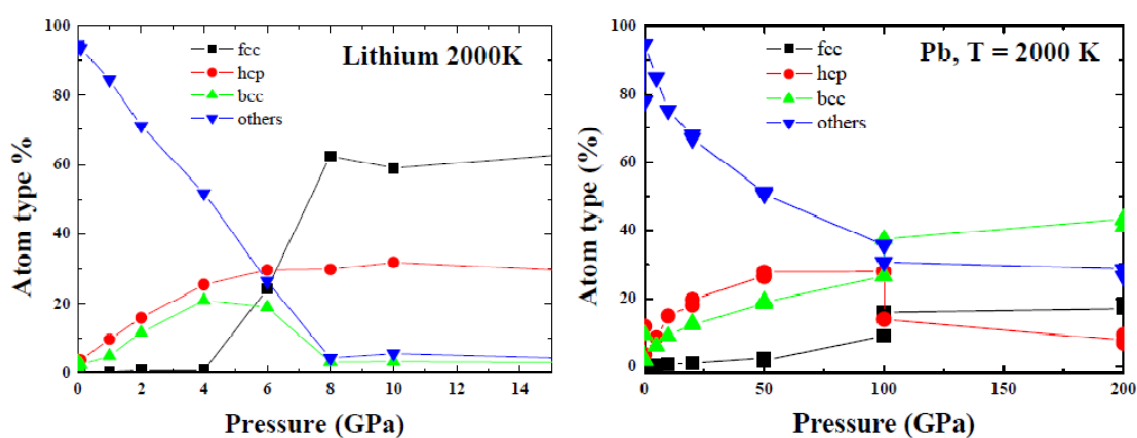


Fig. A9. Left) Li CNA analysis at 2000 K vs pressures. A clear jump in the number of atoms in an fcc structure takes place around 7 GPa, as expected. Right) Pb CNA analysis at 2000 K vs pressures. Some ordering to a bcc structure takes place around 100 GPa.

The results presented in Figure A9 are not definitive. Size effect has been checked and the CNA results are size dependent (See Fig A10). In both simulations the number of atoms is around 120000. However the main result about lithium remains. At high pressures, our liquid lithium becomes a mixture of nanocrystals with different crystal structures (see Fig. A10 (left)), what explain the CNA graphics shown above. For Pb the ordering to a high pressure bcc phase is not clear if the simulation is big enough (see Fig A10 (right)).

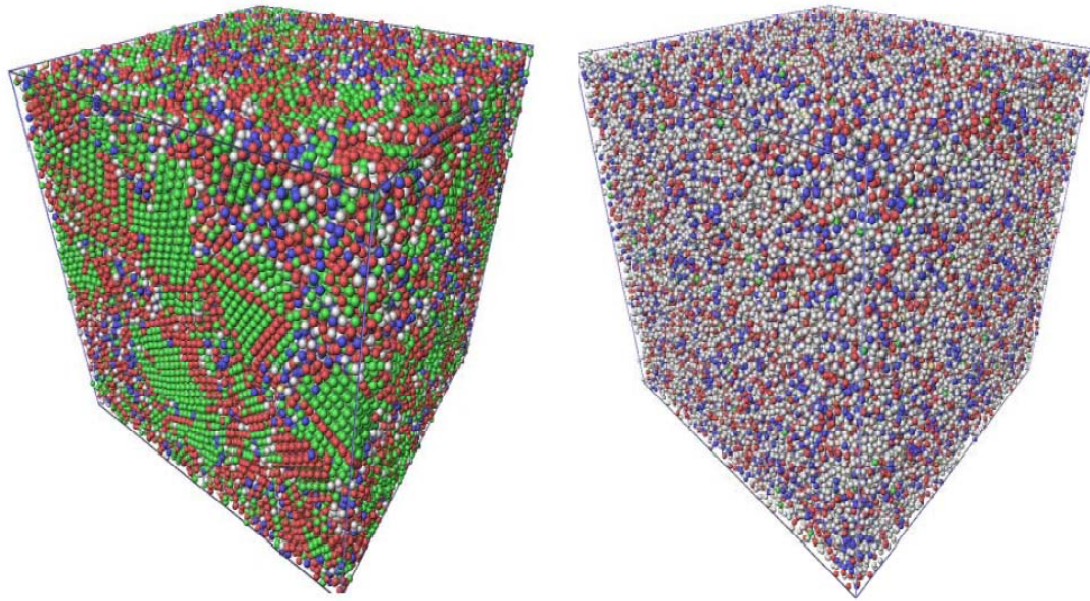


Fig. A10. Left) Li CNA visualization at 2000 K and $P = 20$ GPa. ($N = 120000$ Atoms). Green spheres correspond to fcc atoms, red ones to hcp, blue to bcc and white to others. Right) Pb under pressure ($P = 200$ GPa and $T = 2000$ K) visualization of CNA.

A3.6. Thermodynamics

Thermodynamic properties under high pressure are, in general, difficult to measure. We pay attention in this section to the prediction by both potentials of the melting temperature change with applied pressure of Li and Pb and we will compare with experimental and or theoretical predictions.

A3.6.1 Melting point

Melting point changes in general when applying pressure. But most of the interatomic potentials are not developed to study materials under high pressures. Changes in melting point and phase transitions are due to rearrangement or changes of electronic structures so one should not expect to simulate correctly this kind of behaviour with simple interatomic potentials.

Melting point of metals under high pressure has been studied by *ab initio* methods (Mujica 2003, Yang 2010) and also in CMD simulations (Belonoshko 2000). Every technique has its own limitations and drawbacks, for example because of the mentioned sequence of phase transitions. In our previous work (See Chapter 4) we made use of the Hamiltonian switching method (Ciccotti & Hoover 1986) to calculate the melting point of Li and Pb with fairly good agreement with experimental values (Fraile 2012). However that technique presents a number of difficulties for high pressure calculations. Here we have tested both Li and Pb potentials just doing a simple estimation of melting point from jump in enthalpy (and or volume) in MD runs. In figure A11 we present the MD runs for Pb at different pressures applied from the beginning of the simulation, starting from an fcc perfect lattice.

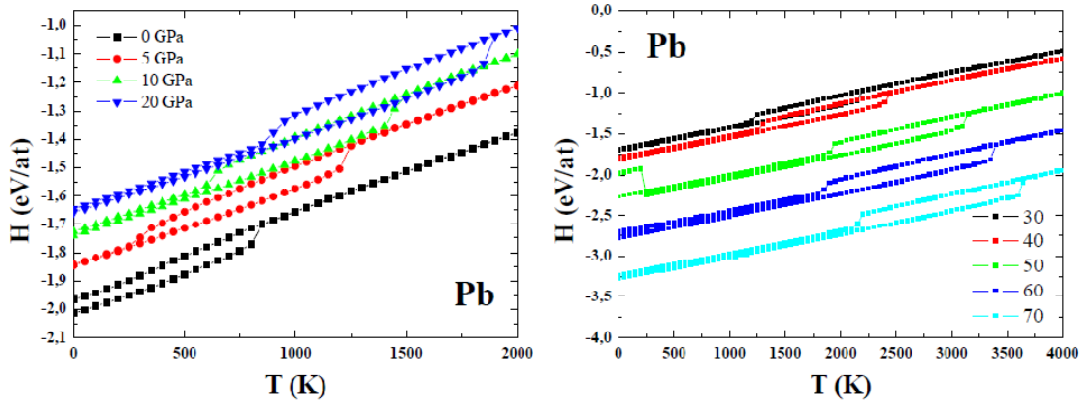


Fig. A11. Low (left) and high (right) pressure heating-cooling Pb MD simulations: Enthalpy vs temperature at different pressures as labelled.

Enthalpy first decreases (in absolute value) with pressure up to 20 GPA and then increases when we apply higher pressures.

The jump overestimates the melting point as expected, but interestingly the melting temperature vs pressure slope, dT_m/dP , (see Fig. A.13) is very close to the experimental one (Cricchio 2006).

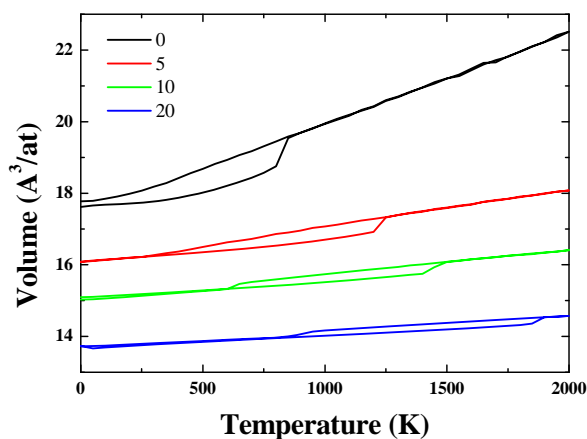


Fig. A12. Low pressure Pb MD simulations. Pb volume versus temperature at different pressures. Clearly the jump in volume decreases when pressure is applied.

Same method was attempted for lithium but the melting was not as clear as in Pb at pressures higher than 10 GPa. Inset in Figure A.13 shows the results at low pressure for Li.

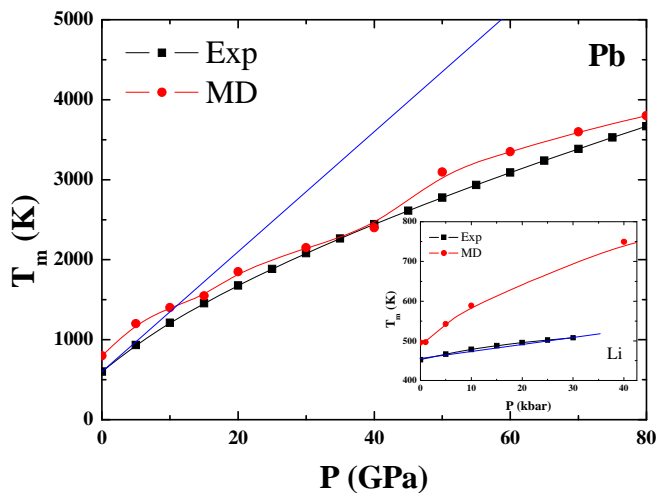


Fig. A13. Pb and Li (inset) melting point estimated from MD runs (red circles) compared with experimental values (black squares) at different pressures; from 0 to 5 GPa for Li and up to 80 GPa for Pb. Blue line stands for the Lindemann predictions for Pb (Errandonea 2010) and Li (Kraut 1996).

For lead, the change in melting point is about 36 K/GPa, pressures ranging from 0 to 80 GPa. For Li the experimental value is around 18 K/GPa but only from 0 to 3 GPa. At higher pressures

Li behaviour is complex and melting points decreases with pressure showing a minimum around 65 GPa according to ab initio calculations (Tamblyn 2008). But experimental confirmation is not yet available. Our simulations overestimate the value of dT_m/dP for lithium giving a value of 50 K/GPa. Nevertheless our heating-cooling simulations again show some kind of transition around 7-8 GPa as observed in the experiment and reported above. For lead the MD results are better.

The melting temperature as a function of pressure can be roughly estimated using the Lindemann law (Lindemann 1910). The validity of the Lindemann law to estimate the melting curve of different metals has been discussed (Errandonea 2010). As can be seen in Fig. 11 the Lindemann law remains valid for Pb only up to 5-10 GPa. For Li the estimation following (Kraut 1966) seems to be valid at low pressures ($P < 4$ GPa).

A4 Conclusions

At high temperatures and pressures, thermal excitation of collectivized and internal ionic core electrons can occur, and a contribution to energy (and pressure) not related to the interparticle potential can appear. The main difficulty of using the EAM method for liquid metals simulation under extreme conditions is uncertainty about the electronic contribution to heat capacity at a high temperature. This uncertainty is especially large for highly compressible alkali metals because of unclear role of electron heat capacity [D. Belaschenko private communication]. Also important, at high pressure, the overlap between diffuse Li 2p orbitals become progressively stronger (Yang 2010) so CMD is not expected to correctly describe the system anymore.

An interesting result is found regarding bulk modulus of liquid Li (see figure A2). The origin of the anomaly observed in the calculated values is not clear. It has to be noted that liquids can exist in two qualitatively different states: “rigid” and “nonrigid” liquids as recently proposed by Brazhkin and coworkers (Brazhkin 2012). They call the division line the “Frenkel line”. Crossing this line qualitative changes in the temperature dependencies of sound velocity, diffusion, viscous flow and many others are found.

As far as we are concerned this Frenkel line has not been calculated for lithium (or lead) yet. However, regarding liquid Li, what have been already reported are the two relaxation processes,

fast and low, present in the liquid according to diffraction experiments (Scopigno 2000). The effect of these two modes in the bulk modulus of liquid lithium is not clear at present. Work is in progress to fully clarify this point.

However, classical Molecular Dynamics simulations via EAM potentials have showed to be a powerful tool to simulate and understand liquid metals, in our particular case, lead and lithium. Our results prove the validity of these potentials and provide useful structural and thermodynamic data under high pressures (up to 5 or 10 GPa). Reported figures are in agreement with experimental results available in the literature up to certain limits. In addition, our work represents a base methodology for the extrapolation of liquid Pb and Li properties into regions of temperature and pressures where direct experimental measurements either do not exist, or are not accessible.

In general, both potentials are realistic up to pressures around half the bulk modulus of the solid material. Structural properties can be well modeled with EAM potentials. Thermodynamic properties are much more difficult to match. For a realistic study of liquid under pressure ZBL modification (Ziegler 1985) of short range part of pair potentials is strongly encouraged as anticipated in Chapter 3.7.

References and bibliography

Ahmed E., Akhter J. I. and Ahmad M. Molecular dynamics study of thermal properties of noble metals. *Computational Materials Science* 31 (2004) 309–316

Angelo J. E. *et al.* Trapping of hydrogen to lattice-defects in nickel. *Modelling Simul. Mater. Sci. Engr.* 3, 289-307 (1995). Correction: M. I. Baskes *et al.*, *Modelling Simul. Mater. Sci. Eng.* 5, 651-652 (1997).

Albrecht J, Thompson A W and Bernstein I M 1979 *Metall. Trans. A* 10 1759

Alder, B. J.; T. E. Wainwright (1959). "Studies in Molecular Dynamics. I. General Method". *J. Chem. Phys.* 31 (2): 459.

Alejaldre C. *et al.*, TJ-II project: A flexible heliac stellarator, *Fusion Technol.* 17, 131 (1990).

Alejaldre C. *et al.*, First plasmas in the TJ-II flexible heliac, *Plasma Phys. Control. Fusion* 41, A539 (1999).

D. Alfè, M. J. Gillan and G. D. Price, *J. Chem. Phys.* 116, 6170 (2002).

Allen M. P. and Tildesley D. J., *Computer Simulations of Liquids*, (1987), Clarendon Press, Oxford.

Allen H. Boozer. *Phys. Plasmas* 19, 058101 (2012); (25pp). Theory of tokamak disruptions.

Almazouzi A, Victoria M, Caturla M.J. and Rubia T.D.d.l. A Hierarchical Computer Simulation Model for the Evolution of the Microstructure Produced By Displacement Cascades In Metals, *EPFL Supercomputing Review*, 10(Nov), 1998.

Amendt P. *et al.* *Phys. Rev. Lett.* 105, 115005 (2010).

Anusionwu B.C. *et al.* Influence of strong heterocoordination on surface properties of Li–Pb melts. *Physics and Chemistry of Liquids* Vol. 43, No. 6, (2005), 495–506

Apostol F. and Mishin Y. Angular-dependent interatomic potential for the aluminum-hydrogen system. *Phys. Rev. B* 82, 144115 (2010).

Appleton B., 'Status of the Oak Ridge Spallation Neutron Source (ORSNS) Project' *Proc. ICANSXIII*, Villigen, 1995 PSI Proceedings 95-02 p.814

Arndt R. E. A. Cavitation in Fluid Machinery and Hydraulic Structures. *Annual Review of Fluid Mechanics*. Vol. 13: 273-326 (1981)

Ashcroft N. W. and Langreth D. C. 1967 *Phys. Rev* 156 500.

Ashcroft, N. W. and Mermin, N. D. (1976). *Solid State Physics*. Holt, Rinehart and Winston.

ASM alloy Phase Diagram centre website

Atkins P. W., *Physical Chemistry* (Oxford University Press, Oxford, 1990).

Atzeni S and Meyer-ter-Vehn J 2004 *The Physics of Inertial Fusion* (Oxford: Oxford University Press)

Atzeni S. *et al.* Studies on targets for inertial fusion ignition demonstration at the HiPER facility. *Nucl. Fusion* 49 (2009) 055008 (7pp)

- Atzeni S. Studies on the robustness of shock-ignited laser fusion targets. *Plasma Phys. Control. Fusion* 53 (2011) 035010 (15pp)
- Bader R. F. W. 1990 *Atoms in Molecules: a Quantum Theory* (New York: Oxford University Press).
- Bader R. F. Theory to characterize atoms and chemical bonds from the topology of the electron density. (http://www.chemistry.mcmaster.ca/faculty/bader/aim/aim_0.html)
- Bader Code website: <http://theory.cm.utexas.edu/vtsttools/bader/>
- Bagchi B. et al, *Adv. Chem. Phys.* 116, 67 (2001).
- Barker M.G. and Capaldi M. J. The deposition of corrosion products in Pb17Li. *Journal of Nuclear Materials*. Vol. 212–215, B, 1994, Pp 1534–1537
- Baskes M. I., *Phys. Rev. B*, 62 (1992) 2727.
- Baskes M. I., *Mater. Chem. Phys.*, 50 (1997) 152.
- Baskes M. I. (1988), *MRS Bulletin*, 13, 28
- Bazhiron T. T., Norman G. E. and Stegailov V. V. Cavitation in liquid metals under negative pressures. *Molecular dynamics modeling and simulation. J. Phys.: Condens. Matter* 20 (2008) 114113 (11pp).
- Bearman R.J. and Jolly D.L., *Mol. Phys.* 44, 665 (1981)
- Beck D.E. A new interatomic potential function for helium. *Mol. Physics: Vol.* 14, 4, 311-315 (1968).
- Becker C. A. and Kramer M. J. Atomistic comparison of volume-dependent melt properties from four models of aluminum. *Modelling Simul. Mater. Sci. Eng.* 18 (2010) 074001 (15pp).
- Belashchenko D. Application of the Embedded Atom Model to Liquid Metals: Liquid Lithium. *High Temperature* vol 47 No 2 211-218.(2009).
- Belashchenko D. K. *Inorganic Materials*, Vol.48, No. 1, pp. 79–86 (2012).
- Belonoshko A.B., Ahuja R. and Johansson B. Quasi–Ab Initio Molecular Dynamic Study of Fe Melting. *Phys. Rev. Lett.* 84, 3638–3641 (2000)
- Betti R. et al., *Phys. Plasmas* 17, 058102 (2010).
- Berendsen H. J. C., et al, *J Chem Phys*, 81, 3684 (1984).
- Berendsen H. J. C. et al. "Molecular-Dynamics with Coupling to an External Bath". *Journal of Chemical Physics* 81 (8): 3684–3690 (1984).
- Bergman C and Komarek K L 1985 *Calphad* 9 1-14
- Bezbatchenko A.L. *et al.* *Plasma Physics and the Problem of Controlled Thermonuclear Reactions* (transl) (New York: Pergamon) vol 4 p 116–33
- Bhatia A. B. and Thornton D. E. 1970 *Phy. Rev B* 2 3004-12.
- Bhattacharyya S. et al. *J. Chem. Phys.* 106, 1757 (1997).
- Bhuyan P.J., Goswami K.S. Development of a potential based code for MHD analysis of LLCB TBM. *Fusion Engineering and Design* 85 (2010) 138–145

- Bickerton R. J. Magnetic turbulence and the transport of energy and particles in tokamaks. *Plasma Phys. Control. Fusion* 39 (1997) 339–365.
- Biermann Chr. *et al.* *Journal of Non-Crystalline Solids*. Vol 232–234, Pp 309–313 (1998)
- Biersack J.P., Ziegler J.F., *Nucl. Instr. and Meth.* 194 93 (1982).
- Binder D. & Stauffer K. *Advances in Physics*, Vol 25, 4, (1976) pp 343-396
- Binder K., ed, *Monte Carlo Methods in Statistical Physics*, (1986), second edition, Springer-Verlag.
- Binder K., ed, *Applications of the Monte Carlo Method in Statistical Physics*, (1984), Springer-Verlag.
- Binder K., ed, *The Monte Carlo Method in Condensed Matter Physics*, (1992) Springer-Verlag.
- Birnbaum H. K. and Wert C. A. Diffusion of Hydrogen in Metals. *Berichte der Bunsen-Gesellschaft*. 76 Nr 8 (1972)
- Blander M. and Katz J.L., “Bubble nucleation in liquids”, *AICHE J.*, 21, pp. 833-848 (1975).
- Bloch F., Über die quantenmechanik der elektronen in kristallgittern, *Zeitschrift für Physik* 52 (1928) 555–600.
- Blöchl P. E., *Phys. Rev. B* 50, 17 953 (1994).
- Blöchl P. E., Jepsen O. and Andersen O.K. *Phys. Rev. B* 49, 16223 (1994)
- Bloom E.E., "Structural materials for fusion reactors", *Nucl. Fusion*, 33, 1879-1896 (1990)
- Boehly T. R. *et al.*, *Opt. Commun.* 133, 495 (1997).
- Bogicevic A. *et al.* *Phys Rev. E* Vol. 55, No 5 (1997).
- Bohm D. The characteristics of electrical discharges in magnetic fields; ed A. Guthrie and R. K. Wakerling (New York: McGraw-Hill) (1949).
- Boozer A. H. Physics of magnetically confined plasmas. *Rev. of Modern Physics*, Vol. 76, (2004)
- Born M., Mayer J.E., Zur gittertherorie der ionnenkristalle, *Z. Phys.* 75 (1932) 1–18.
- Braams C. M. and Stott P.E., “Nuclear Fusion. Half a Century of Magnetic Confinement Fusion Research”. IOP Publishing Ltd, Bristol (2002).
- Brandes E.A. (Ed.), *Smithshells Metals Reference Book*, 6th ed., Butterworths, London, 1983.
- Brazhkin, V. V., Popova, S. V. & Voloshin, R. N. High-pressure transformations in simple melts. *High Pressure Res.* 15, 267-305 (1997).
- Brazhkin V. V. *et al.* Two liquid states of matter: A dynamic line on a phase diagram. *Phys. Rev. E* 85, 031203 (2012)
- Brommer P. and Gähler F., *Philos. Mag.* 86, 753 (2006).
- Brommer P. and Gähler F., *Modell. Simul. Mater. Sci. Eng.* 15, 295 (2007); more information about POTFIT is found at <http://www.itap.physik.uni-stuttgart.de/~imd/potfit>
- Brueckner K. A. and Jorna S. Laser-driven fusion. *Reviews of Modern Physics*, Vol. 46, No. 2, (1974).

- Bühler L. Liquid Metal Magnetohydrodynamics for Fusion Blanket. Magnetohydro-dynamics Fluid Mechanics and Its Applications, 2007, Vol. 80, Part II, 171-194.
- Buckingham R. A., The Classical Equation of State of Gaseous Helium, Neon and Argon, Proceedings of the Royal Society of London. Series A, 168 pp. 264-283 (1938)
- Burkert U. and Allinger N. L., Molecular Mechanics, (1982).
- Canales M., Gonzalez D. J., Gonzalez L. E. and Padró J. A., Phys. Rev. E 58, 4747 (1998).
- Cao G. X. *et al.* Diffusion of Hydrogen on Ni(111) over a Wide Range of Temperature: Exploring Quantum Diffusion on Metals. Phys. Rev. Lett. Vol 79, No 19 (1997)
- Carlsson A. E., (1990). Beyond pair potentials in elemental transition metals and semiconductors. Solid State Physics, 43, Academic Press, New York, 1-91.
- Caro A., Crowson D. A. and Caro M. Classical Many-Body Potential for Concentrated Alloys and the Inversion of Order in Iron-Chromium Alloys. PRL 95, 075702 (2005)
- Caro A., Hetherly J. *et al.* Properties of Helium bubbles in Fe and FeCr alloys. Journal. of Nuclear Materials. Vol. 418, 1–3, Pages 261–268 (2011)
- Carstensen E. L. and Foldy L. L., J. Acoust. Soc. Am. 19, 481 (1947); Z. Ye and A. Alvarez, Phys. Rev. Lett. 80, 3503 (1998); M. Kafesaki, R. S. Penciu, and E. N. Economou, *ibid.* 84, 6050 (2000).
- Casey D. T. *et al.* Evidence for Stratification of Deuterium-Tritium Fuel in Inertial Confinement Fusion Implosions. Phys. Rev. Lett. 108, 075002 (2012)
- Causey R. *et al.*, J. Nucl. Mater. 266–269 (1999) 467.
- Chang P.Y. *et al.* Generalized Measurable Ignition Criterion for Inertial Confinement Fusion. Phys. Rev. Lett. 104, 135002 (2010)
- Chanteloup J.-C. *et al.* Multi kJ level Laser Concepts for HiPER Facility. Journal of Physics: Conference Series 244 (2010) 012010
- Chapra S. C., Canale R. P., Numerical Methods for Engineers, (1988), McGraw-Hill, New York.
- Chenoweth, van Duin and Goddard, Journal of Physical Chemistry A, 112, 1040-1053 (2008).
- Chieux P. and Ruppertsberg H. 1980 J. Physique Coll 41 C8 145.
- Christensen N. E. *et al.* First-principles theory of tetrahedral bonding and crystal structure of lead. Phys. Rev. B 34, 5977–5980 (1986).
- Christian J. W., Transformations in Metals and Alloys (Pergamon, New York, 1965).
- Christofilos N. C., J. Fusion Energy 8 (1989)
- Ciccotti G. and Hoover W. G. Molecular-Dynamics Simulation of Statistical-Mechanical Systems, (North-Holland, Amsterdam, 1986), pp. 169–178.
- Clarke A. S. and Jónsson H. 1993 Phys. Rev. E 47 3975
- Cleveland C. L, Luedtke W. D. and Landman U. 1999 Phys. Rev. B 60 5065
- Copestake A. P., Evans R., Ruppertsberg H. and Schirmacher W., J. Phys. F: Met. Phys. 13, 1993 (1983).

- Copley J. R. D. and Lovesey S. W. Rep. Prog. Phys. 38, 461 (1975).
- Cowley J.M., Phys. Rev. 77, 667 (1950).
- Cricchio F. *et al.* High-pressure melting of lead. Phys. Rev. B 73, 140103(R) (2006)
- Daw M. S. *et al.* The embedded-atom method: a review of theory and applications. Materials Science Reports 9 (1993) 251-310
- Debenedetti P. G. Metastable Liquids (Princeton Univ. Press, Princeton, 1997); C. A. Angell, Science 267, 1924 (1995).
- Demmel F., Szubrin D., Pilgrim W.-C. and Morkel C. Diffusion in liquid aluminium probed by quasielastic neutron scattering. Phys. Rev. B 84, 014307 (2011)
- Deurinck P., Creemers C., Surf. Sci., 441 (1999) 493.
- Dewaele A. Melting of lead under high pressure studied using second-scale time-resolved x-ray diffraction. Phys. Rev. B 76, 144106 (2007).
- Dhawan L. L. and Prakash S. Activation energy of hydrogen and muon in transition metals. Phys. Rev. B 24, 3255–3260 (1981).
- Dobson D. P. Self-diffusion in liquid Fe at high pressure. Physics of the Earth and Planetary Interiors 130 (2002) 271–284
- Donnelly S. E. Rad. Effects 90 1 (1985).
- Drexel W. *et al.* J. Phys. Chem. Solids 37 1135 (1976)
- Ducastelle F., Computer simulations in material science, (1991), Kluwer, Dordrecht.
- Dunne M. *et al* 2007 HiPER - Technical Background and Conceptual Design Report Rutherford Appleton Laboratory, report RAL-TR-2007-008; www.hiper-laser.org
- Dunne M. A high-power laser fusion facility for Europe. Nature Physics 2, 2 - 5 (2006)
- Duthie J. C. and Pettifor D. G., Phys. Rev. Lett. 38, 564 (1977); H. L. Skriver, Phys. Rev. B 31, 1909 (1985); A. K. McMahan, *ibid.* 29, 5982 (1984).
- Edao Y., Noguchi H. and Fukada S. Experiments of hydrogen isotope permeation, diffusion and dissolution in LiPb. Journal of Nuclear Materials 417 (2011) 723–726
- Eichenauer W. and Markopoulos J.: Z. Metallkd., 1974, vol. 65 (10), pp. 649–52.
- Einstein A., Ann. Phys. 322, 549 (1905).
- El-Guebaly L. A. Fifty Years of Magnetic Fusion Research (1958–2008): Brief Historical Overview and Discussion of Future Trends. Energies 2010, 3, 1067-1086.
- Emi T. and Pehlke R. D. Theoretical Calculation of the Solubility of Hydrogen in Liquid Metals. 2736-Vol. 1, October 1970 Metallurgical Transactions.
- Ercolessi F., *et al*, Simulation of gold in the glue model, Philos. Mag. A 58, 213 (1988)
- Ercolessi F., Adams J., Europhys. Lett., 26(8) (1994) 583.
- Ercolessi F., A molecular dynamics premiere, Università di Udine, (1997).

- Erents S. K. and McCracken G. M. 1973 *Radiat. Eft* 18 191
- Evans R. K. "Lithium Reserves and Resources", *Energy*, 3, 379-385 (1978).
- Evans D.J. and Morriss G.P. *Computer Physics Reports* 1(6), 297 (1984). Evans D. J. and Morriss G.P. *Statistical Mechanics of Nonequilibrium Liquids* (Academic Press, London, 1990).
- Evtikhin V. A. *et al.* Lithium divertor concept and results of supporting experiments. *Plasma Phys. Control. Fusion* 44 955 (2002)
- Faber T. E. 1972 *An Introduction to the Theory of Liquid Metals* (Cambridge: the University Press)
- Faken D. and Jónsson H. 1994 *Comput. Mater. Sci.* 2 279
- Federici G. *et al.*, Key ITER plasma edge and plasma-material interaction issues, *J. Nucl. Mater.* 313/316 (2003) 11–22.
- Federici G. *et al.*, Effects of ELMs and disruptions on ITER divertor armour materials, *J. Nucl. Mater.* 337/339 (2005) 684–690.
- Fellinger M. R. *et al.* Force-matched embedded-atom method potential for niobium. *Phys. Rev. B* 81, 144119 (2010)
- Finnis M. W. and Sinclair J. E., *Philos. Mag. A* 50, 45 (1984).
- Foiles S., Baskes M. and Daw M., *Phys. Rev. B*, 33 (1986) 7983.
- Foiles S. M., *Phys. Rev. B*, 32 (1985) 7685.
- Foiles S. M. Embedded-atom-method functions for the fcc metals Cu, Ag, Au, Ni, Pd, Pt, and their alloys. *Phys. Rev. B* 33, 7983 (1986).
- Foiles S. M., Adams J.B., *Phys. Rev. B*40 (1989) 5909.
- Foiles S.M. Application of the embedded-atom method to liquid transition metals. *Phys. Rev. B* 32, 3409 (1985)
- Forsblom M. and Grimvall G. *Phys. Rev. B* 72, 132204 (2005)
- Fradera J. *et al.* *Journal of Nuclear Materials* 417 (2011) 739–742
- Fraile A., Cuesta-López S., Iglesias R., Caro A. and Perlado J. M. Atomistic molecular point of view for liquid lead and lithium in Nuclear Fusion technology. *Journal of Nuclear Materials* (2013). In press.
- Fraile A, Cuesta-López S, Caro. A, Perlado J. M. Under publication process.
- Fraile A., Cuesta-López, Caro A. *et al.*, (to be published)
- Freidberg J. P. Ideal magnetohydrodynamic theory of magnetic fusion systems. *Rev. Mod. Phys.*, Vol. 54, No. 3, July 1982
- Frenkel D., Smith B., *Understanding Molecular Simulations: From Algorithms to Applications*, (1996), Academic Press.
- Frenkel D. and Smith B. *Understanding molecular simulations: From algorithms to applications.* Academic Press, Computational Science Series, Vol 1, (2002)
- Frenkel J. *Kinetic Theory of Liquids*, Claredon Press, Oxford (XXXX).

- Fukai Y. and Sugimoto H., *Adv. Phys.* 34, 263 (1985). For reviews, see, e.g., *Hydrogen in Metals*, edited by G. Alefeld and J. Volkl (Springer, Berlin, 1978).
- Fukai Y., in *The Metal-Hydrogen System*, Springer Series in Materials Sciences Vol. 21, edited by U. Gonser *et al.* (Springer-Verlag, Berlin, 1993). *Metals-Hydrogen Systems*, R. Kirchheim, E. Fromm, E. Wicke, eds., Verlag, Munchen, 1989.
- Futakawa M. *et al.* *Journal of Nuc. Sci. and Tech*, Vol. 45, No. 10, p. 1041–1048 (2008).
- Futakawa M. *et al.*, *Int. J. Impact Eng.* 28, 123 (2003).
- Futakawa M. *et al.* *J. Nucl. Sci. Technol.* 40, 895 (2003).
- Gasior W. and Moser Z., *Journal of Nuclear Materials* 294 (2001) 77-83
- Gates D. A. and Delgado-Aparicio L. Origin of Tokamak Density Limit Scalings. *Phys. Rev. Lett.* 108, 165004 (2012).
- Gear C. W. *Numerical initial value problems in ordinary differential equations*, (1971), Prentice-Hall, Englewood Cliffs, NJ.
- Girifalco L.A. and Weizer V.G., *Phys. Rev.* 114, 687, (1959)
- Glenzer S.H. *et al.*, *Science* 327, 1228 (2010).
- Golubchikov L.G. *et al.*, Development of a liquid–metal fusion reactor divertor with a capillary-pore system, *Proceedings of the ICFRM-7, Obninsk, Russia, 1995 (J. Nucl. Mater.* 233–237 (1996) 667–672).
- Gonzalez C. Private communication.
- Gordillo N. *et al.* Compositional, structural and morphological modifications of N-rich Cu₃N films induced by irradiation with Cu ions at 42 MeV. *J. Phys. D: Appl. Phys.* 43 345301 (2010).
- Graham, T., *Phil. Trans. Roy. Soc (London)* 156, 399 (1866)
- Greiner W., Neise L., Stocker H., (1995). *Thermodynamics and Statistical Mechanics*, Springer-Verlag, New York.
- Grimsditch M. *Phys. Rev. Lett.* 52, 2379 (1984).
- Gropp W *et al.*, *Using MPI, 2nd edn: Portable Parallel Programming with the Message Passing Interface, Scientific and Engineering Computation (The MIT Press, MA, 1999).*
- Guerrero C., Cuesta-López S. and Perlado J.M. *Eur. Phys. Journal. Proceedings of the Seventh Conference on Inertial Fusion Sciences and Applications (IFSA 2011). In press (2013).*
- Gurvich L. V. *et al.*, *Thermodynamic Properties of Individual Substances Fourth Edition, Volume 2 Parts 1 and 2*, Hemisphere Pub. Corp. N.Y. (1991).
- Haan S.W. *et al.* *Phys. Plasmas* 18, 051001 (2011).
- Hafner J. *et al.* 1984 *J. Phys. F: Met. Phys.* 14 1137
- Hafner J. and Kahl G. The structure of the elements in the liquid state. *J. Phys. F: Met. Phys.* 14 2259 (1984)
- Haile J. M., *Molecular Dynamics Simulation: Elementary Methods*, (1992), Wiley, New York.

- Hakkinen H. and Manninen M., *J. Phys. Condens. Matter* 1, 9765 (1989).
- Hansen J. P. and McDonald I. R., *Theory of Simple Liquids* (Academic, London, 1986).
- Harrington S. *et al.* Liquid-Liquid Phase Transition: Evidence from Simulations. *Phys. Rev. Lett.* Vol. 78, No 12, 24 (1997)
- Harvey J.P. and Chartrand P. Modeling the Hydrogen Solubility in Liquid Aluminum Alloys. *Metallurgical and materials transactions B*. 908—Vol. 41B, (2010)
- Henkelman G., Arnaldsson A. and Jónsson H. A fast and robust algorithm for Bader decomposition of charge density. *Computational Materials Science* 36 (2006) 354–360
- Henry J., Auger T., Daí Y. Operation of high power liquid metal spallation targets: a challenge for structural materials. Springer Science + Business Media B.V. (2008) V. Ghetta et al. (eds.), *Materials Issues for Generation IV Systems*.
- Hestenes, M. R.; Stiefel, E. (1952). "Methods of Conjugate Gradients for Solving Linear Systems" *Journal of Research of the National Bureau of Standards* 49 (6).
- Hirschfelder J. O., Curtis C. F., and Bird R. B. *Molecular Theory of Gases and Liquids* (Wiley, New York, 1954), pp. 783-792.
- Hirth P 1980 *Metall. Trans. A* 11 861
- Hohenberg P. and Kohn W., *Phys. Rev. B* 136, 864 (1964)
- Honeycutt J. D. and Andersen A. C. 1987 *J. Phys. Chem.* 91 4950
- Hongli C. *et al.* *Plasma Science and Technology*, Vol.10, No.4, 2008
- Hoover W. G., *Molecular Dynamics*, Springer-Verlag, Berlin, 1986.
- Hoover W. G., *Phys. Rev. A*, 31 (1985) 1695.
- Hou J. *et al* Structure change of Pb melt. *Physics Letters A* 358 (2006) 171–175
- Hoyt J. J. *et al*, *Modell. Simul. Mater. Sci. Eng.* 11, 287 (2003).
- Hu S. X. *et al.*, *Phys. Rev. Lett.* 100, 185003 (2008).
- Hubberstey P, Sample T. and Barker M. G., *J. Nucl, Mater* 191-194, 283-287 (1992)
- Hubberstey P. *Journal of Nuclear Materials* 247 (1997) 208-214
- Hünenberger P. H.. *Thermostat Algorithms for Molecular Dynamics Simulations. Adv. Polym. Sci.* (2005) 173:105–149
- Ida M. *et al.* Suppression of cavitation inception by gas bubble injection: A numerical study focusing on bubble-bubble interaction. *Phys. Rev. E* 76, 046309 (2007).
- Insepov Z. *et al.* Computer simulation of bubble formation. *Joint International Topical Meeting on Mathematics & Computation and Supercomputing in Nuclear Applications* (2007)
- Isenberg I.. *Phys Rev.*, 1950 Vol 79, pp 736-37.
- Izvekov S. *et al.* Effective force fields for condensed phase systems from ab initio molecular dynamics simulation: A new method for force-matching. *J. of Chem. Phys.* Vol. 120, No 23 15 June (2004)

- Jacobsen K., Norskov J. and Puska M., Phys. Rev. B, 35 (1987) 7423.
- Jacquinet J and the JET Team, “Deuterium-tritium operation in magnetic confinement experiments: results and underlying physics”, Plasma Phys. Control. Fusion, 41 (1999) A13-A46.
- Jaramillo-Botero, Su, Qi, Goddard. J Comp Chem, 32, 497-512 (2011).
- Jardine A. P. et al. Phys. Rev. Lett. 105, 136101 (2010)
- Jiang G. and Li Y. A Model for Calculating Hydrogen Solubility in Liquid Transition Metals. 1038 - Vol 42A, 2011 Metallurgical and Materials Transactions A.
- Kalashnikov E. V. Thermodynamically stable states in eutectic systems. Zh. Tekh. Fiz. 67, 7–12 (1997)
- Kamat P.V., J. Phys. Chem. C, 2007, 111, 2834.
- Kanzaki H., J. Phys. Chem. Solids 2, 24 (1957);
- Karimi, A. and Martin, J. L. Cavitation erosion of materials. International Materials Reviews, Vol 31, No 1, 1986 , pp. 1-26(26)
- Karpov V. Y. Properties of GASARS – Metallic materials with pores formed by released hydrogen. Materials Science, Vol. 43, No. 5, 2007
- Kawai M. et al. Development of advanced materials for spallation neutron sources and radiation damage simulation based on multi-scale models. Journal of Nuclear Materials Vol 431, 1–3, (2012), Pp 16–25.
- Keilhacker M. et al 2001 Nucl. The scientific success of JET. Fusion 41 1925.
- Kohn W. and Sham L.J. Phys. Rev. 140, 1133 (1965)
- Krall N. A. and Trivelpiece A. W, 1973, Principles of Plasma Physics (McGraw-Hill, New York).
- Kresse G. and Hafner J., Phys. Rev. B 47, R558 (1993).
- Kresse G. and Furthmuller J., Phys. Rev. B 54, 11 169 (1996).
- Kresse G. and Joubert D., Phys. Rev. B 59, 1758 (1999).
- Ladd A. and Woodcock L. Chem. Phys. Lett. **51**, 155 (1977). Ladd A. and Woodcock L. Mol. Phys. **36**, 611 (1978).
- Landa A. *et al* 2000 Acta Mater. 48 1753
- Landau L. D. and Lifshitz E. M. Fluid Mechanics, Course of Theoretical Physics Vol. 6 (Pergamon, Oxford, 1959), pp. 310-346.
- Lange N.A.: Lange’s Handbook of Chemistry, 13th ed., McGraw-Hill, New York, 1985.
- Lawson J. D. Some Criteria for a Power Producing Thermonuclear Reactor, Proc. Phys. Soc. Vol. 70, pt. 1, no. 445, B, 6-10, (1957).
- Lee B-J *et al.* Semiempirical atomic potentials for the fcc metals Cu, Ag, Au, Ni, Pd, Pt, Al, and Pb based on first and second nearest-neighbor modified embedded atom method. Phys Rev B 68, 144112 (2003)
- Lennard-Jones J.E., On the forces between atoms and ions, Proc. Roy. Soc. 109 (1924) 584–597.
- Li C. K. *et al.*, Phys. Rev. Lett. 100, 225001 (2008). C. K. Li et al., Phys. Rev. Lett. 102, 205001 (2009).

- Li Q. *et al.*, Mod. Phys. Lett. B 20, 151 (2006).
- Li Y, Blaisten-Barojas E and Papaconstantopoulos D A 1998 Phys. Rev. B 57 15519
- Li Y. *et al.* Embedded-atom-method tantalum potential developed by the force-matching method. Phys. Rev. B 67, 125101 (2003)
- Li X-C *et al.* Journal of Nuclear Materials 426 (2012) 31–37
- Liepmann H. W., Narasimha R. and Chahine M. T. Phys. Fluids 5, 1313 (1962).
- Lim H S, Ong C K and Ercolessi F 1992 Surf. Sci. 269 1109
- Lindemann F., Z.Phys, 11, 609, (1910)
- Lindhard J. and Scharff M, Energy Dissipation by Ions in the keV Region. *Physical Review*, vol. 124, no. 1, pp. 128-130, (1961).
- Lindl J. D. 1998 Inertial Confinement Fusion (New York: Springer)
- Lindl J. D. Phys. Plasmas 2, 3933 (1995).
- Linn T. H. and Dunn K. J., Phys. Rev. B 33, 807 (1986).
- Liu X. Y. *et al.*, Surf. Sci., 373 (1997) 357.
- Liu H., Zhang L. and Bouchard M.: Recent Dev. Light Met., Proc. Int. Symp., 1994, pp. 257–68.
- Lombardi A. and Palazzetti F. Journal of Molecular Structure: THEOCHEM 852 (2008) 22–29
- Lümmen N. *et al.* Common neighbour analysis for binary atomic systems. 2007 Modelling Simul. Mater. Sci. Eng. 15 319.
- Lyon J.F. *et al.*, “Stellarators”, Nucl. Fusion 30, 1695 (1990).
- Mainwood A. and Stoneham A. M. Theory of hydrogen in liquid and solid metals. Journal of the Less-Common Metals, 49 (1976) 271 – 281.
- Malang S. Limitations on blanket performance. Fusion Engineering and Design 46 (1999) 193–206.
- Manchester F.D.: Phase Diagrams of Binary Hydrogen Alloys, ASM International, Materials Park, OH, 2000.
- Mansfield D. K. *et al.*, Phys. Plasmas 3 (1996) 1892.
- Mansur L.K. *et al.* Journal of Nuclear Materials. Vol 329–333, Part A,(2004), Pages 166–172. Proceedings of the 11th International Conference on Fusion Reactor Materials (ICFRM-11)
- Mao, H. K *et al.*, 1990, Solid State Commun. 74, 1027.
- March N. H.: Liquid Metals, Pergamon, 1968.
- Martyna G. J., Tobias D.J. and Klein M.L. J Chem Phys, 101, 4177 (1994).
- Martyna G. J., Klein M. L. and Tuckerman M. Nosé-Hoover Chains -the Canonical Ensemble via Continuous Dynamics, Journal of Chemical Physics 97, 2635-2643 (1992).
- Marinak M. M. *et al.*, Phys. Plasmas 8, 2275 (2001).

- Mas de les Valls E. *et al.* Lead-lithium eutectic material database for nuclear fusion technology. *Journal of Nuclear Materials* 376 (2008) 353-357.
- Masuyama D., Oda T., Fukada S. and Tanaka S. Chemical state and diffusion behavior of hydrogen isotopes in liquid lithium–lead. *Chemical Physics Letters* 483 (2009) 214–218
- Matyushov D. V. and Schmid R. J. *Chem. Phys.* 104 8627 (1996)
- Mazo R. M. *Brownian Motion. Fluctuation, Dynamics, and Applications* (Clarendon, Oxford, 2002).
- McCrory R. L. *et al.*, *Phys. Plasmas* 15, 055503 (2008).
- Meade D. 50 years of fusion research. 2010 *Nucl. Fusion* 50 014004
- Methfessel M and Paxton A.T. *Phys. Rev. B* 40, 3616 (1989)
- Melius C. F., Bisson C. L. and Wilson W. D. 1978 *Phys. Rev. B* 18 1647
- Merkle K.L. (1990), *MRS Bulletin*, 15, 42 (1990).
- Metropolis N., Rosenbluth A. W., Rosenbluth M. N., Teller A.H. and Teller E. Equation of State Calculations by Fast Computing Machines. *Journal of Chemical Physics*. 21 (1953) 1087.
- Metz B. *et al.*, *Climate Change 2007: Mitigation of Climate Change, Contribution of Working Group III to the Fourth Assessment Report of the Intergovernmental Panel on Climate Change*, Cambridge University Press, New York, 2007.
- Meyer A *et al.* Determination of self-diffusion coefficients by quasielastic neutron scattering measurements of levitated Ni droplets. *Phys. Rev. B* 77, 092201 (2008).
- Mima K, Tikhonchuk V. and Perlado M. Inertial fusion experiments and theory. *Nucl. Fusion* 51 (2011) 094004 (9pp)
- Mirnov S. Plasma-wall interactions and plasma behaviour in fusion devices with liquid lithium plasma facing components. *Journal of Nuclear Materials* 390–391 (2009) 876–885.
- Mitroy J. *et al.* Theory and applications of atomic and ionic polarizabilities. 2010 *J. Phys. B: At. Mol. Opt. Phys.* 43 202001.
- Moir R.W., *Fusion Eng. Des.* 5 (1987) 269. R.W. Moir, *Nucl. Eng. Des.* 29 (1995) 34.
- Molina L. M., Alonso J. A., and Stott M. J. *Phys. Rev. B* 66, 165427 (2002).
- Monkhorst H.J. and Pack J.D. *Phys. Rev. B* 13, 5188 (1976)
- Montroll E. W., *J. Chem. Phys.* 10, 218 (1942); 11,481 (1943).
- Morse P.M., Diatomic molecules according to the wave mechanics. II. Vibrational levels, *Phys. Rev.* 34 (1929) 57 64.
- Morse P.M., *Phys. Rev.* 34, 57, (1930)
- Moses E. I. The National Ignition Facility (NIF): A path to fusion energy. *Energy Conversion and Management* 49 (2008) 1795–1802.
- Moses E. I. Advances in inertial confinement fusion at the National Ignition Facility (NIF). *Fusion Engineering and Design* 85 (2010) 983–986

- Mott N. F. and Jones H.: *The Theory of the Properties of Metals and Alloys*, Dover, New York, 1958.
- Moelevyn-Hughes E. A. 1964 *Physical Chemistry* (Oxford: Pergamon)
- Mustafin, G.M., G.F. Shaikhiev (1983), *Russ. J. Phys. Chem.* 57, 421.
- Nachtrieb N. H., *Phys. Chem.* 80, 678 (1976).
- Nellis W. J. Dynamic compression of materials: metallization of fluid hydrogen at high pressures. *Rep. Prog. Phys.* 69 (2006) 1479–1580.
- Norajitra P., Bühler L., Fischer U. et al, The EU advanced dual coolant blanket concept, *Fusion Eng. Des.* 61–62 (2002) 449–453.
- Nordsieck A., *Math Comp.*, 20 (1962) 13.
- Norman G. E. and Stegailov V. V. 2002 *Comput. Phys. Commun.* 147 678–83
- Norman G. E. and Stegailov V. V. 2001 *Zh. Eksp. Teor. Fiz.* 119 1011 (Norman G. E. and Stegailov V. V. 2001 *J. Exp. Theor. Phys.* 92 879 (Engl. Transl.))
- Nosé S., *Molecular Physics*, 52 (1984) 255.
- Nosé S., *J. Chem. Phys.* 81, 511 (1984).
- Nuckolls J, Wood L, Thiessen A. and Zimmerman G. Laser Compression of Matter to Super-High Densities: Thermonuclear (CTR) Applications *Nature* 239, 139 - 142 (15 September 1972)
- Nygren R. E. et al. Thermal control of the liquid lithium divertor for NSTX. *Fusion Engineering and Design* 84 (2009) 1438–1441
- Ogando F. and Velarde P. 2001 *Journal of Quantitative Spectroscopy and Radiative Transfer* 71 541–550
- Ogando-Arregui E., Caro M. and Caro A., *Phys. Rev. B* 66, 054201 (2002)
- Ogando-Arregui E., Caro M. and Caro A., *Phys Rev B* 66 054201 (2002) b) E. Lopasso, A. Caro et al. *Phys Rev B* 68 21425 (2003)
- Ohse R.W. (Ed.) *Handbook of Thermodynamic and Transport Properties of Alkali Metals*, Intern. Union of Pure and Applied Chemistry Chemical Data Series No. 30. Oxford: Blackwell Scientific Publ., 1985.
- Okamoto H. (1993). Li-Pb phase diagram. APD center.
- Okumura H. and Ito N. Nonequilibrium molecular dynamics simulations of a bubble. *Phys. Rev. E* 67, 045301(R) (2003).
- Oliva E. *et al.* A proposal for multi-tens of GW fully coherent femtosecond soft X-ray lasers *Nature Photonics* 2012 (in press).
- Ongena J. and G. Van Oost. *Energy For Future Centuries. Will Fusion Be An Inexhaustible, Safe And Clean Energy Source? EFDA–JET–RE* (2001)
- Oriani R. A.: *Proc. of the Symposium on Stress Corrosion*, Columbus, Ohio, Sept., 1967: Y. Ebisuzaki and M. O'Keefe: *Progress in Solid State Chemistry*, H. Reiss, ed., 1967, vol. 4, pp. 187-211.
- Orlov A.I. et al, *Zh. Eksp. Teor. Fiz.* 120, 445 (2001) [*JETP* 93, 393 (2001)].
- Oxtoby D. W. Homogeneous nucleation: theory and experiment. *J. Phys.: Condens. Matter* 4 7627 (1992)

- Paisner J. A. Status of the National Ignition Facility Project. *Fusion Engineering and Design* 44 (1999) 23-33
- Pasternak A. D. and Olander D. R. *Diffusion in Liquid Metals*. Vol. 13, No. 6 *AIChE Journal* Page 1053
- Pasturel A., Hafner P. and Hicter P. Thermodynamic variational method for liquid alloys with chemical short-range order. *Phys. Rev. B* 32, 5009–5022 (1985)
- Paxton A. T. and Finnis M. W. *Phys. Rev. B* 77, 024428 (2008)
- Paxton A. T. et al. *Phys. Rev. B* 82, 235125 (2010)
- Pentcheva R and Scheffler M, *Phys. Rev. B* 65, 155418 (2002)
- Pierini G. et al, *Proc. ANS Topical Meeting on Tritium Technology in Fusion*,
- Pierini G. et al, *Nucl. Eng. Des./Fusion* 1 (1984) 159.
- Perdew J. P., Burke K., and Ernzerhof M., *Phys. Rev. Lett.* 77, 3865 (1996)
- Perlado J. M. and Sanz J. *Neutronics on inertial fusion reactors*. Vol 48, I 3–4, Pages 355–370 (2000).
- Pings C J 1968 *Physics of Simple Liquids* ed H N V Temperley *et al* (Amsterdam: North Holland) chapter 10.
- Plimpton S. Fast Parallel Algorithms for Short-Range Molecular Dynamics, *J Comp Phys*, 117, 1-19 (1995).
- Polak, E. *Computational Methods in Optimization* - New York: Academic Press (1971)
- Poole, P. H., Grande, T., Angell, C. A. & McMillan, P. F. Polymorphic phase transitions in liquids and glasses. *Science* 275, 322-323 (1997).
- Ponyatovsky, E. G. & Barkalov, O. I. Pressure-induced amorphous phases. *Mater. Sci. Rep.* 8, 147-191 (1992).
- Raeder J. *et al.*, "Controlled Nuclear Fusion: Fundamentals of its Utilization for Energy Supply", John Wiley & Sons, New York (1986)
- Rahman A. Correlations in the Motion of Atoms in Liquid Argon. *Phys Rev* 136: A405-A411. (1964)
- Rapaport D. C., *The Art of Molecular Dynamics Simulation*, Cambridge University Press, NY, 1995.
- Rapaport D. C., *The Art of Molecular Dynamics Simulation*, (2004), 2nd ed. Cambridge University Press.
- Reed, E. L. and Dropher, J. J. (1970). "Solubility and Diffusivity of inert gases in liquid sodium, potassium and NaK," *Liquid Metal Engineering Center Report LMEC-69-36*
- Refson K. Moldy: a portable molecular dynamics simulation program for serial and parallel computers. *Computer Physics Communications* 126 (2000) 310–329.
- Ribe F. L.. Fusion reactor systems. *Reviews of Modern Physics* vol. 47, no 1 pp. 7-41 (1975).
- Ribeyre X. *et al* *Plasma Phys. Control. Fusion* 51 (2009) 015013
- Ruppertsberg H. and Egger H. J. *Chem. Phys.* 63 4095 (1975)
- Ruppertsberg H. and Reiter H. J. *Phys. F:Met. Phys.* 12 1311 (1982)

- Saar J. and Ruppertsberg H. 1987 J. Phys. F: Met. Phys. 17 305. Ruppertsberg H and Speicher W 1976 Z. Naturf: a 31 47-52.
- Saar J. and Ruppertsberg H. Calculation of $C_p(T)$ for liquid Li/Pb alloys from experimental $\rho(T)$ and $(\delta\rho/\delta T)$ s data. 1987 J. Phys. F: Met. Phys. 17 305
- Sacris E. M. and Parlee N. A. D. The diffusion of hydrogen in liquid Ni, Cu, Ag, and Sn. Metallurgical and Materials Transactions B. Vol. 1, No 12 (1970), 3377-3382.
- Saibene G., Sartori R. and Reiter F., Fusion Technol. 14 (1988) 808.
- Sakharov A.D. Theory of magnetic thermonuclear reactor, part 2 Plasma Physics and the Problem of Controlled Thermonuclear Reactions (transl) (New York: Pergamon) p 20–30
- Sakintuna B. et al, Metal hydride materials for solid hydrogen storage: A review. International Journal of Hydrogen Energy 32 (2007) 1121–1140
- Sagara A. et al., Proc. ISFNT-3, Fusion.Eng. Design 29 (1995).
- Sagara A. Blanket design using FLiBe in helical-type fusion reactor FFHR. Journal of Nuclear Materials 248 (1997) 147-152.
- Sanville E. *et al.* An improved grid-based algorithm for Bader charge allocation, J. Comp. Chem. 28, 899-908 (2007).
- Sarman S.S., Evans D.J. and Cummings P.T. Physics Reports **305**, 1 (1998).
- Saunders N. and Miodownik A. P., CALPHAD: A Comprehensive Guide, edited by R.W. Cahn, Pergamon Materials Series (Oxford, New York, 1998).
- Schultz K. R. *et al.* Status of inertial fusion target fabrication in the USA. Fusion Engineering and Design 44 (1999) 441-448
- Scopigno T. *et al.* Evidence of Two Viscous Relaxation Processes in the Collective Dynamics of Liquid Lithium. Phys. Rev. Lett. Vol. 85, No 19 (2000).
- Scopigno T. *et al.* Microscopic dynamics in liquid metals: Rev. Mod. Phys., Vol. 77, No. 3, (2005)
- Sedano L. A., “He bubble formation in liquid metals”, CIEMAT Internal Report, 2007
- Seletskaja T. *et al.* Magnetic Interactions Influence the Properties of Helium Defects in Iron. PRL 94, 046403 (2005)
- Senda Y., Shimojo F. and Hoshino K.. The ionic structure and the electronic states of liquid Li–Pb alloys obtained from ab initio molecular dynamics simulations. J. Phys.: Condens. Matter 12 (2000) 6101–6112.
- Sethian J.D. *et al.* Fusion energy with lasers, direct drive targets, and dry wall chambers. Nucl. Fusion 43 (2003) 1693–1709.
- Shapiro J. N. Lindemann Law and Lattice Dynamics. Phys. Rev. B, Vol 1, No 10 (1970)
- Sheffield J. The physics of magnetic fusion reactors. Reviews of Modern Physics, Vol. 66, No. 3, (1994)
- Shen G. *et al.* Structure of Liquid Iron at Pressures up to 58 GPa. Phys. Rev. Lett. 92, 185701 (2004)
- Shewchuk J. R., An introduction to the conjugate gradient method without the agonizing pain, (1994), Carnegie Mellon University.

Shpil'rain E. E. *et al.* The Solubility of Helium and Argon in Liquid Lead, Bismuth, and Their Eutectic Alloy at High Temperatures. *High Temperature*, 2007, Vol. 45, No. 1, pp. 127–130.

Simonelli G., Pasianot R. and Savino E.J. *Phys. Rev. B* 50, 727 (1994)

Singh B. N. and Trinkaus H., *J. Nucl. Mater.*, 186(1992), 153.

Sinnott S.B. *et al.*, *Phys. Rev. B* 44 (1991) 8927.

Slater J.C. and Koster G.F., Simplified LCAO method for the periodic potential problem, *Phys. Rev.* 94 (6) (1954) 1498–1524.

Slotnick H., *et al.*, The Solubility of Helium in Lithium and Potassium, PWAC-380, Pratt and Whitney Aircraft, a Division of United Aircraft Corp. Middletown, Conn. (February 1965)

Smirnov V.P. Tokamak foundation in USSR/Russia. 1950–1990. *Nucl. Fusion* 50 (2010) 014003 (8pp)

Soldan P. *et al.* High-quality interatomic potential for $\text{Li}^+\text{-He}$. *Chem Physics Letters*, 343, (3-4), 429-436.

Song J. and Curtin W.A. *Acta Materialia* 59, 1557 (2011)

Smolentsev S. *et al.*, Characterization of key magnetohydrodynamic phenomena in PbLi flows for the US DCLL blanket. *Fusion Engineering and Design* 83 (2008) 771–783

Spitzer L, “The stellarator concept”, *Physics of Fluids* 1, 253 (1958).

Stambaugh R. D. *et al.* Enhanced confinement in tokamaks. *Phys. Fluids B* 2, I 12, 2941 (1990).

Stankus S. V., Khairulin R. A. and Mozgovoï A. G. An Experimental Investigation of the Density and Thermal Expansion of Advanced Materials and Heat-Transfer Agents of Liquid-Metal Systems of Fusion Reactor: Lead-Lithium Eutectic. *High Temperature*. Vol. 44, No. 6, 2006, pp. 829–837.

Stokes G. G., *Proc. Cambridge Philos. Trans.* 9, 8 (1851).

Stoller R.E. and Odette G. R. The effects of helium implantation on microstructural evolution in an austenitic alloy. *Journal of Nuclear Materials*. Vol.154, Issues 2–3, 1, Pages 286–304 (1988).

Strachan J.D. TFTR L mode energy confinement related to deuterium influx. *Nuclear Fusion* (1999) 39 1093.

Stukowski A., Sadigh B., Erhart P. and Caro A. Efficient implementation of the concentration-dependent embedded atom method for molecular-dynamics and Monte-Carlo simulations. *Modelling Simul. Mater. Sci. Eng.* 17 (2009) 075005 (13pp)

Stukowski A. Visualization and analysis of atomistic simulation data with OVITO - the Open Visualization Tool. *Modelling Simul. Mater. Sci. Eng.* 18 (2010), 015012

Sutton A., *Electronic Structure of Materials*, (1993), Clarendon Press, Oxford.

Swenson C. A. Lithium metal: An experimental equation of state. *Journal of Physics and Chemistry of Solids*. Vol. 27, Iss 1, (1966), pp 33–38

Swope W. C., Anderson H. C., Berens P. H. and Wilson K. R. *J. Chem. Phys.* 76 (1982) 637.

Sze D.K., *Fusion Technol.* 8 (1985) 887.

Tabak M. Ignition and high gain with ultrapowerful lasers. 1626 *Phys. Plasmas* 1 (5), May 1994

- Tabarés F. L. *et al.* The Lithium Wall Stellarator Experiment in TJ-II. Proceedings of ITC18, 2008.
- Tabarés F. L. *et al.*, The lithium stellarator experiment. TJ-II as a benchmark, Problems of atomic science and technology, 2008. N 6, Series: Plasma Physics (14), 3-7.
- Takahashi, T., H. K. Mao, and W. A. Basset, 1969, Science 165, 1352.
- Tamblyn I. *et al.* Tetrahedral Clustering in Molten Lithium under Pressure. Phys. Rev. Lett. 101, 075703 (2008).
- Tamm I.E. 1959 Theory of the magnetic thermonuclear reactor, part I Plasma Physics and the Problem of Controlled Thermonuclear Reactions (transl) (New York: Pergamon) p 3–19
- Tamm I.E. Theory of magnetic thermonuclear reactor, part 3 Plasma Physics and the Problem of Controlled Thermonuclear Reactions (transl) (New York: Pergamon) p 31–41
- Tamm I.Y. and Sakharov A., “Theory of a magnetic thermonuclear reactor”. Pergamon, Oxford (1961).
- Tanaka H., Phys. Rev. Lett. 80, 5750 (1998).
- Tang W. *et al.* A grid-based Bader analysis algorithm without lattice bias, J. Phys.: Condens. Matter 21, 084204 (2009).
- Thomas A.G.R. *et al.* A review of Vlasov–Fokker–Planck numerical modeling of inertial confinement fusion plasma. Journal of Computational Physics 231 (2012) 1051–1079
- Thomaes, G., and J. Van Itterbeek, J. Mol. Phys., 2, 372 (1959).
- Terai T., Uozumi K. and Takahashi Y., Fusion Technol. 21 (1992) 781.
- Tillack M.S. and Malang S., High Performance PbLi Blanket, in: Proc. 17th IEEE/NPSS Symp. Fusion Engineering, San Diego, USA, October 6–10, vol. 2, Institute of Electrical and Electronics Engineers/Nuclear and Plasma Science Society, 1997, pp. 1000–1004.
- Toloukian Y.S. *et al.*, in: Thermophysical Properties of Matter, Vol. 1, IFI /Plenum, New York, 1970.
- Trioni M. I. *et al.* Ab initio adiabatic He and Ne interaction on Ag: An all-electron calculation. Phys. Rev. B Vol. 58, No 16 15 (1998)
- Tsuda S. *et al.* A study on the growth of cavitation bubble nuclei using large-scale molecular dynamics simulations. *Fluid Dyn. Res.* 40 606 (2008).
- Tyrrell, H. J. V., and Harris, K. R., 1984, Diffusion in Liquids (London: Butterworths).
- Ullmaier H., Rad. EK, 78(1983), 1.
- Ullmaier H. (1986) Radiat. Eff. 101 147
- Ullmaier H. and Trinkaus H., Mater. Sci. Forum., 97-99 (1992), 451.
- Vanderborgh, C. A., Y. K. Vohra, and A. L. Ruoff, 1989, Phys. Rev. B 40, 12 450.
- Velarde G., Aragonés J. M. and IFN team. Analysis of directly driven ICF targets. Laser and Particle Beams, Vol. 4, Issue3-4, pp 349-392 (1986).
- Velarde G. *et al.* Simulation code for ICF including radiative energy transfer. Laser and Particle Beams, Vol 7 Issue 02), pp 305-313 (1989).

- Velarde P., Ogando F., Eliezer S. and Martinez-Val J. 2005 Nuclear Instruments and Methods in Physics Research A 544 329–332.
- Verlet L., Phys. Rev. 159 (1967) 98.
- Vertkov A. *et al.* Technological aspects of liquid lithium limiter experiment on FTU tokamak. Fusion Engineering and Design 82 (2007) 1627–1633
- Victoria M., *et al* J. Nucl. Mater. 276 (2000) 114. b) M. Victoria *et al*, Modelling irradiation effects in fusion materials. Fusion Engineering and Design Vol. 82, 15–24, Pages 2413–2421 (2007)
- Wagner C.: Acta Metall., 1971, vol. 19 (8), pp. 843–49.
- Wakatani M. “Stellarator and Heliotron Devices”. Oxford University Press, Oxford (1998).
- Wanner M. *et al.*, “Status of Wendelstein 7-X construction”, Nucl. Fusion 43, 416 (2003).
- Warren B. E., Averbach B. L. and Roberts B. W. 1951 J. Appl. Phys 22 1493.
- Warren B.E., X-Ray Diffraction (Addison-Wesley, Reading MA, 1969).
- Waseda Y. The Structure of Non-Crystalline Materials: Liquids and Amorphous Solids (McGraw-Hill, New York, 1980)
- Waseda Y and Ohtani M., Z. Phys. B 21 (1975) 229.
- Waseda website: <http://res.tagen.tohoku.ac.jp/~waseda/scm/AXS/index.html>
- Wendt H. R. and Abraham F. F., Phys. Rev. Lett. 41, 1244 (1978).
- Wesson J. "Tokamaks", Second Edition, Oxford Science Series nr. 48, Clarendon Press, Oxford (1997).
- Wijngaarden L. V. Annu. Rev. Fluid Mech. 4, 369 (1972); K. W. Commander and A. Prosperetti, J. Acoust. Soc. Am. 85, 732 (1989); M. Kameda and Y. Matsumoto, Phys. Fluids 8, 322 (1996).
- Wilhelm E. and Battino R. Estimation of Lennard-Jones (6,12) Pair Potential Parameters from Gas Solubility Data. J. Chem. Phys. 55, 4012 (1971);
- Wilson D. Rutherford - Simple Genius. The MIT Press 1983
- Wimmer E. *et al*, Temperature-dependent diffusion coefficients from ab initio computations: Hydrogen, deuterium, and tritium in nickel. Phys Rev B 77, 134305 (2008)
- Wong C.P.C. *et al.* An overview of dual coolant Pb–17Li breeder first wall and blanket concept development for the US ITER-TBM design. Fusion Engineering and Design 81 (2006) 461–467
- Wong C. P. C. *et al.* Molten salt self-cooled solid first wall and blanket design based on advanced ferritic steel. Fusion Engineering and Design 72 (2004) 245–275
- Wright S. private communication
- Wu Y. and the FDS Team. Design status and development strategy of China liquid lithium–lead blankets and related material technology. Journal of Nuclear Materials 367–370 (2007) 1410–1415
- Xie Y. Origin of bcc to fcc phase transition under pressure in alkali metals. New Journal of Physics 10 (2008) 063022 (16pp).

- Yang J. et al. First-principles studies of liquid lithium under pressure. *J. Phys.: Condens. Matter* 22 (2010) 095503 (7pp).
- Yao Y. *Phys Rev B* 85, 214122 (2012).
- Yoder C. F. *et al.* Fluid Core Size of Mars from Detection of the Solar Tide. *Science* 300, 299 (2003).
- Yokoyama I. Temperature dependence of sound velocity and self-diffusion coefficient in liquid alkali metals: a hard-sphere description. *Physica B* 293 (2001) 338-342
- Young, D. A. *Phase Diagram of the Elements* (Univ. California Press, 1991).
- Yoshikawa S. "Design of a helical-axis stellarator", *Nucl. Fusion* 23, 667 (1983).
- Yuan X. *et al.* Development of modified embedded atom method for a bcc metal: lithium. *Modelling Simul. Mater. Sci. Eng.* 11 (2003) 447–456.
- Zalkin A. and Ramsey W. J. 1958 *J. Chem. Phys.* 62 689-93
- Zalkin A. and Ramsey W.J. *Phys. Chem.*, 1957, 61 (10), pp 1413–1415
- Zaremba E. and Kohn W. Theory of helium adsorption on simple and noble-metal surfaces. *Phys Rev B* Vol 15, No 4 15 (1977).
- Zel'dovich Y. B. and Raizier Y. P. *Physics of Shock Waves and High Temperature Hydrodynamic Phenomena* (Academic, New York, 1966), Vol. I, pp. 45-69.
- Ziegler J. F., Biersack J. P. and Littmark U., *The Stopping and Range of Ions in Matter* (Pergamon, New York, 1985).
- Zinkle S.J. Summary of Physical Properties for Lithium, Pb-17Li, and (LiF)_nBeF₂ Coolants, ORNL. APEX Study Meeting. Sandia National Lab, July 27-28, 1998
- Zhang Y. and Maginn E. J. A. *J. Chem. Phys.* 136, 144116 (2012)
- Zhou X. W. Atomic scale structure of sputtered metal multylayers. *Acta Mater.* 49, 4005 (2001).
- Zhou X. W. *et al.* An embedded-atom method interatomic potential for Pd–H alloys. *J. Mater. Res.*, Vol. 23, No. 3, (2008)
- Zhou *et al* X.W. Atomistic simulation study of atomic size effects on B1 (NaCl), B2 (CsCl), and B3 (zinc-blende) crystal stability of binary ionic compounds. *Computational Materials Science* 50 (2011) 2470–2481.
- Zhu Z.Q. *et al.* Preliminary experiment on compatibility of SiCf/SiC composites in static liquid LiPb at 700 C. *Fusion Engineering and Design* 84 (2009) 2048–2051
- Zu X. T. *et al.* Properties of helium defects in bcc and fcc metals investigated with density functional theory. *Phys. Rev. B* 80, 054104 2009



(*) Picture courtesy of Jesus Salvador Martínez.

Dear Prof. Dyson

[....]

What approach do you think is more intelligent and elegant? Magnetic confinement or inertial?

Do you think that ITER is a waste of money and time?

What about NIF?

What do you think about cold fusion?

Thank you very much in advance

Best regards

Alberto Fraile

Dear Alberto,

[.....]

I do not know much about plasma physics but I have some strong opinions. Your questions are easy to answer.

1. Both magnetic and inertial confinement are intelligent and elegant, considered as scientific problems. Neither is likely to be an economic source of energy. It is far too soon to make a choice for one or the other.
2. ITER is a huge waste of money and time.
3. NIF is even worse. NIF is just a welfare program for the Livermore laboratory.
4. Cold fusion is nonsense.

General remark. The fusion programs in all countries made a fundamental mistake when they stopped doing science and started doing large-scale engineering projects. As a result, we have only big projects which are not likely to be useful. To develop economic fusion power, we need new ideas which can only come from new science.

We need small-scale scientific experiments in many different directions to explore the science of plasma physics. Science must come first, engineering later.

Yours sincerely, Freeman Dyson